

# **Conditional Protein Degradation with Novel PROteolysis-TArgeting Chimeras (PROTACs)**

Qisi Zhang

Supervisor: Prof. Edward William Tate

A thesis submitted in partial fulfilment of the requirements for the degree of  
Doctor of Philosophy

Department of Chemistry

Imperial College London

October 2023

## **Statement of Originality**

I, Qisi Zhang, declare that this thesis and the work to which it refers are the results of my own efforts. Any ideas, data, images or text resulting from collaborative work, or the contributions of others have been fully identified as such within the work and attributed to their originator in the text, bibliography or footnotes. This thesis has not been submitted in whole or in part for any other academic degree or professional qualification.

Qisi Zhang

## **Copyright Declaration**

The copyright of this thesis rests with the author. Unless otherwise indicated, its contents are licensed under a Creative Commons Attribution-Non Commercial 4.0 International Licence (CC BY-NC).

Under this licence, you may copy and redistribute the material in any medium or format. You may also create and distribute modified versions of the work. This is on the condition that: you credit the author and do not use it, or any derivative works, for a commercial purpose.

When reusing or sharing this work, ensure you make the licence terms clear to others by naming the licence and linking to the licence text. Where a work has been adapted, you should indicate that the work has been changed and describe those changes.

Please seek permission from the copyright holder for uses of this work that are not included in this licence or permitted under UK Copyright Law.

## **License**

An Elsevier electronic license (License number: 5518691360514) was obtained for reproduction of text and figures in Chapter 1. The license refers to the publication below: Maneiro, M., de Vita, E., Conole, D., Kounde, C. S., Zhang, Q., & Tate, E. W. (2021). PROTACs, molecular glues and bifunctionals from bench to bedside: Unlocking the clinical potential of catalytic drugs. *Progress in Medicinal Chemistry*, 60, 67–190. <https://doi.org/10.1016/BS.PMCH.2021.01.002>

## Abstract

PROteolysis-TArgeting Chimeras (PROTACs) are novel heterobifunctional degraders that catalytically induce targeted protein degradation through the Ubiquitin-Proteasome System (UPS). Offering unique advantages over conventional small molecule inhibitors, PROTACs have successfully degraded a wide range of oncogenic proteins and showed potential as a promising paradigm in drug discovery. Despite the rapid expansion of the field, achieving conditional activation control of PROTAC-mediated protein degradation remains relatively unexplored. In this thesis, two novel PROTAC design strategies were developed to enhance spatiotemporal control and tissue specificity in PROTAC-mediated protein degradation.

In the first design, a novel photoswitchable multi-kinase PROTAC, **AP-PROTAC-2**, was developed to enable conditional light-mediated control of protein degradation. This design incorporates a novel arylazopyrazole photoswitchable linker, combined with a multi-kinase inhibitor capable of engaging approximately 40% of the kinome. **AP-PROTAC-2** can be reversibly switched between *E* and *Z* isomer-enriched states and exhibits superior photochemical properties compared to previous photoswitchable PROTACs. Multiplexed proteomics studies demonstrated that **AP-PROTAC-2** selectively depleted four protein kinases *in vitro* in a light-switchable manner. This research marks the first instance of simultaneous photoswitchable degradation of multiple proteins, achieving selective spatiotemporal modulation of targeted kinase degradation.

In the second design, peptide-based PROTACs were conjugated to monoclonal antibodies to design antibody-peptide degrader conjugates (Ab-peptides), building upon the concept of antibody-drug conjugates (ADCs). These Ab-peptides were designed to utilise ADC's antibody-mediated internalisation pathways for the targeted delivery of peptide payloads to antigen-positive cells. This approach aimed to enhance tissue specificity, cellular uptake, and intracellular degradation potency of peptide-based degraders. The development of three types of Ab-peptides targeting distinct proteins and employing different ADC linkers was reported. The resulting Ab-peptides exhibited enhanced target degradation efficacy surpassing that of unconjugated peptides, underscoring their promising potential.

Collectively, these novel strategies offer valuable perspectives and insights into conditional protein degradation with a focus on photoswitchable multi-target PROTACs and peptide-based PROTACs.

## Acknowledgements

I would like to express my heartfelt gratitude to everyone who has played a part in my journey throughout my PhD. These past four years have been an extraordinary experience in my life. The memories will forever hold a special place in my heart.

First, I want to extend my deepest appreciation to my supervisor, Prof. Ed Tate. Thank you for giving me the opportunity to work in this amazing lab and for providing consistent encouragement and support. Your guidance and mentoring have been instrumental in shaping my scientific understanding as well as fostering my personal and professional development.

I also wish to convey my sincere gratitude to the PROTAC team and the bifunctional discussion group. Cyrille, your mentorship has been invaluable. Thank you for guiding me into the journey of PROTAC research, for your guidance in chemistry, and for the inspiring scientific discussions. My sincere thanks also go to Maria and Elena for their consistent helpfulness and care. Milon, your training in proteomics, patience, and kindness have been greatly appreciated. To Dan, Wouter, Jack and Andrea, I am grateful for your helpful discussions and professional support on proteomics.

My appreciation extends to our ever-expanding ADC team and the peptide group. Rita, your assistance in getting me started with peptide synthesis has been invaluable. Ammar and Archie, you have been wonderful friends and colleagues, thank you for your insightful discussions about ADCs, support on purification techniques, and help with our needy and challenging lab equipment.

I am also grateful to the other members of the Tate research group. I consider myself fortunate to have been surrounded by such talented and inspiring individuals. The collaborative environment fostered by my colleagues has enriched my research experience in many ways. Thanks to the colleagues in charge of maintaining our important lab facilities. Thank you, Leran, for being a wonderful friend, colleague and good teacher in the lab. To Zhangping, Fangyuan, Xinyue, Roxani, Sarah, Sofia, Ana, Masha, Josephine, Lame, Shradda, Amrita and Vincent, thank you for the insightful discussions and knowledge sharing. Ravi, Edward, Tom, and Erika, your lab management and consistent support are greatly appreciated. I would also like to thank Prof. Matthew Fuchter and Dr Jake Greenfield for their assistance in characterising the photoswitching properties and finalising our paper.



I extend my appreciation to the faculty and staff of Imperial MSRH for providing exceptional resources and a conducive research environment. This includes Andrew Coulson, Lisa Haigh, Peter Haycock, Mike Ray, Doris Pappoe and Kamil Skirlo.

To our collaborators at ADC Therapeutics, I am grateful for the funding support and opportunities you have provided. Paul, Nico, Alina, Matt and Francesca, thank you for your technical assistance and inspiring meetings.

My sincere gratitude goes to my proofreaders, Zhangping, Archie, and Ammar, for your invaluable feedback that significantly contributed to improving the quality of this thesis. I am also deeply grateful to my internal examiner, Dr Louise Walport, and external examiner, Dr James Hodgkinson, for their insightful discussions during the viva, and for the comments and feedback that enhanced the overall quality of this thesis.

To my friends, the companionship we've enjoyed and the delightful moments we've shared, whether in person or virtually, have truly enriched this journey. A special mention goes to my BBF Yixi Gao, your support and love have meant a lot to me, I will always stand by your side just as you have been for me.

To my husband Dr Xiao Liu, you have been my inspiration and driving force. Pursuing a PhD alongside you has been the most courageous and adventurous endeavour I've ever undertaken. I could not have accomplished this without you by my side. Your unconditional support and love have been a constant source of strength, and I am truly fortunate to have you in my life. Love you.

And lastly, to my wonderful parents, thank you for raising me, supporting me, and encouraging me to explore the broader world. You have taught me to be humble, resilient, and persistent through your examples. Your unwavering encouragement, understanding, and love have sculpted me into the person I am today. Your belief in my abilities has been a tremendous source of motivation throughout this journey. I hope I have made you proud.

## Publications

1. Zhang, Q., Kounde, C. S., Mondal, M., Greenfield, J. L., Baker, J. R., Kotelnikov, S., Ignatov, M., Tinworth, C. P., Zhang, L., Conole, D., de Vita, E., Kozakov, D., McCluskey, A., Harling, J. D., Fuchter, M. J., & Tate, E. W. (2022). Light-mediated multi-target protein degradation using arylazopyrazole photoswitchable PROTACs (AP-PROTACs). *Chemical Communications*, 58(78), 10933–10936. <https://doi.org/10.1039/d2cc03092f>
2. Maneiro, M., de Vita, E., Conole, D., Kounde, C. S., Zhang, Q., & Tate, E. W. (2021). PROTACs, molecular glues and bifunctionals from bench to bedside: Unlocking the clinical potential of catalytic drugs. *Progress in Medicinal Chemistry*, 60, 67–190. <https://doi.org/10.1016/BS.PMCH.2021.01.002>

## Oral and poster presentation

- 33<sup>rd</sup> Fine Chemical Group Postgraduate symposium, oral presentation, University of Newcastle, May 2023
- Scientific Seminar of Graduate School, Life Science Engineering, oral presentation, TU Darmstadt, Nov 2022
- Department of Chemistry Postgraduate Symposium, oral presentation, Imperial College London, July 2022
- Department of Chemistry Postgraduate Symposium, poster presentation, Imperial College London, July 2021

## Table of Contents

Statement of Originality .....	2
Copyright Declaration .....	2
License.....	2
Abstract.....	3
Acknowledgements .....	4
Publications .....	6
Oral and poster presentation .....	6
Table of Contents .....	7
List of Figures.....	12
List of Tables .....	17
List of Abbreviations .....	18
Chapter 1 Introduction <sup>1</sup> .....	20
1.1 PROTAC-mediated targeted protein degradation .....	21
1.2 Historical timeline and milestones of PROTACs.....	23
1.3 Advantages of PROTACs over traditional small molecule inhibitors .....	25
1.4 Key parameters of PROTAC activity and design considerations .....	28
1.5 Emerging approaches in targeted protein degradation .....	32
1.5.1 Light-responsive PROTACs enable spatiotemporal control .....	33
1.5.2 Multi-target PROTACs: Transitioning from promiscuous kinase inhibitors to target-selective degraders .....	35
1.5.3 Peptide-based PROTACs: expanding the toolbox .....	38
1.5.4 Antibody-PROTAC conjugates: achieving tissue-selective protein degradation .....	41
1.6 Thesis aims and objectives .....	46
Multi-kinase degradation with photoswitchable PROTACs (AP-PROTACs, Chapter 2) .....	46
Antibody-peptide degrader conjugates (Ab-peptide, Chapter 3).....	47
Chapter 2 Photoswitchable multi-kinase degradation with novel arylazopyrazole-based photoswitchable PROTAC .....	48
2.1 Introduction.....	48
2.2 Synthesis and characterisation of novel arylazopyrazole-based photoswitchable linker 49	
2.2.1 Light-responsive photoswitches enable spatiotemporal control.....	49
2.2.2 Synthesis of an arylazopyrazole photoswitchable linker.....	51
2.2.3 Photoswitching properties characterisation of linker 4 .....	53

<b>2.3 Targeting multiple kinases with photoswitchable PROTACs .....</b>	<b>58</b>
2.3.1 Protein kinases as drug targets .....	58
2.3.2 Promiscuous kinase inhibitors CTx-0294885 .....	59
2.3.3 Photoswitchable multi-kinase PROTAC: the design .....	60
<b>2.4 Synthesis and photoswitching properties characterisation of AP-PROTAC-2.....</b>	<b>61</b>
2.4.1 Synthesis of AP-PROTAC-2.....	61
2.4.2 Photoswitching properties characterisation of AP-PROTAC-2 (7).....	63
<b>2.5 Cytotoxicity assay of AP-PROTAC-2 .....</b>	<b>65</b>
<b>2.6 Quantitative multiplexed proteomics analysis of kinase degradation .....</b>	<b>66</b>
<b>2.7 Immunoblots verification of degraded kinase targets .....</b>	<b>69</b>
<b>2.8 In-cell Western .....</b>	<b>71</b>
<b>2.9 Computational studies of the ternary complex .....</b>	<b>72</b>
<b>2.10 Discussion and conclusion .....</b>	<b>74</b>
2.10.1 Potential optimisation of the immunoblot results.....	74
2.10.2 Comparison of AP-PROTAC-2 with reported photoswitchable PROTACs .....	75
2.10.3 Conclusion .....	77
<b>Chapter 3 Antibody-peptide degrader conjugates (Ab-peptides): the use of peptide-based degraders as ADC payloads .....</b>	<b>78</b>
<b>3.1 Introduction.....</b>	<b>78</b>
<b>3.2 Peptide synthesis .....</b>	<b>80</b>
<b>3.3 ADC linkers .....</b>	<b>81</b>
<b>3.4 Targeting ER<math>\alpha</math> with trastuzumab-conjugated peptide-based PROTACs .....</b>	<b>84</b>
3.4.1 TD-PROTAC: a peptide-based PROTAC degrading ER $\alpha$ .....	84
3.4.2 Design of Ab-peptide degrader conjugates: trastuzumab-TD-PROTAC conjugates .....	86
3.4.3 Synthesis of the reported peptide-PROTAC (TD-PROTAC) .....	88
3.4.4 Immunoblot profiling of TD-PROTAC <i>in vitro</i> .....	90
3.4.5 Synthesis of ADC linker-peptide constructs .....	93

3.4.6 Conjugation of trastuzumab to linker-peptide constructs.....	95
3.4.7 Immunoblot profiling of antibody-peptide conjugate HER2-15 .....	97
3.4.8 Summary .....	98
<b>3.5 Targeting CREPT with cetuximab-conjugated peptide-based PROTACs .....</b>	<b>99</b>
3.5.1 PRTC: A linear peptide-PROTAC targeting CREPT for pancreatic cancer treatment .....	99
3.5.2 Design of cetuximab-PRTC conjugates and peptide synthesis .....	100
3.5.3 <i>In vitro</i> immunoblot profiling of PRTC analogue QZ-017 .....	103
3.5.4 Conjugation of cetuximab to linker-peptide constructs.....	104
3.5.5 Immunoblot profiling of cetuximab-PRTC conjugate EGFR-21 .....	105
3.5.6 Immunoblot analysis of the degradation mechanism of EGFR-21 .....	107
3.5.7 Summary .....	109
<b>3.6 Targeting bromodomains with peptide-based protein degraders through direct proteasome recruitment .....</b>	<b>112</b>
3.6.1 Novel strategy for protein degradation through direct 26S proteasome recruitment.....	112
3.6.2 Synthesis of QZ-027, an analogue of the reported peptide degrader .....	114
3.6.3 Immunoblot profiling of QZ-027 <i>in vitro</i> .....	115
3.6.4 Design and synthesis of linker-peptide constructs for QZ-027 .....	116
3.6.5 Summary .....	118
<b>3.7 Conclusion .....</b>	<b>119</b>
<b>Chapter 4 Conclusion, Limitations and Future Directions.....</b>	<b>120</b>
<b>4.1 Conclusion .....</b>	<b>120</b>
<b>4.2 Limitations and future perspectives.....</b>	<b>121</b>
Multi-kinase degradation with Photoswitchable PROTAC (AP-PROTACs) .....	121
Antibody-peptide degrader conjugates (Ab-peptides).....	122
<b>Chapter 5 Materials and methods.....</b>	<b>125</b>
<b>5.1 Chemistry.....</b>	<b>125</b>

5.1.1 Materials and instrumentations .....	125
5.1.2 Synthesis .....	125
5.1.3 Peptide synthesis .....	131
<b>5.2 Photoswitching properties characterisation .....</b>	<b>136</b>
5.2.1 Instrumentation .....	136
5.2.2 LC-MS method for PSS determination .....	136
5.2.3 UV-Vis spectroscopy determination of the PSS of linker 4 .....	136
5.2.4 NMR spectroscopy determination of PSS of linker 4 .....	138
5.2.5 UV-Visible spectroscopy determination of thermal half-life .....	138
<b>5.3 Bioconjugation.....</b>	<b>139</b>
5.3.1 Conjugation methods for peptide-based PROTACs.....	139
5.3.2 Determination of new molecular weight (MW) of the ADC:.....	140
5.3.3 HIC and SEC analysis .....	140
<b>5.4 Biology.....</b>	<b>141</b>
5.4.1 Cell culture and treatment.....	141
5.4.2 Cell lysis .....	141
5.4.3 Immunoblotting .....	142
5.4.4 In-cell western.....	142
5.4.5 Cell toxicity assay .....	143
<b>5.5 Proteomics .....</b>	<b>143</b>
5.5.1 Sample preparation.....	143
5.5.2 LC-MS/MS and data analysis .....	144
<b>5.6 Computational modelling of PROTAC ternary complex .....</b>	<b>145</b>
<b>Chapter 6 Bibliography.....</b>	<b>146</b>
<b>Chapter 7 Appendix.....</b>	<b>171</b>

<b>7.1 Chapter 2 Additional data .....</b>	<b>171</b>
7.1.1 NMR spectra of Chapter 2 compounds .....	171
7.1.2 NMR spectroscopy determination of PSS of linker 4 .....	184
7.1.3 LC-MS chromatograms .....	186
7.1.4 UV-Vis spectra .....	190
7.1.5 Cytotoxicity assay of AP-PROTAC-2 .....	190
7.1.6 Fold change plot in proteomics analysis of AP-PROTAC-2 .....	191
7.1.7 Immunoblots .....	192
<b>7.2 Chapter 3 Additional data .....</b>	<b>194</b>
7.2.1 LC-MS spectra of ADC linkers in TFA .....	194
7.2.2 Investigation of aspartimide formation during the synthesis of TD-PROTAC .....	196
7.2.3 HPLC traces and LC-MS spectra of peptides in Chapter 3 .....	197
7.2.4 Characterisation of ADCs in Chapter 3 .....	207
7.2.5 Investigation of antibody conjugation: NAC assay of QZ-015 .....	210
<b>7.3 Reprint Permissions .....</b>	<b>211</b>

## List of Figures

Figure 1-1. The Ubiquitin-Proteasome system (UPS) and PROTACs .....	22
Figure 1-2. Historical timeline of PROTAC development, showing the most significant milestones and some representative PROTAC structures .....	24
Figure 1-3. Structures of selected PROTAC examples .....	27
Figure 1-4. Key parameters to evaluate PROTAC activity .....	29
Figure 1-5. Representative E3 ligase ligands used for PROTAC design and structural considerations of PROTACs.....	30
Figure 1-6. Distribution of proteins degraded by PROTACs according to (A) target class (B) cellular localisation and (C) therapeutic area.....	32
Figure 1-7. Light-responsive PROTAC strategies.....	33
Figure 1-8. Structures of representative photo-caged PROTACs and photoswitchable PROTACs .....	34
Figure 1-9. Multi-target PROTAC developed from promiscuous inhibitors.....	36
Figure 1-10. Mechanisms of drug delivery mediated by an internalising ADC .....	42
Figure 1-11 The general structure of an ADC and the roles of each component .....	43
Figure 1-12. Mechanism of action of Antibody-PROTAC conjugates .....	44
Figure 1-13. Ab-PROTAC design by Maneiro <i>et al.</i> .....	45
Figure 2-1 Azobenzene photoswitch .....	50
Figure 2-2 Arylazopyrazole photoswitch 4pzMe .....	51
Figure 2-3 UV-Vis spectra of linker 4 .....	53
Figure 2-4. LC-MS chromatograms of linker 4. ....	55
Figure 2-5. Characterisation of the photostationary state of linker 4 isomers using NMR .....	56



Figure 2-6. Model of the Cullin-RING ligase 4 complex .....	61
Figure 2-7 Photoswitching properties characterisation of AP-PROTAC-2.....	64
Figure 2-8 Cytotoxicity assays of AP-PROTAC-2.....	65
Figure 2-9 Quantitative proteomics workflow employed.....	67
Figure 2-10 Volcano plots showing changes in protein levels with AP-PROTAC-2 treatment .....	68
Figure 2-11. AP-PROTAC-2 differentially degrades FAK and AURORA-A on immunoblots .....	69
Figure 2-12. Immunoblots and quantification for FAK, AURORA-A, TBK1, and $\beta$ -actin in bortezomib (BTZ) pre-treated MDA-MB-231 cells .....	70
Figure 2-13. In-cell western results .....	71
Figure 2-14. Structural model of the CRBN/(E)-AP-PROTAC-2/FAK complex.....	73
Figure 2-15. Histogram of the distances between the linker attachment nitrogens for <i>E</i> and <i>Z</i> ETKDG-derived MMFF-optimised PROTAC conformers .....	74
Figure 3-1. The structure and characteristics of a devised antibody-peptide degrader conjugate .....	79
Figure 3-2. Fmoc-based solid-phase peptide synthesis (Fmoc-SPPS) used in this chapter.....	81
Figure 3-3. ADC linkers used in this study and their predicted intracellular ADC catabolism and payload release mechanism.....	83
Figure 3-4 Structure of peptides and the immunoblot studies of TD-PROTAC .....	85
Figure 3-5. X-ray structure of ER $\alpha$ in complex with PERM-1.....	86
Figure 3-6. Structure of peptide PROTACs and the proposed structure of an antibody-peptide conjugate .....	87
Figure 3-7. Schematic representation of synthetic routes of TD-PROTAC .....	88

Figure 3-8. The proposed mechanism for aspartimide formation during the synthesis of TD-PROTAC linear peptide .....	89
Figure 3-9. A modified synthetic route to precursors of TD-PROTAC and its analogues.....	90
Figure 3-10. <i>In vitro</i> testing of TD-PROTAC in three cell lines .....	91
Figure 3-11. Structure of peptides and the immunoblot studies of ER $\alpha$ peptide-based PROTACs from Dai <i>et al.</i> .....	92
Figure 3-12. Schematic representation of synthetic routes of linker-peptide constructs .....	94
Figure 3-13 <i>In vitro</i> testing of HER2-15 (trastuzumab-QZ-015 conjugate) in BT-474 cell line .....	97
Figure 3-14. Schematic diagram of CREPT-targeting peptide PROTAC PRTC and its immunoblot studies .....	100
Figure 3-15. Co-crystal structure of the HIF-1 $\alpha$ peptide bound to the VHL/ElonginB/ElonginC (VBC) complex.....	101
Figure 3-16. Structures of PRTC analogue QZ-017, linker-peptide conjugates QZ-019 and QZ-021 .....	102
Figure 3-17. <i>In vitro</i> testing of PRTC analogue QZ-017 in Panc-1 cells .....	103
Figure 3-18. <i>In vitro</i> testing of EGFR-21 (cetuximab-QZ021 conjugate) in Panc-1 cells ....	106
Figure 3-19. <i>In vitro</i> testing of EGFR-21 (cetuximab-QZ021 conjugate) in Panc-1 cell line with co-treatment of the proteasome inhibitor bortezomib (BTZ) .....	108
Figure 3-20. Targeted degradation via direct 26S proteasome recruitment.....	113
Figure 3-21. Schematic representation of synthetic routes of CIDE analogue CIDE-JQ1 (QZ-027) .....	115
Figure 3-22. <i>In vitro</i> testing of CIDE-JQ1 QZ-027 in HEK293 cell line .....	116
Figure 3-23. Schematic representation of synthetic routes of MC1 analogue with ADC linker, QZ-028.....	117

Figure 5-1. Synthesis of AP-PROTAC-2.....	128
Figure 5-2. Synthesis of JQ1-azide .....	129
Figure 7-1 LC-MS chromatograms of AAP linker 4 .....	186
Figure 7-2. LC-MS chromatograms of AP-PROTAC-2.....	187
Figure 7-3. LC-MS chromatograms of AP-PROTAC-2, after 8 min of 457 nm irradiation .	188
Figure 7-4. LC-MS chromatograms of AP-PROTAC-2 with irradiation, after 8 min of 457 nm irradiation and followed by 8 min of 365 nm irradiation .....	189
Figure 7-5 UV-Vis spectra of a solution of CTx-0294885 in DMSO (ca. 10 $\mu$ M) .....	190
Figure 7-6 Cytotoxicity assays of AP-PROTAC-2.....	190
Figure 7-7 Fold change plot in proteomics analysis of AP-PROTAC-2 .....	191
Figure 7-8. Immunoblots and quantification of GAK and $\beta$ -actin in MDA-MB-231 cells after treatment .....	192
Figure 7-9. Immunoblots and quantification of FAK, AURORA-A, TBK1, GAK in MDA-MB-231 cells after treatment .....	193
Figure 7-10 LC-MS spectra of ADC linker 1 in 20% MeCN in water with 0.1% formic acid with eq20 gradient.....	194
Figure 7-11. LC-MS spectra of ADC linker 2 in 20% MeCN in water with 0.1% formic acid with eq20 gradient.....	195
Figure 7-12. LC-MS spectra of ADC linker 3 in 20% MeCN in water with 0.1% formic acid with eq20 gradient.....	195
Figure 7-13. Investigation of aspartimide formation during synthesis of TD-PROTAC .....	196
Figure 7-14. TD-PROTAC peptide characterisation .....	197
Figure 7-15. QZ-014 peptide characterisation .....	198
Figure 7-16. QZ-015 peptide characterisation .....	199

Figure 7-17. QZ-016 peptide characterisation .....	200
Figure 7-18 QZ-017 peptide characterisation .....	201
Figure 7-19. QZ-019 peptide characterisation .....	202
Figure 7-20. QZ-021 peptide characterisation .....	203
Figure 7-21. QZ-026 crude peptide characterisation .....	204
Figure 7-22. QZ-027 peptide characterisation .....	205
Figure 7-23. QZ-028 crude peptide characterisation .....	206
Figure 7-24. Trastuzumab-QZ015 (HER2-15) ADC characterisation with hydrophobic interaction chromatography (HIC).....	207
Figure 7-25. B12-21 ADC characterisation data .....	208
Figure 7-26. EGFR-21 ADC characterisation data.....	209
Figure 7-27. Structure and MS positive spectra of QZ-015 before and after reaction with NAC.....	210

## List of Tables

Table 1. The top 20 most frequently degraded kinases in Donovan <i>et al.</i> 's study.....	38
Table 2. Comparison of peptide-based PROTAC and small molecule PROTAC. <sup>129</sup> .....	40
Table 3. Representative peptide-based PROTACs. ....	41
Table 4. Summary of PSS ratio results determined with different methods.....	57
Table 5. Summary of representative photoswitchable PROTACs.....	76
Table 6. Conditions employed in small-scale test bioconjugation of trastuzumab to linker-peptide constructs.....	95
Table 7. Bioconjugation conditions employed for cetuximab to linker-peptide constructs. .	104
Table 8. Attempted CuAAC conditions to conjugate QZ-028 (1 eq.) and JQ1-azide (1 eq.). .....	118
Table 9. Microwave methods used .....	133

## List of Abbreviations

AAP	Arylazopyrazole	DMA	Dimethylacetamide
ADC	Antibody-Drug Conjugate	DMEM	Dulbecco's Modified Eagle's Medium
AHX	6-aminohexanoic acid	DMF	Dimethylformamide
ASGPR	Asialoglycoprotein receptors	DMP	Dess-Martin periodinane, 1,1,1-Tris(acetyloxy)-1,1-dihydro-1,2-benziodoxol-3-(1H)-one
ATP	Adenosine triphosphate	DMSO	Dimethyl sulfoxide
ATTEC	AuTophagosome-TEthering Compounds	DNA	Deoxyribose nucleic acid
AUC	Area under curve	DUB	Deubiquitinase
AURORA-A	Aurora kinase A	EDTA	Ethylenediaminetetraacetic acid
AUTAC	Autophagy Targeting Chimera	EGFR	Epidermal growth factor receptor
AUTOTAC	AUTophagy-TArgeting Chimera	ELISA	Enzyme-linked immunosorbent assay
BET	Bromodomain and extra-terminal domain	ESI	Electrospray ionization
BRD	Bromodomain proteins	FAK	Focal adhesion kinase
BSA	Bovine serum albumin	FBS	Fetal bovine serum
BTK	Bruton's tyrosine kinase	FDA	Food and Drug Administration
BTZ	Bortezomib	FDR	False discovery rate
CAA	Chloroacetamide	FFT	Fast fourier transform
CCT	Coiled-coil terminus	FITC	Fluorescein isothiocyanate
CDK	Cyclin-dependent kinase	FKBP	FK506 binding proteins
CIDE	Chemical inducers of degradation	Fmoc	Fluorenylmethyloxycarbonyl protecting group
CLL1	C-type lectin-like molecule-1	GAK	Cyclin G-associated kinase
CML	Chronic myelogenous leukemia	GAPDH	Glyceraldehyde 3-phosphate dehydrogenase
CNS	Central nervous system diseases	GFP	Green fluorescent protein
CPP	Cell-penetrating peptide	GSH	Glutathione
CRBN	Cereblon	GST	Glutathione S-transferase
CRC	Colorectal cancer	HATU	1-[Bis(dimethylamino)methylene]-1H-1,2,3-triazolo[4,5-b]pyridinium 3-oxide hexafluorophosphate
CREPT	Cell cycle-related and expression-elevated protein in tumour	HBA	Hydrogen bond acceptor
CRISPR/Cas9	Clustered Regularly Interspaced Short Palindromic Repeats/CRISPR associated protein 9	HBD	Hydrogen bond donor
CRLs	Cullin-RING E3 ligases	HEPES	2-[4-(2-hydroxyethyl)piperazin-1-yl]ethanesulfonic acid
CRPET	Cell cycle-related and expression-elevated protein in tumour	HER2	Human epidermal growth factor receptor 2
DAD	Diode-Array Detection	HIC	Hydrophobic interaction chromatography
DAR	Drug-to-antibody ratio	HIF1 $\alpha$	Hypoxia-inducible factor 1 $\alpha$
DBU	1,8-Diazabicyclo [5.4.0] undec-7-ene	HOBt	Hydroxybenzotriazole
DC <sub>50</sub>	Half-maximal degradation concentration	HPLC	High-performance liquid chromatography
DCAF	DDB1 and CUL4 associated factor	HRMS	High-resolution mass spectrometry
DCM	Dichloromethane	HRP	Horseradish peroxidase
DEL	DNA-encoded library	HTS	High-throughput screening
DIC	N,N'-Diisopropylcarbodiimide		
DIPEA	Diisopropylethylamine		

IA	Inflammation and autoimmune diseases	PTM	Post-Translational Modification
IAP	Inhibitor of apoptosis protein	RBM39	RNA Binding Motif Protein 39
IC <sub>50</sub>	Half maximal inhibitory concentration	RING	Really interesting new gene
ICW	In-cell western	RIPK2	Receptor-interacting serine/threonine-protein kinase 2
IKZF1	IKAROS Family Zinc Finger 1	RNA	Ribonucleic acid
IKZF3	IKAROS Family Zinc Finger 3	RNAPII	RNA polymerase II
IMiDs	Immunomodulatory imide drugs	RNF	RING (really interesting new gene) finger
IPA	Isopropyl alcohol	RP	reversed phase chromatography
KCN	Potassium cyanide	RT	Room temperature
kDa	kilo Daltons	RTK	Receptor-tyrosine kinase
KEAP1	Kelch-like ECH-associated protein 1	SAR	Structure-activity relationships
LBD	ligand-binding domain	SDS	Sodium dodecyl sulfate
LC-MS	Liquid chromatography-mass spectrometry	SEC	Size-exclusion chromatography
LED	Light-emitting diode	SERD	Selective estrogen receptor degrader
LYTAC	Lysosome-targeting chimeras	SERM	Selective estrogen receptor modulator
MALDI	Matrix-assisted laser desorption/ionization	SNIPERs	Specific and Nongenetic Inhibitor of Apoptosis Protein (IAP)-dependent Protein Erasers
mc	Maleimidocaproyl	SPAAC	Strain-promoted azide-alkyne cycloaddition
MeCN	Acetonitrile	SPPS	Solid Phase Peptide Synthesis
MDM2	Mouse Double Minute 2 homologue	SPR	Surface plasmon resonance
MDS	Myelodysplastic syndrome	STAT	Signal transducers and activator of transcription
MMAE	Monomethyl auristatin E	TBK1	TANK binding kinase 1
MOA	Mechanism of action	TBS-T	Tris-buffered saline with 0.1 % Tween-20
MS	Mass spectrometer	TCEP	Tris(2-carboxyethyl)phosphine
MWCO	Molecular weight cut-off	TFA	Trifluoroacetic acid
NAC	N-Acetyl Cysteine	THPTA	Tris(3-hydroxy-propyltriazolylmethyl)amine
NHR	Nuclear hormone receptor	TIPS	Triisopropylsilane
NMR	Nuclear magnetic resonance	TLC	Thin-layer chromatography
ONC	Oncology	TMT	Tandem mass tags
PABC	<i>para</i> -Amino benzyloxycarbonyl	TOF	Time-of-flight
PBS	Phosphate-buffered saline	TPD	Targeted protein degradation
PDA	Photodiode array	Ub	Ubiquitin
PDB	Protein Data Bank	UPS	Ubiquitin Proteasome System
PEG	Polyethylene glycol	UV	Ultraviolet
PHOTAC	PHOtochemically TARgeting Chimeras	UV-Vis	Ultraviolet-visible
PK	Pharmacokinetic	va	Valine-alanine
POI	Protein of interest	VBC	VHL/ElonginB/ElonginC
PPI	Protein-protein interaction	vc	Valine-citrulline
PROTAC	PROteolysis Targeting Chimera	VHL	von-Hippel Lindau
PRTC	PROTAC against CREPT	WB	Western Blotting
PS20	Polysorbate 20		
PSMD2	Proteasome 26S subunit ubiquitin receptor, non-ATPase 2		
PSS	Photostationary states		

## Chapter 1 Introduction<sup>a,1</sup>

Over the past century, drug discovery has evolved significantly, with the refinement of two predominant strategies: small molecule drugs and monoclonal antibodies.<sup>2,3</sup> Traditional small molecule inhibitors, extensively researched and frequently marketed, operate on an ‘occupancy-driven’ mechanism of action (MOA). The efficacy of these therapeutic inhibitors depends on target engagement to achieve high equilibrium target occupancy and prolonged exposure in the diseased tissue. Such outcomes often require high dosages and enhanced drug exposure at the target site, thus increasing the risk of undesired off-target toxicities.<sup>4</sup> Although small molecule drugs have served as effective treatments for decades, addressing a variety of disease-relevant targets with a defined binding site, many relevant therapeutic targets remain challenging to drug. Deemed ‘undruggable’, these targets lack a well-defined binding pocket or their large protein-protein interaction (PPI) interfaces present difficulties for small molecule inhibition.<sup>5</sup> On the other hand, monoclonal antibodies, despite often exhibiting high affinity and specificity for their targets, are constrained by restricted distribution to the target site and poor cell permeability. Consequently, most approved therapeutic antibodies target extracellular antigens.<sup>6</sup>

In the quest for alternative therapeutic approaches to address diverse pathologies and enhance efficacy whilst reducing side effects, ligand-induced targeted protein degradation (TPD) has drawn the attention of numerous research groups both in academia and industry over the last two decades. This approach employs bifunctional small molecule degraders, termed PROteolysis TArgeting Chimeras (PROTACs), to redirect proteins of interest (POI) to the cellular protein homeostasis machinery for proteasomal degradation.<sup>7</sup> With their unique

---

<sup>a</sup> Some passages and figures in Chapter 1 , section 1.1 to 1.4 have been adapted from the author’s original work in this previous publication with obtained copyright: M. Maneiro, E. De Vita, D. Conole, C. S. Kounde, **Q. Zhang** and E. W. Tate, *Prog Med Chem*, 2021, **60**, 67–190.



catalytic protein degradation MOA, PROTACs represent a novel paradigm in drug discovery, divergent from conventional small molecule inhibitors.

In this chapter, a literature review of PROTACs was provided, elucidating their mode of action and the key factors in structural design. A historical perspective on the development of PROTACs was presented, summarising the experimental progress made to unravel this novel therapeutic modality. Moreover, the unique advantages of PROTACs and their potential applications as therapeutic agents or molecular tools in biology were discussed, and the relevant emerging strategies for TPD were highlighted. This chapter concluded with the aims and objectives of this thesis.

## **1.1 PROTAC-mediated targeted protein degradation**

Dynamic modulation of protein levels is a fundamental process for the maintenance of cellular homeostasis. Protein degradation machinery, alongside protein expression and regulatory mechanisms, have evolved as essential players in protein recycling and regulation.<sup>8</sup> Endogenous protein degradation needs to be tightly regulated to favour the disposal of aberrant or abnormal proteins, without incurring pathological or uncontrolled depletion of functional proteins and other cellular components. Different protein degradation pathways have been identified in cells, the most important being the ubiquitin-proteasome system (UPS) and lysosomal degradation.<sup>9</sup> PROTACs are compounds designed to hijack the UPS system to induce the degradation of specific POIs.

The UPS is a highly regulated intracellular protein degradation machinery, responsible for recycling most proteins in eukaryotes (Figure 1-1A).<sup>10</sup> Substrate proteins destined for degradation are covalently tagged with ubiquitin (Ub), a highly conserved 76-amino acid protein. This process is stepwise regulated by the coordinated action of three ubiquitinating enzymes: E1 (ubiquitin-activating enzyme), E2 (ubiquitin-conjugating enzyme) and E3 (ubiquitin-protein ligase). These enzymes sequentially activate, conjugate, and transfer an ubiquitin molecule to a lysine or the N-terminal of protein substrates, operating in an ATP-dependent manner. Varied ligases sequences are associated with differing substrates. Deubiquitinases (DUBs), functioning as cysteine or metallo-proteases, remove mono- or poly-Ub chains from proteins and antagonise protein ubiquitination. DUBs contribute to the tight regulation of programmed protein degradation, ultimately influencing the localisation, activity, protein-protein interactions of the substrate proteins.<sup>11</sup>

For protein degradation to occur, the ubiquitination cycle is repeated at least four times, forming a polyubiquitin chain on the protein substrate, which is thus tagged for recognition by the 26S proteasome. The proteasome is a macromolecular protein complex of a cylindrical structure composed of a 20S proteolytic core, where threonine proteases with different substrate specificity catalyse the degradation of proteins, and a 19S regulatory cap that recognises ubiquitin-tagged proteins and directs them to the core for degradation. Proteolysis catalysed by the proteasome converts the protein into peptide fragments and ubiquitin molecules, which are released into the cytosol and recycled for anabolism.<sup>12–14</sup>

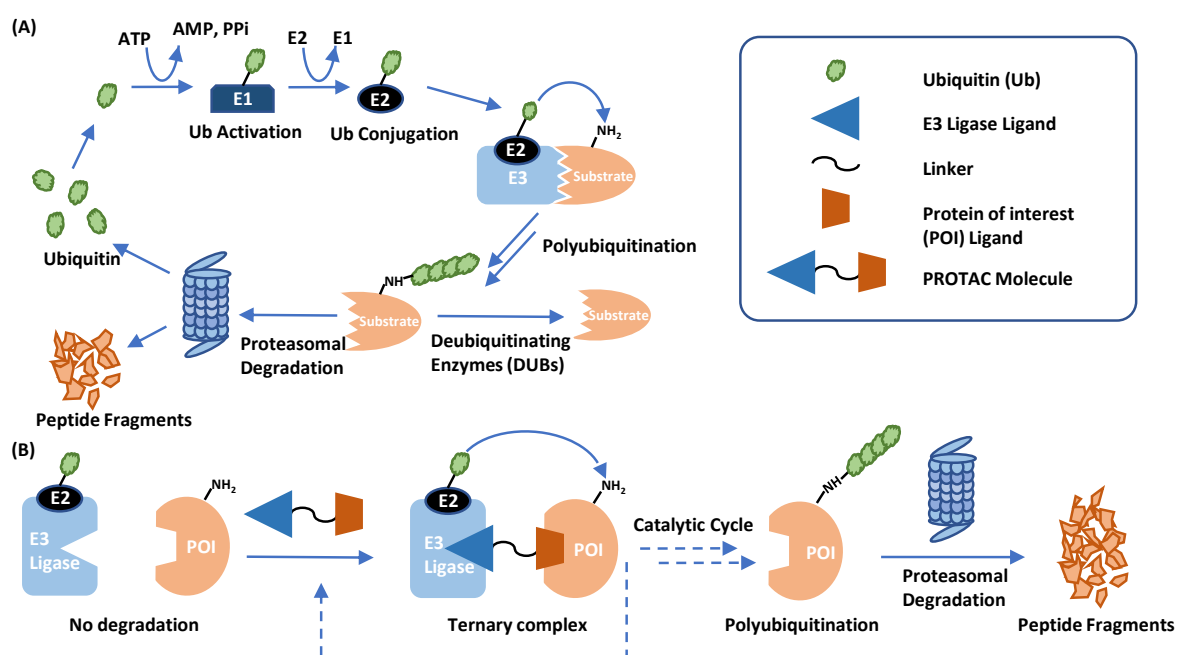


**Figure 1-1. The Ubiquitin-Proteasome system (UPS) and PROTACs**

(A) The ubiquitin-proteasome system (UPS) is one of the main regulatory mechanisms for protein homeostasis in eukaryotes. (B) The catalytic MOA of PROTACs involves the formation of a key ternary complex with an E3 ligase and a POI resulting in polyubiquitination of the POI and subsequent proteasomal degradation. Image adapted with permission.<sup>1</sup>

On the basis of an emerging understanding of the proteasomal degradation pathway, PROTACs have been designed as heterobifunctional molecules consisting of three basic components: an E3 ligase-recruiting ligand, a POI-binding warhead, and a suitable linker connecting these units (Figure 1-1B). This chimeric structure enables simultaneous recruitment of both the POI and the E3 ligase, forming a stable ternary complex (E3-PROTAC-POI). Consequently, the PROTAC induces sufficient proximity between the E3 ligase and the POI to allow for the transfer of the first ubiquitin molecule from the E2 enzyme to the POI. This is followed by the

rapid transfer of additional ubiquitin units leading to a polyubiquitin-tagged POI, which is then recognised by the 26S proteasome and degraded in a manner similar to native UPS substrates.

## 1.2 Historical timeline and milestones of PROTACs

The concept of chimeric degraders was first described in patent literature in 1999 by Proteinix, a biotech company. The company described bifunctional compounds comprising an ubiquitination recognition element and a POI binding element to regulate protein levels and activity.<sup>15</sup> The term PROteolysis-TArgeting Chimaeras (PROTACs) was first introduced in 2001, in a pioneering work by the Crews group, who designed a phosphopeptide to recruit the SCF <sup>$\beta$ -TRCP</sup> E3 ligase for the degradation of methionine aminopeptidase-2 (MetAP-2).<sup>16</sup> In 2003, the Crews group reported the ability of PROTACs to degrade hormone nuclear receptors androgen (AR) and estrogen (ER), demonstrating the broader applicability of this methodology.<sup>17</sup>

Following these reports, in 2004, the design of PROTACs evolved to include the first usage of a short hydroxyproline-containing peptide sequence derived from the von Hippel–Lindau tumour suppressor (VHL) natural substrate, the transcription factor hypoxia-inducible factor 1 $\alpha$  (HIF1 $\alpha$ ), to recruit the VHL E3 ligase.<sup>18</sup> In the presence of physiological oxygen levels, HIF1 $\alpha$  gets enzymatically hydroxylated on a proline residue and is subsequently recognised by VHL for degradation, thus maintaining homeostasis by preventing the expression of hypoxic-response genes.<sup>19</sup> Exploiting this specific PPI, PROTACs recruiting VHL successfully degraded GFP-fused FKBP12 protein and AR. However, these first-generation PROTAC molecules were peptide-based and suffered from limited cell permeability, thus have significantly compromised cellular activity.

The pursuit of improved drug-like properties in PROTACs led to the development of the first small molecule PROTAC in 2008 (Figure 1-2, PROTAC 14).<sup>20</sup> This compound successfully recruited the Mouse Double Minute 2 homologue (MDM2) E3 ligase and AR resulting in targeted degradation at 10  $\mu$ M.<sup>21</sup> In 2010, bestatin methyl esters were used to develop inhibitor of apoptosis protein (IAP)-based PROTACs that target cellular retinol- and retinoic acid-binding proteins (CRABP-I and II).<sup>22</sup> These types of degraders were named ‘specific and non-genetic inhibitor of apoptosis protein (IAP)-dependent protein eraser’ (Figure 1-2, SNIPERs). Uniquely, SNIPERs facilitate the simultaneous degradation of both the IAP E3 ligase and the POI. Since 2010, new potent IAP ligands have been incorporated into SNIPERs and a wide

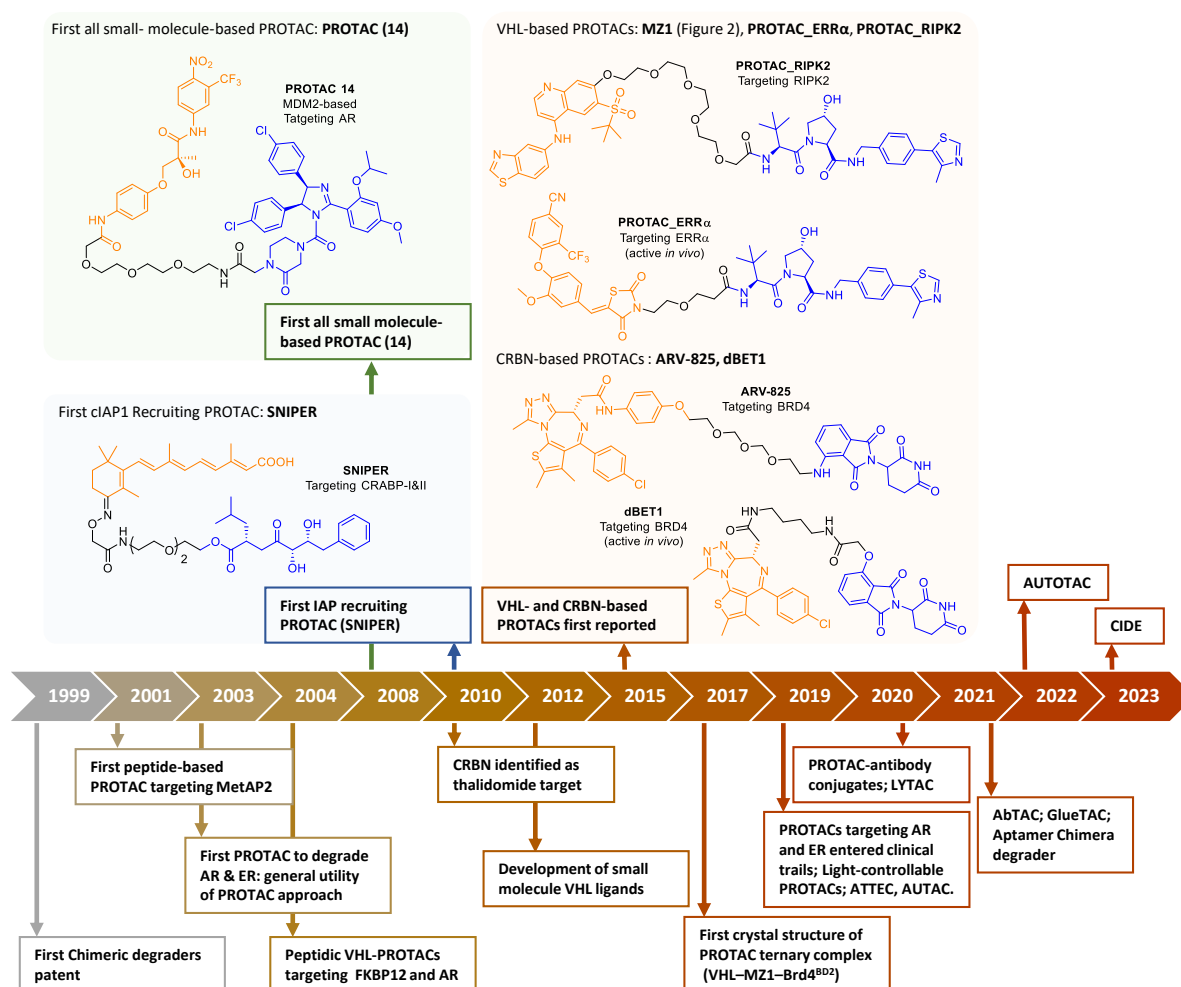


**Figure 1-2. Historical timeline of PROTAC development, showing the most significant milestones and some representative PROTAC structures**

Image adapted with permission.<sup>1</sup>

range of targets have been explored, effectively showcasing the ability of SNIPERs to degrade various POIs with high potency.<sup>22–28</sup>

In 2010, the immunomodulatory imide drug (IMiD) thalidomide, infamous for its deleterious effects, was found to target the E3 ligase cereblon (CRBN).<sup>29,30</sup> Later, in 2015, the first instance of a CRBN-based PROTAC targeting the bromodomain and extra terminal domain (BET) bromodomain-containing protein 4 (BRD4) was reported (Figure 1-2, ARV-825).<sup>31</sup> This development, coupled with subsequent confirmation of PROTAC's activity *in vivo* (Figure 1-2, dBET1),<sup>32</sup> has established the role of IMiDs as a significant E3 ligase recruiter in PROTAC technology.<sup>33</sup>

The PROTAC field further expanded in 2015 when VHL E3 ligase was successfully recruited by small molecule PROTACs.<sup>34,35</sup> The Ciulli group reported a VHL PROTAC targeting BRD4 (Figure 1-2, MZ1),<sup>34</sup> while Crews group hijacked VHL to degrade the receptor-interacting serine/threonine-protein kinase 2 (RIPK2) in cells (Figure 1-2, PROTAC\_RIPK2) and the ERR $\alpha$  in mice (Figure 1-2, PROTAC\_ERR $\alpha$ ).<sup>35</sup> These proof-of-concept studies stimulated subsequent successful PROTAC work and applications, leading to increased research interest from academia and investment from industry. This culminated in 2019 with two orally bioavailable PROTACs, targeting AR (ARV-110) and ER (ARV-471) respectively, progressing to phase I clinical trials.

Since 2019, the PROTAC field has expanded with the introduction of innovative applications, including light-responsive PROTACs whose activity can be modulated with light,<sup>36</sup> and PROTAC-antibody conjugates to enable antigen-specific targeted degradation (Section 1.5 ).<sup>37,38</sup> Significant advancements were made in the development of other targeted protein degradation methods with heterobifunctional molecules. These include the introduction of novel methods that utilise different degradation pathways, with a particular focus on the lysosome.<sup>39</sup> These novel methods, including lysosome-targeting chimera (LYTAC),<sup>40</sup> bispecific aptamer chimera,<sup>41</sup> Antibody-based PROTAC (AbTAC),<sup>42</sup> and GlueTAC,<sup>43</sup> operate through the endosome-lysosome system. While autophagy-targeting chimera (AUTAC),<sup>44</sup> autophagy-tethering compounds (ATTEC),<sup>45</sup> and AUTOPhagy-TArgeting Chimera (AUTOTAC)<sup>46</sup> function *via* the autophagy-lysosome system. In 2023, Chemical Inducers of Degradation (CIDE) was reported with a peptide that directly recruits proteasome 26S subunit ubiquitin receptor, non-ATPase 2 (PSMD2) and a small molecule POI ligand.<sup>47</sup> These advancements have broadened the toolkit of targeted protein degradation and have demonstrated therapeutic potential.

### **1.3 Advantages of PROTACs over traditional small molecule inhibitors**

Possibly the most successful characteristic of PROTACs that has led to their widespread use and success is their catalytic mechanism of action, which offers new opportunities for drug discovery to address some inherent limitations of traditional small molecule drugs. This MOA is described as an ‘event-driven’ process, where the formation of a ternary complex triggers ubiquitination, leading to the subsequent degradation of the POI.<sup>48</sup> This is in contrast to competitive, ‘occupancy-driven’ traditional small molecules, where effectiveness is reliant on

sustained POI binding and typically requires high doses for effective target engagement, which often induces off-target toxicity.<sup>49,50</sup>

Unlike traditional drugs, non-covalent PROTACs can dissociate from the ternary complex once the POI is ubiquitinated and are thus recycled for further ternary complex formation. Consequently, only sub-stoichiometric doses are required, mitigating the risk of off-target effects.<sup>51,52</sup> This indicates that PROTACs can feasibly deliver fast and quantitative degradation of the POI at low doses, which results in robust and sustained phenotypic effects compared to small molecule drugs. Several examples in the literature highlight the enhanced potency of PROTACs in phenotypic assays than the parent compound.<sup>53–55</sup> For example, VHL or CRBN-based PROTACs targeting BET family proteins (dBET1,<sup>32</sup> ARV-711,<sup>56</sup> ARV-825,<sup>31</sup> and MZ1<sup>34</sup>), could induce more than 90% degradation of the target at nanomolar concentrations or even at a picomolar range.<sup>57</sup>

Another valuable aspect of PROTACs is the long-lasting effects of protein degradation compared to modulatory binding of small molecules. Prolonged perturbation of protein levels has been observed *in cellulo* and also *in vivo*, where resynthesis of the target protein becomes the rate-determining step for duration of action, as opposed to dissociation and systemic clearance of the drug.<sup>58,59</sup> For example, an experiment in mice with a PROTAC against FKBP12 showed that, following a single day treatment with two 30 mg/kg injections, FKBP12 degradation could be observed for over a week.<sup>60</sup>

Interestingly, a potent PROTAC is not necessarily produced by a high-affinity POI warhead.<sup>61</sup> Thus, it has been suggested that weak binding may be sufficient for effective PROTACs, allowing the targeting of previously inaccessible POIs provided a weak-affinity ligand is known.<sup>62</sup> From a drug discovery perspective, over 75–80% of the human proteome is currently considered pharmaceutically inaccessible with small molecule drugs and protein therapeutics. This is mostly due to protein targets lacking well-defined binding pockets for small molecules, or to the inaccessibility of intracellular POIs for protein therapeutics, which can only target extracellular antigens.<sup>63,64</sup> Furthermore, many proteins have been shown to possess non-catalytic functions, such as scaffolding, that are essential in the regulation of multiple biological processes and cannot be always modulated by small molecule binding. These targets are deemed ‘undruggable’, or ‘challenging to drug’, including transcription factors, scaffolding proteins, and non-enzymatic proteins.<sup>65,66</sup> Hence, PROTACs present a unique opportunity to degrade such POIs and modulate their function. A prominent example is protein kinases, which

are ideal POIs for PROTACs, since many small molecule inhibitors are available.<sup>67</sup> For instance, while inhibitors of Focal adhesion kinase (FAK) can only modulate kinase activity, the scaffolding functions of this protein remain intact, promoting cell migration and invasion. PROTACs against FAK, such as **PROTAC-3** (Figure 1-3), have been shown to moderate kinase-independent scaffold signalling.<sup>68</sup>

The ternary, proximity-dependent nature of PROTAC-mediated degradation can also lead to altered selectivity profiles compared to parent compounds, a phenomenon demonstrated in several proteome-wide studies of target depletion.<sup>32,35,54,69,70</sup> For example, a multi-kinase targeting PROTAC, **THAL-SNS-032** (Figure 1-3), based on a multi-targeting kinase inhibitor SNS-032, shows selective degradation of CDK9 over other known CDK targets of SNS-032.<sup>54</sup> More examples were presented in Section 1.5.2.

Another benefit of the event-driven MOA of PROTACs is the postulated potential to overcome conventional drug resistance mechanisms arising from active site mutations or compensatory upregulation.<sup>71</sup> Although mutation in a target protein could lead to weaker binary binding, PROTAC efficacy may remain and further offers the opportunity to degrade multiple mutants simultaneously.<sup>72</sup> Indeed, several reported PROTACs outperform their parent inhibitor in treatment by degrading resistance-causing mutants of the POI.<sup>73–76</sup> Inhibition of BTK kinase with covalent inhibitor ibrutinib is effective against chronic lymphocytic leukaemia (CLL) and other B-cell malignancies but patients often develop drug resistance due to mutation of the

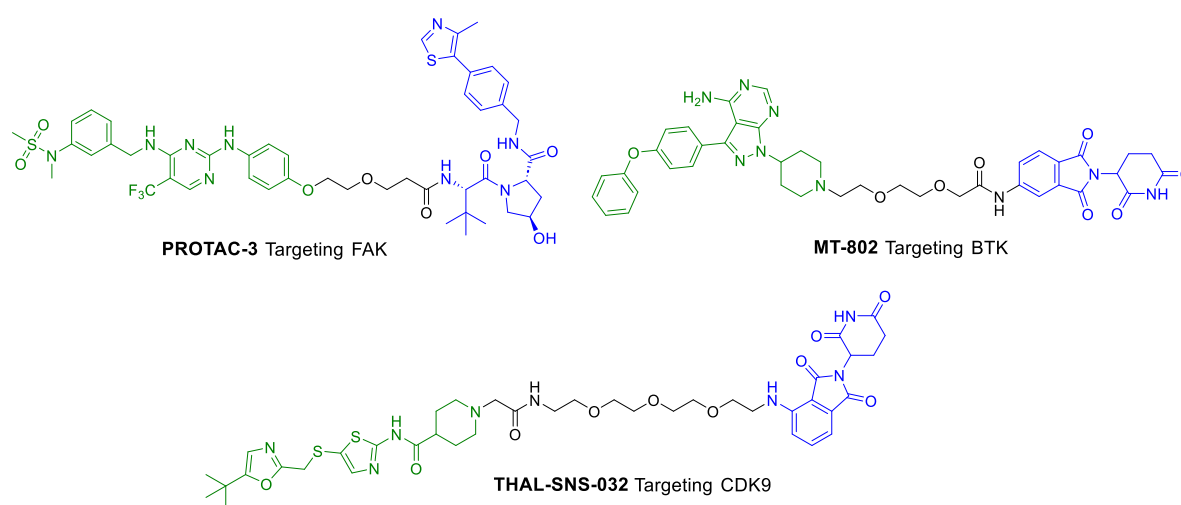


**Figure 1-3. Structures of selected PROTAC examples**

The moieties highlighted in blue engage with the E3 ligase, moieties in green recruit the protein targets.

target cysteine to serine in the kinase domain, which impairs the irreversible binding of the acrylamide covalent warhead of ibrutinib. PROTAC **MT-802** (Figure 1-3) with a reversible ibrutinib derivative warhead can degrade both wild-type and C481S BTK at equivalent potency.<sup>73</sup> Following PROTACs for BTK showed improved properties and were able to induce the degradation of six other BTK single-point mutants at the key 481 position with half-maximal effective concentrations around 30 nM.<sup>75</sup>

Specific mechanisms of resistance against PROTACs have also been recently identified, caused by targeted E3 ligase under-regulation or loss-of-function mutations affecting the UPS system components.<sup>77,78</sup> Proteins involved in this functional axis play essential roles for cellular homeostasis, offering in principle an overall lower risk, albeit resistance mechanisms have been observed upon prolonged treatment with PROTACs.<sup>77</sup> While compensatory upregulation of the POI could be overcome by PROTACs, another theorised escape mechanism would involve upregulation of DUBs to promote POI deubiquitination over PROTAC-mediated ubiquitination. Different classes of DUB inhibitors have been developed recently and co-treatment with PROTACs could help prevent resistance against TPD, at least in the deubiquitinating axis.<sup>79</sup>

Finally, PROTACs can also serve as chemical biology probes and a useful alternative to genetic modification strategies such as RNA interference (RNAi) or clustered regularly interspaced short palindromic repeats (CRISPR)–Cas9 for protein knockdown or knockout. These techniques can be invaluable tools to study protein function, signalling pathways, cellular activities, and target validation in drug discovery. However, they can require laborious and time-consuming manipulation of mRNA or genomic DNA and have limited use for essential genes, also they do not provide information regarding the post-translational activities of a POI in a complex biological system.<sup>80</sup> Hence PROTACs offer a convenient, rapid and selective alternative for protein knockdown at the post-translational level, with potential for temporal and spatial control.<sup>81</sup>

## **1.4 Key parameters of PROTAC activity and design considerations**

PROTACs introduce a novel paradigm for externally initiating a cellular event, and thus differ significantly from conventional small molecule drugs. In the course of optimising PROTACs, several parameters are assessed and evaluated. *In vitro* assays for the binary interaction of a PROTAC with a POI or E3 ligase employ  $K_d$  values to compare binding affinity with the parent compounds. The potency of PROTAC-induced POI degradation is quantified using  $DC_{50}$ ,



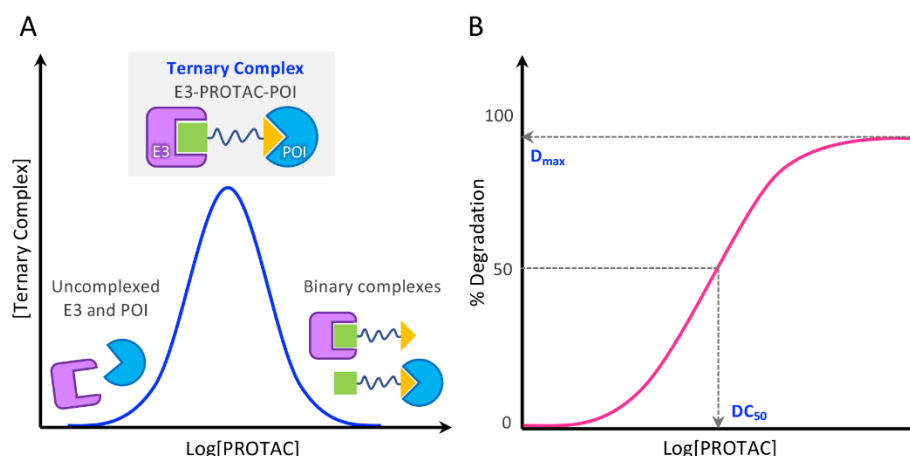


**Figure 1-4. Key parameters to evaluate PROTAC activity**

(A) The concentration-response curve for PROTAC-mediated ternary complex formation is bell-shaped. The maximal ternary complex is obtained at an optimal PROTAC concentration. At higher PROTAC concentrations the presence of binary complexes is predominant, and this phenomenon is known as the ‘hook effect’. (B) Dose-response curve for POI degradation with PROTACs.  $DC_{50}$  and  $D_{max}$  values are obtained by interpolation. Image adapted with permission.<sup>1</sup>

which signifies the concentration of PROTAC inducing 50% degradation of the POI (Figure 1-4B).  $D_{max}$  is another critical parameter for evaluating PROTACs, as it represents the maximal level of POI degradation.

To determine the optimal PROTAC concentration, the formation of a ternary complex should be evaluated across a range of concentrations relative to the POI and E3 ligase. In this context, the concentration-response curve may take on a bell shape, emphasising the delicate equilibrium required to favour ternary over binary interactions (Figure 1-4A).<sup>69</sup> This is primarily due to the ‘hook effect’,<sup>82</sup> a phenomenon where POI degradation decreases beyond an optimal PROTAC concentration. This occurs because excess PROTAC drives the formation of binary complexes at the expense of ternary interactions. As PROTAC concentrations increase, ternary complex formation also increases until a maximum is reached, after which binary complexes begin to dominate due to the excess of PROTAC.

As the principles governing PROTAC efficacy differ substantially from those of conventional small molecules, innovative design strategies are necessary for achieving effective POI degradation. The formation of a stable ternary complex is vital for ubiquitin transfer and ultimately determines whether target degradation will occur.<sup>35</sup> Significant insights into PROTAC ternary complexes were obtained through X-Ray crystallographic structure studies

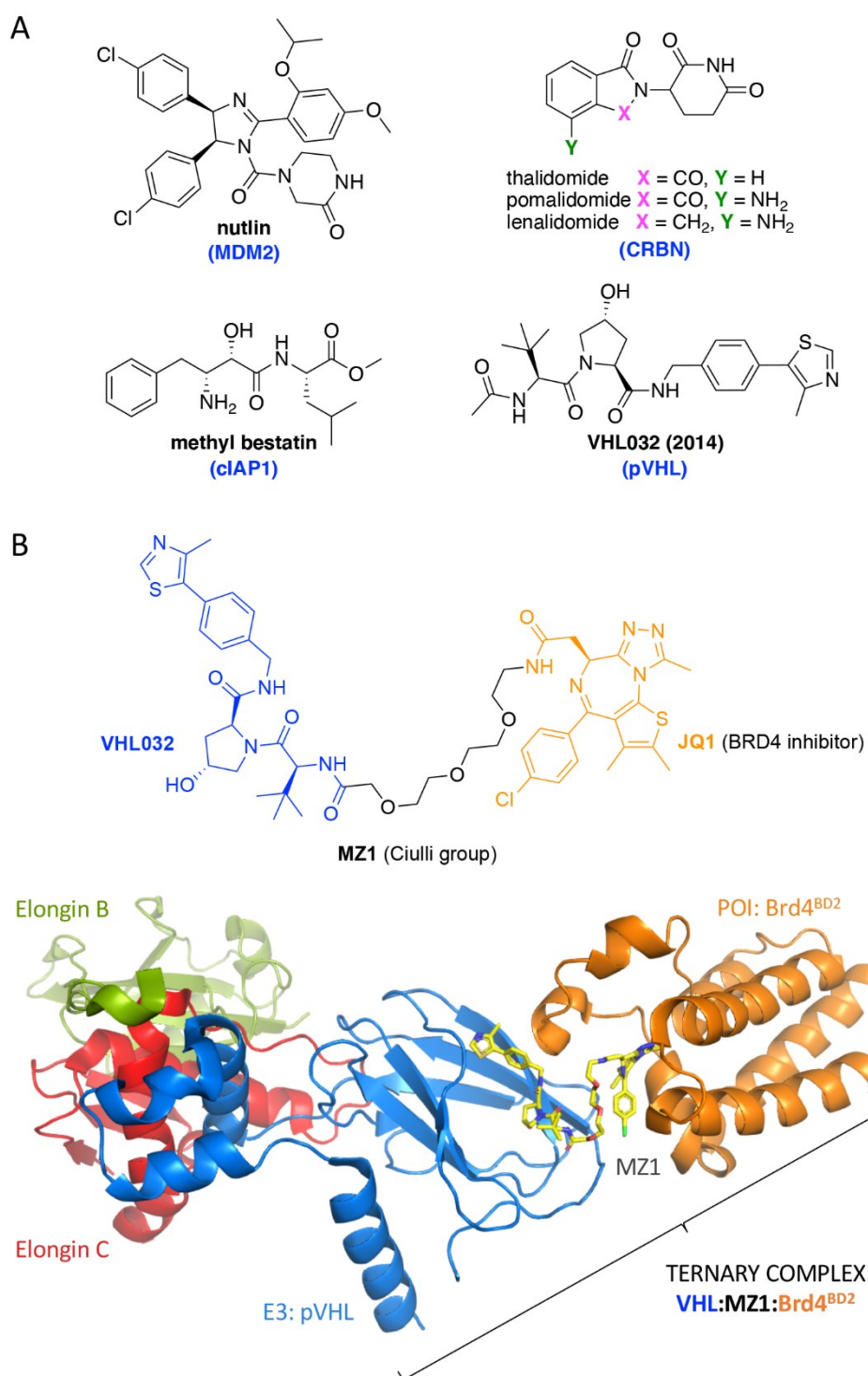


**Figure 1-5. Representative E3 ligase ligands used for PROTAC design and structural considerations of PROTACs**

(A) Representative E3 ligase ligands used for PROTAC design. (B) The first determined crystallographic structure of a PROTAC ternary complex: BRD4 degrader MZ1 fold in place to create a cooperative binding between human VHL and BRD4 bromodomain (Brd4<sup>BD2</sup>) (PDB: 5T35, 2.70 Å). Image adapted with permission.<sup>1</sup>

(Figure 1-5).<sup>69,83,84</sup> In addition, assays and technologies to study ternary complex formation under more dynamic conditions have been developed. It has become clear that multiple factors, such as the type of E3 ligase, design of the PROTAC linker, choice of POI ligand and binding site exit vector, and the nature of the PPI interface between the E3 ligase and the POI, can influence the structure and stability of ternary complexes. Modular design is often employed to examine PROTAC structure-activity relationships (SAR), with different combinations of PROTAC components frequently leading to varied and unpredictable degradation profiles. While the optimisation of ternary complex stability is critical for designing effective and potent PROTACs, predicting the effect of specific PROTAC designs remains a major challenge in the field. For instance, the study of PROTAC linkers alone, referred to as ‘linkerology’, can greatly affect the degradation, permeability, efficacy, and selectivity of the designed PROTAC through minor variations in the chemical nature, length, and geometry of the linker.<sup>84–86</sup>

More than 600 E3 ligases have been identified in the human proteome, but only a small fraction have been effectively recruited by small-molecule PROTACs.<sup>87,88</sup> The most frequently used E3 ligases in PROTAC design include CRBN,<sup>31,32</sup> VHL,<sup>18,34</sup> IAPs,<sup>22,89</sup> and MDM2<sup>20</sup> (Figure 1-5A).<sup>20</sup> Among these E3 ligases, VHL and CRBN are the most commonly recruited, accounting for over 80% of the reported PROTACs since 2015.<sup>90</sup>

In recent years, the array of available E3 ligase ligands has expanded, with an increased set of small-molecule ligands successfully employed in PROTAC-mediated targeted degradation to recruit new E3 ligases. These E3 ligases include Kelch-like ECH-associated protein 1 (KEAP1) from the BTB-type E3 ligase family,<sup>91</sup> ring finger protein 4 (RNF4)<sup>92</sup> and protein 114 (RNF114),<sup>93</sup> and the DDB1-associated and Cul4-associated factor (DCAF) family members DCAF15,<sup>94</sup> DCAF16,<sup>95</sup> and the arylhydrocarbon receptor (AhR) E3 ligase.<sup>96</sup> The development of screening approaches incorporating DNA-encoded libraries (DELs) or covalent warhead ligands, and display technologies for cyclic peptide binder development, holds great promise for expanding the chemical space of current PROTACs.<sup>97</sup> With the increased understanding and accessibility of different E3 ligases, it is anticipated that PROTACs can be fine-tuned to target specific proteins and address distinct disease contexts.<sup>98</sup>

PROTAC technology holds the potential to be applied to any intracellular POI for which a ligand has been optimised, and to repurpose low-affinity ligands or binders that themselves have no effect on protein activity. To date, PROTACs have been used to degrade a broad range of protein classes, including epigenetic targets, kinases, nuclear hormone receptors and

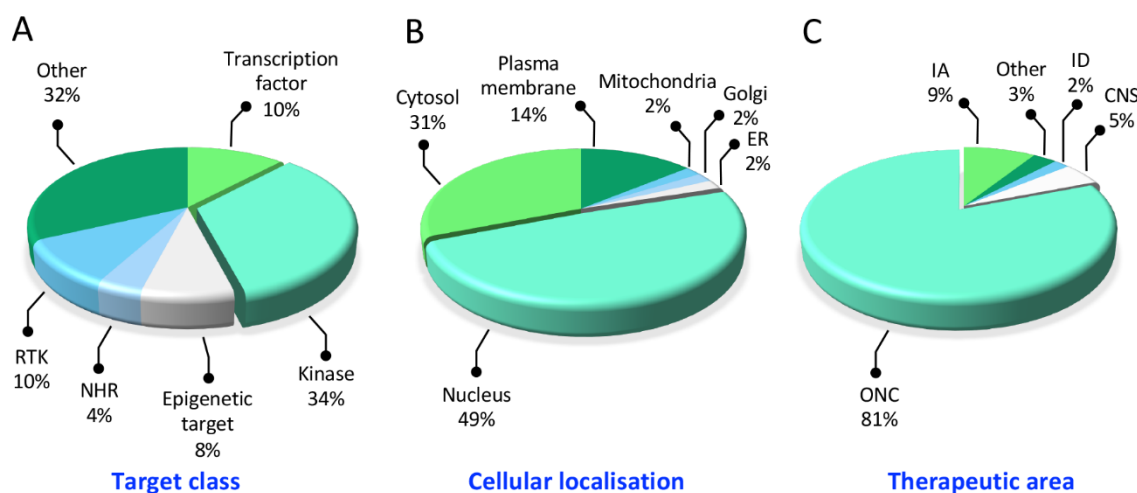


**Figure 1-6. Distribution of proteins degraded by PROTACs according to (A) target class (B) cellular localisation and (C) therapeutic area**

NHR, Nuclear hormone receptor; RTK, Receptor-tyrosine kinase; ER, Endoplasmic reticulum; CNS, Central nervous system diseases; IA, Inflammation and autoimmune diseases; ID, Infectious diseases; ONC, Oncology. Image adapted with permission.<sup>1</sup>

transcription factors (Figure 1-6). However, almost infinite possibilities for modular design are now at the hands of researchers, with the fast expansion of liganded E3 ligases, increased understanding of linkerology effects and modest requirements for warhead affinity. With these opportunities will come substantial challenges of activity-guided PROTAC design, cryptic side-effects of liganding E3 ligases, and the potential for promiscuous degradation due to potent degradation of low-affinity off-targets, requiring careful deconvolution with proteomic analysis.

## 1.5 Emerging approaches in targeted protein degradation

Despite the tremendous potential of PROTACs and the expanding list of degradable protein targets, achieving target- and tissue-selective degradation remains a challenge that hinders the full realisation of PROTACs as a therapeutic modality.<sup>99</sup> In recent years, the field of PROTAC research has witnessed the emergence of several novel technologies aimed at enhancing the effectiveness and selectivity of PROTACs. In this section, a summary of the various strategies employed to enhance selective conditional degradation by PROTACs was provided.

### 1.5.1 Light-responsive PROTACs enable spatiotemporal control

Biology operates within a spatial and temporal framework, ensuring effective communication across complex biochemical pathways. While effective PROTACs have been developed against a wide array of protein targets, the spatiotemporal control of degradation remains an area that is still relatively unexplored. The application of photopharmacology to the development of light-responsive PROTACs holds great potential for enabling precise and non-invasive control of protein degradation. This approach enables high spatiotemporal resolution and can significantly improve localised specificity and reduce off-target effects.<sup>100</sup> Designs demonstrating spatiotemporal activation of light-responsive PROTAC-mediated targeted degradation have been reported and summarised thoroughly in the reviews referenced herein.<sup>36,101,102</sup> Light-responsive PROTACs can be classified into two categories: photo-caged PROTACs and photoswitching PROTACs (Figure 1-7).

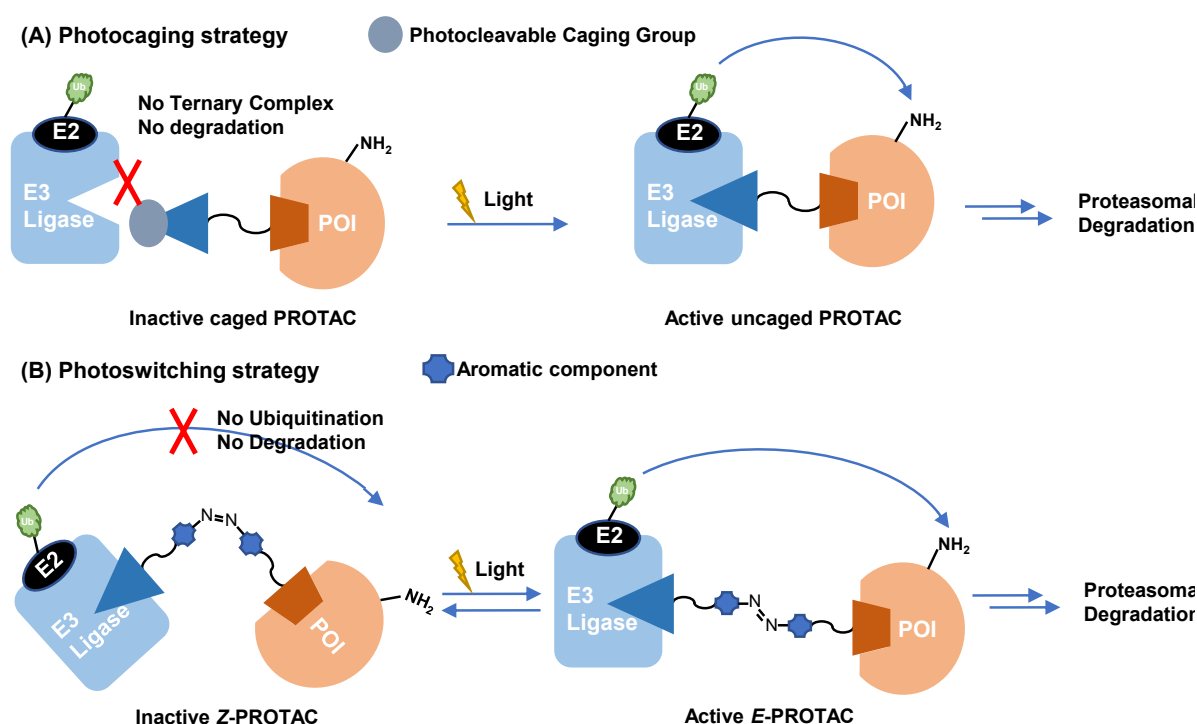


**Figure 1-7. Light-responsive PROTAC strategies**

(A) The photocaging strategy involves incorporating a caging group into the PROTAC structure, rendering it inactive. Upon light irradiation, the caging group is cleaved, activating the PROTAC and initiating polyubiquitination and subsequent proteasomal degradation of the POI. (B) The photoswitchable strategy enables control over targeted protein degradation. In the illustrated example, the active *E* isomer induces the formation of a ternary complex and protein degradation. Upon irradiation with light, the photoswitchable PROTAC switches to the inactive *Z* isomer, which fails to form an effective ternary complex and inhibits protein degradation.

Photo-caged PROTACs incorporate a photo-labile caging group into the PROTAC structure (Figure 1-7A), which caged the degradation activity of the PROTAC. Upon exposure to specific wavelengths of light, the photo-labile caging group, such as 4,5-dimethoxy-2-nitrobenzyl (DMNB), undergoes irreversible cleavage. In the cases where the photo-caged groups are attached to the E3 ligase ligands (Figure 1-8, Kounde *et al.*), light-triggered uncaging exposes the E3 ligand. The uncaged PROTACs then effectively recruit the E3 ligases and promote the formation of a ternary complex, which facilitates the ubiquitination and subsequent degradation of the target protein.<sup>103–105</sup> It is worth noting that currently there is only one example of photocaging on the linker near the POI ligand side, potentially due to the synthetic chemistry challenges involved (Figure 1-8, Xue *et al.*).<sup>106</sup>

Another strategy for introducing optical spatiotemporal control into targeted protein degradation involves the incorporation of a photoswitchable moiety into the PROTAC structure. Photoswitchable PROTACs can switch between the *E* or *Z* isomer upon irradiation with specific wavelengths of light. This introduces geometry changes to the PROTAC and

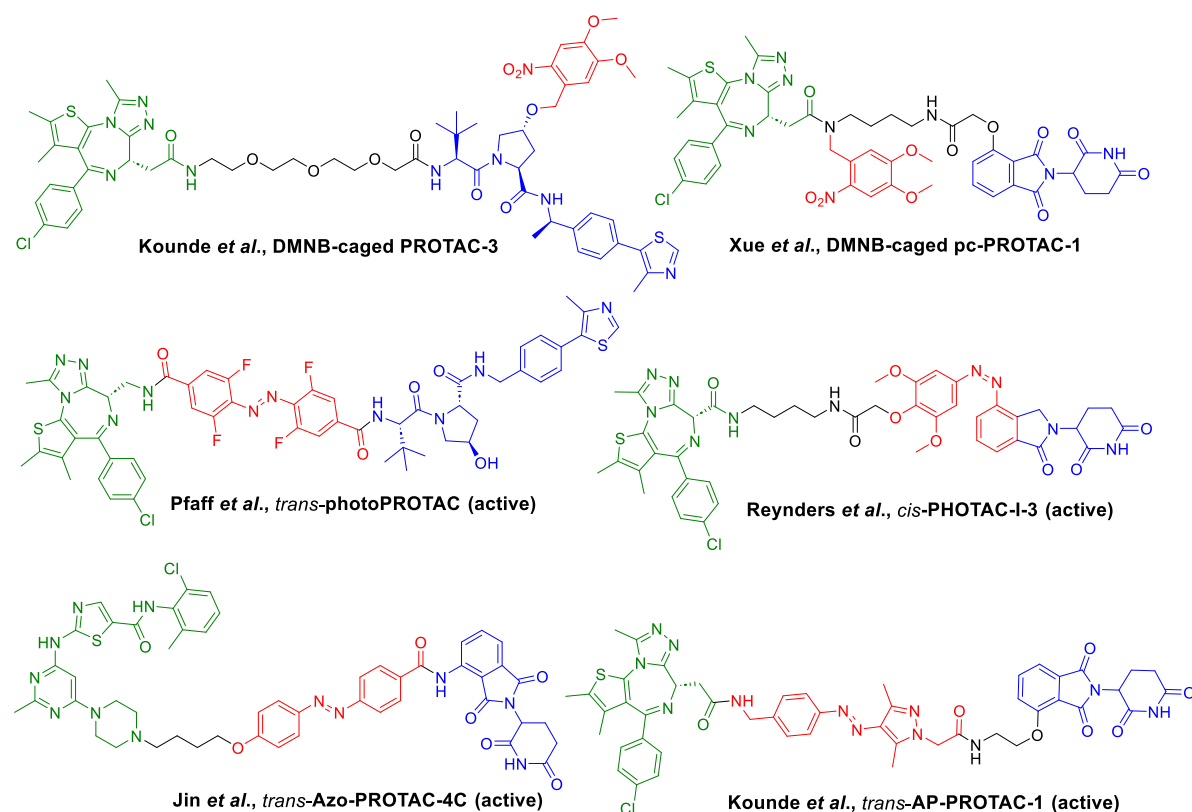


**Figure 1-8. Structures of representative photo-caged PROTACs and photoswitchable PROTACs**

The moieties highlighted in blue engage with the E3 ligase, moieties in green recruit the protein targets, and red are the light-responsive groups.

affects the formation of a ternary complex and the degradation of the POI. These two distinct photoswitchable PROTAC isomers allow reversible tuning of protein degradation, enabling alternation between different biological outcomes. A limited number of photoswitchable PROTACs, also known as PHOtochemically TArgeting Chimeras (PHOTACs), have been reported to date (Figure 1-8, Table 5). These PHOTACs incorporate an azobenzene photoswitch, with either the *E* (*trans*) or *Z* (*cis*) isomer demonstrating greater activity than the alternate isomer in inducing protein degradation of specific target proteins such as FKBP12, BCR-ABL fusion protein, and BET proteins BRD2–4.<sup>107–109</sup>

In the photoswitchable PROTAC designs by Pfaff *et al.* (targeting BRD2) and Jin *et al.* (targeting BCR-ABL fusion and ABL proteins), the photoswitch served as the linker of the PROTAC. It was observed that the *E* conformation effectively induced target protein degradation, while upon irradiation, the resultant *Z* conformation was inactive for protein degradation.<sup>107,109</sup> Conversely, in the design by Reynders *et al.* (targeting BRD2/3/4), the phthalimide on the E3 ligase ligand was used to form the azobenzene photoswitchable motif, and the *Z* isomer was found to exhibit greater activity in inducing protein degradation.<sup>108</sup> These examples highlight the significance of linker geometry in PROTAC-induced degradation.

In our research group, a collaborative effort led by Dr. Cyrille S. Kounde and myself resulted in the development of a novel class of arylazopyrazole photoswitchable PROTACs (AP-PROTACs).<sup>110</sup> **AP-PROTAC-1**, employing an arylazopyrazole photoswitch as the linker, along with a bromodomain (BRD) ligand and a thalidomide moiety to recruit CRBN E3 ligase, demonstrated excellent degradation efficacy in degrading BRD2 and BRD4 when in the *E*-enriched state. However, the *Z* isomer exhibited little degradation effect. The promising results from this study inspired my subsequent work on developing a photoswitchable multi-kinase PROTAC using the novel arylazopyrazole photoswitchable linker. Further details and findings of this research are presented in Chapter 2.

### **1.5.2 Multi-target PROTACs: Transitioning from promiscuous kinase inhibitors to target-selective degraders**

Target selectivity is pivotal in drug discovery, as compounds with selectivity and specificity for the protein of interest tend to exhibit reduced off-target effects and associated toxicity. Owing to their unique mode of action, PROTACs have the potential to achieve greater selectivity compared to the parent protein inhibitor. Several examples of multi-target

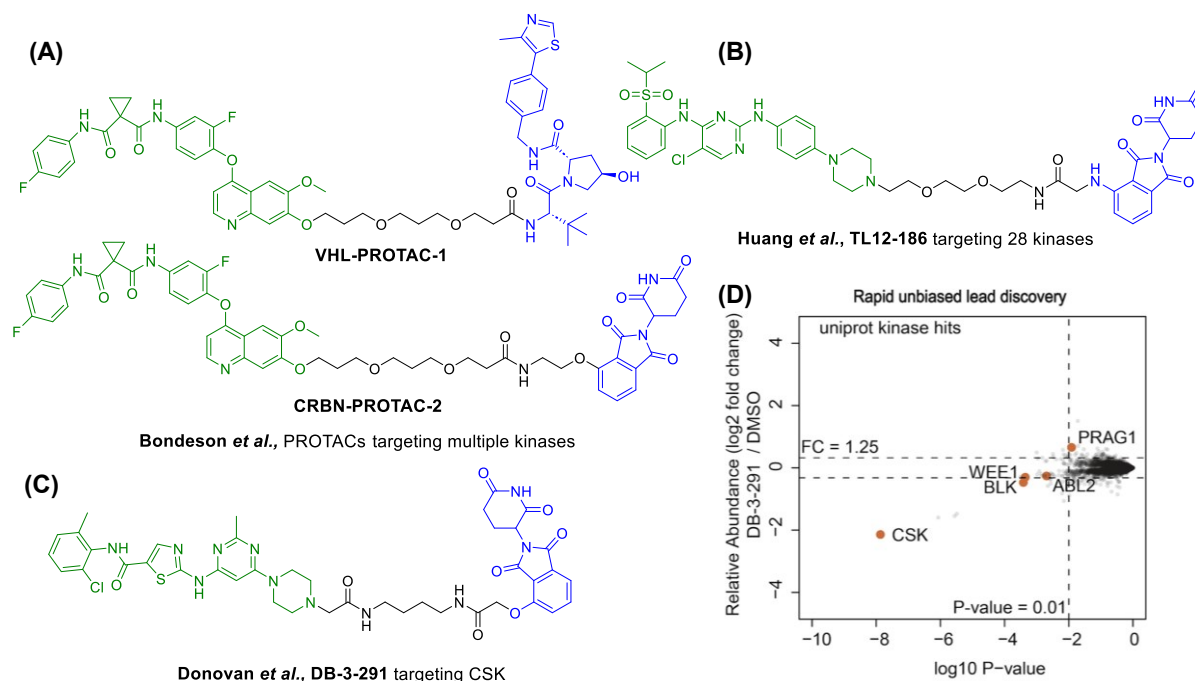


**Figure 1-9. Multi-target PROTAC developed from promiscuous inhibitors**

(A) (B) (C) Structures of representative multi-target PROTACs. (D) Scatterplot displaying relative fold change in protein abundance following treatment with 1 mM DB-3-291 for 5 h in MOLT-4 cells. Image adapted with permission.<sup>113</sup>

PROTACs using promiscuous multi-kinase inhibitors as the POI ligand have shown engagement with a reduced number of targets, resulting in enhanced selectivity compared to the parent promiscuous inhibitors.<sup>55,62,111–113</sup> To gain a comprehensive understanding of the degradation profiles of these multi-target PROTACs, quantitative multiplexed proteomics studies have been conducted to assess the global proteome changes after PROTAC treatment and to examine the abundance of multiple POIs. These studies have revealed that multi-target PROTACs, recruiting either the CRBN or VHL E3 ligase for ubiquitin transfer and proteasomal degradation, only degrade a subset of the targeted POIs of the parent inhibitor. These proteome-wide studies have significantly contributed to our knowledge of degradable protein kinases for designing future kinase degraders and have shed light on the unique advantages of PROTAC degradation compared to inhibition.

In the study by Bondeson *et al.*, **VHL-PROTAC-1** and **CRBN-PROTAC-2** were designed using the promiscuous kinase inhibitor foretinib (Figure 1-9A).<sup>62</sup> Interestingly, despite foretinib inhibiting over 133 kinases at a concentration of 10  $\mu$ M, the resulting PROTACs bound to only around 50 kinases. Moreover, **VHL-PROTAC-1** selectively degraded 9 kinase targets, while



**CRBN-PROTAC-2** degraded 14 kinases, with only 6 common kinases degraded by both PROTACs. These findings suggest that the transformation of inhibitors into PROTAC degraders significantly altered the binding affinity of the PROTAC warhead and resulted in enhanced selective kinase degradation. The binding affinity and selectivity of the parent inhibitor or the PROTAC do not necessarily correlate with target degradation. The authors proposed that the formation of an effective ternary complex plays a key role in protein degradation. It was suggested that protein-protein interactions between the E3 ligase and the target protein may facilitate the formation of the ternary structure, resulting in varying degradation potency against kinase targets. Huang *et al.* also reported that PROTAC designed from multi-target kinase inhibitor have shown increased selectivity.<sup>112</sup> Their CRBN-based PROTAC **TL12-186** degraded a total of 28 kinases in two leukemic cell lines, despite the PROTAC binding to 193 kinases in the previous affinity screening with the kinome (Figure 1-9B).

In a comprehensive chemo-proteomics study conducted by Donovan *et al.*, the degradable kinome was mapped using a library of 91 kinase-targeting PROTACs.<sup>113</sup> The degrader library was constructed using FDA-approved kinase inhibitors or promiscuous inhibitors characterised in the literature. It covered a wide range of kinase targeting scaffolds and binding modes and incorporated both the CRBN or VHL E3 ligase ligands. In the global proteomics profiling across seven different cell lines, 212 degraded protein kinases or kinase-related targets were identified. A ‘degradability score’ was assigned to the detected kinases based on the frequency of degradation hits within the degrader library, supplemented by a search for previously reported kinase degradation in the literature. Table 1 presents a list of the top 20 highly degradable kinases from this study. From this extensive degradable kinome dataset, the authors identified **DB-3-291**, a degrader in the library developed from the multi-kinase inhibitor dasatinib, as a potent selective CSK kinase degrader (Figure 1-9C and D). This was the first report of selective CSK kinase degradation in the literature, possibly due to the previous lack of a selective inhibitor for CSK. The degrader **DB-3-291** provides a promising starting point as a lead compound that could be optimised in the future for selective CSK degrader development. Furthermore, the study revealed that p97 was involved in most of the kinase degradation observed. This extensive dataset provides valuable information about the degradable kinome and kinase target tractability for the future design of kinase-targeting PROTACs. The study also highlights the potential of proteomics technology in facilitating the

development of novel PROTACs and advancing our understanding of the mechanisms involved in the ubiquitin-proteasome system and related processes.

**Table 1. The top 20 most frequently degraded kinases in Donovan *et al.*'s study**

1	CDK4	4	WEE1	7	CDK6	10	AAK1	13	CSK	16	CDK17	19	ABL2
2	AURKA	5	LIMK2	8	GAK	11	LCK	14	SIK2	17	CDK2	20	CDK9
3	FER	6	BLK	9	LIMK1	12	PTK2B	15	SRC	18	CDK5		

### 1.5.3 Peptide-based PROTACs: expanding the toolbox

#### 1.5.3.1 Peptides as a drug candidate

Peptides present unique advantages as drug candidates, effectively bridging the gap between small molecule drugs and biologics in terms of chemical space. They have been widely explored in drug discovery and more than 80 peptides have been approved by the FDA, covering a broad range of therapeutic areas.<sup>114–116</sup> Peptides combine the benefits of small molecules and biologics, offering high specificity and affinity for proteins with the potential to target protein-protein interactions (PPIs). They also have lower production costs, lower toxicity, and the ability to penetrate cells.<sup>117</sup> However, peptides face inherent challenges in terms of their pharmacokinetic (PK) profiles, including poor membrane permeability, low *in vivo* stability against proteases, low circulation half-lives due to rapid clearance, and limited oral bioavailability.<sup>118</sup> Current research efforts are focused on overcoming these limitations to enhance the therapeutic potential of peptides in drug development.

Chemical modification is a common strategy employed to improve the biological activity, stability, and solubility of peptide drug candidates. Various modifications can be implemented to mimic and stabilise peptide secondary structures, such as backbone and side chain modifications. These include peptide cyclisation, side chain cross-linking (e.g., lactam-based cross-links and peptide stapling), and the introduction of non-standard amino acids like D-amino acids and N-methylated amino acids.<sup>119</sup>

The development of high-throughput screening (HTS) platforms to screen peptide libraries has revolutionised the discovery of therapeutic peptides. Phage display technology has been a prominent approach since its introduction in 1985.<sup>120</sup> This technique involves generating large and diverse peptide libraries by incorporating random DNA sequences into the genome of a phage. The resulting peptides are displayed on the phage surface through expression with the

phage coat protein. By incubating the phage library with the target protein of interest, peptide binders can be screened and selected. Subsequent gene sequencing of the selected phage allows for the determination of the amino acid sequence of the binding peptides.<sup>121,122</sup>

Another powerful method for the discovery of highly potent macrocyclic peptide ligands is mRNA display technology, exemplified by random nonstandard peptide integrated discovery (RaPID).<sup>123,124</sup> This technology allows for the inclusion of non-standard amino acids, such as N-terminal chloroacetyl amino acid, which enables cyclisation of the peptide and significantly expands the chemical diversity of the library. Both phage display and mRNA display technologies connect the phenotype (the displayed peptide) with the genotype (the gene sequence encoding the peptide), facilitating the selection of specific clones and the rapid identification of peptide sequences.<sup>125,126</sup> These approaches have greatly contributed to therapeutic peptide discovery and are promising for future advancements.

### 1.5.3.2 Peptide-based PROTACs

Small molecule PROTACs have emerged as a promising approach for novel drug discovery, enabling the targeted degradation of numerous protein targets both *in vitro* and *in vivo*.<sup>1</sup> However, the efficacy of these PROTACs relies on the binding interaction between the warheads and the active sites or pockets on the POI. This dependence on specific small molecule binders poses a challenge when targeting ‘undruggable’ protein targets that lack potent small molecule binders. In terms of E3 ligase recruitment, significant progress has been made in determining the crystal structures of the less explored E3 ligases with bound ligands or substrate proteins.<sup>97</sup> Although these developments provide valuable insights, the application of these novel E3 ligases in PROTACs remains limited. This limitation may be attributed to the requirement for the formation of a stable ternary complex and the favourable PPIs between the POI and the E3 ligase.<sup>69</sup>

**Table 2. Comparison of peptide-based PROTAC and small molecule PROTAC.<sup>127</sup>**

	Peptide-based PROTAC	Small molecule PROTAC
Advantages	Ability to target undruggable POIs with specificity; Straightforward synthesis, solid-phase synthesis; Low toxicity; High safety <i>in vivo</i> ; Easier discovery, design and modification.	Higher cellular permeability; High stability; Good pharmacokinetics; Ligands available.
Disadvantages	Poor cell membrane permeability; Low stability; Few studies on their efficacy.	Limitation on ‘undruggable’ protein degradation; Severe side effects.
Examples (estimated)	<20 reported, <20 protein targets, <i>in vitro</i> & <i>in vivo</i>	>3000 reported, >280 protein targets, <i>in vitro</i> & <i>in vivo</i>

Peptide-based PROTACs, among the earliest examples of PROTAC molecules reported, offer several potential benefits (Table 2). Peptides can target larger surface areas or shallow pockets on undruggable proteins, thus providing potential solutions to the challenges encountered with small molecule PROTACs. This is particularly valuable for expanding the library of available ligands for ‘undruggable’ proteins. Recent advancements in peptide discovery, including the effective design of peptide inhibitors based on structural information and the development of high-throughput screening (HTS) platforms, have facilitated the generation of potent peptide binders that target POI epitopes specifically.<sup>125,128,129</sup>

The reported peptide-based PROTACs have demonstrated efficacy in degrading several protein targets associated with cancers and neurodegenerative diseases, including ER $\alpha$ , PI3K, AKT, CREPT, X-protein, and Tau protein.<sup>127</sup> However, it is worth noting that the current examples of peptide-based PROTACs generally exhibit much lower degradation efficacy (half-maximal degradation concentration DC<sub>50</sub> in the micromolar range) compared to small molecule PROTACs (Table 3). This is primarily due to the inherent limitations of peptides, particularly their poor cell permeability. Nonetheless, ongoing efforts to enhance the permeability, stability, and efficacy of peptide-based binders through peptide design and modification techniques hold great promise. Such efforts could unlock the full potential of peptide-based PROTACs and expand their applicability in diverse disease settings.

**Table 3. Representative peptide-based PROTACs.**

Name [Ref.]	Target	Warhead	E3 ligase	Cancer	Efficacy, DC <sub>50</sub>
Tri_a-PROTAC <sup>130</sup>	Akt	Tri_a	VHL	Ovarian cancer	DC <sub>50</sub> around 128 $\mu$ M in OVCAR3 cells with 4 h treatment
TD-PROTAC <sup>131</sup>	ER $\alpha$	PERMs	VHL	Breast cancer	DC <sub>50</sub> around 20 $\mu$ M in T47D cells with 24 h treatment
PRTC <sup>132</sup>	CREPT	CREPT peptide ligand	VHL	Pancreatic cancer	DC <sub>50</sub> around 10 $\mu$ M in Panc-1 cells with 24 h treatment
PROTAC <sub>Tau</sub> <sup>91</sup>	Tau-protein	Peptide targeting Tau	KEAP1	Neurodegenerative disease	DC <sub>50</sub> around 20 $\mu$ M in SH-SY5Y cells with 10 h treatment
xStAx-VHLL <sup>133</sup>	$\beta$ -catenin	xStAx stapled peptide	VHL	Colorectal cancer (CRC)	DC <sub>50</sub> around 50 $\mu$ M in HCT116 cells with 24 h treatment

## 1.5.4 Antibody-PROTAC conjugates: achieving tissue-selective protein degradation

### 1.5.4.1 Antibody-drug conjugate

Antibody-drug conjugates (ADCs) represent a promising class of targeted therapeutics. ADCs combine the specificity of monoclonal antibodies (mAbs) with the potent cytotoxicity of small-molecule drugs. Initially developed to reduce the toxicity associated with cytotoxins and chemotherapeutic drugs, ADCs deliver drug payloads specifically to antigen-positive cells, minimising damage to healthy tissue. This targeted approach enhances efficacy and increases the therapeutic index of the payloads, making ADCs an appealing strategy for anti-cancer therapy.<sup>134</sup> Currently, twelve ADCs have received approval from the FDA, and over 100 ADCs are undergoing clinical trials.<sup>135,136</sup>

An ADC comprises a tumour-specific monoclonal antibody linked to a cytotoxic payload through a linker (Figure 1-11). In a typical mechanism targeting an internalising antigen (Figure 1-10), the antibody first recognises and binds to the antigen on the surface of targeted cells. After the antibody-antigen binding, the ADC-antigen complex is internalised through endocytosis into endosomes. Subsequently, the lysosomes fuse with the endosomes, leading to antibody metabolism and linker cleavage, releasing the cytotoxic payload. In some cases, the payload might diffuse out of the cell or be released extracellularly, causing potential cytotoxicity to the cells that do not express the antigen, a phenomenon known as bystander

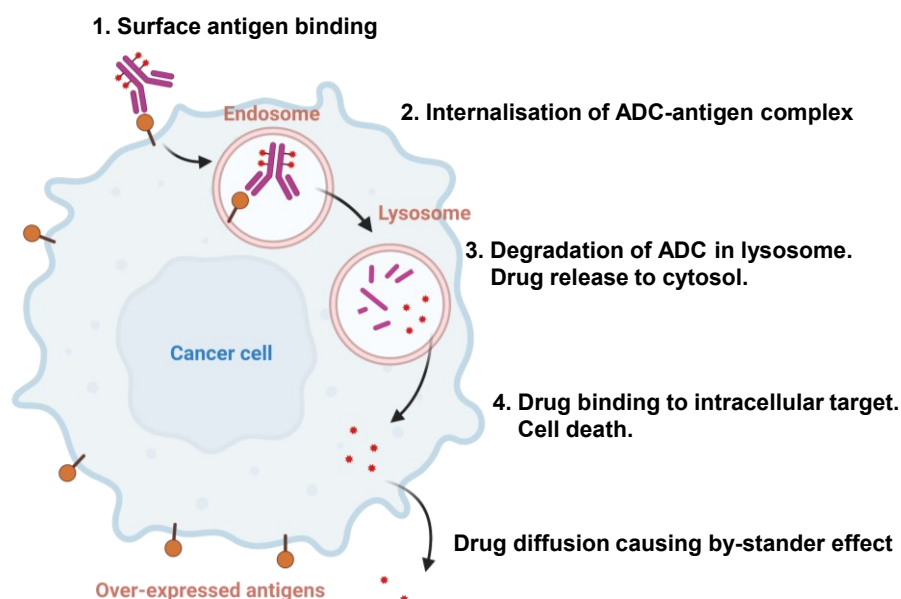


**Figure 1-10. Mechanisms of drug delivery mediated by an internalising ADC**

Upon binding to tumour cell surface antigens, ADCs are internalised via receptor-mediated endocytosis. The ADC is trafficked to the lysosome where the cytotoxic drugs are released into the cytosol. The drugs can bind to their targets, leading to cellular responses and resulting cell death. Alternatively, the drug may diffuse or be transported outside the targeted cell and cause the bystander effect to non-targeted cells. The figure was created with BioRender.com.

cytotoxicity.<sup>137</sup> For non-internalising ADCs, endocytosis is not required, the linker cleavage and payload release occur in the extracellular tumour microenvironment.

The antibody is responsible for the specific recognition and binding of the ADC to the target antigen on the surface of targeted cells. The selection of an appropriate target antigen is critical for ADCs. Ideally, the antigen should be predominantly or exclusively expressed on tumour cells, with minimal presence on normal cells. It is also preferable for the antigen to be able to internalise upon antibody binding. The affinity between the antibody and antigen is also important to achieve the desired balance of specific internalisation and tumour penetration.<sup>138</sup>

The cytotoxic payload drug should be highly potent to effectively kill the target cells upon release. The payload's stability under physiological conditions is essential. The two main types of ADC payloads are potent microtubule inhibitors and DNA-damaging agents.<sup>139,140</sup>

The ADC linker plays a crucial role in controlling the release of the cytotoxic payload. It is responsible for achieving optimal drug delivery to target cells while minimising off-target toxicity. The linker should remain stable in circulation and selectively release the cytotoxic

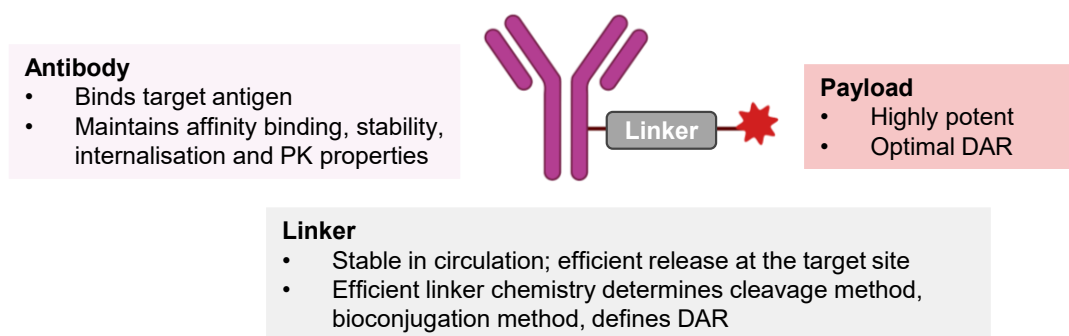


**Figure 1-11 The general structure of an ADC and the roles of each component**

The clinical properties of antibody-drug conjugates are determined by their three components: the antibody, the cytotoxic payload, and the linker.<sup>208</sup>

payload in the intracellular environment of target cells.<sup>141</sup> Linkers are categorised as cleavable or non-cleavable. Novel ADC linker technologies have emerged to enable more selective payload release. For example, the tandem-cleavage linker strategy requires two sequential enzyme cleavages for payload release.<sup>142,143</sup>

Despite increasing interest in ADCs as anti-cancer therapeutics, only a limited number of ADCs have been approved by the FDA. ADCs face inherent limitations, including uptake into non-targeted cells leading to antigen-independent toxicity, which can limit their therapeutic efficacy. Another limitation is the high cytotoxicity of payloads, which can become dose-limiting if released prematurely.<sup>144</sup>

#### 1.5.4.2 Antibody-PROTAC Conjugates (Ab-PROTACs)

The concept of ADCs has been extended to PROTACs, leading to the development of antibody-PROTAC conjugates (Ab-PROTACs). Several examples of PROTAC molecules employed as ADC payloads have shown their potential to induce targeted protein degradation in antigen-positive cells.<sup>145</sup> In comparison to the potent yet dose-limiting cytotoxic payloads commonly used in conventional ADCs, PROTACs function catalytically to induce rapid and sustained protein degradation at lower doses. This characteristic positions them as promising candidates for ADC payloads. Similar to ADCs, Ab-PROTACs selectively bind to overexpressed antigens and internalise, allowing for the subsequent lysosomal release of the PROTAC payload and protein degradation (Figure 1-12). This antigen-dependent internalisation ensures that antigen-expressing cells are exclusively targeted for protein

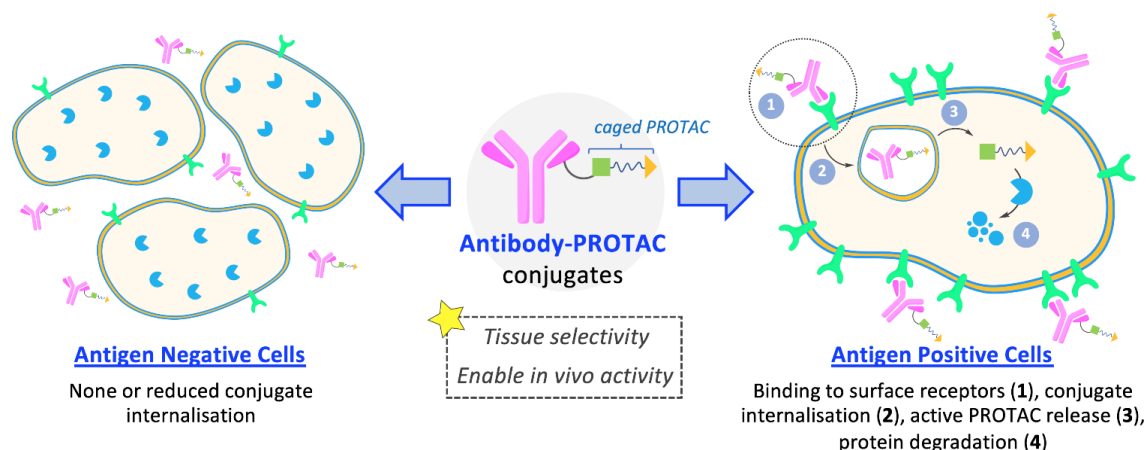


**Figure 1-12. Mechanism of action of Antibody-PROTAC conjugates**

Image adapted with permission.<sup>1</sup>

degradation, while cells lacking the antigen remain unaffected by PROTAC-mediated degradation.

In a pioneering study conducted by the Tate group, Maneiro *et al.* reported the development of **Ab-PROTAC-3**, an Ab-PROTAC that targets bromodomain-containing protein 4 (BRD4) in conjugation with the HER2-targeting antibody trastuzumab (Figure 1-13).<sup>146</sup> The authors initially developed a PROTAC analogue to MZ1 and demonstrated its ability to induce complete BRD4 degradation at 100 nM after a 4-hour treatment. The free hydroxyl group on the VHL ligand moiety of the PROTAC was functionalised with an azido-PEG linker through an ester bond to create an azido-PROTAC. This ester bond would effectively cage the activity of the Ab-PROTAC until the lysosomal hydrolysis of the cleavable ester bond after the internalisation of Ab-PROTAC. The azido-PROTAC was linked to the antibody through copper-free strain-promoted azide-alkyne cycloaddition (SPAAC) and the next-generation maleimides (NGMs) antibody conjugation strategy by interchain disulfide bridging.<sup>147</sup> In their *in vitro* cell studies, Maneiro *et al.* demonstrated that **Ab-PROTAC-3** effectively induced BRD4 degradation only in HER2-positive cells while sparing HER2-negative cells. This finding underscores the potential of antibody-PROTAC conjugates for achieving tissue-specific protein degradation.

Antigen-dependent internalisation can potentially enhance the cell delivery efficiency of the PROTAC molecule, thereby improving its PK properties and enabling *in vivo* activity. In research by Genentech, their anti-CLL1-GNE-987 conjugate displayed improved PK



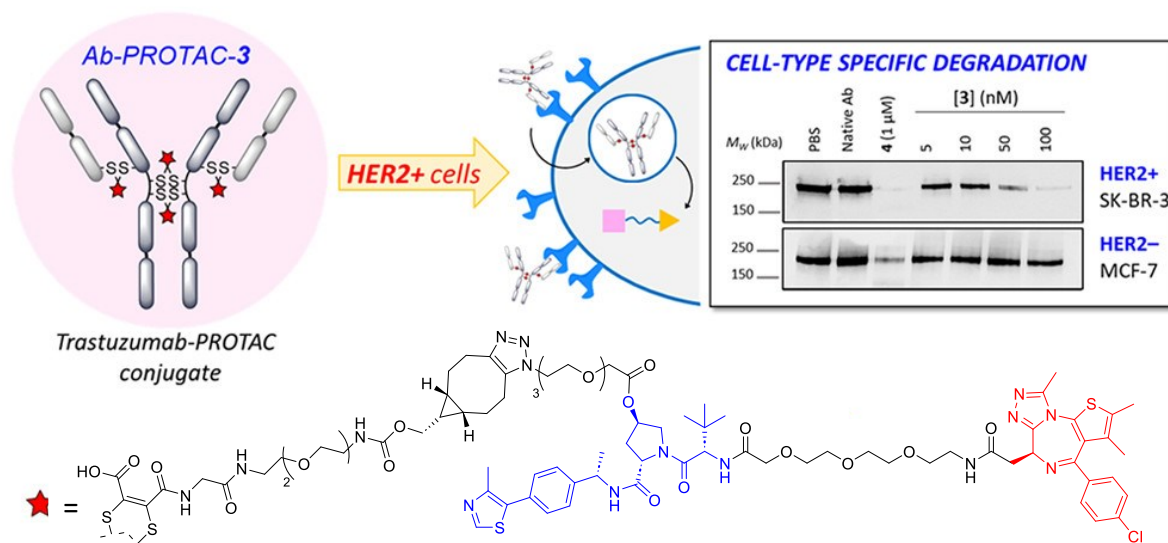


**Figure 1-13. Ab-PROTAC design by Maneiro *et al.***

Left: Structure of Ab-PROTAC-3. Top right: Ab-PROTAC-3 induces selective dose-dependent degradation of BRD4 in HER2-positive cell lines. Western blot analysis of following 4-hour treatment of MCF-7, SK-BR-3 cells with Ab-PROTAC-3, or control compounds. Image adapted with permission.<sup>146</sup>

properties compared to the parent BRD4 PROTAC GNE-987, a potent degrader with picomolar cell potencies but demonstrated low *in vivo* exposures.<sup>148</sup> The conjugate demonstrated sustained antigen-specific, dose-dependent tumour regressions *in vivo* following a single intravenous administration in mice.

Despite the potential benefits of Ab-PROTACs, their design presents several challenges and requires careful consideration. One critical challenge involves the attachment of the linker to the PROTAC molecule while retaining the essential bifunctional binding interaction and ternary complex formation for optimal PROTAC activity. Sub-optimal linker design or attachment could significantly impair the degradation efficacy of the PROTAC, as outlined in an extensive work by Genentech.<sup>149</sup> The optimisation of the PROTAC degrader could also enhance the activity of the resulting ADCs *in vivo*. The choice of antibody is another crucial consideration in ADC development, as varying antibodies may result in differing ADC activity across disease settings.<sup>150</sup> Moreover, the large molecular weight (MW > 800) and presence of multiple hydrogen bond donors (HBDs) and acceptors (HBAs) on PROTACs raise concerns about the potential aggregation of the antibody-PROTAC conjugates.<sup>151,152</sup> Overcoming these challenges requires the development of novel linker design and conjugation approaches, which surpass traditional strategies employed in the ADC field, to allow high drug-to-antibody ratio (DAR) loading of PROTACs.<sup>145</sup>

## 1.6 Thesis aims and objectives

Owing to increasing interest and concerted efforts in the field, highly potent PROTACs targeting a wide array of therapeutic targets have been developed, with several progressing to clinical trials. However, the lack of precise conditional activation of these catalytic degraders hinders their broad application. In this thesis, two novel methods to achieve conditional activation of PROTAC-mediated degradation were reported. These methods aimed to enhance the spatiotemporal precision and improve the target and tissue specificity of protein degradation, allowing for more accurate manipulation of the processes.

### **Multi-kinase degradation with photoswitchable PROTACs (AP-PROTACs, Chapter 2)**

The first part of this thesis investigated the use of light as a stimulus for the spatiotemporal control of bifunctional degraders. Although prior research had successfully incorporated azobenzene photoswitchable linkers into PROTAC structures for light-mediated control of degradation activity against specific targets,<sup>153</sup> these studies only demonstrated degradation of a single protein or a specific protein class, and solely utilised azobenzene as photoswitches. The exploration of alternative photoswitch designs and the development of photoswitchable PROTACs capable of simultaneous multi-target degradation remains a gap in the current research. In Chapter 2, I aimed to develop novel photoswitchable PROTACs with enhanced photoswitching properties and the capacity for multi-target degradation.

The study primarily aimed to design and characterise a novel arylazopyrazole photoswitchable linker. This linker could potentially improve the photoswitching properties of PROTACs beyond those of existing azobenzene-based photoswitchable PROTACs. Additionally, I aimed to expand the application of light-responsive protein degradation activation to include a broader set of protein targets. For this purpose, it was proposed to use a promiscuous kinase inhibitor as the ligand for the protein target, which would be combined with the CRBN ligand lenalidomide through the arylazopyrazole linker. This combination would create an arylazopyrazole photoswitchable multi-kinase targeting PROTAC. To examine the degradation profile of this degrader, I planned to develop whole-cell multiplexed quantitative proteomics methods and validate the results with immunoblotting techniques. If successful, this design might allow simultaneous degradation of multiple kinases, with light-activable on/off control.

### **Antibody-peptide degrader conjugates (Ab-peptide, Chapter 3)**

The second part of this thesis focused on applying ADC technology to develop antigen-specific peptide-based PROTACs. The primary goal was to enhance the tissue specificity and cellular activity of peptide-based PROTACs by converting them into antibody-peptide degrader conjugates (Ab-peptide).

Previous research on antibody-PROTAC conjugates (Ab-PROTACs) has highlighted their capacity to induce targeted protein degradation with specificity for antigens, cell types, or tumours. However, the current Ab-PROTACs exploit small molecule PROTACs, which presents significant synthetic challenges. Given the challenges in the discovery of small molecule binders for novel E3 ligases and ‘undruggable’ protein targets, the exploration of peptide binders—facilitated by screening and display technologies—offers a promising alternative.

It was hypothesised that peptide-based degraders have the potential to serve as payloads for ADCs. The conjugation of peptide-based degraders to suitable antibodies for ADC internalisation could significantly enhance their PK, cellular uptake, and cell-type specificity. By overcoming the cellular uptake challenges faced by peptides through ADC internalisation, these peptide degraders could facilitate catalytic protein degradation with substoichiometric target engagement, leading to sustained and robust protein degradation comparable to small molecule PROTACs. To validate the hypothesis, my strategy involved converting three distinct peptide-based degraders into antibody-peptide conjugates, followed by evaluations of the resulting ADCs.

## Chapter 2 Photoswitchable multi-kinase degradation with novel arylazopyrazole-based photoswitchable PROTAC<sup>b</sup>

### 2.1 Introduction

As discussed in Section 1.5.1, the application of photopharmacology in PROTAC technology has led to the development of photoswitchable PROTACs, also known as PHOTACs (PHOtochemically TArgeting Chimeras). Despite the few examples in the literature, these PROTACs primarily focused on targeting a single protein or a specific protein class. All previously reported photoswitchable PROTACs employed the azobenzene photoswitch, which exhibits incomplete photoswitching and limited stability of the *Z* isomer.

In this chapter, a new class of photoswitchable PROTACs was introduced, referred to as AP-PROTACs. AP-PROTACs incorporate a novel arylazopyrazole photoswitch,<sup>110</sup> which constitutes one of the first instances of non-azobenzene-based PHOTAC technology. The arylazopyrazole photoswitch was implemented into the PROTAC design with a promiscuous kinase inhibitor warhead (**AP-PROTAC-2**). Unlike the previous single-protein targeting photoswitchable PROTAC designs, this approach allows for the simultaneous degradation of multiple protein kinases with on/off photoswitchable control, which is without any precedent in the literature.

The synthesis and characterisation of the arylazopyrazole photoswitch **4** were first described, followed by the design, synthesis, and characterisation of the photoswitchable multi-kinase PROTAC, **AP-PROTAC-2**. To examine the cellular response and degradation profile of **AP-PROTAC-2**'s cellular treatment, whole-cell quantitative multiplexed proteomics methods and immunoblotting analysis were employed. The findings represented the first example of light-

---

<sup>b</sup> Chapter 2 is based on the author's previous publication and some passages and figures have been adapted with permission: **Q. Zhang**, C. S. Kounde, M. Mondal, J. L. Greenfield, J. R. Baker, S. Kotelnikov, M. Ignatov, C. P. Tinworth, L. Zhang, D. Conole, E. De Vita, D. Kozakov, A. McCluskey, J. D. Harling, M. J. Fuchter and E. W. Tate, *Chem. Commun.*, 2022, **58**, 10933 DOI: 10.1039/D2CC03092F

tuneable degradation of multiple protein kinases using a broad-spectrum kinase inhibitor as the warhead.

## **2.2 Synthesis and characterisation of novel arylazopyrazole-based photoswitchable linker**

### **2.2.1 Light-responsive photoswitches enable spatiotemporal control**

Life on Earth possesses a fundamental and ancient ability to respond to light through chromophores such as retinal. Inspired by this natural phenomenon, the development of synthetic photoswitches emerged less than a century ago. These synthetic compounds can undergo reversible photoisomerisation, wherein their structure changes upon irradiation with specific wavelengths of light. This advancement has also given rise to the field of photopharmacology.<sup>1</sup> Photopharmacology uses light as an external trigger to control the activation of compounds in both time and space, with the aim of improving the drug selectivity and reducing toxicity-related side effects.<sup>100</sup> Light is generally non-invasive and does not contaminate the sample. It is also orthogonal in most chemical and biochemical systems, as most cells do not react to light. More importantly, light can be precisely delivered to intracellular targets in a qualitative or quantitative manner by adjusting the wavelength and intensity, allowing for precise spatial and temporal resolution with minimal toxicity to cells.<sup>154</sup> Light-responsive moieties have been successfully incorporated into the design of peptides, proteins, and nucleic acids, serving as valuable tools for investigating and manipulating biological processes and biological systems.<sup>155</sup> However, to make photopharmacology clinically relevant for non-transparent tissues could be challenging. With significant progress in the field, several technologies have been developed to enable precise light delivery to the diseased tissue, including injectable LED systems and implantable wireless optogenetic devices.<sup>156,157</sup>

Photopharmacology encompasses non-reversible photocaging strategies as well as reversible approaches involving photoswitchable compounds.<sup>100,158,154,155</sup> Photoswitchable molecules are compounds capable of reversible structural and chemical property changes upon exposure to light, a process known as photoisomerisation. The most important attributes of a photoswitch include the degree of photoisomerisation achieved at a specific wavelength of light, photoconversion efficiency or the photostationary state (PSS) ratio, and the thermal stability of the resultant isomers.<sup>159,160</sup> Among synthetic photoswitches, azobenzenes are the most

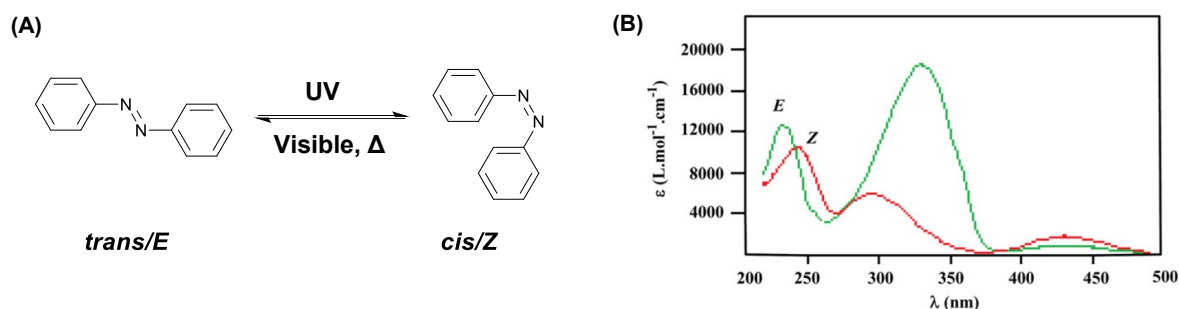


**Figure 2-1 Azobenzene photoswitch**

(A) Reversible photoisomerisation of azobenzene upon light irradiation. (B) UV–Vis absorption spectra of *E* and *Z* azobenzene isomers in ethanol. Image adapted with permission.<sup>269</sup>

extensively studied class due to their straightforward synthesis process, high quantum yields, and rapid photoisomerisation, which induces significant conformational changes.<sup>160</sup>

Azobenzenes exist in two isomeric states: *trans* (*E* isomer) and *cis* (*Z* isomer, Figure 2-1). The *E* isomer, being thermodynamically more stable, is the predominant form at equilibrium in the absence of light, accounting for over 99.99% of the total. The *Z* isomer, however, represents a metastable state and spontaneously reverts back to the *E* form. The *E* to *Z* isomerisation can be induced by UV light irradiation at wavelengths around 340 nm. The reverse process, from *Z* to *E*, occurs either thermally or upon irradiation with light of a longer wavelength, exceeding 450 nm.<sup>159</sup>

However, azobenzenes exhibit several limitations. A common issue with azobenzenes is their incomplete photoswitching, with a maximum achievable population of approximately 80% *Z* isomer or 95% *E* isomer. This incomplete switching is attributed to the overlapping absorbances of the isomers at the irradiation wavelength. Additionally, azobenzenes can rapidly revert to the *E* isomer through thermal conversion. Consequently, photoswitchable PROTACs designed from azobenzene photoswitches are inherently plagued by these drawbacks. The properties of the photoswitch can vary significantly based on the substituents on the benzene ring, further complicating the design of photoswitchable PROTACs with favourable photoswitching properties and biological response.

In response to these challenges, Fuchter *et al.* from Imperial College London developed a novel class of azophotoswitches, known as azoheteroarene photoswitches. This unique class is characterised by a five-membered azoheteroarene core structure.<sup>161,162</sup> The arylazopyrazole

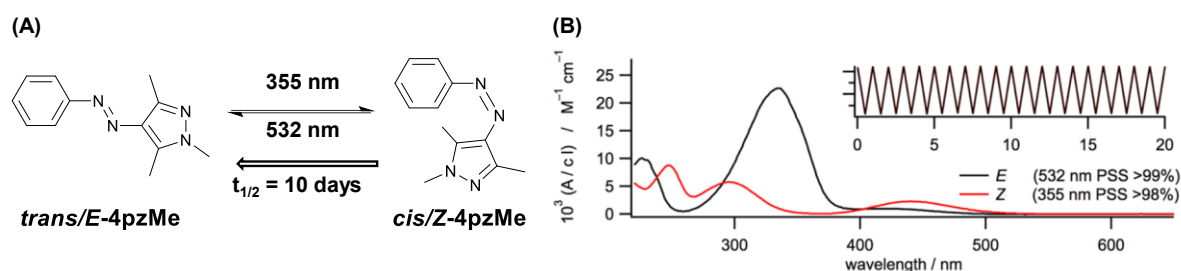


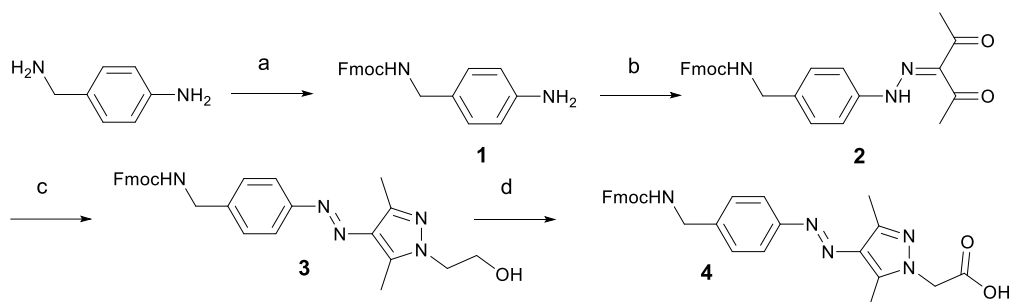
**Figure 2-2 Arylazopyrazole photoswitch 4pzMe**

(A) Reversible photoisomerization of arylazopyrazole **4pzMe** upon light irradiation. (B) UV-Vis absorption spectra of *E* and *Z* arylazopyrazole **4pzMe** isomers in MeCN. Inset: repeated photoswitching cycles of arylazopyrazole. Image adapted with permission.<sup>161</sup>

(AAP) photoswitches, exemplified by **4pzMe** (Figure 2-2), exhibited quantitative photoisomerisation in both directions (*E* to *Z* and the reverse), with a PSS containing up to 98% *E/Z* isomer. Notably, the AAP photoswitches demonstrated high *Z* isomer thermal stability in solution, with half-lives spanning from 10 to 1000 days. This stability is comparable to the highest half-life observed for an azobenzene photoswitch.<sup>163</sup> Furthermore, AAP photoswitches exhibited robust reversible photoswitching from multiple photoswitching cycles. These highly valued photoswitching characteristics of the azopyrazole photoswitch, including high PSS ratios and extended half-lives, made it an ideal choice for the design of our photoswitchable degraders.

### 2.2.2 Synthesis of an arylazopyrazole photoswitchable linker

A versatile N-Fmoc-protected arylazopyrazole linker, compound **4**, was synthesised by myself using reaction schemes previously developed by Dr. Cyrille S. Kounde, a former member of our research group (Scheme 2-2).<sup>164</sup> This linker has an amino acid structure featuring a fluorenylmethyloxycarbonyl (Fmoc) protected amine group at one terminus and a carboxylic acid group at the other. 4-Aminomethyl aniline was protected with an Fmoc group using 9-Fluorenylmethyl-succinimidyl carbonate (Fmoc-OSu), resulting in the formation of aniline **1**. Under acidic conditions, aniline **1** was converted to a benzenediazonium intermediate, which subsequently reacted with acetylacetone to produce diketone **2**. Diketone **2** was subjected to reflux at 50 °C with 2-hydrazinoethanol, leading to the formation of alcohol **3**, which features a pyrazole ring and an ethyl alcohol side chain. Finally, alcohol **3** underwent a two-step oxidation process, involving initial Dess-Martin periodinane oxidation followed by subsequent Pinnick oxidation, resulting in the desired carboxylic acid linker **4**. The initial Dess-Martin

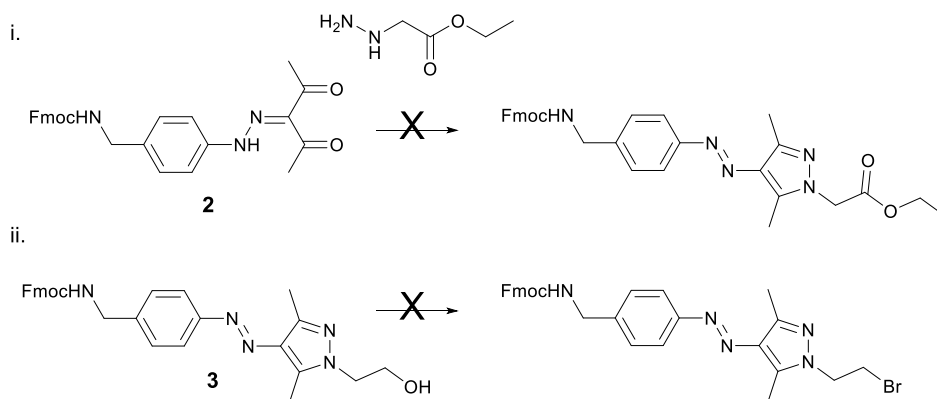


**Scheme 2-2. Synthetic route to arylazopyrazole (AAP) photoswitchable linker 4**

Reagents and conditions: (a) Fmoc-OSu, DIPEA, DCM, RT, 16 h; 82%; (b) i. NaNO<sub>2</sub>, acetic acid, 37% HCl, 0 °C, 1 h; ii. acetylacetone, ethanol, sodium acetate, 0 °C to RT, 3 h; 83% over two steps; (c) 2-Hydrazinoethanol, DCM, MeOH, 50 °C, 2 h; 98%; (d) i. Dess-Martin periodinane, DMSO, RT, 16 h; ii. NaClO<sub>2</sub>, NaH<sub>2</sub>PO<sub>4</sub>, 2-methylbut-2-ene, RT, 16 h; 53% over two steps.

oxidation results in a mixture of aldehyde and carboxylic acid, with a low isolation yield of the aldehyde constituent. Therefore, the second oxidation was conducted directly following the first oxidation to obtain the carboxylic acid product.

Attempts were made to enhance the yield and reduce the steps of synthesis. However, these efforts did not yield better results than the established route. For instance, an alternative



Reaction	Reagents and solvents	Conditions	Result
i	DCM, MeOH	2 h at 50 °C	No product
	DCM, MeOH	20 h at 50 °C	No product
	MeCN	1 h at 70 °C	No product
	MeCN	1 h at 70 °C then 1 h at 80 °C	No product
ii	PPh <sub>3</sub> , CBr <sub>4</sub> , DCM	2 h at RT	No product
	PPh <sub>3</sub> , CBr <sub>4</sub> , DCM	2 h at 50 °C	No product
	48% HBr	22 h at 85 °C	No product

**Scheme 2-1 Attempted reactions and conditions to synthesise alternative AAP linker precursors**



approach involved coupling diketone **2** with ethyl hydrazinoacetate instead of hydrazinoethanol, with the expectation that subsequent ester hydrolysis would result in the desired carboxylic acid. Unfortunately, these attempts were unsuccessful, possibly due to the electron-withdrawing effect of the acetate group on the hydrazine, which prevented the formation of the pyrazole ring. Additionally, bromination of alcohol **3** was performed, but no desired brominated product was obtained. Therefore, I returned to the established two-step oxidation method to synthesise carboxylic acid **4**.

## 2.2.3 Photoswitching properties characterisation of linker **4**

### 2.2.3.1 UV-Vis Characterisation of linker **4**

The photoswitching properties of AAP linker **4** were evaluated following its synthesis. Given the photoswitchable nature of the linker, to accurately characterise its properties, the samples were protected from light and precautions were taken to limit the sample's exposure to ambient light during experiments. I started with the investigation of the ultraviolet-visible (UV-Vis) absorption spectra under varied light irradiation conditions. A solution of linker **4** was prepared in water with 0.2% DMSO, which was then irradiated with specific wavelengths of light for a minimum of 1 min, after which a UV-Vis spectrum was recorded. It was observed that irradiation for more than 1 min resulted in no change in the sample's UV-Vis spectra, which suggested that a 1-min irradiation period was sufficient to establish the PSS at a concentration of 20  $\mu$ M.

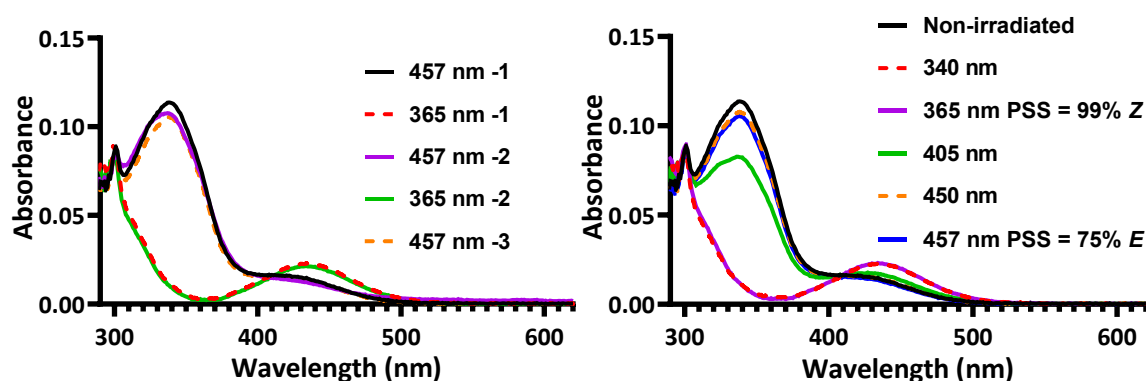


**Figure 2-3 UV-Vis spectra of linker **4****

UV-Vis spectra of a 20  $\mu$ M solution of **4** in water with 0.2% DMSO. The solution was irradiated under the stated irradiation conditions for 1 min and the UV-Vis spectrum was then recorded with minimized exposure to ambient light. Left: reversible switching of linker **4**. Right: photoswitching with different wavelengths of light irradiation.

The UV-Vis spectra of linker **4** after 1-min intervals of alternating irradiation cycles at 457 nm and 365 nm were sequentially recorded (Figure 2-3, left). The UV-Vis spectra derived from this sequential irradiation scheme confirmed the reversible photoswitching between the *E* and *Z* isomers of linker **4**. Upon irradiation of **4** at 365 nm, the *E* isomer underwent photoisomerisation to form the *Z* isomer, and with 457 nm irradiation, the *Z* isomer reverted to the *E* isomer. The resulting UV-Vis spectra displayed a significant shift in the absorption maximum between the *E* and *Z* isomers of linker **4**. The *E* isomer presented a notable absorption band within the 320-360 nm range, while the *Z* isomer showed a strong absorption band between 420-460 nm, indicating its preferential light absorption in this range.

To determine the photostationary state (PSS) composition of the *E/Z* isomers following irradiation, Fischer's method was employed.<sup>165</sup> This method calculates the PSS composition using data from UV-Vis spectrometry, and allows determination of the PSS ratio in a bistable photoswitching system (in this case, '*E/Z*'), even when only spectra containing one pure isomer are known (in this case, only the spectra of the pure *E* isomer obtained from thermal relaxation of the sample were available). The calculation required the spectroscopy data of the sample at two wavelengths where the photoisomerisation equilibrium has been established (please refer to Section 5.2.3 for detailed calculation). This calculation was based on the assumption that the ratio of quantum yields of the two isomers ( $\Phi E/\Phi Z$ ) remains consistent at the two selected wavelengths. Therefore, it is preferable to select wavelengths that are not significantly different. Hence, data from 340 nm and 365 nm were employed to calculate the PSS ratio after 365 nm wavelength irradiation. For the PSS calculation after 457 nm irradiation, data from 450 nm and 457 nm were used (Figure 2-3, right). Using Fischer's method, it was confirmed that linker **4** undergoes quantitative isomerisation resulting in over 99% of the *Z* isomer following 365 nm irradiation, consistent with the results reported by Fuchter and colleagues. Irradiation with a 457 nm LED resulted in a PSS composition of 75% *E* isomer.

#### 2.2.3.2 LC-MS characterisation of linker **4**

The PSS ratio of linker **4** was also determined using liquid chromatography-mass spectrometry (LC-MS). A 1 mM sample solution of the linker in water with 40% MeCN and 0.1% formic acid was prepared. Following the acquisition of the LC-MS chromatogram of the non-irradiated sample, the sample was irradiated with a 365 nm LED for 3 or 10 minutes and the corresponding chromatograms were recorded. Using mass spectra, the peaks representing the

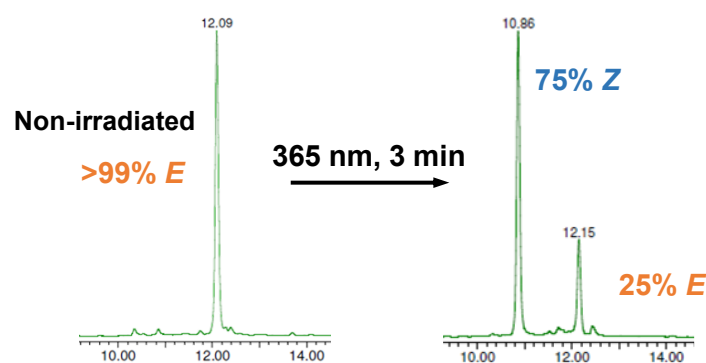


**Figure 2-4. LC-MS chromatograms of linker 4.**

LC-MS chromatograms of a solution of 1 mM AAP linker **4** in water with 40% MeCN and 0.1% formic acid, recorded without irradiation or after irradiated with 365 nm LED for 3 min. The peaks were assigned according to the MS trace and integrated.

*E* or *Z* isomers of linker **4** in the liquid chromatogram were identified. Upon integrating the area under the curve (AUC) of these isomer peaks in the liquid chromatogram, it was found that 3 min of UV light irradiation resulted in a composition of 75% *Z* isomer and 25% *E* isomer in the sample (Figure 2-4). Extending the irradiation time to 10 min did not alter this ratio, suggesting the solution reached its PSS within the first 3 min of irradiation.

### 2.2.3.3 NMR characterisation of the photostationary state of linker **4**

Further characterisation of the PSS of linker **4** was performed using proton nuclear magnetic resonance ( $^1\text{H}$  NMR) spectroscopy, which enabled the monitoring of the photoswitching process at a molecular level.<sup>166</sup> A solution of linker **4** was prepared freshly from a solid sample of **4** which was stored protected from light. The sample was prepared in deuterated DMSO at an approximate concentration of 15 mM in an NMR tube, with minimal exposure to ambient light. To investigate the impact of different irradiation conditions on the isomeric composition of the solution, I sequentially recorded NMR spectra after each irradiation step. Considering the high sample concentration used in this experiment, a longer irradiation period would likely be necessary to reach the PSS.<sup>167</sup> The first NMR spectrum was taken pre-irradiation, followed by spectra after irradiation with 457 nm light for 5 min and another 5 min, and then 365 nm light irradiation for 3 min, 5 min, and 10 min and another 10 min.<sup>167</sup>

Changes in the chemical shifts and peak intensities in the spectra enabled determination of the relative abundance of *E* and *Z* isomers in the sample after irradiation (Figure 2-5). Through analysis of the NMR spectra following each irradiation step, an increase in the size of the peaks was observed which corresponded to photoisomerisation to the *Z* isomer in response to

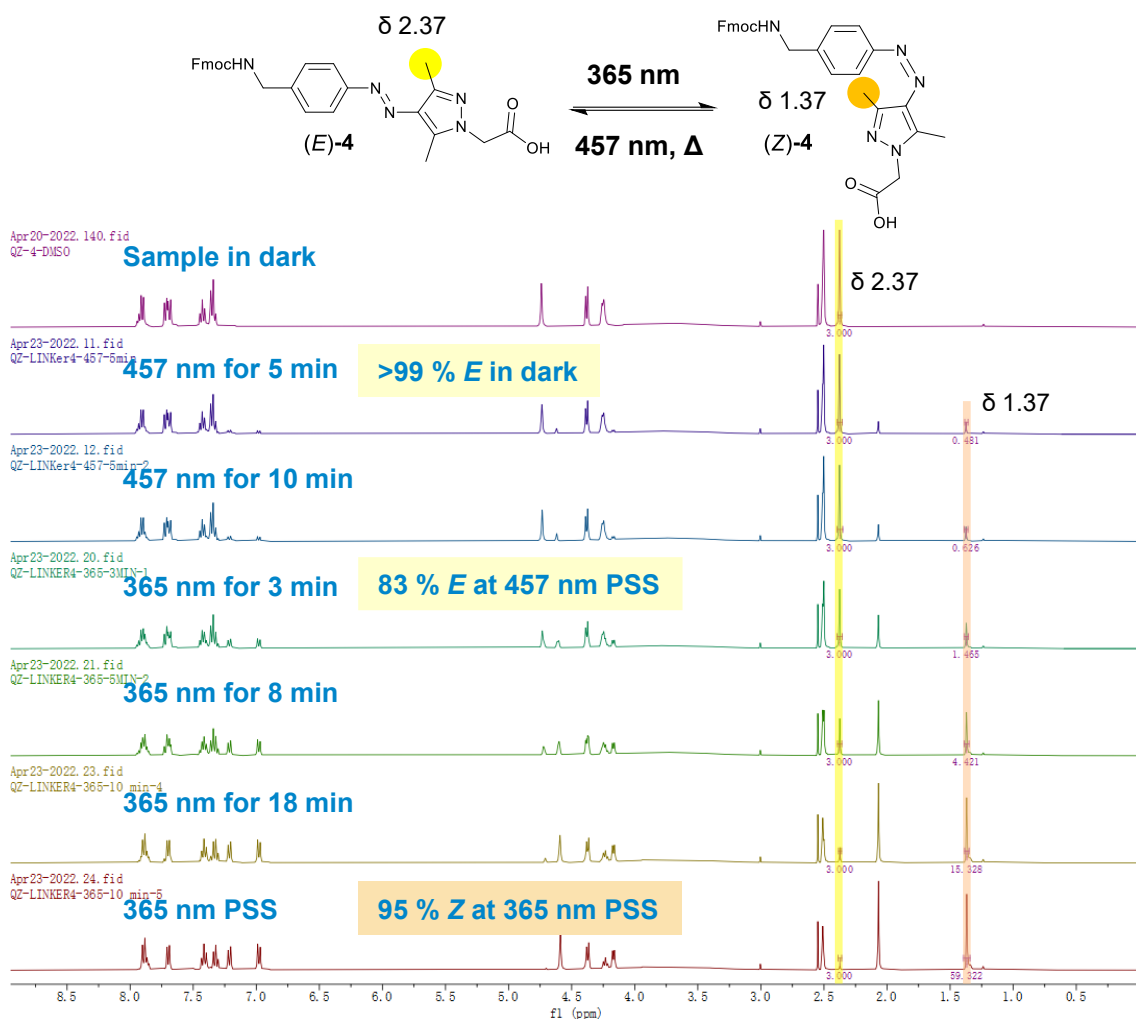


**Figure 2-5. Characterisation of the photostationary state of linker 4 isomers using NMR**

The proton NMR signal integration of the highlighted methyl protons was used to calculate the relative abundance of *E/Z* isomers in the sample after irradiation.

prolonged irradiation with 365 nm light. Integration of peaks corresponding to the methyl groups on *E/Z* isomers (highlighted in Figure 2-5, Section 7.1.2) revealed that the non-irradiated sample consisted predominantly of the *E* isomer (>99% *E*). Upon irradiation with 457 nm light, a PSS comprising 83% *E* isomer was achieved, and with 365 nm light irradiation, a PSS composition of 95% *Z* was achieved.

#### 2.2.3.4 Summary of photoswitching properties of linker 4

The photoswitching properties of linker 4 were investigated and its potential as a photoswitchable linker for PROTAC was evaluated using multiple methods (Table 4). Near-quantitative *E* to *Z* photoisomerisation under 365 nm light irradiation was unveiled by NMR and UV-Vis analyses of linker 4. In contrast, the LC-MS results exhibited a lower proportion

of the *Z* isomer (75%). This discrepancy could be due to the LC-MS traces reflecting the diode array results of compounds, which represent the summation of compound absorbance across all wavelengths. While in the UV-Vis analysis, calculations were predicated with a specific wavelength ( $\lambda_{\text{max}}$ ). Isomers *E* and *Z* at wavelengths distinct from  $\lambda_{\text{max}}$  possess different molar attenuation coefficients, which could contribute to the LC trace results. Alternatively, the noted discrepancy might arise from the isomer interconversion on the column due to the acidic pH conditions within the LC-MS system. The different solvent systems used for these methods could also influence the photoisomerisation process and the results obtained.

A high *E* isomer photoisomerisation was achieved *via* 457 nm LED light irradiation. It should be noted that a greater *E* isomer PSS ratio might be achieved using varying visible light wavelengths or a combination of multiple wavelengths. The objective with 457 nm LED irradiation was to convert most of the *Z* isomer in the mixture to its more thermodynamically stable *E* counterpart, thereby minimising the *Z* isomer presence. In our experimental setup, 457 nm LED irradiation was sufficient for achieving a significant enrichment of the *E* isomer. The *Z* isomer in the mixture following irradiation could thermally isomerise back to the *E* isomer unless further exposed to UV light irradiation.

The discrepancy in results acquired from different analytical techniques underscores the significance of utilising a variety of methods to determine the composition of a photoswitchable system. It is important to consider the different sensitivities and detection limits of these analytical techniques when interpreting the results.

**Table 4. Summary of PSS ratio results determined with different methods**

Method	Isomeric composition		Irradiation time	Sample concentration and solvent
	457 nm	365 nm		
UV-Vis	75% <i>E</i> , 25% <i>Z</i>	>99% <i>Z</i>	1 min	20 $\mu\text{M}$ in water with 0.2% DMSO
LC-MS	Not determined	75% <i>Z</i> , 25% <i>E</i>	3 min	1 mM in water with 40% MeCN and 0.1% formic acid
NMR	83% <i>E</i> , 17% <i>Z</i>	95% <i>Z</i> , 5% <i>E</i>	3-20 min	15 mM in deuterated DMSO

Despite the variation observed, it is evident that linker **4** exhibited rapid and reversible photoswitching between *E/Z* isomers and features a high conversion to the *Z* isomer. The capability to manipulate the isomeric composition of linker **4** through light irradiation and the maintenance of a high *Z* isomer-containing PSS demonstrate its potential application in the development of photoswitchable PROTACs.

## 2.3 Targeting multiple kinases with photoswitchable PROTACs

### 2.3.1 Protein kinases as drug targets

Protein kinases serve as key components within the cell signalling network, playing fundamental roles in biological processes such as cell proliferation, metabolism, and survival.<sup>168</sup> They regulate the activity and function of substrate proteins through phosphorylation, an important post-translational modification (PTM) that involves the transfer of a  $\gamma$ -phosphate from ATP to the substrate protein. Based on the phosphorylated residues, kinases can be categorised into serine/threonine kinases, tyrosine kinases (both receptor and non-receptor), and tyrosine kinase-like enzymes. Serine or threonine kinases phosphorylate hydroxyl groups on serines and threonines of their substrate proteins, while tyrosine kinases target tyrosine residues.

Dysregulation or aberrant activity of protein kinases may lead to the development and progression of various diseases. Protein kinases represent the most frequently observed domain among known cancer genes.<sup>169</sup> Reports indicate that up to a quarter of all protein kinases might be involved in oncogenesis, with over 85% of kinases in the kinome exhibiting dysregulation in at least one human disease.<sup>170,171</sup> Consequently, the inhibition of these kinases has emerged as a promising strategy for the development of effective cancer therapies, positioning protein kinases among the extensively researched therapeutic tumour targets.<sup>172</sup>

The approval of the kinase inhibitor Imatinib (STI-571, Gleevec) for chronic myelogenous leukemia (CML) treatment spurred a surge in kinase inhibitor discovery. This breakthrough was followed by successes in antibody-based drugs like trastuzumab, which targets the epidermal growth factor receptor (erbB2, HER2) in breast cancer, and cetuximab for colon cancer.<sup>173</sup> As of January 2023, the US Food and Drug Administration (FDA) has approved 72 small molecule kinase inhibitors for the treatment of cancer and other diseases, with hundreds more currently in clinical trials.<sup>174</sup> However, the high complexity of the kinome family, has led current drug discovery research to explore less than 10% of the human kinome, leaving a vast portion of potential kinase drug targets uncharacterised. Moreover, the development of drugs that selectively target specific kinases while sparing others remains a significant challenge due to the high degree of conservation at the ATP binding site.<sup>175</sup>

Targeting kinases with PROTACs has emerged as a promising approach for modulating kinase dysfunctions. Kinase inhibitors are readily available and can be easily modified, making them suitable starting points for PROTAC design. By 2020, the literature had reported around 57 kinases that have been successfully degraded with PROTACs.<sup>176</sup> However, thanks to large-scale chemo-proteomics studies by Donovan *et al.* (as mentioned in Section 1.5.2), the number of degradable kinases has significantly expanded to over 200.<sup>113</sup> Kinase-targeting PROTACs offer a significant advantage in that they can selectively degrade various kinase subtypes, even in instances of high structural homology.<sup>50</sup> My goal was to leverage this advantage to develop kinase-targeting PROTACs with robust target selectivity.

### **2.3.2 Promiscuous kinase inhibitors CTx-0294885**

The majority of kinase inhibitors in clinical use bind to the ATP site, and their selectivity is often achieved by modifying functional groups to target regions adjacent to the ATP binding site.<sup>177</sup> Selective inhibitors, which bind and inhibit a small subset or subfamily of kinases, allow for more precise and effective modulation of kinase activity while minimising side effects. Such selectivity is vital in cancer treatment as off-target effects might compromise their therapeutic efficacy and induce adverse side effects.<sup>178,179</sup> However, large-scale selectivity screening platforms have revealed that several approved kinase inhibitors displayed limited selectivity and targeted multiple kinases.<sup>173,180,181</sup> These promiscuous, non-selective kinase inhibitors can bind and inhibit multiple kinases across different classes simultaneously, potentially resulting in off-target effects and increased toxicity.

Immobilised non-selective kinase inhibitors have been used as kinase-capturing tools in chemical proteomics kinome profiling studies, culminating in the development of ‘Kinobeads’, which represents the most efficient kinase enrichment strategy to date.<sup>182,183</sup> Zhang *et al.* reported the characterisation of the promiscuous kinase inhibitors CTx-0294885, using it as a kinase capture tool in large-scale kinome profiling experiments.<sup>184</sup> In their study, MDA-MB-231 cell lysate was incubated with CTx-0294885-immobilised affinity resins and then subjected to quantitative proteomics profiling. The researchers identified 235 protein kinases that were enriched by CTx-0294885-immobilised beads. Among these kinases, CTx-0294885 demonstrated high affinity towards a broad spectrum of kinase families and effectively captured all members of the AKT family. Through the combination of CTx-0294885 with other kinase inhibitors, the researchers expanded the scope of kinome profiling, thereby opening new

avenues for in-depth analysis of kinase-associated signalling networks and the development of innovative combination therapies for cancer.

### 2.3.3 Photoswitchable multi-kinase PROTAC: the design

Previously in our research group, Dr. Kounde designed an AAP-based photoswitchable PROTAC, **AP-PROTAC-1**, for the switchable degradation of BRD2/4.<sup>110,164</sup> Encouraged by his promising results, I sought to extend the application of the AAP linker **4** to another protein class. In this study, a photoswitchable, multi-kinase targeting PROTAC (**AP-PROTAC-2**) was designed, employing the promiscuous kinase inhibitor CTx-0294885 as the POI ligand and the developed arylazopyrazole photoswitch **4** as the linker.

The incorporation of the novel arylazopyrazole photoswitch **4** into the PROTAC structure could introduce an additional layer of control over multi-kinase degradation activation. This incorporation could offer favourable PSS ratios, high thermostabilities, and the capability for reversible switching between the *E* and *Z* PROTAC conformations. These enhanced photoswitchable properties of the PROTACs could facilitate the independent exploration of protein degradation profiles associated with each conformation, while avoiding frequent intermittent irradiation during *in vitro* analysis.

Previous studies on non-switchable multi-kinase PROTAC designs have revealed that PROTAC's degradation of target proteins can exhibit enhanced and distinct selectivity compared to the parent inhibitor. This selectivity arises from the stringent requirement for active ternary complex formation, rather than merely target inhibition. Developing photoswitchable PROTACs targeting a specific protein often requires extensive linker optimisation, as demonstrated in the literature (Section 1.5.1). By introducing the promiscuous kinase inhibitor CTx-0294885 into the PROTAC design, I aimed to significantly broaden the potential scope of targeted kinases, thereby increasing the likelihood of achieving photoswitchable isomer-selective protein kinase degradation. The resultant compound holds the potential for simultaneously engaging and degrading multiple kinases, thus also expanding its potential therapeutic applications.

In summary, this approach integrated the arylazopyrazole photoswitch **4** and the promiscuous kinase inhibitor CTx-0294885 into the PROTAC design. The aim was to achieve photoswitchable and selective degradation of kinases using the *E* and *Z* PROTAC isomers. The



primary objective was to explore the impact of converting a non-selective multi-kinase inhibitor into a PROTAC under the stimulus of light. This investigation aimed to provide insights into the alteration in selectivity towards target kinases and the relationship between the inhibitory activity of the warhead and the degradation mediated by PROTACs. The results could contribute to advancing future research in light-responsive targeted protein degradation and the development of more precise, selective, and efficacious degraders for diseases associated with kinases.

## 2.4 Synthesis and photoswitching properties characterisation of AP-PROTAC-2

### 2.4.1 Synthesis of AP-PROTAC-2

The designed photoswitchable PROTAC, **AP-PROTAC-2**, incorporates the AAP photoswitchable linker **4**, a commercially available cereblon (CRBN) E3 ligase ligand lenalidomide, and the multi-kinase inhibitor CTx-0294885. CRBN is the substrate receptor of the E3 ubiquitin ligase Cullin-RING ligase 4 complex (CRL4<sup>CRBN</sup>, Figure 2-6A). This ligase complex is formed by interactions between CRBN, DNA damage-binding protein 1 (DDB1), Cullin-4A (Cul4A) and the regulator of Cullins-1 (RoC1).<sup>185</sup> Within this complex, CRBN recognises and directs protein substrates for ubiquitination, thereby initiating substrate degradation. Immunomodulatory imide drugs (IMiDs), which are small molecule inhibitors targeting CRBN (Figure 2-6), are exemplified here by lenalidomide, an FDA-approved IMiD. Lenalidomide exerts its anti-cancer effects by acting as a molecular glue that binds CRBN and

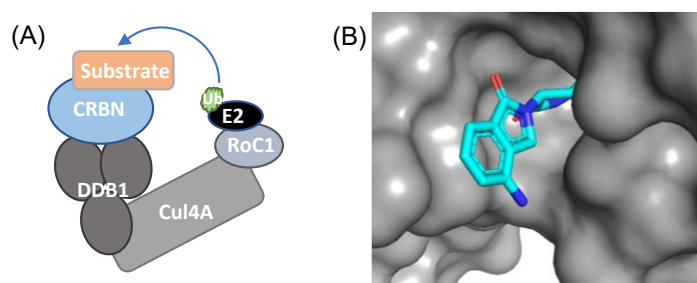
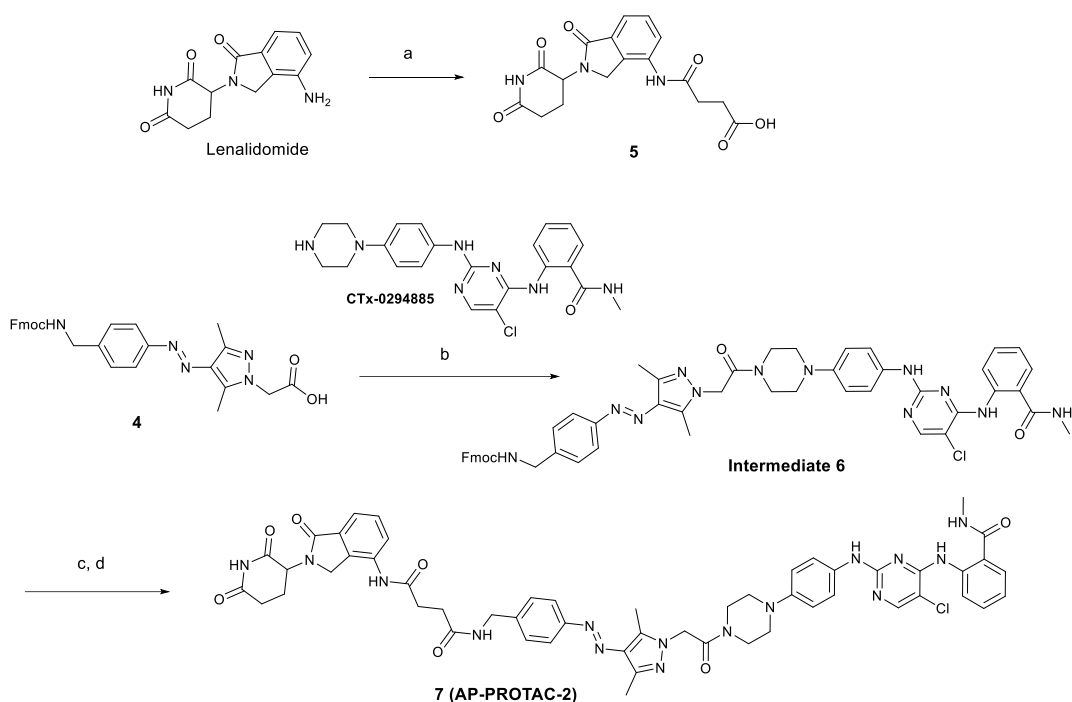


**Figure 2-6. Model of the Cullin-RING ligase 4 complex**

(A) Illustration of CRL4<sup>CRBN</sup> complex model. (B) Crystal structure displaying lenalidomide (cyan stick) bound to *G. gallus* CRBN (grey surface). PDB: 4CI2.<sup>187</sup>



### Scheme 2-3. Synthetic route to compound 7 (AP-PROTAC-2)

Reagents and conditions: (a) Succinic anhydride, DMF, 60 °C, 24 h; 100% yield; (b) HATU, DIPEA, DMSO, RT, 16 h; (c) Piperidine, DMF, 16 h; (d) HATU, DIPEA, **5**, RT, 16 h. 3-step b-d yield = 6.8%.

neosubstrates such as cancer-related proteins Ikaros and casein kinase 1 alpha, inducing the formation of a ternary complex.<sup>186</sup> These events lead to ubiquitination and subsequent degradation of the substrate. In the design of AP-PROTAC, to incorporate a short linker, commercially available lenalidomide was coupled with succinic anhydride. This process yielded ligand **5**, comprising a short carboxylic acid linker connected to the solvent-exposed C4 phthalimide aniline of lenalidomide, which retains compatibility with CRBN binding (Figure 2-6B).<sup>187</sup>

The synthesis of **AP-PROTAC-2** involved two amide coupling reactions on linker **4** (Scheme 2-3). The kinase inhibitor CTx-0294885 was provided by GlaxoSmithKline Ltd. or synthesised by our collaborator Jennifer R. Baker *et al.* using an integrated flow and microwave approach.<sup>188</sup> CTx-0294885 was coupled to linker **4** in an amide coupling reaction to form intermediate **6**. Then the Fmoc group on intermediate **6** was deprotected, and the resultant amine was coupled to carboxylic acid **5** in a second amide coupling reaction, to yield the final product **7 (AP-PROTAC-2)**.

#### 2.4.2 Photoswitching properties characterisation of AP-PROTAC-2 (7)

The examination of **AP-PROTAC-2**'s photoswitching properties was conducted following the procedures described in Section 2.2.3. The samples were prepared under dim light conditions to shield them from ambient light and were allowed to relax in darkness to facilitate isomerisation to the *E* isomer. During the measurement, the samples were minimally exposed to ambient light. Analysis of the samples by LC-MS revealed that **AP-PROTAC-2** could be reversibly switched to a PSS containing 80% *E* isomer with 457 nm irradiation or to a PSS containing 90% *Z* isomer with 365 nm irradiation (Figure 2-7A).

UV-Vis spectroscopy was employed to record the UV-Vis spectra of a solution of **AP-PROTAC-2** following light irradiation (Figure 2-7B, C). The obtained spectra showed that a 1 min irradiation time was sufficient to establish the PSS in aqueous solutions of **AP-PROTAC-2**. The UV-Vis spectra exhibited distinct absorption bands for the *E* and *Z* isomers, with a  $\lambda_{\text{max}}$  at 350 nm. Irradiation at 457 nm resulted in an enrichment of *E* isomers which showed a notable absorption band between 340-380 nm. Irradiation with 365 nm UV light led to the formation of the *Z* isomer, as evidenced by the absorption band between 420-460 nm.

Notably, the *Z* isomer of **AP-PROTAC-2** exhibited stronger absorption within the range of 340-380 nm compared to the *Z* isomer of linker **4**. Further analysis of the UV-Vis spectra of the kinase inhibitor CTx-0294885 revealed that the ligand has strong absorption in the range of 300-360 nm, which overlaps with the  $\lambda_{\text{max}}$  region of interest (Figure 7-5). Both the CTx-0294885 ligand and the photoswitchable linker absorb 365 nm light, which could affect the accuracy of PSS calculation using UV-Vis. Therefore, PSS ratio determination using the UV-Vis method was avoided, and the PSS ratio determined with LC-MS was used in the subsequent analysis.

The thermal stability of the *Z* isomer of **AP-PROTAC-2** at 37 °C was examined with UV-Vis spectroscopy. A solution of **AP-PROTAC-2** in water was first irradiated with 365 nm light to enrich the *Z* isomer and then kept at 37 °C in darkness, with UV-Vis spectra recorded every 30 min (Figure 2-7D). The absorbance change at  $\lambda_{\text{max}}$ , 350 nm was plotted against time, and the *Z* isomer proportion in the sample was calculated using the PSS ratio determined with LC-MS (Figure 2-7E). The *Z* isomer proportion gradually decreased from 90% immediately after irradiation to 80% after 3 hours due to thermal isomerisation. The half-life of the *Z* isomer in water at 37 °C was calculated as 31.7 hours. To ensure a sustained high content of the *Z* isomer

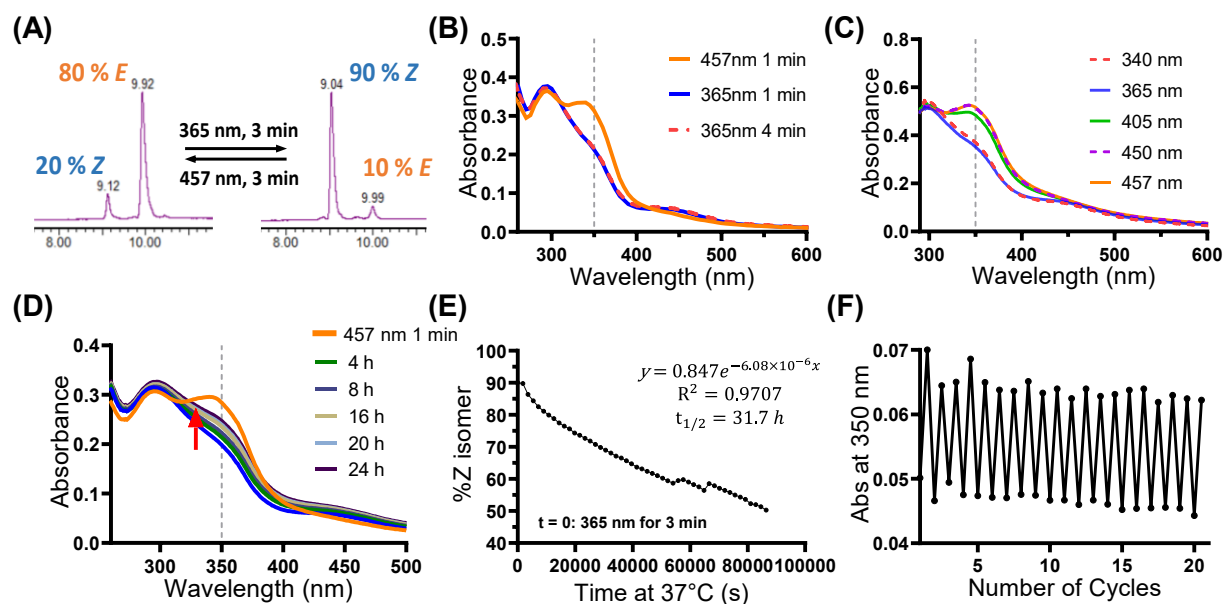


**Figure 2-7 Photoswitching properties characterisation of AP-PROTAC-2**

(A) LC-MS chromatograms of 0.1 mM AP-PROTAC-2 in 20% MeCN in water with 0.1% formic acid under the specified irradiation conditions. Peaks were assigned based on the MS trace and integrated to give the PSS ratio. (B) UV-Vis spectra of 10 μM AP-PROTAC-2 in water with 0.1% DMSO under the stated irradiation conditions. (C) UV-Vis spectra of 20 μM AP-PROTAC-2 in water with 0.2% DMSO under different wavelengths of light irradiation. (D) UV-Vis spectra of 12 μM AP-PROTAC-2 in water with 0.1% DMSO after 365 nm irradiation recorded over time at 37 °C. (E) The Z isomer population was calculated from the change in absorbance at 350 nm from the UV-Vis spectra recorded in (C). The Z isomer population was plotted against time. (F) Reversible switching of 10 μM AP-PROTAC-2 solution in water with 0.1% DMSO at room temperature following 365 nm or 457 nm irradiation for 20 cycles. Images adapted with permission.<sup>110</sup>

for subsequent cell treatments, samples treated with Z isomer-enriched medium were kept in foil and subjected to intermittent irradiation with 365 nm light every 3 hours. This periodic irradiation helped maintain a higher Z isomer proportion, allowing more accurate assessments of distinct outcomes from E or Z isomer treatments.

To evaluate the reversibility of the photoisomerisation between E and Z isomers, a solution of AP-PROTAC-2 was subjected to multiple irradiation cycles with 365 nm or 457 nm light. Examination of the recorded UV-Vis spectra revealed that the compound was stable and reversible across 20 switching cycles (Figure 2-7F).

Overall, in comparison to previously reported PROTACs incorporating azobenzene photoswitchable linkers,<sup>107–109</sup> AP-PROTAC-2 demonstrates improvements, including an enhanced PSS ratio, faster isomer switching, and an extended Z isomer half-life. These features

position **AP-PROTAC-2** as a promising candidate to control protein degradation with light irradiation.

## 2.5 Cytotoxicity assay of AP-PROTAC-2

To assess the cytotoxicity of **AP-PROTAC-2**, its effect on MDA-MB-231 cell growth was tested using an IncuCyte®-based assay (Figure 2-8). The IncuCyte system enables the

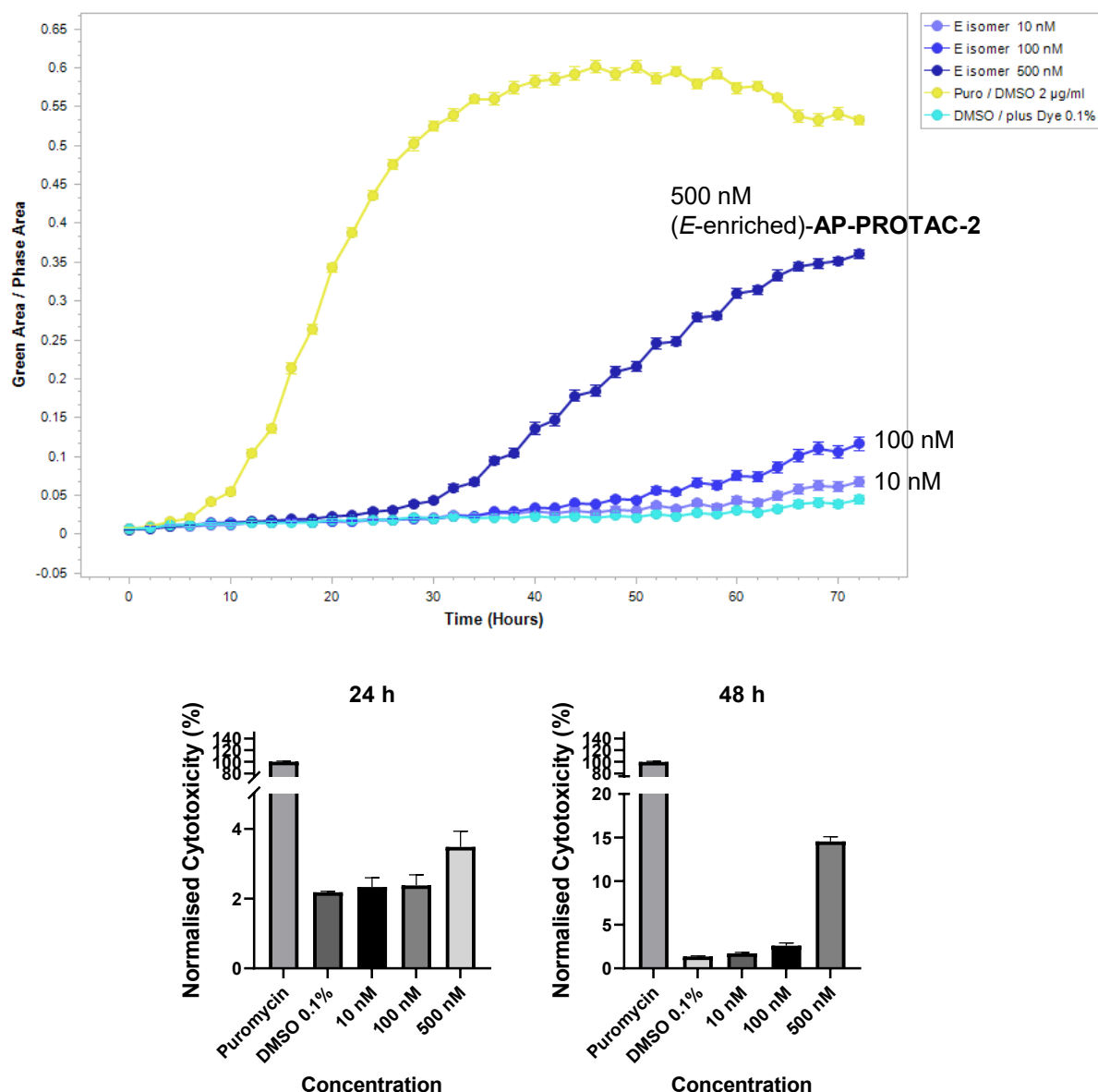


**Figure 2-8 Cytotoxicity assays of AP-PROTAC-2**

MDA-MB-231 cells were treated with 10 nM, 100 nM, 500 nM (*E*-enriched)-**AP-PROTAC-2**, along with 0.1% DMSO and puromycin (2 µg/mL) as the controls. Top: Signal plot of SYTOX™ Green Nucleic Acid Stain normalised to cell phase area over a duration of 72 h. Bottom: Cytotoxicity plots at 24 h and 48 h normalised to the puromycin-induced death control.

continuous monitoring of cell proliferation through label-free cell confluence measurement, which quantifies the cell area on the plate. Cell viability is evaluated by real-time quantification of the cell death signal emitted by SYTOX™ Green Nucleic Acid Stain. This stain binds to nucleic acids and emits a green fluorescence signal (upon excitation within 450 to 490 nm range) when cell membrane integrity is compromised due to cell death. Cytotoxicity is then determined by calculating the ratio of the area of dead cells to the total cell area. However, it should be noted that this method does not allow for a direct real-time assessment of the cytotoxicity of the *Z* isomer of **AP-PROTAC-2**, as excitation by IncuCyte during dye signal measurement can induce photoisomerisation of the *Z* isomer to the *E* isomer.

Cells were cultured in a 96-well plate and treated with varying concentrations of **AP-PROTAC-2** along with SYTOX™ Green Nucleic Acid Stain. The control cells were treated with 2 µg/mL puromycin in 0.1% DMSO with the dye, serving as the 100% cytotoxicity group. Our results revealed that MDA-MB-231 cells treated with 500 nM *E*-enriched-**AP-PROTAC-2** exhibited only 2% cytotoxicity compared to the puromycin-induced cell death controls after 24 hours of treatment (Figure 2-8, bottom). This finding indicates that **AP-PROTAC-2** does not exhibit cytotoxicity in MDA-MB-231 cells under the conditions tested.

In contrast, the cytotoxicity assay for cells treated with the kinase inhibitor CTx-0294885 showed approximately 50% cytotoxicity at a concentration of 100 nM after 12 hours of treatment (Figure 7-6). This result underscores that the conversion of the broad-spectrum kinase inhibitor into a PROTAC design significantly reduced the cytotoxicity associated with the warhead compound.

## 2.6 Quantitative multiplexed proteomics analysis of kinase degradation

For the *in vitro* characterisation of **AP-PROTAC-2**, since it was unclear which of the diverse kinases engaged by the PROTAC warhead CTx-0294885 might be degraded by each isomer of **AP-PROTAC-2**, I conducted a set of expression proteomics experiments to determine the kinase degradation profile of **AP-PROTAC-2**. A quantitative isobaric tandem mass tag (TMT) labelling proteomic analysis was employed to quantify changes in protein levels after PROTAC treatment (Figure 2-9).

The breast tumour cell line MDA-MB-231 was selected for these experiments, as approximately 75% of the kinome is expressed in these cells, and the kinase inhibitor CTx-

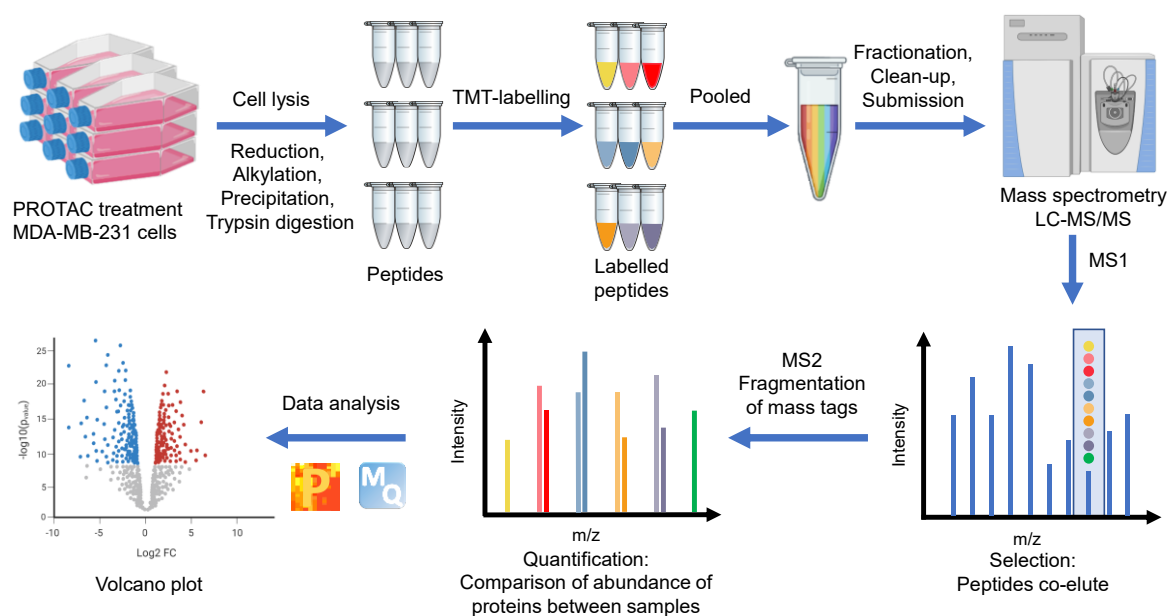


**Figure 2-9 Quantitative proteomics workflow employed**

Figure created with BioRender and PowerPoint.

0294885 had previously been characterised in this cell line.<sup>189</sup> In the pursuit of understanding the cellular impact of the *E* and *Z* isomers of **AP-PROTAC-2**, prior to the cell treatment, the media containing 100 nM **AP-PROTAC-2** was irradiated for 3 min with 457 nm light to produce (*E*-enriched)-**AP-PROTAC-2**, or irradiated with 365 nm light to produce (*Z*-enriched)-**AP-PROTAC-2**. The cells were then treated in triplicate for 24 h, with 0.1% DMSO serving as a control. The cell treatment was performed in a dark room under red light to avoid compound irradiation and minimise the impact of ambient light on the samples. The treated cell flasks were wrapped in foil to protect them from light. To maximise the *Z/E* isomer ratio, cells treated with (*Z*-enriched)-**AP-PROTAC-2** received intermittent irradiation for 1 min every 3 h during the first 17 h. After treatment, the cells were washed and lysed, with the resulting lysate subjected to reduction and alkylation, followed by protein precipitation. Trypsin protease was then added to digest the proteins into peptides. The peptides were subsequently labelled with 9 of the 10-plex TMT reagents. The labelled peptides were combined and analysed in mass spectrometers.

This implementation of TMT labelling brings advantages such as sample multiplexing, reduced machine time, improved accuracy, and the prevention of missing values from low-abundance proteins.<sup>190</sup> The incorporation of TMT tags allowed the TMT-labelled peptides from different samples with the same *m/z* value to co-elute during the first mass spectrometer (MS1) analysis

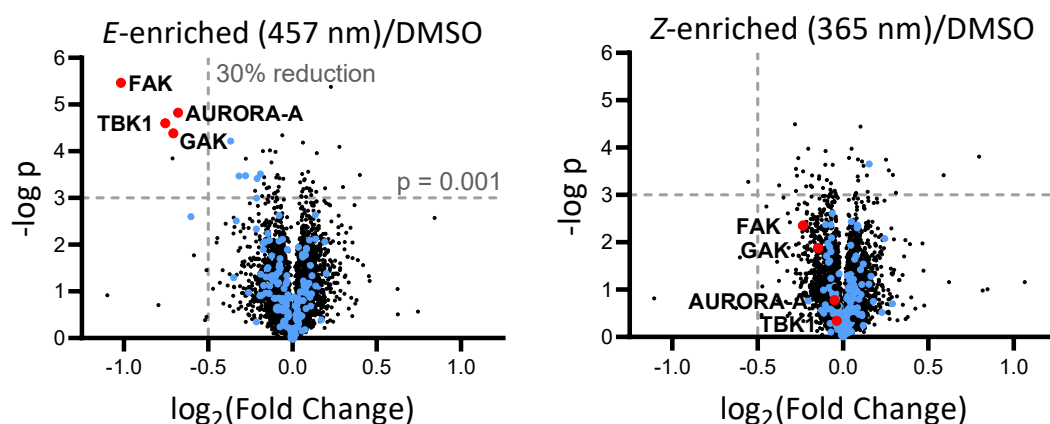


**Figure 2-10 Volcano plots showing changes in protein levels with AP-PROTAC-2 treatment**

MDA-MB-231 cells were treated for 24 h with 100 nM AP-PROTAC-2 irradiated with either 457 nm (for *E*-enriched) or 365 nm (*Z*-enriched). The *Z*-treated cells received intermittent irradiation for 1 min every 3 h during the first 17 h of treatment. The proteome was then analysed by multiplexed quantitative proteomics. The fold change in the relative abundance of 4,915 identified proteins when comparing treated samples and the DMSO control is plotted against significance,  $-\log(p)$  ( $n = 3$ , false discovery rate FDR < 5%). Blue dots: protein kinases identified. Red dots: significantly and differentially affected kinases. The dashed grey lines indicate  $p = 0.001$  and the protein abundance was reduced by 30%. Images adapted with permission.<sup>110</sup>

(Figure 2-9). These peptides then underwent fragmentation in the second mass spectrometer (MS2), leading to the production of TMT reporter ions and peptide fragment ions. To identify the parent protein, peptide fragment ions were analysed and compared against a database containing peptide sequence and mass information, using software such as MaxQuant. Peptide quantifications were achieved by comparing the intensities of reporter ions, which reflected the relative abundance of peptides in specific samples. The data was then processed, analysed, and presented in volcano plots using software such as Perseus, providing information on the relative abundance of the detected proteins across different samples.

A total of 4,913 unique proteins including 159 kinases were identified with the treatment of 100 nM (*E*-enriched)-AP-PROTAC-2, (*Z*-enriched)-AP-PROTAC-2, or 0.1% DMSO in triplicate (Figure 2-10). Kinase targets showing at least a 30% reduction ( $\log_2(\text{Fold Change})$  cut-off at  $-0.5$ ) in protein levels in treated samples compared to DMSO controls were prioritised for further analysis of isomer-dependent degradation (Figure 7-7). Remarkably, only four kinases (2.5% of the detected kinome), including GAK (Cyclin G-associated kinase), FAK (focal adhesion kinase), AURORA-A (Aurora kinase A) and TBK1 (TANK binding kinase 1), were found to be statistically significantly and consistently degraded by (*E*-



enriched)-AP-PROTAC-2, while remaining unaffected by (Z-enriched)-AP-PROTAC-2 (Figure 2-10, red dots,  $p < 0.001$ ). Notably, FAK displayed the most pronounced degradation response, with approximately 50% of the kinase being degraded following treatment with (E-enriched)-AP-PROTAC-2.

## 2.7 Immunoblots verification of degraded kinase targets

To validate the kinase targets identified in multiplexed quantitative proteomics, immunoblot analysis was conducted. MDA-MB-231 cells were subjected to AP-PROTAC-2 treatment,

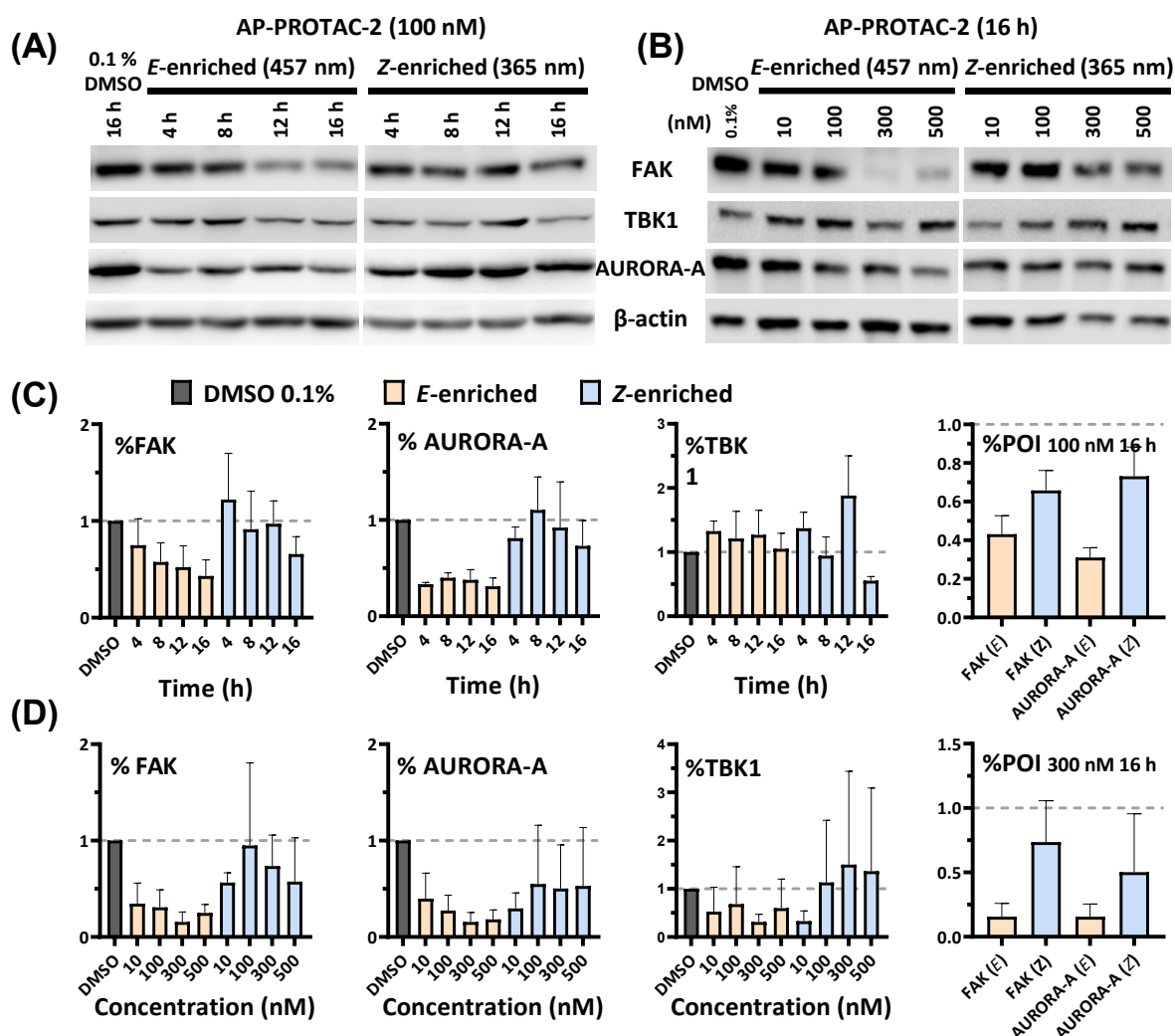


**Figure 2-11. AP-PROTAC-2 differentially degrades FAK and AURORA-A on immunoblots**

(A) Immunoblots and (C) quantification of FAK, AURORA-A, and  $\beta$ -actin in MDA-MB-231 cells after 4 h, 8 h, 12 h, or 16 h treatment with 100 nM AP-PROTAC-2 irradiated with 457 nm (E-enriched) or 365 nm (Z-enriched) (with intermittent 365 nm irradiation every 3 h for Z-enriched flasks). (B) Immunoblots and (D) quantification of 16 h treatment with indicated concentrations of compounds. Blots shown are representative of three replicates. Bars represent the mean signal normalised to  $\beta$ -actin, reported as mean  $\pm$  standard deviation (SD,  $n = 3$ ). Images adapted with permission.<sup>110</sup>

and the protein levels of the identified kinases were evaluated using immunoblotting. To find optimal conditions for isomer-selective degradation, MDA-MB-231 cells were treated with either 100 nM (*E*-enriched)-**AP-PROTAC-2** or (*Z*-enriched)-**AP-PROTAC-2** for durations of 4, 8, 12 or 16 hours (Figure 2-11A). In alignment with initial proteomics findings, whilst (*E*-enriched)-**AP-PROTAC-2** degraded 57% of FAK and 69% of AURORA-A by 16 h, (*Z*-enriched)-**AP-PROTAC-2** displayed significantly reduced activity, degrading FAK only up to 35% and AURORA-A up to 27% (Figure 2-11C). However, no substantial degradation of GAK or TBK1 was observed at 100 nM concentration (Figure 7-8).

In dose-response analysis undertaken at 16 h treatment (Figure 2-11B), (*E*-enriched)-**AP-PROTAC-2** achieved up to 85%  $D_{\max}$  for both FAK and AURORA-A, and up to 70% for TBK1, at 300 nM concentration. In comparison, (*Z*-enriched)-**AP-PROTAC-2** required 500 nM concentration to achieve degradation levels of up to 43% for FAK and 47% for AURORA-A, with no observed TBK1 degradation (Figure 2-11D, Figure 7-9). Through co-treatment with the proteasome inhibitor bortezomib (BTZ), it was further verified that the degradation of FAK, TBK1 and AURORA-A by (*E*-enriched)-**AP-PROTAC-2** is dependent

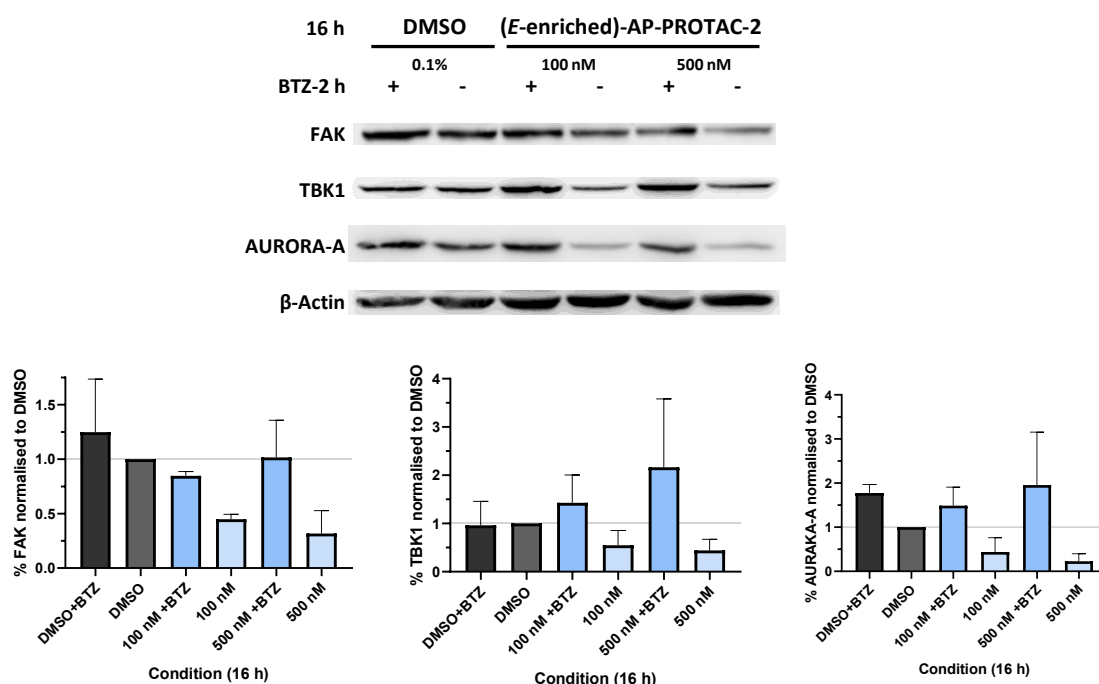


**Figure 2-12. Immunoblots and quantification for FAK, AURORA-A, TBK1, and β-actin in bortezomib (BTZ) pre-treated MDA-MB-231 cells**

Cells were pre-treated for 2 h with or without 10 μM BTZ, and then treated with 0.1% DMSO, 100 nM or 500 nM of (*E*-enriched)-**AP-PROTAC-2** for 16 h. Bars represent the mean signal normalised to β-actin, and were reported as the mean and SD of n = 3 biological replicates. Blots shown are representative of three replicates.

on the proteasome activity (Figure 2-12). Degradation of GAK was not observed under any tested condition using a commercially available GAK antibody, so the degradation of this kinase could not be confirmed by immunoblot (Figure 7-9C).

## 2.8 In-cell Western

In the pursuit of analysing multi-target protein degraders with improved throughput and efficiency, I employed the in-cell western assay to assess PROTAC-mediated degradation. This assay combines the specificity of western blotting with the reproducibility and throughput of an enzyme-linked immunosorbent assay (ELISA). The in-cell western assay offers rapid and accurate quantification of multiple proteins simultaneously, which could greatly reduce the analysis time during the development of multi-target PROTACs.

The in-cell western assay was conducted on MDA-MB-231 cells using (*E*-enriched)-**AP-PROTAC-2**. Since only the antibody for AURORA-A kinase had previously been validated for immunofluorescent analysis among the four identified kinase targets, the experiment only assessed AURORA-A levels post-treatment. MDA-MB-231 cells were treated with increasing concentrations of (*E*-enriched)-**AP-PROTAC-2**. Following treatment, the cells were fixed in the culture plate, permeabilised, and subjected to antibody incubation. The plate was incubated with primary antibody for AURORA-A and then incubated with fluorescent labelled secondary antibody along with a cell staining dye CellTag 520, which enabled signal normalisation to the

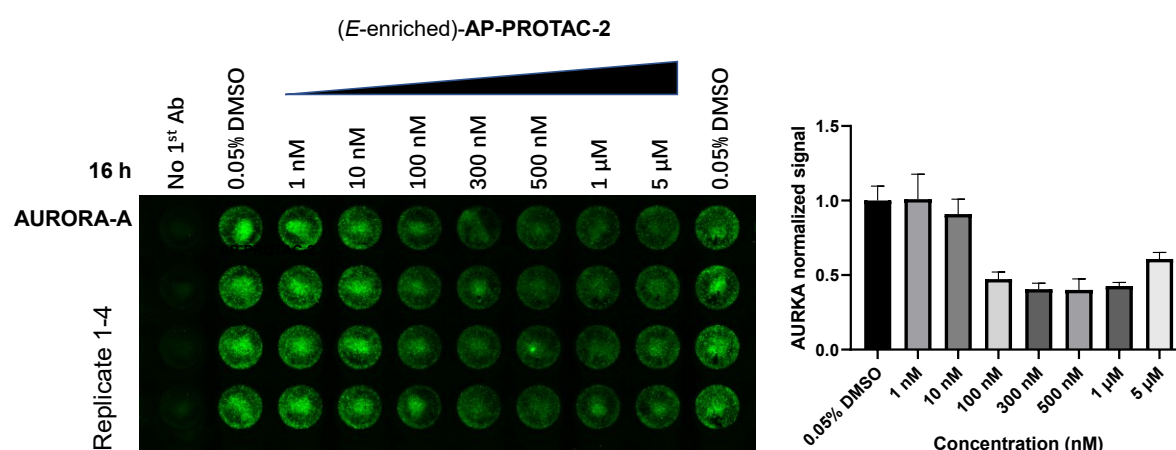


**Figure 2-13. In-cell western results**

MDA-MB-231 cells were treated with increasing doses of *E*-enriched-**AP-PROTAC-2**. After treatment, the cells in the plate were washed, fixed, permeabilised, and blocked, followed by incubation with antibodies and cell stain. Left: Image of in-cell western at 800 nm channel representing the AURORA-A signal. Right: Quantification of the AURORA-A signal normalised to cell number and was reported as the mean and SD of *n* = 4 biological replicates.

cell number. The in-cell western analysis was performed using the LI-COR ODYSSEY M system, with the AURORA-A signal and total cell number acquired using different wavelength channels. The AURORA-A signal was then normalised to the cell number, allowing for a quantitative evaluation of protein levels (Figure 2-12).

This analysis further unveiled the dose-dependent degradation effects of *E*-enriched-**AP-PROTAC-2** on AURORA-A protein levels within MDA-MB-231 cells, aligning with our immunoblot results (Figure 7-9). At a concentration of 100 nM, treatment with **AP-PROTAC-2** resulted in significant degradation of 53% of the AURORA-A protein. Increasing the PROTAC concentration to 300 nM further enhanced protein degradation, reaching a plateau with a 60% reduction in AURORA-A levels. However, no further decrease was observed when the dose was increased to 1  $\mu$ M. A higher PROTAC concentration of 5  $\mu$ M led to a slight increase in protein levels compared to the 1  $\mu$ M treatment, potentially indicating a trend that corresponds to the phenomenon known as the ‘hook effect’. However, there is a notable difference in the maximal degradation value  $D_{\max}$ , with a decrease from 85% on the blots to 60% in the in-cell assay. This might be attributed to variations in cell permeability and the binding of the primary antibody. Also, the influence of antibody specificity on the results appears more pronounced in the in-cell western assay than on the blots. It is therefore necessary to include additional controls in the in-cell western assay, such as a potent AURORA-A PROTAC or siRNA tools for AURORA-A knockdown. Nonetheless, the in-cell western assay demonstrated a smaller standard deviation among replicate samples, suggesting greater reliability and reproducibility in the obtained results.

## 2.9 Computational studies of the ternary complex<sup>c</sup>

In collaboration with Prof. Dima Kozakov of Stony Brook University, we conducted computational studies to delve into the putative ternary complex of either (*E*)-**AP-PROTAC-2** or (*Z*)-**AP-PROTAC-2** with FAK and CRBN using a novel half-linkers approach.<sup>191</sup> Models of the protein-ligand complex were generated first, including the E3 ligase-ligand complex

---

<sup>c</sup> The work presented in subsection 2.9 was conducted by Sergei Kotelnikov, Mikhail Ignatov, and Dima Kozakov from the Department of Applied Mathematics and Statistics and Laufer Center for Physical and Quantitative Biology, Stony Brook University, Stony Brook, NY, USA.

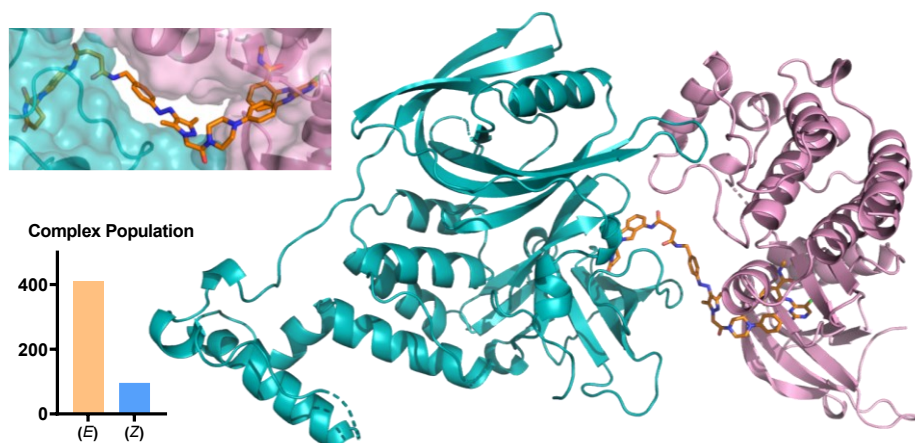


**Figure 2-14. Structural model of the CRBN/(E)-AP-PROTAC-2/FAK complex**

Cyan - E3 ligase CRBN; pink - FAK; orange stick - (*E*)-AP-PROTAC-2. Bottom left: Overall population of feasible low energy complex conformations formed with the *E* isomer compared to the *Z* isomer of AP-PROTAC-2.

based on the crystal structures of lenalidomide binds to CRBN, and the POI-ligand complex formed through a ligand docking model of CTx-0294885 to FAK kinase. Then, a large ensemble of PROTAC conformations was generated. Each conformation was then divided at the midpoint of the linker, resulting in two ‘half-linkers’ containing either the POI ligand or the E3 ligase ligand along with half of the linker and all conformations collectively formed the ‘half-linker clouds’. After excluding clashing conformers, the E3 and POI complexes, together with the docked ligands and the generated half-linker clouds, were docked to each other. To generate energetically favourable ternary complex poses, the docking was performed by a modified version of the PIPER program employing the fast Fourier transform (FFT)-based docking approach. An additional ‘silent’ convolution term was introduced to efficiently exclude infeasible complex poses.<sup>192,193</sup> The structures where the half-PROTACs could successfully connect into a complete PROTAC underwent energy minimisation and clustering to produce complete ternary PROTAC complex models.<sup>194</sup> Our modelling demonstrated that the overall population of feasible low-energy complex conformations formed with the *E* isomer was significantly larger than that of the *Z* isomer (Figure 2-14, bottom left). As suggested by previous studies, the configurational volume of feasible low-energy ternary complex poses serves as a good indicator of PROTAC’s degradation efficiency.<sup>195</sup> This modelling finding aligns with our empirical degradation efficiency observed with the *E* isomer.

A representative putative complex model of CRBN/(*E*)-AP-PROTAC-2/FAK is shown in Figure 2-14. This model illustrates that (*E*)-AP-PROTAC-2 interacts with FAK and CRBN, forming a cooperative ternary complex. The kinase-binding moiety of CTx-0294885 is fully

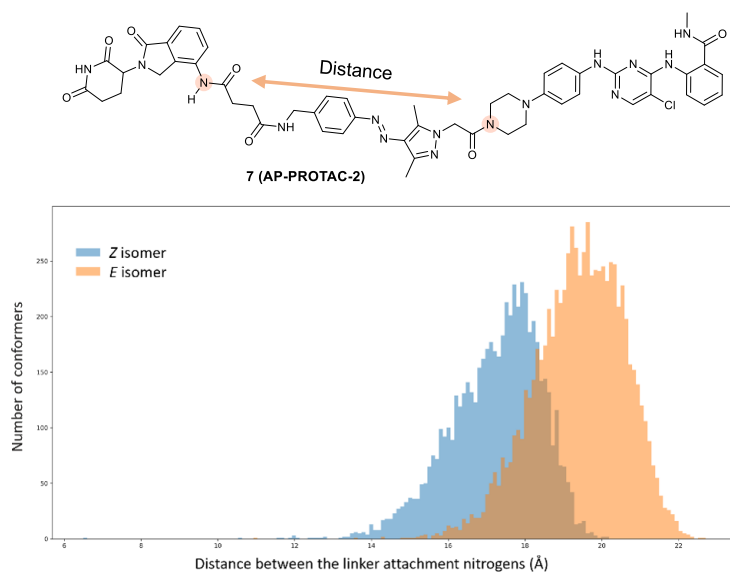


**Figure 2-15. Histogram of the distances between the linker attachment nitrogens for *E* and *Z* ETKDG-derived MMFF-optimised PROTAC conformers**

enclosed by the FAK protein. The distances between the two linker attachment nitrogen atoms on the E3 ligase ligand and the kinase inhibitor were calculated, and a distance histogram was generated (Figure 2-15). The histogram indicated that the distances among the top-ranked ternary complexes formed with the *E* isomer ranged from 19.3 to 21.1 Å. In contrast, the distance in the ternary complex formed with the *Z* isomer was shorter due to the ring stacking in the *cis* conformation, which could give rise to steric clashes between the two proteins. These results also helped to explain why the *Z* isomer was less effective in stabilising the CRBN-FAK lower energy conformation compared to the *E* isomer.

## 2.10 Discussion and conclusion

### 2.10.1 Potential optimisation of the immunoblot results

In the multiplexed quantitative proteomics experiments, four kinases that exhibited differential degradation upon photoswitchable PROTAC treatment (100 nM for 24 h) were identified. However, with the similar treatment conditions (100 nM for 16 h), GAK degradation could not be confirmed by immunoblots, indicating that the conditions used in the immunoblots may not have been optimal for detecting GAK degradation.

It is also important to consider the detection limit and sensitivity of the primary antibodies used in immunoblots. Reliable and reproducible immunoblot results depend heavily on the availability of high-quality, specific antibodies, which can significantly impact the dynamic

range and accurate quantification of protein levels.<sup>196</sup> In the study, I initially acquired three primary polyclonal antibodies for GAK, TBK1, and AURORA-A proteins from Invitrogen, but observed no degradation of these kinases with treatment. To investigate further, I tried monoclonal antibodies for TBK1 and AURORA-A proteins from Cell Signaling Technology. With these antibodies, I was able to consistently detect significant protein degradation under suitable conditions. This suggests that the failure to observe GAK degradation may have been due to the quality of the primary antibodies. Unfortunately, due to limited access to alternative commercial GAK antibodies, I was unable to further explore GAK protein degradation with immunoblot methods.

In addition to antibody selection, it is crucial to optimise various steps and reagents in immunoblot procedures to ensure reliable and reproducible results. For instance, different blocking buffers can influence the intensity of the horseradish peroxidase (HRP) signal and the detection of the primary antibody. In the experiments, it was found that using 5% milk in TBS-T as the blocking buffer reduced the background during imaging but required longer exposure times due to a weaker HRP signal. In contrast, the use of 3% bovine serum albumin (BSA) as the blocking buffer led to more nonspecific bands but a stronger HRP signal. Additionally, it is crucial to optimise the protein loading amount during immunoblotting to establish a linear relationship between protein quantity and the HRP signal readout.<sup>197</sup> By carefully fine-tuning these parameters, it is possible to enhance the quality and reliability of immunoblot data.

### **2.10.2 Comparison of AP-PROTAC-2 with reported photoswitchable PROTACs**

A summary of the photochemical properties and biological activities of representative photoswitchable PROTACs reported to date is provided in Table 5 (structures are illustrated in Figure 1-8), including a comparison with **AP-PROTAC-2**. The results highlight the superior photochemical properties of **AP-PROTAC-2**, made possible by the incorporation of the novel arylazopyrazole photoswitch. These characteristics include rapid photoisomerisation, allowing for quicker structural changes; an extended half-life of the Z isomer, ensuring stability for cell treatments; the capacity for multicycle photoswitching, enabling repeated activations; and a high PSS ratio of isomers, which facilitates accurate interpretation of degradation results from isomers. Collectively, these features underline the potential of arylazopyrazole-based photoswitches in the development of photoswitchable PROTACs, offering enhanced photoisomerisation kinetics and versatility to this emerging therapeutic modality.

**Table 5. Summary of representative photoswitchable PROTACs**

PROTAC name [Ref.]	Target Proteins, ligand	Photoswitch type, location	E3 ligase, ligand	Degradation efficacy	Irradiation method during cell treatment	Z half-life	PSS with irradiation (determined using various methods)	Active isomer	Reversibility for multiple cycles
<b>PhotoPROTAC</b> 107	Targeting BRD2 with JQ1	Ortho-F4-Azobenzene, as the PROTAC linker	Targeting VHL with VH032	Significant BRD2 degradation observed at 6.5 h with 50 nM <i>trans</i> -photoPROTAC-1 treatment in Ramos cells	Single initial irradiation	Several days (37 °C)	530 nm (30 min) to 68% <i>Z</i> ; 415 nm (30 min) to 95% <i>E</i>	<i>E</i>	Not determined
<b>PHOTAC-I-3</b> 108	Targeting BRD4 with JQ1	Azobenzene, the phthalimide on the E3 ligase ligand was used to form the photoswitchable motif	Targeting CRBN with lenalidomide	Complete degradation of BRD2/3/4 with 1 µM treatment of PHOTAC-I-3 for 4 h in RS4;11 cells	Pulse irradiated for 100 ms every 10 s	$t_{1/2}$ around 8.76 h (37 °C)	390 nm (5 min) to >90% <i>Z</i> ; >450 nm (5 min) to >70% <i>E</i>	<i>Z</i>	Yes (>30 cycles)
<b>Azo-PROTAC-4C</b> 109	Targeting BCR-ABL with dasatinib	Azobenzene, as the PROTAC linker	Targeting CRBN with lenalidomide	>90% Degradation of BCR- ABL observed with 250 nM of Azo-PROTAC-4C treatment for 32 h in K562 cells	UV-C light irradiation every 4 h	10.3 h at 25 °C	UV-C light or White light; PSS not determined	<i>E</i>	Yes (5 cycles, with exposure to UV-C for 1 h or white light for 2 h)
<b>AP-PROTAC-1</b> 110,164	Targeting BRD4 & 2 with JQ1	Arylazopyrazole, as the PROTAC linker	Targeting CRBN with thalidomide	86% Dmax for BRD4 and 75% for BRD2 with 100 nM AP-PROTAC-1 treatment for 6 h in HeLa cells	Intermittent irradiation for 1 min every 2 hours	> 5 h (37°C, water)	365 nm (1 min) to 85% <i>Z</i> ; 457 nm (1 min) to 78 % <i>E</i>	<i>E</i>	Yes (20 cycles)
<b>AP-PROTAC-2</b> (this work)	Targeting 4 kinases with CTx-0294885: FAK, AURORA-A, TBK1, GAK	Arylazopyrazole, as the PROTAC linker	Targeting CRBN with lenalidomide	85% Dmax for both FAK and AURORA-A, and 70% for TBK1, with 300 nM <i>E</i> -enriched-AP- PROTAC-2 treatment for 16 h in MDA-MD-231 cells	Intermittent irradiation for 1 min every 3 hours	$t_{1/2}$ around 31.7 h (37°C, water)	365 nm (1 min) to 90% <i>Z</i> ; 457 nm (1 min) to 80 % <i>E</i>	<i>E</i>	Yes (20 cycles)



### 2.10.3 Conclusion

In summary, the development of the first generation of arylazopyrazole PROTACs (AP-PROTACs) has demonstrated the promising potential of the AAP photoswitchable linker **4** to be applied in bifunctional compounds as a versatile ‘plug and play’ switch to control biological outcomes. **AP-PROTAC-2** exhibited favourable photoswitching characteristics, including a high abundance and extended stability of the *Z* isomer, rapid switching kinetics, and reliable reversibility over multiple cycles. This work introduced a new class of photoswitch and paved the way for the future development of novel light-responsive targeted therapeutics.

The development of **AP-PROTAC-2** represents an innovative stride in the field, being the first multi-target PROTAC with photoswitchable degradation activity. Quantitative proteomics analysis revealed that (*E*-enriched)-**AP-PROTAC-2** significantly and selectively degraded only four protein kinases, while (*Z*-enriched)-**AP-PROTAC-2** was much less active. The light-switchable degradation of FAK, AURORA-A, and TBK1 was successfully validated with immunoblots. The exceptionally selective photoswitchable degradation observed with **AP-PROTAC-2** was hypothesised to arise from a combination of altered affinity for kinase binding and the ability to form a catalytically competent kinase/**AP-PROTAC-2**/CRBN ternary complex. Notably, both FAK and AURORA-A kinases—promising therapeutic targets in cancer—were successfully targeted in this study. AURORA-A, an essential mitotic kinase for cell cycle progression,<sup>198</sup> and FAK, which plays important roles in tumour progression and metastasis,<sup>199</sup> both hold potential for anti-cancer therapeutic interventions. Several PROTACs targeting FAK have been reported, some of which have shown anti-cancer therapeutic potential by eliminating the non-enzymatic functions of FAK.<sup>176,200</sup>

This study not only explores the integration of a photoswitch into a multi-target PROTAC but also introduces exciting opportunities for the development of multi-targeted degraders. This can be achieved using readily available promiscuous inhibitors, leading to enhanced or synergistic target degradation. Overall, our findings contribute to the expanding field of PROTAC research and open avenues for the design and optimisation of multi-targeted degraders with improved therapeutic potential.

## **Chapter 3 Antibody-peptide degrader conjugates (Ab-peptides): the use of peptide-based degraders as ADC payloads**

The previous chapter reported the development of photoswitchable multi-kinase PROTACs for light-responsive selective degradation of multiple kinases. While PROTAC degraders have shown efficacy across a wide range of drug targets, they often lack specificity for cancer cells overexpressing target proteins and exhibit limitations in tissue selectivity. Moreover, their relatively large size and challenging physicochemical properties can compromise aspects like oral bioavailability, cellular uptake, and *in vivo* pharmacokinetic (PK) properties.<sup>201,202</sup>

To address some of these challenges, I turned to the antibody-drug conjugates (ADCs) platform as a strategy for delivering peptide-based degraders. In this chapter, our aim was to enhance the cellular uptake and specificity of PROTACs towards cancer cells by designing antibody-peptide degrader conjugates. It was hypothesised that ADC technology can serve as a viable approach for delivering peptide-based degraders.

### **3.1 Introduction**

The potential of ADC technology within the field of targeted protein degradation (TPD) was discussed in Section 1.5.4, with a focus on the development of antibody-PROTAC conjugates (Ab-PROTACs). These conjugates have demonstrated promise in inducing antigen-dependent target degradation through various ADC linker strategies. However, current antibody-conjugated PROTAC payloads primarily consist of small molecule PROTACs, and their design, synthesis and optimisation for ADC conjugation have been proven challenging.

The identification of small molecule ligands for novel E3 ligases has posed a significant obstacle in PROTAC development. Peptide-based ligands, with their promising discovery platforms, have emerged as attractive alternative therapeutic candidates. Although peptide-based PROTACs show great potential for TPD, peptides often surpass the ‘rule of 5’ and have inherent limitations in their PK properties, including limited cell permeability, biological instability and susceptibility to proteolytic degradation.<sup>203</sup> Among the limited examples of

peptide-based degraders, their target degradation efficacy falls short compared to small molecule-based PROTACs targeting the same POI (as outlined in Table 3).

I hypothesised that peptide-based degraders could serve as effective ADC payloads and aimed to develop antibody-peptide degrader conjugates, referred to as Ab-peptide (Figure 3-1). Ab-peptide consists of a monoclonal antibody, an ADC linker, and the peptide degrader payload. This design aimed to leverage ADC internalisation mechanisms to specifically deliver peptide-based degraders into antigen-positive cells, enhancing cellular uptake and inducing protein degradation. Following ADC internalisation and subsequent linker cleavage, the released peptide payloads could cross the lysosome membrane and enter the cytosol. This proposed design could overcome the potential challenges typically encountered by peptides attempting direct penetration of the cell membrane. By achieving a higher proportion of peptide degraders within cells, the intracellular protein degradation effect could be amplified. This approach might also enable the recruitment of novel drug targets and effectors beyond the currently available options.

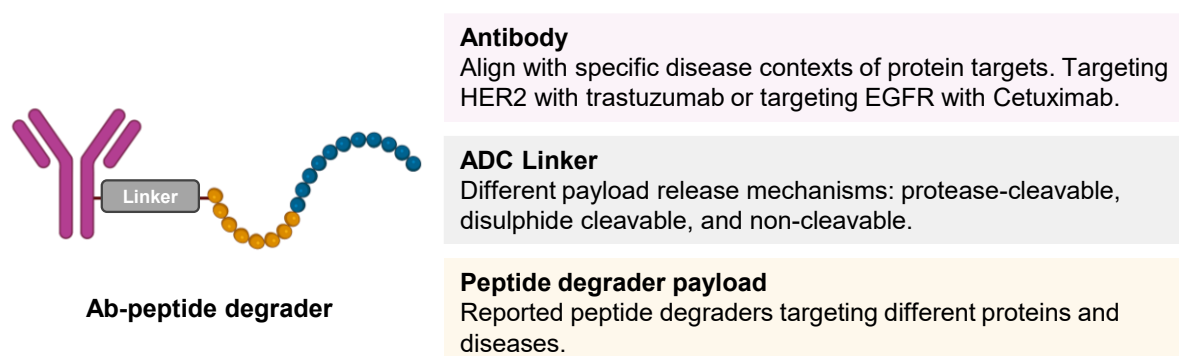


**Figure 3-1. The structure and characteristics of a devised antibody-peptide degrader conjugate**

The core components including antibody, ADC linker, and peptide payload along with their key functions are demonstrated.

To validate the feasibility of utilising ADC technology for peptide-based degrader delivery, our research was envisioned to progress through three stages. (i) Initially, I intended to conjugate known peptide-based PROTACs to monoclonal antibodies using established technologies previously described for cytotoxic payloads. The assessment would evaluate whether the antibody conjugation strategy enhances the cellular delivery and target engagement of the peptide degraders. (ii) If this initial stage proved successful, the subsequent phase would focus on developing a novel bifunctional degrader from reported peptide ligands and a small molecule E3 ligand. (iii) Finally, the aim was to explore a ‘plug and play’ approach,

employing the *de novo* mRNA display ligand discovery platform. This would allow the development of a broad array of new peptide-based degraders targeting various protein targets, designed specifically for antibody conjugation to produce Ab-peptide degraders conjugates, thereby expanding the scope and potential applications of TPD.

This chapter summarised my efforts in the initial stage, providing proof-of-concept for the hypothesis. I designed and synthesised three previously reported peptide-based degraders, evaluating their potential as ADC payloads with the integration of various ADC linkers. *In vitro* assessments of resulting Ab-peptide were then conducted to identify any enhancements in target protein degradation compared to unconjugated peptide controls. The goal was to validate the feasibility of ADCs as delivery mechanisms for peptide-based degraders and assess the potential advantages of Ab-peptide in terms of PK and cellular uptake over unconjugated counterparts.

### **3.2 Peptide synthesis**

Peptides were synthesised using the standard fluorenylmethoxycarbonyl (Fmoc) solid-phase peptide synthesis (SPPS) method, as depicted in Figure 3-2 and detailed in Section 5.1.3. Linear peptides were constructed on insoluble resin support through stepwise coupling of Fmoc-protected amino acids, using either an automatic microwave-assisted peptide synthesiser or manual synthesis in a fritted syringe. The first step was the loading of the first Fmoc-protected amino acid onto the resin. The Fmoc-protected N-terminus of the resin-bound peptides was then deprotected with piperidine, before coupling with the subsequent amino acid in the peptide sequence. During SPPS, amino acids with protecting groups were used to prevent unwanted reactions, and orthogonal protecting groups were employed to enable selective deprotection and cyclisation of peptides on the resin. When necessary, a small-scale peptide cleavage (mini-cleavage) was performed, and a liquid chromatography-mass spectrometry (LC-MS) analysis was conducted on the cleaved residue to verify the peptide product. After completing peptide chain elongation, the peptides were cleaved from the resins using a cleavage cocktail containing trifluoroacetic acid (TFA). The crude peptides were subsequently purified using high-performance liquid chromatography (HPLC) and analysed by LC-MS.

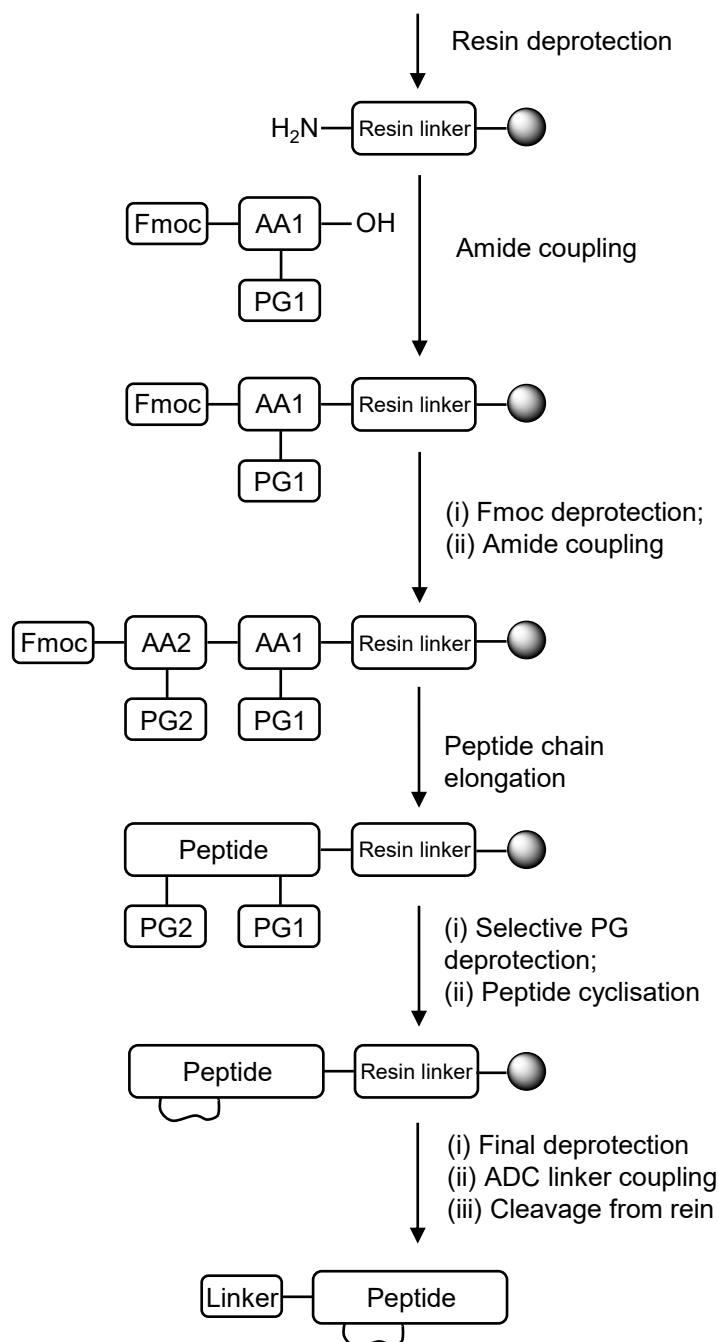


**Figure 3-2. Fmoc-based solid-phase peptide synthesis (Fmoc-SPPS) used in this chapter**

### 3.3 ADC linkers

The ADC linker is a critical component in ADC design, connecting the monoclonal antibody to the cytotoxic payload. Its stability in circulation is crucial to prevent premature and non-specific release of the cytotoxic payload, which could lead to off-target toxicity and reduced ADC efficacy. The linker is responsible for the efficient and specific release of the cytotoxic payload-linker metabolite. Achieving an optimal balance between conjugate stability and

efficient payload release presents a major challenge in linker design.<sup>204</sup> Therefore, the design of the linker requires careful consideration to ensure the successful targeted delivery of the cytotoxic payload. The ADC linker consists of three main parts: the linker-antibody attachment, the trigger, and the linker-drug attachment. The linker-antibody attachment is key in determining the bioconjugation method and the drug-to-antibody ratio (DAR).<sup>205</sup> The linker-drug attachment defines the nature of the payload metabolite that is produced, potentially influencing off-target toxicity.

ADC linkers can be classified as non-cleavable and cleavable. Non-cleavable linkers lack a chemical trigger and release the payload only when the antibody and linker are metabolised and degraded after ADC internalisation and entry into the lysosome. Cleavable linkers contain a chemical trigger in their structure, allowing for specific linker cleavage. Disulphides and dipeptides are common cleavable linkers in ADCs currently in clinical development.<sup>141</sup> The valine-citrulline (VC) dipeptide linker, which can be cleaved by lysosomal enzymes such as cathepsin B,<sup>206</sup> is widely used in approved ADCs and clinical trials. In protease-cleavable ADC linker designs, a self-immolative spacer, *para*-amino benzyloxycarbonyl (PABC), is often employed between the protease-cleavable peptide and the cytotoxic payload. When protease cleaves the dipeptide, the PABC spacer undergoes fragmentation, releasing the payload without any appendage from the linker.<sup>207</sup> Other cleavage triggers include acid-cleavable triggers, GSH-cleavable triggers, and novel mechanisms like Fe (II)-cleavable triggers, photo-responsive-cleavable triggers, and biorthogonal cleavable triggers.<sup>208</sup> In this chapter, three types of ADC linkers were selected and provided by our collaborator ADC Therapeutics, and were employed in the Ab-peptide development. Here, their potential influence on the overall ADC performance was discussed (Figure 3-3).

Linker 1 (**L1**) is a protease-cleavable maleimidocaproyl (mc) linker, which comprises a maleimidocaproyl spacer and a newer generation protease-cleavable dipeptide, valine-alanine (VA). Recent studies have demonstrated that VA exhibits improved hydrophilicity and stability compared to VC when coupled with the monomethyl auristatin E (MMAE) payload.<sup>209</sup> We selected the VA dipeptide due to its cost-effectiveness, ease of synthesis, and potential to reduce ADC aggregation in comparison to VC. The carboxylic acid on Linker 1 allows peptide payload attachment through amide bond formation, and the maleimide moiety enables bioconjugation through Michael addition from the thiol of cysteine residues on the monoclonal antibody.<sup>210</sup> During the linker cleavage of ADC-peptide conjugates containing Linker 1, the

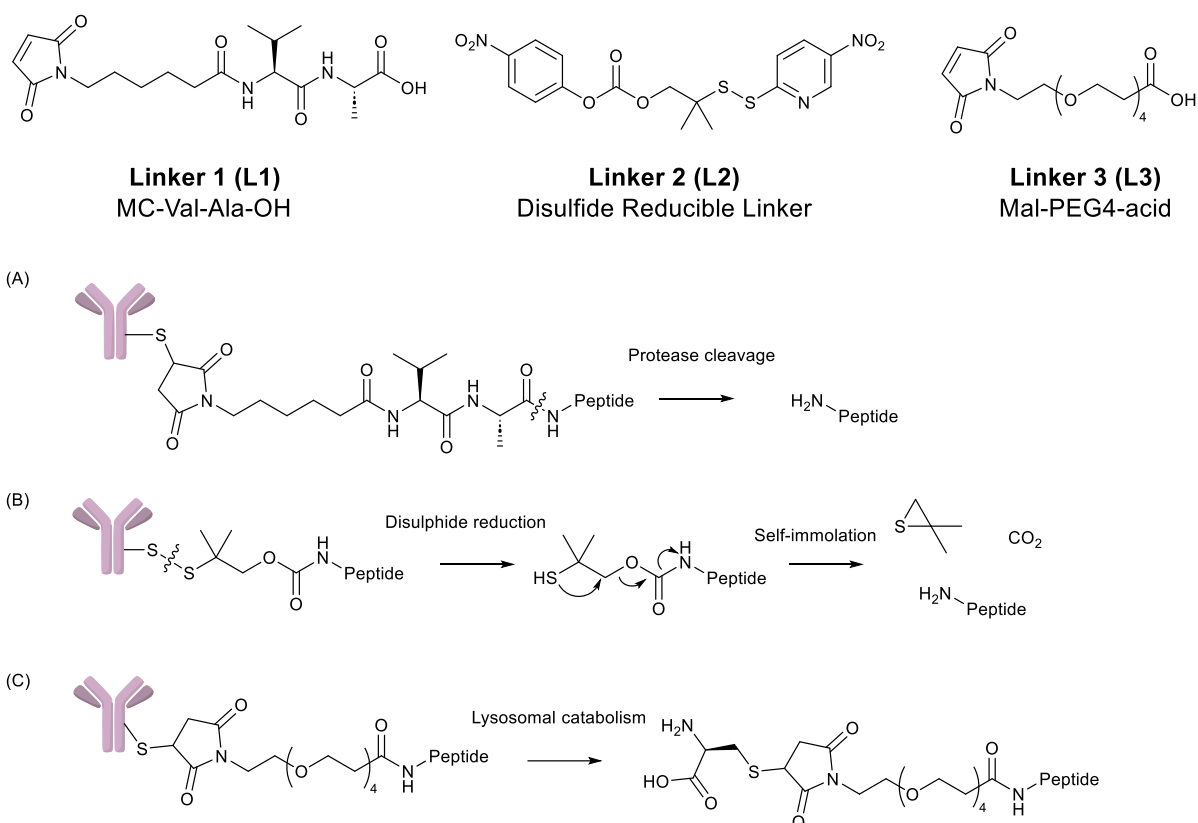


**Figure 3-3. ADC linkers used in this study and their predicted intracellular ADC catabolism and payload release mechanism**

Predicted intracellular payload release mechanism of antibody-peptide conjugates derived from linker-peptides with (A) Linker 1, (B) Linker 2 (The exact cellular compartment in which disulfide reduction occurs is uncertain), and (C) Linker 3.

protease was presumed to cleave the amide bond between the VA dipeptide and the peptide payload, resulting in payload release with a free amine and without additional appendage (Figure 3-3A).

Linker 2 (L2), a GSH-cleavable disulfide linker, features a carbonate moiety facilitating nucleophilic substitution of amines from the peptide payload, forming a carbamate on the linker-peptide construct. This construct can be conjugated to the monoclonal antibody through disulfide bond formation with the cysteine residue on the antibody.<sup>211</sup> During the cleavage process of Ab-peptide conjugates containing Linker 2, the disulfide bond was anticipated to be first reduced by GSH, then the remaining portion of the linker undergoes self-immolation to release the peptide payload with a free amine (Figure 3-3B).

Linker 3 (L3) is a non-cleavable linker that incorporates a maleimide moiety and a PEG linker and is not susceptible to protease cleavage. ADCs using non-cleavable linkers generally

demonstrate improved plasma stability and reduced systemic toxicity from premature payload release.<sup>212</sup> The carboxylic acid functionality of Linker 3 enables attachment to the free amine on the peptide payload *via* amide bond formation. The peptide payloads on Ab-peptide containing Linker 3 can only be released following the lysosomal metabolism of the antibody, during which a cysteine residue on the linker remains attached to the released payload (Figure 3-3C).

The stability of these three linkers in pure TFA was assessed using LC-MS, with all linkers proving stable after a one-hour incubation in TFA (Section 7.2.1). This stability enables the coupling of linkers to peptides on solid resin support during synthesis and the peptide cleavage from the resin using TFA-containing cocktails. Solution-phase reactions were avoided to reduce potential side reactions of the linkers with the peptide side chains. In the synthesis of linker-peptide constructs, ADC linkers were coupled to the free amine on resin-bound peptides, serving as the synthetic handle for antibody bioconjugation. Subsequently, these linker-peptide constructs were cleaved from the resin and purified using HPLC for further reactions.

### **3.4 Targeting ER $\alpha$ with trastuzumab-conjugated peptide-based PROTACs**

#### **3.4.1 TD-PROTAC: a peptide-based PROTAC degrading ER $\alpha$**

The estrogen receptor (ER) family is crucial in regulating various physiological processes, and ER $\alpha$ , a prominent subtype, is often overexpressed in breast cancer cells, driving estrogen-dependent proliferation. This makes ER $\alpha$  a promising target for breast cancer therapy.<sup>213,214</sup> Selective estrogen receptor modulators (SERMs) and selective estrogen receptor degraders (SERDs) represent two classes of drugs targeting ERs, commonly used in the treatment of hormone-dependent breast cancers. While SERMs like tamoxifen and raloxifene are employed to treat ER-positive breast cancer, their therapeutic potential is often limited by the development of endocrine resistance during treatment.<sup>215</sup> SERDs, such as fulvestrant, induce proteasomal degradation of ER $\alpha$  and show promise in treating advanced or metastatic ER-positive breast cancer. Despite being the first FDA-approved SERD, fulvestrant suffers from limitations such as poor oral bioavailability and high toxicity.<sup>216</sup> To overcome these limitations, bifunctional ER $\alpha$  PROTACs have been developed by coupling ER $\alpha$  ligands to E3 ligands. This approach holds promise for targeted ER $\alpha$  degradation and overcoming treatment resistance developed in traditional ER-targeted therapies. ARV-471, the first ER $\alpha$  PROTAC in clinical



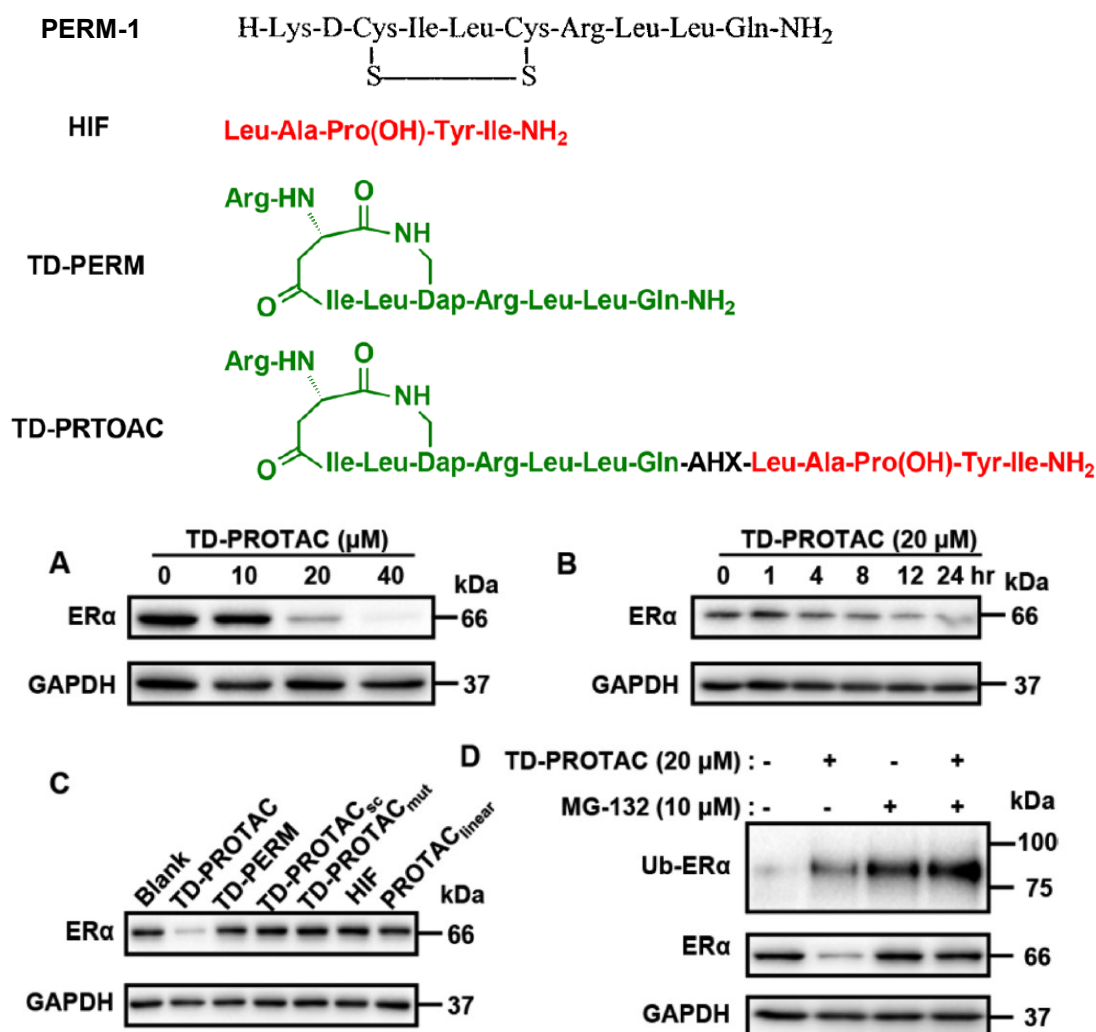


**Figure 3-4 Structure of peptides and the immunoblot studies of TD-PROTAC**

(A) ER $\alpha$  levels in T47D cells after treatment with **TD-PROTAC** for 24 h. (B) ER $\alpha$  levels in T47D cells after treatment with 20  $\mu$ M **TD-PROTAC** for varying time intervals. (C) ER $\alpha$  levels in T47D cells after treatment with different peptides at 20  $\mu$ M for 24 h. (D) ER $\alpha$  levels in T47D cells after treatment with 20  $\mu$ M **TD-PROTAC** with or without 10  $\mu$ M MG-132 for 6 h and immunoprecipitation-Western blot analysis of the ubiquitinated ER $\alpha$  levels. Images adapted with permission from Jiang *et al.*<sup>218</sup>

trials, represents a positive step towards more effective and tolerable breast cancer treatments.<sup>217</sup>

Jiang *et al.* reported the development of a peptide-based PROTAC targeting ER $\alpha$ , named **TD-PROTAC**.<sup>218</sup> This peptide PROTAC consists of an N-terminal aspartic acid cross-linked stabilised ER $\alpha$  peptide modulator (TD-PERM) and a hydroxyproline-containing pentapeptide IYP(OH)AL, which binds to the VHL E3 ligase.<sup>219</sup> N-terminal aspartic acid cross-linking (TD strategy, Figure 3-9) was employed to constrain peptides into helical structures to develop

peptidomimetic estrogen receptor modulators (TD-PERM). This technique enhanced both the stability and cell permeability of the peptide.<sup>220</sup> In their study, **TD-PROTAC** labelled with fluorescein isothiocyanate (FITC) engaged with ER $\alpha$  in a fluorescence polarisation assay and demonstrated satisfactory cell permeability in MCF-7 and T47D cells in flow cytometry analysis and immunofluorescence assays. Immunoblot experiments revealed that TD-PROTAC induced ER $\alpha$ , VHL and proteasomal-dependent degradation of ER $\alpha$ , with a DC<sub>50</sub> of approximately 20  $\mu$ M (Figure 3-4). **TD-PROTAC** significantly reduced transcription of ER $\alpha$  downstream genes and inhibited the proliferation of ER $\alpha$ -positive breast cancer cells compared to the control peptide modulator TD-PERM. Subsequent *in vivo* studies of **TD-PROTAC** revealed its antitumour activity in the MCF-7 xenograft animal model. This study highlights the potential of peptide-based PROTACs, like **TD-PROTAC**, as a valuable strategy for inducing targeted protein degradation in cancer therapy.

### 3.4.2 Design of Ab-peptide degrader conjugates: trastuzumab-TD-PROTAC conjugates

With the encouraging findings from Jiang *et al.*, I decided to develop antibody-**TD-PROTAC** conjugates as our primary strategy to validate our hypothesis. The peptidomimetic ER modulator PERM binds to the carboxyterminal ligand-binding domain (LBD) of ER $\alpha$  through the hydrophobic interaction with the LXXLL consensus sequence in the groove.<sup>221</sup> In the crystal structure of the first-generation peptidomimetic modulators **PERM-1** in complex with ER $\alpha$ , it was observed that the N-terminal lysine residues was in an exposed, solvent-accessible position, suggesting its potential suitability as a site for conjugation to an ADC linker (Figure 3-5). Therefore, I redesigned the **TD-PROTAC** peptide, introducing an N-terminal lysine to

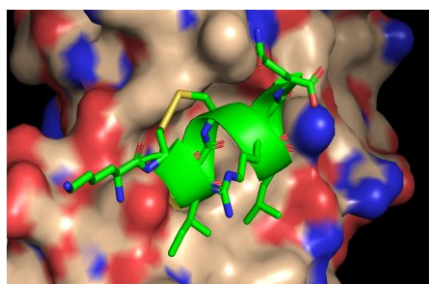


**Figure 3-5. X-ray structure of ER $\alpha$  in complex with PERM-1**

PDB:1PCG, 2.70 Å.<sup>270</sup> The X-ray structure showcases the ligand-binding domain (LBD) of estrogen receptor alpha (ER $\alpha$ ) bound to the peptidomimetic modulator **PERM-1**. The N-terminal lysine is positioned at the lower left of this figure, and the C-terminal glutamine is positioned at the upper right. The image was created with PyMOL.

replace the N-terminal arginine on **TD-PROTAC** to create an analogue named **Lys-rp-TD-PROTAC** (Figure 3-6). For ADCs incorporating Linker 1 and Linker 2, cleavage of the ADC linker would result in the release of the peptide payload, exposing the lysine residue with a free side chain. The flexible nature of lysine's side chain could also serve as a spacer, potentially reducing steric hindrance during protease-mediated cleavage of the dipeptide.

In terms of the monoclonal antibody selection, I decided to conjugate the linker-peptides to trastuzumab (Herceptin), an antibody targeting the human epidermal growth factor receptor 2 (HER2). Given that approximately 20% of breast cancer patients exhibit HER2 overexpression, trastuzumab or its ADC derivatives have demonstrated notable improvements in the overall survival rates of patients with HER2-positive metastatic breast cancer.<sup>222,223</sup> An ADC targeting HER2 could help to establish the proof-of-concept for the hypothesis.

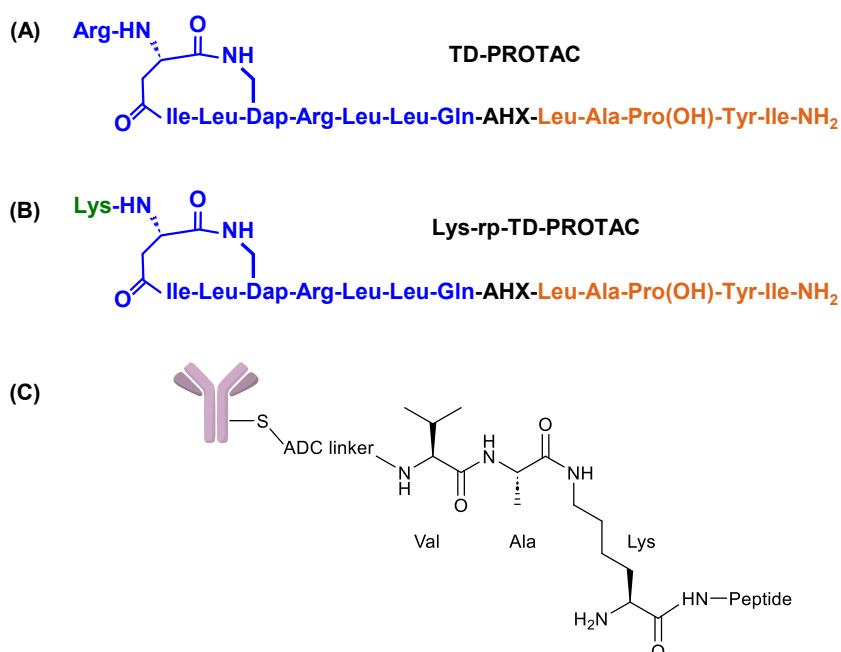


**Figure 3-6. Structure of peptide PROTACs and the proposed structure of an antibody-peptide conjugate**

(A) Structure of **TD-PROTAC**. Residues in orange engage with VHL E3 ligase, residues in blue engage with ER $\alpha$ . (B) Structure of **TD-PROTAC**'s analogue, **Lys-rp-TD-PROTAC**. (C) The proposed structure of an antibody-peptide conjugate derived from the **TD-PROTAC** analogue. The N-terminal lysine residue is connected to the Val-Ala ADC linker, which is then conjugated to a cysteine residue on the antibody through a thiol bond.

### 3.4.3 Synthesis of the reported peptide-PROTAC (TD-PROTAC)

The synthesis of the reported **TD-PROTAC** began with the synthesis of complete linear peptides using the Fmoc-based SPPS method, incorporating appropriate orthogonal protecting groups in the automated microwave peptide synthesiser. In the construction of the N-terminal aspartic acid cross-linked stabilising structure of **TD-PROTAC**, Fmoc-Asp-O(All) (aspartic acid with a free side chain and an allyl-protected C-terminal) and Fmoc-Dap(Alloc)-OH were incorporated in the linear peptide synthesis (Figure 3-7). The allyl ester and allyl carbamate on the resin-bound linear peptides were removed using a palladium catalyst. The resulting carboxylic acid and amine side chains were cyclised using coupling reagents. After the final deprotection step to remove the N-terminal Fmoc group, the peptides were cleaved and purified. This led to the successful synthesis and purification of **TD-PROTAC** (Figure 7-14) and it was used in subsequent cellular studies.

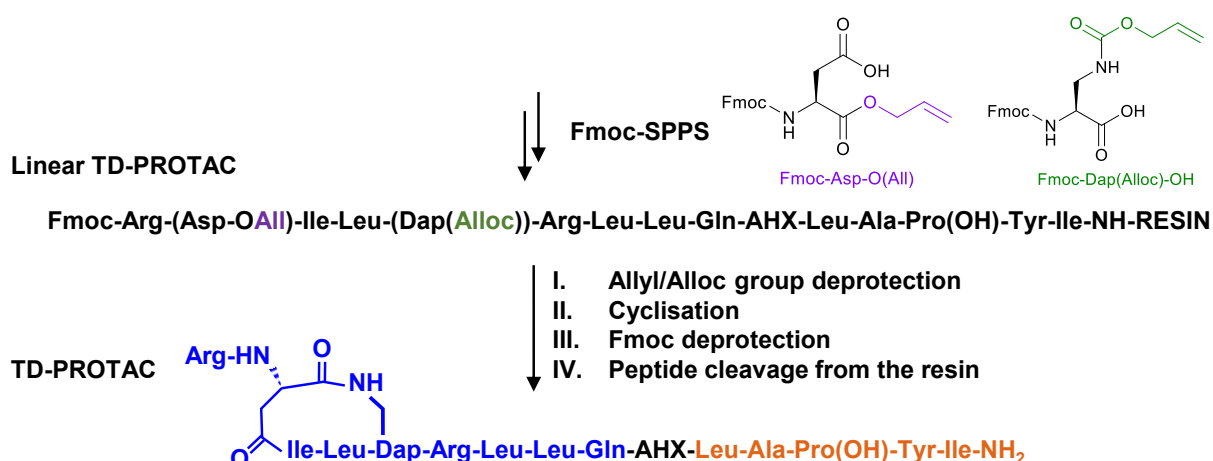


**Figure 3-7. Schematic representation of synthetic routes of TD-PROTAC**

Reagents and conditions. Fmoc-SPPS: Fmoc amino acids, DIC, Oxyma, DMF. Allyl/alloc deprotection: Pd(PPh<sub>3</sub>)<sub>4</sub> (0.1 eq.), 1,3-dimethylbarbituric acid (4 eq.) in DCM for 2 h and repeated overnight. Cyclisation: PyBOP (2 eq.)/HOBt (2 eq.)/ N-Methylmorpholine (2.4 eq.) in DMF for 5 h twice. Fmoc deprotection: 20% piperidine in DMF, 10 min twice. Peptide cleavage: TFA:TIPS:H<sub>2</sub>O:thioanisole (91:3:3:3 v/v/v/v) cocktail, 10 mL for 0.05 mmol peptide, 3 h. Protected amino acids were used during Fmoc-SPPS (not shown on the resin-bound sequence).

However, during the synthesis and purification of **TD-PROTAC**, a significant amount of a by-product was observed. To understand the origin of this by-product, I performed a manual stepwise synthesis of the linear peptide. In the course of the synthesis, the peptide formed on the resin was analysed by mini cleavage and LC-MS. These investigations revealed that the by-product's formation occurred after coupling arginine to the allyl ester-protected aspartic

acid residue on the peptide. Further analysis showed that the by-product formation was attributed to the formation of aspartimides.

Aspartimide formation is a widely recognised and problematic side reaction in Fmoc-SPPS. Such by-products can significantly reduce the overall synthetic yield and may result in chain termination of the peptide synthesis.<sup>224,225</sup> In our proposed mechanism for the formation of aspartimides, facilitated by the base introduced during Fmoc removal or peptide coupling, the secondary amine within the isoleucine residue nucleophilically attacked the ester group on the aspartic acid residue (Figure 3-8, Asp-O(All)).<sup>226</sup> In this process, allyl alcohol was cleaved, and its mass corresponded to the observed mass difference between the expected product and the by-product (Section 7.2.2).

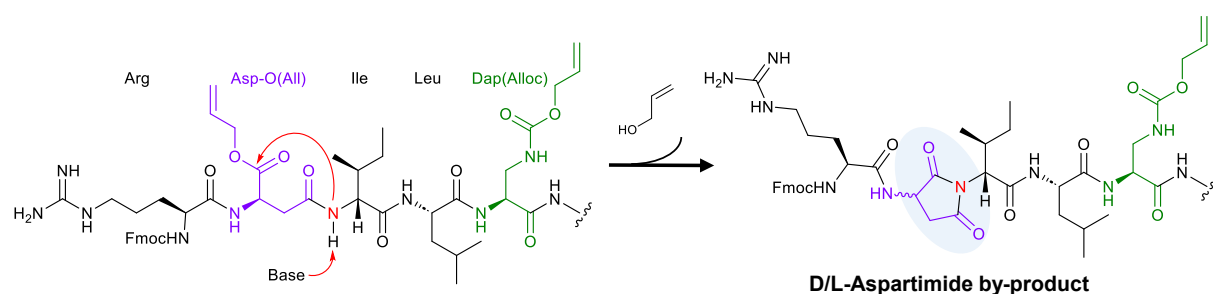


**Figure 3-8. The proposed mechanism for aspartimide formation during the synthesis of TD-PROTAC linear peptide**

Arg was protected by Pbf protecting group which was not shown.

To mitigate the formation of the aspartimide by-product and increase the synthetic yield of peptides including **TD-PROTAC**, its analogue **Lys-rp-TD-PROTAC**, and the yield of the linker-peptide constructs following the coupling of ADC linkers, a modification was implemented within our synthetic strategy. Specifically, I synthesised the linear peptide until the aspartic acid residue and paused the chain elongation. I then performed the deprotection and cyclisation of the Asp and Dap residue. This was meticulously performed to ensure complete cyclisation, confirmed by mini-cleavage and LC-MS analysis that showed a negligible presence of aspartimide. Finally, the coupling of the final residue was performed (Figure 3-9). This strategy avoided direct contact between the aspartyl peptide and the piperidine, thereby efficiently preventing the generation of the undesired aspartimide by-product.<sup>227</sup>

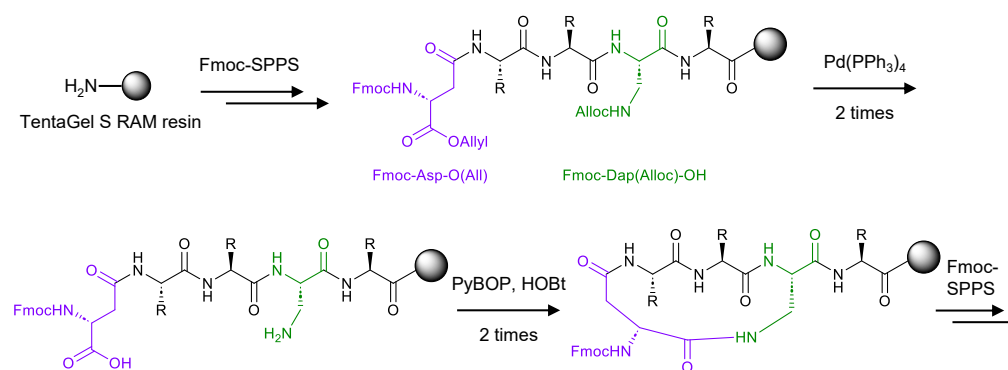


**Figure 3-9. A modified synthetic route to precursors of TD-PROTAC and its analogues**

Figure redrawn from Zhao *et al.*<sup>220</sup>

### 3.4.4 Immunoblot profiling of TD-PROTAC *in vitro*

In the paper of Jiang *et al.*, **TD-PROTAC** was shown to degrade the targeted protein ER $\alpha$  in a dose and time-dependent manner, with a DC<sub>50</sub> lower than 20  $\mu$ M in the T47D cell line.<sup>218</sup> An immunoblot study was conducted in the MCF-7 cell line, where **TD-PROTAC** exhibited reduced degradation activity, as detailed in their supplementary information. Both the T47D and MCF-7 cell lines are ER-positive breast cancer cell lines that do not express HER2. Considering that our ADC design involves targeting HER2 with the monoclonal antibody trastuzumab, I sought to validate the degradation activity of **TD-PROTAC** in a HER2-positive cell line. Accordingly, I selected the BT-474 cell line as an additional model to test **TD-PROTAC**'s degradation activity, alongside the T47D and MCF-7 cell lines. A dose-dependent immunoblot analysis of **TD-PROTAC** in these three cell lines was conducted following the procedure described in the paper.

Briefly, the purified and freeze-dried **TD-PROTAC** peptide was dissolved in DMSO to prepare a 40 mM stock solution, which was then diluted into the cell growth medium for treatment. After a 24-hour compound treatment, the cells were washed, and the proteins were extracted and analysed using gel electrophoresis and western blotting techniques. The band signals of immunoblots were quantified to give the ER $\alpha$  protein levels post-treatment (Figure 3-10). Surprisingly, no statistically significant degradation of the ER $\alpha$  protein was observed in any of the three cell lines.

Interestingly, Dai *et al.* from another research group, reported the development of cyclic peptide PROTACs targeting ER $\alpha$  in 2020.<sup>228</sup> Without reference to the report in 2018 by Jiang

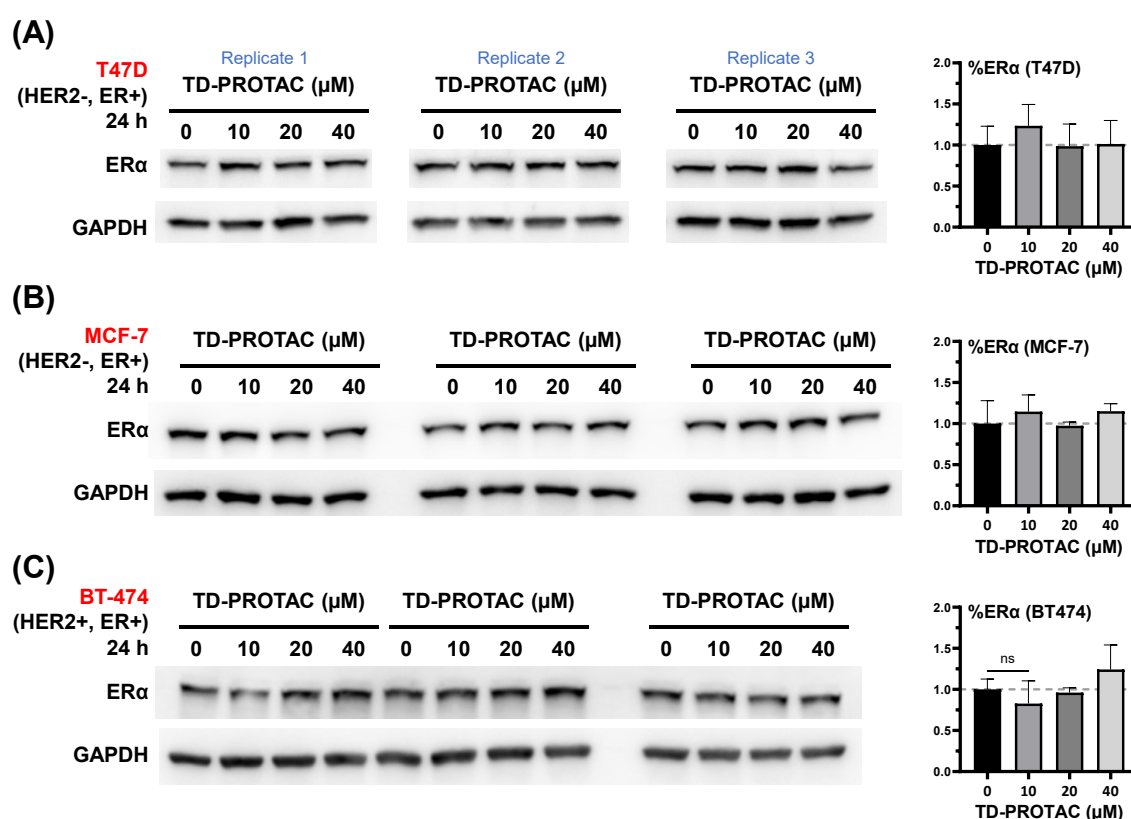


**Figure 3-10. *In vitro* testing of TD-PROTAC in three cell lines**

Immunoblots and quantification of ERα level after 24 h treatment with DMSO control or increasing dose of **TD-PROTAC** in (A) T47D cell line, (B) MCF-7 cell line, and (C) BT-474 cell line with cell growth medium supplemented with 10% FBS. Condition '0' represents the cells were treated with 0.1% DMSO in the medium. Bars represent the mean signal normalised to GAPDH, reported as mean ± standard deviation (SD, n = 3). One-way ANOVA analysis was performed, and all treated groups were not significantly different (ns) from the control group.

*et al.*, the authors designed an identical peptide PROTAC to **TD-PROTAC**, named **I-2** and characterised it in the MCF-7 cell line. They showed that at a concentration of 10 μM, **I-2** degraded ERα to 70% compared to the control treatment (Figure 3-11). This finding suggests the potential reproducibility of the degradation effect observed with **TD-PROTAC**, or **I-2**. In their further ERα PROTAC design, Dai *et al.* introduced the unnatural amino acid neopentyl glycine (Npg, *L-tert*-Leucine) to replace Leu, and the resulting peptide **I-6** exhibited improved degradation activity.

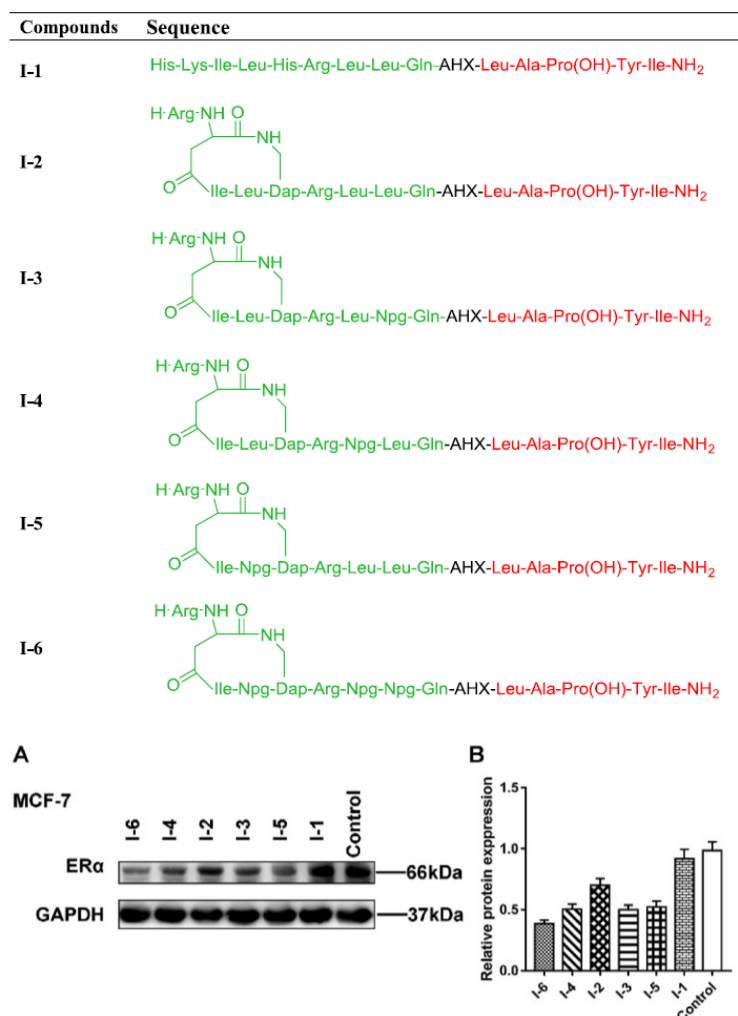


**Figure 3-11. Structure of peptides and the immunoblot studies of ER $\alpha$  peptide-based PROTACs from Dai *et al.***

(A) ER $\alpha$  levels in MCF-7 cells after treatment with different compounds (**I-1** to **I-6**) at 10  $\mu$ M for 12 h. (B) Quantification of ER $\alpha$  levels in (A). Images adapted with permission from Dai *et al.*.<sup>228</sup>

It was hypothesised that the observed discrepancies in degradation activity could potentially be attributed to variations in the specific cell systems utilised. Such differences can exert a profound influence on PROTAC efficacy, thereby leading to diverse degradation outcomes across distinct cell lines.<sup>229</sup> This inherent variability is also evident in the findings of these two studies, where **TD-PROTAC** demonstrated varying degradation activities within the T47D and MCF-7 cell lines, as well as with **I-2**. Further investigations are needed to understand the observed differences in **TD-PROTAC** activity. Techniques to increase cell permeability, such as electroporation,<sup>230</sup> could be useful in validating whether the lack of ER $\alpha$  degradation is due



to differences in cell permeability of our chosen cell model, peptide target engagement, or other factors.

Another potential factor that could contribute to the inconsistencies in degradation activity is the variation in the salt form of the peptides. Peptides are typically prepared as trifluoroacetate (TFA) salts if a TFA cocktail was used during peptide cleavage or if the peptides were purified by HPLC using solvent systems with TFA as the mobile phase additive. Upon closer examination, it was ascertained the reported peptides **TD-PROTAC** and **I-2** were cleaved and purified using TFA-based protocols, and both reports did not mention any subsequent counterion exchange step, implying that these peptides were also in the form of TFA salts. Furthermore, in spite of the potential toxicity of residual TFAs to cells, there was no observable cell death during our peptide treatments.

Despite the challenges encountered during the initial *in vitro* testing of **TD-PROTAC**, I decided to proceed with the synthesis of linker-peptide constructs of **TD-PROTAC** that incorporate ADC linkers and to prepare antibody-peptide conjugates. Our hypothesis was that antibody-mediated internalisation might enhance the cellular uptake of the peptide payload and achieve more robust degradation of the target protein.

### 3.4.5 Synthesis of ADC linker-peptide constructs

The modified synthetic route was implemented to synthesise **TD-PROTAC** analogues integrated with ADC linkers (referred to as ‘linker-peptides’, Figure 3-12). Specifically, the residues Asp and Dap were cyclised prior to further peptide chain elongation. This adjustment significantly reduced the aspartimide by-product observed in the resin cleavage mixture. I began by synthesising a cyclised peptide analogue, **cut14-cyc-TD**, which lacked the final N-terminal amino acid. The peptide **cut14-cyc-TD** was then coupled to a side chain Fmoc-protected lysine, Boc-Lys(Fmoc)-OH, forming the analogue **Fmoc-Lys-rp-TD**. After deprotecting the Fmoc group on the lysine side chain, the exposed primary amine was coupled to three selected ADC linkers. Linker 1 and Linker 3 were coupled to the primary amines on the lysine side chain of the cyclic peptide through amide coupling reactions. For Linker 2, the carbonate moiety on the linker reacted with the amine on the lysine side chain, forming a carbamate ester on the resulting linker-peptide construct. Following confirmation of successful linker attachment to the cyclic peptides on resin by mini-cleavage, the linker-peptides were cleaved from the resin and purified. I successfully prepared and characterised three linker-

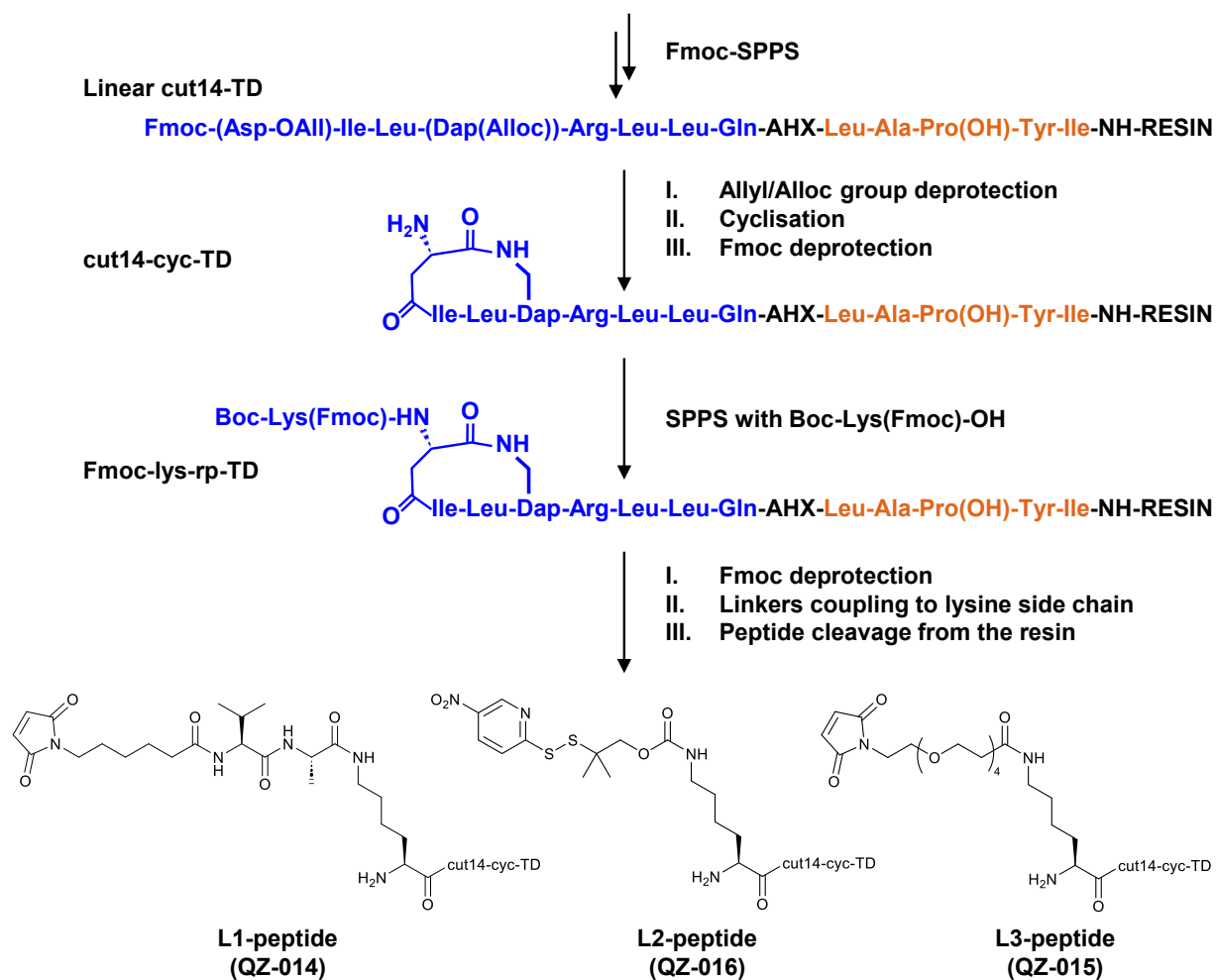


**Figure 3-12. Schematic representation of synthetic routes of linker-peptide constructs**

Reagents and conditions for linker coupling. **L1-peptide (QZ-014):** L1 (1.5 eq.), HATU (1.5 eq.), DIPEA (5 eq.), dry DMF, N<sub>2</sub>, RT, 48 h. **L2-peptide (QZ-016):** L2 (1.15 eq.), pyridine (2.5 eq.), HOBT (2 eq.), dry DMF, N<sub>2</sub>, RT, 18 h. **L3-peptide (QZ-015):** L3 (1.5 eq.), HATU (1.5 eq.), DIPEA (5 eq.), dry DMF, N<sub>2</sub>, RT, 30 h. Protected amino acids were used during Fmoc-SPPS (not shown on the sequences), including Fmoc-Arg(Pbf)-OH, Fmoc-Gln(Trt)-OH, Fmoc-Tyr(<sup>t</sup>Bu)-OH, Fmoc-Hyp(<sup>t</sup>Bu)-OH, Boc-Lys(Fmoc)-OH.

peptide constructs, **QZ-014**, **QZ-015** and **QZ-016** (Section 7.2.3), each with a different ADC payload release mechanism.

### 3.4.6 Conjugation of trastuzumab to linker-peptide constructs<sup>d</sup>

The conjugation of the monoclonal antibody trastuzumab to the linker-peptide constructs was performed by our collaborator, ADC Therapeutics (Table 6). Successful conjugation was achieved only with the non-cleavable L3-peptide construct **QZ-015**, giving the first antibody-peptide degrader conjugate, **HER2-15**, with an average drug-to-antibody (DAR) ratio of 3.8 as determined using hydrophobic interaction chromatography (HIC). However, no conjugation was observed for L1-peptide **QZ-014** and L2-peptide **QZ-016** in small-scale experiments, despite varying concentrations of the reducing agent and different peptide-to-antibody ratios were employed.

**Table 6. Conditions employed in small-scale test bioconjugation of trastuzumab to linker-peptide constructs.**

Peptide	Antibody (1 eq.)	TCEP (eq.)	Peptide (eq.)	Drug-to-antibody (DAR) Results
QZ014	Trastuzumab	1.5	5	No conjugation
		3	7	No conjugation
		8	12	No conjugation
QZ016		1.5	5	No conjugation
		3	7	No conjugation
		8	12	No conjugation
QZ015		2.0	12	DAR 3.3
		2.3	12	DAR 4.0
		2.3	9	DAR 2.0
	2.3	10.8	DAR 3.8*	

DAR was determined using hydrophobic interaction chromatography (HIC). \*Conjugates with a DAR of 3.8 were used in the subsequent immunoblot analysis.

To assess the reactivity of **QZ-014** and **QZ-016**, N-acetyl cysteine (NAC) assays were conducted by incubating the peptides with an excessive amount of NAC. If the maleimide and disulphide functionalities on the linker-peptides were available for reaction, the thiol group on the cysteine moiety could engage in the nucleophilic attack on the maleimide of **QZ-014** or

<sup>d</sup> Bioconjugation and NAC assays were conducted by Dr Alina Chrzastek et al., ADC Therapeutics, Translation & Innovation Hub Building Imperial College White City Campus, 84 Wood Lane, London, W12 0BZ.

react with the disulphide on **QZ-016**, leading to a detectable mass shift evident in the LC-MS analysis. However, in these NAC assays, neither of the peptides displayed reactivity with NAC (Figure 7-27). Reactivity assays of the ADC linker starting material, incubating N-acetyl-L-cysteine methyl ester with Linker 1 or Linker 3, demonstrated reactivity between the two linkers and the thiol (data not shown).

Further investigations are required to unravel the discrepancy in bioconjugation reactivity. Although the synthesised linker-peptides are detected with the expected correct mass, due to the limited peptide material I was unable to confirm the presence of reactive groups on the linker-peptides, specifically the maleimide in **QZ-014** or the disulfide in **QZ-016**, using spectroscopic methods such as Nuclear Magnetic Resonance (NMR) spectroscopy or Infrared (IR) spectroscopy. Here, possible causes of the failed antibody conjugation were discussed and potential solutions were proposed:

**Impurities or residual reagents:** Conjugation efficiency could have been affected by impurities or residual reagents from the previous synthesis and purification steps. The use of a palladium catalyst to remove the Alloc and Allyl protecting groups might have compromised the stability and reactivity of the cysteine residues on the monoclonal antibody during bioconjugation. A potential improvement could involve further purification of the linker-peptide constructs with chromatography to remove impurities that might interfere with the conjugation process. Alternatively, other orthogonal protecting groups could be employed for the peptide synthesis to avoid the use of the palladium catalyst, such as ivDde and Dmab which can be removed by 2% hydrazine.

**Peptide hydrophobicity:** The high proportion of hydrophobic residues in both **TD-PROTAC** and the linker-peptides makes these peptides very hydrophobic. During antibody conjugation, the hydrophobic nature of the linker and payload could induce antibody aggregation and precipitation. In contrast, the successful conjugation with **QZ-015**, which incorporates the hydrophilic PEG Linker 3, suggests that increased hydrophilicity might facilitate successful conjugation by mitigating hydrophobic interactions.<sup>231</sup> One potential improvement could be to adopt alternative linkers with increased hydrophilicity.

**Peptide conformations and potential incompatibilities:** Potential peptide folding might have made the maleimide or disulfide moiety inaccessible for cysteine thus leading to the failed

conjugation. Interactions or incompatibilities between **QZ-014** or **QZ-016** solution conformations and the antibody could also hinder the conjugation process.

Multiple factors could contribute to the failed conjugations and further investigation would improve results and guide future studies. However, given the constrained timeframe, I proceeded with the characterisation of the **HER2-15** conjugate.

### 3.4.7 Immunoblot profiling of antibody-peptide conjugate **HER2-15**

With the only successfully conjugated Ab-peptide **HER2-15**, I proceeded to conduct cell treatment experiments to assess its degradation activity on ER $\alpha$ . BT-474 cells were treated with increasing concentrations of **HER2-15**, followed by subsequent immunoblot analysis (Figure 3-13). The quantified results showed a statistically significant degradation of ER $\alpha$  following treatment with 100 nM of **HER2-15**, reducing ER $\alpha$  levels to 64% compared to the control group treated with buffer in the growth medium. In direct contrast to the synthesised parent peptide, **TD-PROTAC**, which displayed no statistically significant degradation activity in our previous experiments despite its reported DC<sub>50</sub> being below 20  $\mu$ M, **HER2-15** exhibited much improved degradation efficacy. However, no further significant reduction of ER $\alpha$  levels was observed with increased doses of **HER2-15**. These findings suggest that while cells may have responded to **HER2-15** treatment at specific doses or timepoints, the changes in protein levels were not significant enough to be quantified under the tested conditions, and no dose-dependent degradation pattern was observed. While further studies on the degradation mechanism of

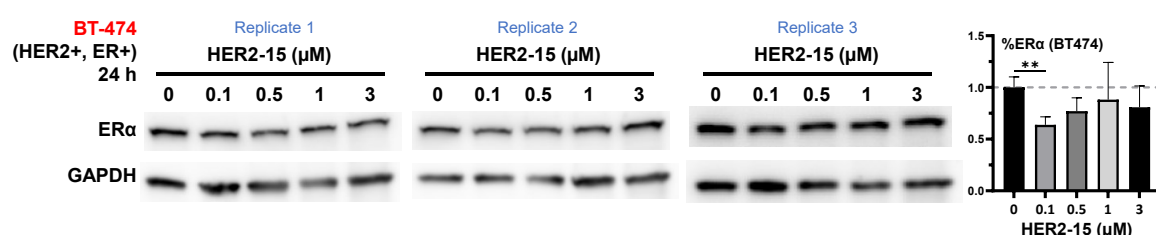


**Figure 3-13 *In vitro* testing of **HER2-15** (trastuzumab-QZ-015 conjugate) in BT-474 cell line**

Immunoblots and quantification of ER $\alpha$  levels after a 24 h treatment with buffer control and increasing doses of **HER2-15** in the BT-474 cell line with cell growth medium supplemented with 5% FBS. Condition '0' represents cell treatment with 10% ADC buffer in the medium. ADC buffer: 30 mM Histidine, 175 mM sucrose, 0.02% Tween 20, pH 6. Bars represent the mean signal normalised to GAPDH, reported as mean  $\pm$  standard deviation (SD, n = 3). \*P < 0.05, \*\*P < 0.01, and \*\*\*P < 0.001 from unpaired t-test when compared with the control group. Data not marked with a P value were not significantly different from the control group.

**HER2-15** are required, these promising results motivated us to synthesise additional Ab-peptide constructs to validate our hypothesis and expand the scope of our investigation.

### 3.4.8 Summary

This section outlined my efforts on the selection of the cyclic peptide-based PROTAC targeting ER $\alpha$ , known as **TD-PROTAC**, as our starting point to validate our hypothesis. The successful synthesis and characterisation of **TD-PROTAC** were achieved, and peptide synthetic yield was improved with synthetic route optimisation. However, no significant ER $\alpha$  degradation was observed in *in vitro* assays upon **TD-PROTAC** treatment.

Subsequently, I synthesised three linker-peptide conjugates, each with distinct payload release mechanisms, including a peptide-cleavable maleimide linker, a disulfide-reducible linker, and a non-cleavable linker. However, challenges were encountered during the antibody conjugation process, leading to successful conjugation only with the non-cleavable linker-peptide construct, resulting in our first Ab-peptide, **HER2-15**.

The cellular treatment with **HER2-15** demonstrated an improved efficacy in target protein degradation compared to the parent peptide **TD-PROTAC**. This promising result underscored the potential of antibody-mediated delivery to enhance the degradation efficacy of peptide degraders. The next steps involved further exploration and optimisation of the design with additional ADC-peptide PROTAC conjugates to refine this approach.

### 3.5 Targeting CREPT with cetuximab-conjugated peptide-based PROTACs

In the previous section, I described the work to redesign **TD-PROTAC** into an Ab-peptide degrader conjugate which showed enhanced degradation efficacy. Given the challenges encountered during the synthesis of **TD-PROTAC**, I decided to simplify our synthetic approach and selected a linear peptide PROTAC, **PRTC**. This peptide targets CREPT (the cell cycle-related and expression-elevated protein in tumour) and is also known as RPRD1B (regulation of nuclear pre-mRNA domain containing 1B).

#### 3.5.1 PRTC: A linear peptide-PROTAC targeting CREPT for pancreatic cancer treatment

CREPT is highly expressed in many human tumours, particularly in pancreatic cancer. It plays a crucial role in tumorigenesis by regulating the transcription of cell-cycle-related genes, including RNA polymerase II (RNAPII).<sup>232</sup> Furthermore, CREPT enhances the transcriptional activity of the Wnt/ $\beta$ -catenin pathway, thus promoting cell proliferation and invasion.<sup>233</sup> However, the lack of available CREPT inhibitors presents a significant challenge for studying CREPT's function.

Ma *et al.* reported the design and characterisation of a CREPT-targeting peptide PROTAC (**PRTC**, Figure 3-14).<sup>234</sup> Initially, they investigated the role of CREPT overexpression in pancreatic cancer and confirmed its promotion of cell proliferation in the Panc-1 cell line, a widely used pancreatic cancer cell line. They then discovered that CREPT forms homodimers *in vitro*. Based on this finding, they designed a CREPT peptide ligand (**CL**) derived from a 21-amino acid  $\alpha$ -helical leucine-zipper-like motif located on the C-terminus coiled-coil terminus (CCT) domain of CREPT. The CREPT-targeting PROTAC, named **PRTC**, was developed by coupling **CL** to a 6-aminohexanoic acid (AHX) linker, which was then connected to the VHL binding pentapeptide IYP(OH)AL. To improve cell permeability, a cell-penetrating peptide (CPP), RRRRK, was added to the C-terminus of the peptide.

In microscale thermophoresis experiments, FITC-labelled **PRTC** exhibited association with GST-tagged CREPT with a  $K_d$  of approximately 0.34  $\mu$ M. Immunoblot analysis of **PRTC** treatment in Panc-1 cells showed that **PRTC** induces the ubiquitination and proteasome-dependent degradation of endogenous CREPT protein in a dose and time-dependent manner,

with a  $DC_{50}$  of 10  $\mu$ M. **PRTC** demonstrated inhibitory effects on tumour cell proliferation, colony formation, and migration *in vitro*. It also exhibited significant anti-tumour activity in a xenograft mouse model.

These findings highlight the promising potential of **PRTC** as a specific and effective approach to degrade CREPT proteins and inhibit tumorigenesis. **PRTC** serves as a promising peptide-PROTAC to test our hypothesis, offering advantages such as a favourable  $DC_{50}$  value and a relatively straightforward synthetic process.

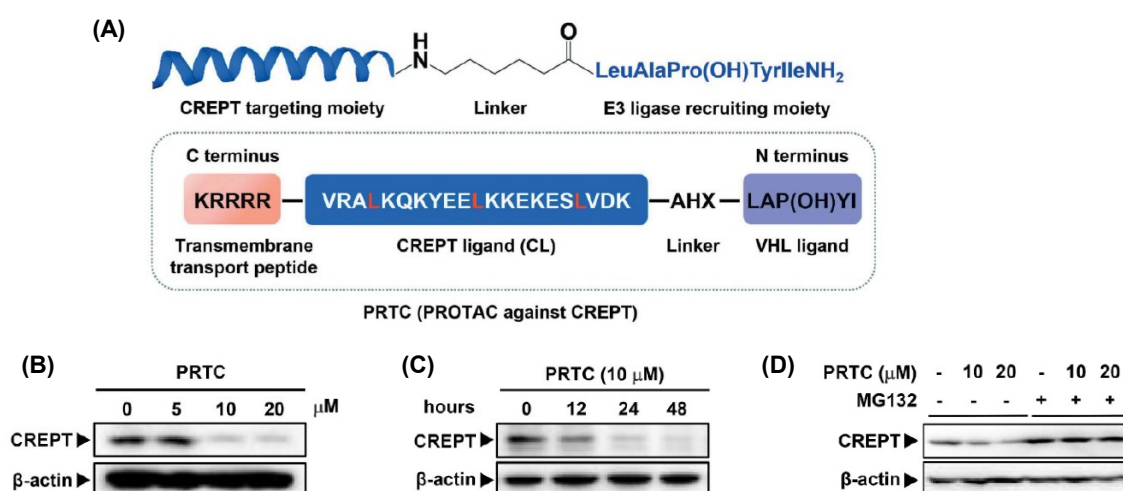


**Figure 3-14. Schematic diagram of CREPT-targeting peptide PROTAC PRTC and its immunoblot studies**

(A) Schematic diagram of **PRTC** design. (B) Immunoblot analysis of CREPT following a 24 h incubation with various dosages of **PRTC** in Panc-1 cells. (C) Immunoblot analysis of CREPT in Panc-1 cells treated with 10  $\mu$ M **PRTC** for different durations. (D) Immunoblot analysis of CREPT following a 24 h incubation with **PRTC** in Panc-1 cells, co-treated with proteasome inhibitor MG132. Images adapted with permission from Ma *et al.*<sup>234</sup>

### 3.5.2 Design of cetuximab-PRTC conjugates and peptide synthesis

The peptide PROTAC **PRTC** displayed promising degradation activity towards CREPT. With its relatively straightforward synthesis compared to other peptide degrader constructs, I aimed to convert **PRTC** into an ADC payload by coupling ADC linkers. A detailed analysis of the crystal structure of the VHL/ElonginB/ElonginC (VBC) complex, bound to the hydroxyproline-containing 20-residue destruction sequence of HIF-1 $\alpha$ ,<sup>235</sup> revealed that modifications to residues adjacent to the VHL binding pentapeptide sequence (Leu-Ala-Pro(OH)-Tyr-Ile) would not hinder its VHL recruitment (Figure 3-15). Interestingly, **PRTC**'s VHL-binding sequence, IYP(OH)AL, is the reverse of HIF-1 $\alpha$ 's sequence. The N-terminal



amine of the peptide, following the isoleucine residue from the VHL binding sequence, was selected as the attachment point for the ADC linker.

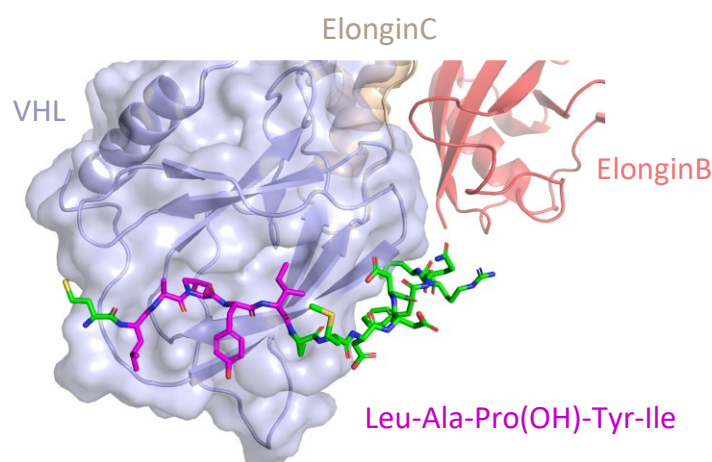


**Figure 3-15. Co-crystal structure of the HIF-1 $\alpha$  peptide bound to the VHL/ElonginB/ElonginC (VBC) complex**

PDB: 1LM8,<sup>235</sup> 1.85 Å. VHL is depicted in blue, ElonginC in light orange, and ElonginB in red. The hydroxyproline-containing 20-residue destruction sequence of HIF-1 $\alpha$  is presented as sticks, with the pentapeptide VHL ligand highlighted in magenta. The image was produced using PyMOL.

While the reported **PRTC** peptide possesses a free C-terminal carboxylic acid, I followed the previously established peptide synthesis protocols using the Tentagel resin, which produces peptide with a C-terminal amide after resin cleavage. The peptide chain elongation was carried out using a microwave-assisted peptide synthesiser, leading to the synthesis of a **PRTC** analogue, named **QZ-017**, featuring a C-terminal amide instead of the free C-terminal carboxylic acid present on **PRTC**.

For the synthesis of linker-peptide constructs, 6-aminocaproic acid (AHX) was introduced as a spacer following the N-terminal isoleucine residue. This spacer could potentially minimise hindrances during protease cleavage of the VA dipeptide. Based on the challenges encountered during the antibody conjugation of our previous study of **TD-PROTAC**, I designed two linker-peptide constructs for **PRTC**: one with Linker 1 (**QZ-019**) and the other combining Linker 3 with the VA dipeptide (**QZ-021**) (Figure 3-16). The peptide chain elongation process was conducted using the synthesiser up to the AHX spacer. Thereafter, manual coupling was performed to introduce the linkers to the resin-bound peptides. Specifically, Linker 1 was coupled to AHX-modified **QZ-017** to give **QZ-019**. For **QZ-021**, the alanine and valine residues were first coupled to AHX-modified **QZ-017**, followed by the coupling of Linker 3.

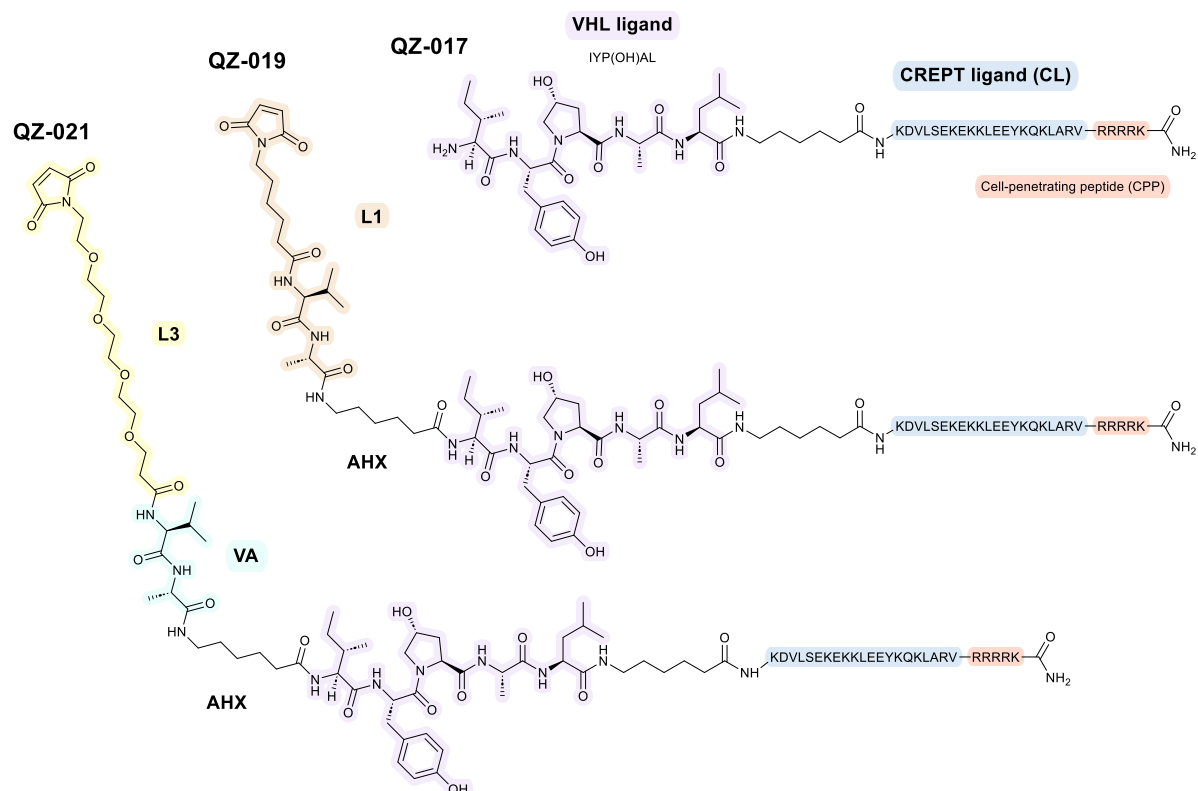


**Figure 3-16. Structures of PRTC analogue QZ-017, linker-peptide conjugates QZ-019 and QZ-021**

After the final deprotection of the Fmoc group on the N-terminus, the linker-peptides were cleaved and purified.

In terms of selecting the antigen target for ADC production, I chose the Epidermal Growth Factor Receptor (EGFR). EGFR is a prominent ADC target and a member of the epidermal growth factor receptor tyrosine kinase family (ErbB family) alongside HER2.<sup>236,237</sup> It plays a crucial role in regulating various cellular processes, including growth, proliferation, and migration.<sup>238</sup> Its overexpression is detected in approximately 90% of pancreatic cancer cases which is correlated with a poor prognosis.<sup>239</sup> Given that **PRTC** specifically targets CREPT degradation for pancreatic cancer treatment and has been previously assessed in the EGFR-expressing Panc-1 human pancreatic cancer cell line, EGFR was an ideal antigen for the antibody-**PRTC** conjugates. To achieve this, the EGFR antibody cetuximab was employed for the conjugation process.

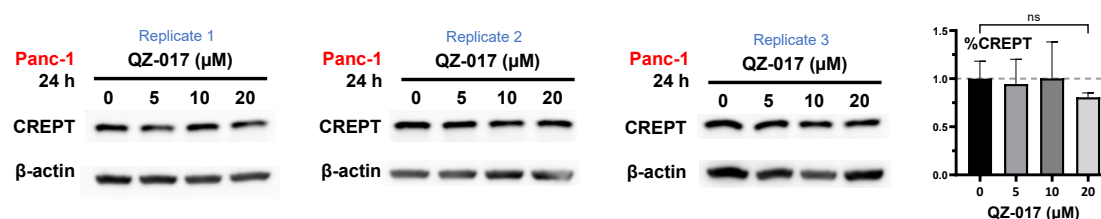


**Figure 3-17. *In vitro* testing of PRTC analogue QZ-017 in Panc-1 cells**

Immunoblots and quantification of CREPT levels following a 24 h treatment with either DMSO control or increasing doses of **QZ-017** in Panc-1 cells. The '0' condition indicates cells treated with 0.1% DMSO in the medium. Bars represent the mean signal normalised to β-actin, reported as mean ± standard deviation (SD, n = 3). Unpaired t-test was performed, and all treated groups were not significantly different (ns) from the control group.

### 3.5.3 *In vitro* immunoblot profiling of PRTC analogue QZ-017

After the successful synthesis of the **PRTC** analogue **QZ-017**, I proceeded to evaluate its degradation activity in Panc-1 cells using gel electrophoresis and western blotting techniques (Figure 3-17). Surprisingly, treatments with **QZ-017** at concentrations of 10 μM and 20 μM showed no significant degradation of the CREPT protein. A noticeable reduction in CREPT levels to 80% of the control was observed at 20 μM treatment, but was found to be statistically not significant. Increasing the concentration to 100 μM did not result in significant degradation (Figure 3-18, **QZ-017** treatment). This observed efficacy contrasts markedly with the original **PRTC** study, where a DC<sub>50</sub> of 10 μM was reported, with near-complete degradation of CREPT at 20 μM.

Considering that our modifications to **QZ-017** from the original **PRTC** were primarily focused on the C-terminus cell-penetrating peptide, the pronounced shift in degradation efficacy was unexpected. Despite this, I decided to proceed with the antibody conjugation and subsequent ADC testing stages.

### 3.5.4 Conjugation of cetuximab to linker-peptide constructs<sup>e</sup>

In collaboration with ADC Therapeutics, the monoclonal antibody cetuximab was conjugated to linker-peptide constructs (Table 7). Successful conjugation was only achieved for **QZ-021**. By adjusting the peptide-to-antibody ratio, our collaborators generated two cetuximab-**QZ021** ADC conjugates with drug-to-antibody ratios (DAR) of 4.2 and 7.8, denoted as **EGFR-21** (D4) and **EGFR-21** (D8) respectively. We also conducted the conjugation of the linker-peptides to antibody B12, which lacks specific binding to EGFR, producing the negative control antibody-peptide conjugates, **B12-21** (D4) and **B12-21** (D8).

**Table 7. Bioconjugation conditions employed for cetuximab to linker-peptide constructs**

Peptide	Antibody (1 eq. )	TCEP (eq.)	Peptide (eq.)	Drug-to-antibody (DAR) Results
QZ-019	Cetuximab	1.5	5	No conjugation
		3	7	No conjugation
		8	12	No conjugation
		40	20	No conjugation
QZ-021		1.5	5	DAR 2.0
		3	8	DAR 4.2*
		8	12	DAR 7.8**

DAR was determined using hydrophobic interaction chromatography (HIC). \*Conjugates with a DAR of 4.2 were denoted as DAR4 or D4. \*\* Conjugates with a DAR of 7.8 conjugates were denoted as DAR8 or D8. Both conjugates were used in subsequent immunoblot analyses.

However, despite multiple adjustments to the concentration of the reducing agent and the peptide-to-antibody ratio, the conjugation of **QZ-019** was unsuccessful. **QZ-019** was developed using ADC Linker 1, integrated with a maleimidocaproyl (mc) spacer and a VA dipeptide structure, while **QZ-021** employed Linker 3 and coupled with the VA dipeptide. These results reminded us of our previous antibody conjugation results described in Section 3.4.6, where the ER $\alpha$  targeting PROTAC **TD-PROTAC** showed similar successful conjugation exclusively with Linker 3-peptide constructs, but failed to conjugate with Linker 1 and 2 constructs. Given the distinct structural differences and varying lengths between the

<sup>e</sup> Bioconjugation was conducted by Dr Alina Chrzastek et al., ADC Therapeutics, Translation & Innovation Hub Building Imperial College White City Campus, 84 Wood Lane, London, W12 0BZ.

payload peptides **TD-PROTAC** and **PRTC**, we speculate that the observed conjugation challenges were associated with the specific linkers used.

In comparing Linker 1 and Linker 3, their differing hydrophobic properties were evident. It was hypothesised that the conjugation failure of constructs with Linker 1 could be attributed to the hydrophilicity. Utilising a PEG-based ADC linker, as seen with Linker 3, appeared to enhance the hydrophilic attributes of the payload, thereby facilitating the successful conjugation of **QZ-021**. As discussed in Section 3.4.6, during ADC production, the hydrophobic nature of both the payload and the linker can contribute to ADC aggregation. Such aggregation might induce adverse effects, including an increased propensity for ADC clearance from the bloodstream. This could reduce ADC circulation time, and potentially limit their therapeutic efficacy.<sup>240</sup> In specific scenarios, the inclusion of hydrophilic linkers with polyethylene glycol (PEG) groups demonstrated efficacy in addressing issues linked to ADC aggregation, leading to the development of more potent ADCs.<sup>241,242</sup> My results further underscore the pivotal influence of a linker's physicochemical attributes, particularly its hydrophilicity, on the successful outcome of the conjugation process.

### **3.5.5 Immunoblot profiling of cetuximab-PRTC conjugate EGFR-21**

Having achieved successful conjugation of the Ab-peptides **EGFR-21** (D4) and **EGFR-21** (D8), I proceeded to conduct cell treatment experiments to assess their degradation activity. Panc-1 cells were subjected to increasing doses of ADCs for 24 hours. For comparison, the cells were also treated with B12 ADC controls (D4 or D8), the monoclonal antibody cetuximab, B12, and the unconjugated parent peptide **QZ-017**.

Following the treatment, cell lysates were processed for gel electrophoresis and immunoblotting (Figure 3-18). When evaluating CREPT protein levels, no reduction was observed with **EGFR-21** (D4) treatment. In contrast, treatment with 500 nM of **EGFR-21** (D8) resulted in a significant decrease of CREPT levels to 56% compared to buffer treatment. However, increasing the dose to 3  $\mu$ M did not result in further reduction, suggesting that CREPT degradation is not dose-dependent within the tested concentration range. Notably, none of the control treatments reduced CREPT levels.

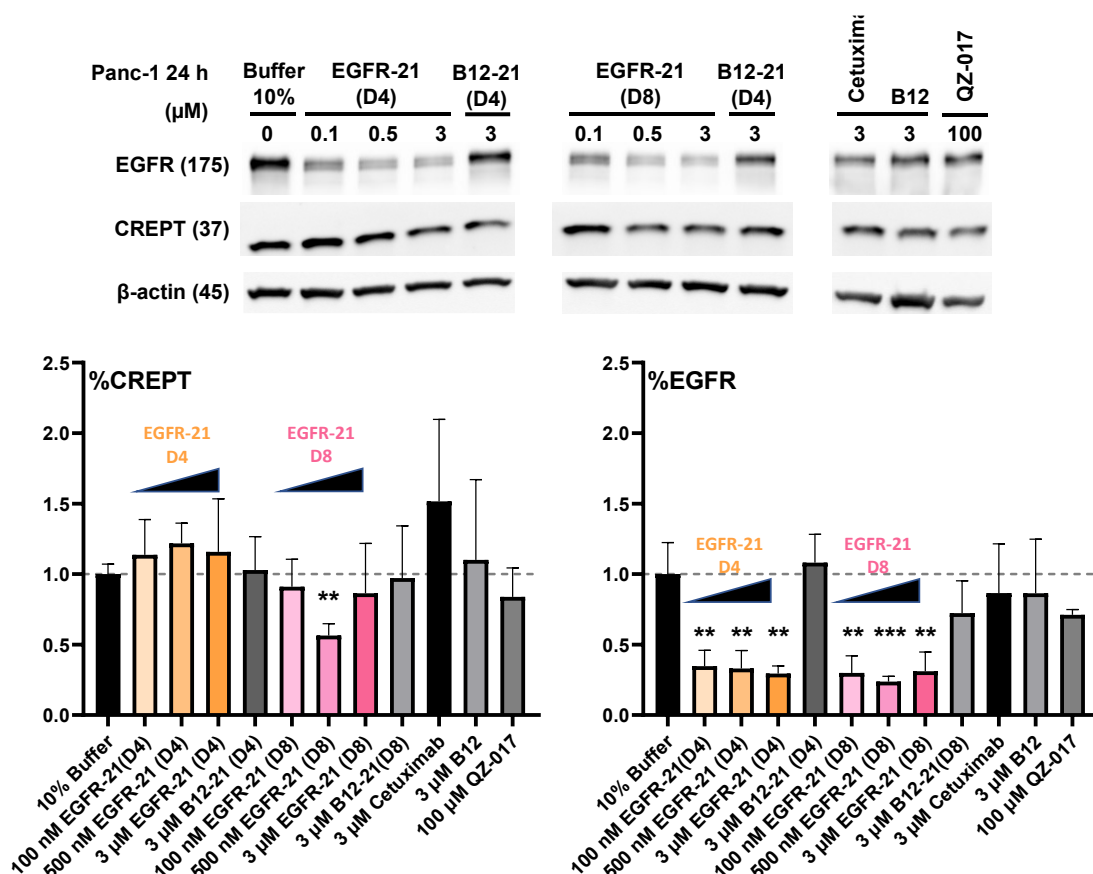


**Figure 3-18. In vitro testing of EGFR-21 (cetuximab-QZ021 conjugate) in Panc-1 cells**

Immunoblots and quantification of CREPT and EGFR levels after 24 h treatment with the indicated compounds in Panc-1 cell line. D4 represents DAR4 ADCs, and D8 represents DAR8 ADCs. Condition '0' represents cell treatment with 10% ADC buffer in the medium. ADC buffer: 30 mM Histidine, 175 mM sucrose, 0.02% Tween 20, pH 6. Blots are representative of three replicates. Bars represent the mean signal normalised to β-actin, reported as mean ± standard deviation (SD, n = 3). Unpaired t-tests were performed. \*P < 0.05, \*\*P < 0.01, and \*\*\*P < 0.001 from unpaired t-tests when compared with the control 10% ADC buffer treatment group. Data not marked with a P value were not significantly different from the control group.

When assessing the level of the ADC antigen EGFR, significant EGFR degradation was observed upon treatment with both **EGFR-21** (D4) and **EGFR-21** (D8). Treatments of 100 nM, 500 nM, and 3 μM **EGFR-21** (D4) reduced the EGFR levels to 35%, 33%, and 29% respectively. The **EGFR-21** (D8) treatments showed similar results, decreasing EGFR levels to 30%, 24%, and 31% at the respective doses. Interestingly, the control treatments did not affect the levels of CREPT or EGFR. Cetuximab and B12 caused a minor EGFR reduction to 86%, **B12-21** (D4) had a negligible impact, whereas **B12-21** (D8) reduced EGFR levels to 72%. These reductions in EGFR levels were not found to be significant in unpaired t-tests.

Literature has highlighted the differential internalisation rates of cell surface antigens influenced by ADC treatments as compared to the unconjugated antibody.<sup>138</sup> In some instances, ADCs have shown enhanced internalisation efficacy.<sup>243,244</sup> Diving deeper into EGFR as an ADC antigen, certain antibody bindings have been noted to shift EGFR's internalisation route away from its typical receptor-mediated endocytosis involving clathrin.<sup>245,246</sup> Specifically, under cetuximab treatment, EGFR internalisation was seen to bypass clathrin and dynamin, leaning instead on actin polymerisation – indicating the activation of micropinocytosis, known to amplify receptor internalisation efficiency.<sup>247</sup> This differential internalisation could potentially underlie the pronounced EGFR degradation observed following our ADC treatments.

A small reduction of EGFR levels to 71% upon cells treatment with 100  $\mu$ M **QZ-017** was observed. Although this result did not reach statistical significance, it is worth noting the documented role of CREPT in enhancing the transcriptional activity of the Wnt/ $\beta$ -catenin pathway<sup>233</sup> and the known interplay between EGFR and Wnt/ $\beta$ -catenin signalling pathways.<sup>248,249</sup> This result could suggest a potential relationship between CREPT expression and EGFR in specific cellular contexts. Nonetheless, **QZ-017**'s degradation activity on CREPT wasn't comparable to **PRTC**, rendering it suboptimal for in-depth CREPT and EGFR interaction investigations. Future research should prioritise the use of potent CREPT degraders to deepen our understanding of complex regulatory mechanisms governing these pathways.

### 3.5.6 Immunoblot analysis of the degradation mechanism of EGFR-21

To investigate the mechanism of EGFR and CREPT degradation, I conducted **EGFR-21** (D4) or **EGFR-21** (D8) treatment in combination with the covalent proteasome inhibitor bortezomib (BTZ). It was hypothesised that if the observed decrease in protein level was facilitated through the PROTAC mechanism, specifically the proteasomal pathway, then co-treatment with BTZ would attenuate the degradation of the target protein.

The cells were first treated with 10  $\mu$ M BTZ for 2 h, followed by treatment with 1  $\mu$ M BTZ alongside the ADCs for an additional 24 h (Figure 3-19). Contrary to our expectations, BTZ co-treatment did not significantly rescue the degradation of either EGFR or CREPT (in one-way ANOVA). Specifically, with **EGFR-21** (D4) treatment, the CREPT levels decreased to 86% post-treatment without BTZ, contrasting with 97% with BTZ. For **EGFR-21** (D8), CREPT levels decreased to 71%, as opposed to 65% with BTZ. When subjected to the

monoclonal antibody cetuximab, CREPT levels were reduced to 84% without BTZ and to 75% with BTZ. When assessing the level of EGFR, BTZ also did not rescue EGFR degradation when co-treated with **EGFR-21** (D4), **EGFR-21** (D8), or cetuximab. These results indicate that the proteasome has a limited role in both CREPT and EGFR degradation with **EGFR-21** treatment. This suggests that, instead of relying on the UPS proteasomal degradation system, other degradation pathways were involved in mediating the observed degradation process.

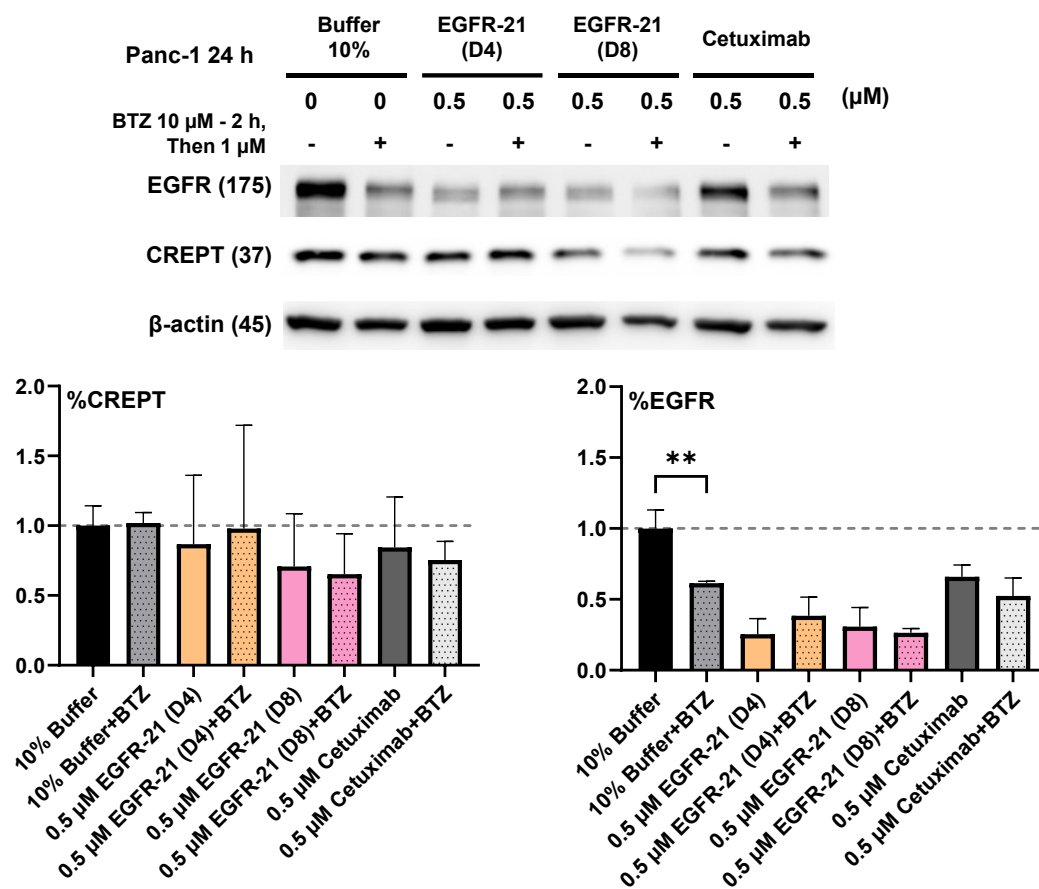


**Figure 3-19. *In vitro* testing of EGFR-21 (cetuximab-QZ021 conjugate) in Panc-1 cell line with co-treatment of the proteasome inhibitor bortezomib (BTZ)**

Immunoblots and quantification of CREPT and EGFR levels after 24 h treatment with buffer control or 0.5  $\mu$ M of **EGFR-21**, with or without BTZ co-treatment in Panc-1 cell line. For BTZ co-treatment, cells were pre-treated with 10  $\mu$ M of BTZ for 2 h, and then washed and treated with 1  $\mu$ M of BTZ and the ADCs for 24 h. Condition '0' represents cell treatment with 10% ADC buffer in the medium. Blots shown are representative of three replicates. Bars represent the mean signal normalised to  $\beta$ -actin, reported as mean  $\pm$  standard deviation (SD, n = 3). \*P < 0.05, \*\*P < 0.01, and \*\*\*P < 0.001 from one-way ANOVA when compared with the control group. Data not marked with a p-value were not significantly different compared to the control group.



Surprisingly, a co-treatment of cells with 10% buffer and BTZ significantly reduced EGFR levels to 61%, suggesting that proteasomal inhibition with BTZ might facilitate EGFR degradation. The multiubiquitination of the EGFR kinase domain is known to be associated with ligand-mediated endocytosis and endosomal sorting processes, highlighting its crucial role in the regulation of EGFR internalisation.<sup>250</sup> This may explain why EGFR is particularly sensitive to changes within the ubiquitin-proteasome system.

Beyond the proteasome, other degradation pathways, such as lysosomal degradation, might played a pivotal role in modulating CREPT and EGFR protein degradation. To explore the potential role of lysosomal degradation, future experiments should consider co-treatments with lysosomal inhibitors. Such inhibitors include the anti-malarial drug chloroquine, which can inhibit lysosomal functions by preventing autophagosome-lysosome fusion and impeding lysosomal acidification.<sup>251,252</sup>

### 3.5.7 Summary

In summary, **QZ-017**, an analogue of the CREPT peptide PROTAC **PRTC**, was successfully synthesised. However, *in vitro* characterisations showed that the degradation activity of **QZ-017** did not align with that of **PRTC**. Nonetheless, **QZ-017** was successfully conjugated to cetuximab through ADC linkers. Ab-peptide conjugate **EGFR-21** were successfully produced, with a drug-to-antibody ratio of 4 or 8. Cell treatments revealed significant CREPT degradation with **EGFR-21** (D8) treatment and EGFR degradation with both **EGFR-21** (D4) and (D8) treatment. Notably, these degradation effects were found to be proteasome-independent, suggesting the involvement of alternative degradation pathways. While the mechanisms remain unclear, these promising outcomes have encouraged further validation of the antibody-peptide degrader concept.

Here, I also highlighted several compelling observations beyond the initial research objectives. These insights offer invaluable directions for upcoming research in antibody-degrader conjugates:

**The impact of ADC linker:** The choice of ADC linker crucially affects antibody conjugation success. It was noted that PEG-based Linker 3 showed a higher conjugation rate with **TD-PROTAC** and **PRTC** analogues, underscoring the need for careful linker design and optimisation in subsequent research.

**The antigen levels and ADC efficacy:** The observed decrease in EGFR levels following ADC treatment poses challenges regarding optimal antibody-mediated peptide payload delivery. Increased receptor internalisation due to ADC administration may limit available receptors on the cell surface, potentially compromising the peptide payload delivery efficiency. Future research should investigate strategies to optimise receptor availability and payload efficacy.

**Opportunities in antigen degradation:** Our findings suggest that peptide-loaded ADCs could degrade cell-surface antigens like EGFR. This presents a promising opportunity for harnessing ADCs as targeted degradation tools for membrane proteins. While the exact mechanism behind this ADC-mediated EGFR degradation remains unclear, discrepancies in internalisation rates from the payload conjugation could be a contributing factor. Research into ADC internalisation dynamics and trafficking, using techniques such as confocal microscopy, could be useful to determine the underlying mechanism. Other potential studies could investigate the conjugation of mAbs with varying peptide sequences, exploring factors contributing to EGFR degradation. This exploration could include peptides with or without E3 ligase or specific protein target binding sequences, fluorophores, as well as peptide sequences varying in their physicochemical properties.

**EGFR degradation with antibody-based strategies:** The concept of inducing EGFR degradation *via* an antibody-based reagent aligns with LYTAC technology.<sup>40</sup> The LYTAC study achieved EGFR degradation using a LYTAC, comprised of cetuximab and GalNAc ligands. They confirmed that LYTAC's GalNAc ligands effectively recruited the liver-specific lysosome-targeting receptor, asialoglycoprotein receptors (ASGPR), leading to clathrin-mediated LYTAC endocytosis. This prompts speculation that **EGFR-21** might interact with additional proteins to aid ADC-EGFR complex internalisation.

A more recent publication reported the conjugation of cetuximab with the CRBN recruiter pomalidomide to create an cetuximab-based 'PROTAC' for EGFR degradation.<sup>253</sup> This strategy is similar to our proposal of antibody-peptide degrader conjugates, initially aimed at leveraging ADC technology and the UPS for targeted protein degradation. While the authors claimed that their degrader functions as a PROTAC, they did not provide evidence demonstrating the proteasome dependency of the observed EGFR degradation.

**The interplay between CREPT and EGFR:** Our preliminary data suggest a possible correlation between CREPT expression and EGFR levels. Advancing the development of potent CREPT degraders or using RNAi techniques could help validate this correlation.

To conclude, our work underscores the potential of peptide-based degraders as payloads in antibody-drug conjugates to enhance the degradation of the targeted protein. Together with the directions suggested, these findings offer fresh avenues for developing novel targeted protein degradation strategies.

## 3.6 Targeting bromodomains with peptide-based protein degraders through direct proteasome recruitment

### 3.6.1 Novel strategy for protein degradation through direct 26S proteasome recruitment

In the later stages of our project, we came across a study by Bashore *et al.* that detailed a peptide-based protein degradation method termed chemical inducers of degradation (CIDEs).<sup>47</sup> CIDEs are bifunctional molecules consisting of a cyclic peptide ligand that binds to the proteasome, a PEG linker, and a bromodomain ligand. Unlike PROTACs, CIDEs do not rely on the ubiquitin-proteasome system for targeted protein degradation. Instead, they directly recruit the 26S proteasome subunit PSMD2 to the target protein, inducing proteasomal degradation. This approach eliminates the need for target ubiquitination and the formation of a ternary complex with an E3 ligase, suggesting its versatility as a degradation strategy across a wider range of protein targets.

Bashore *et al.* first developed a potent ligand for the PSMD2 subunit of the 26S proteasome. Using mRNA display, they screened cyclic peptides and identified a peptide named MC1 with an IC<sub>50</sub> of around 5 nM and a K<sub>d</sub> value of 1.3 nM for PSMD2 (Figure 3-20C). The specificity of MC1's interaction with PSMD2 was validated through pull-down and quantitative proteomics experiments, wherein MC1<sub>biotin</sub> showed significant enrichment of 26S subunits in comparison to control samples. To delve deeper into the MC1-PSMD2 interaction, the authors examined the Cryo-EM structure of an engineered complex of PSMD2 with two fragment antigen-binding (Fab) 'chaperones' in the presence of MC1. This analysis highlighted the importance of the HRYxGW motif on MC1 in the interaction (Figure 3-20A and B), which was further supported by mutagenesis studies.

The authors identified the valine residue (V4, Figure 3-20C) as an appropriate solvent-exposed amino acid residue on MC1 for substitution with an alkyne-bearing residue, which then served as a synthetic handle for subsequent click chemistry. Following that, the alkyne-substituted MC1 peptide was conjugated to a BRD4 ligand (BETi)<sup>254</sup> using PEG linkers of varying lengths (Figure 3-20D). These resulting CIDEs exhibited high binding affinity to PSMD2 and BRD4, as demonstrated in AlphaScreen and NanoBret assays, respectively. Pulldown experiments confirmed that CIDEs could promote ternary complex formation between PSMD2 and BRD4. Subsequent immunoblot degradation analysis further revealed that the most potent degrader,

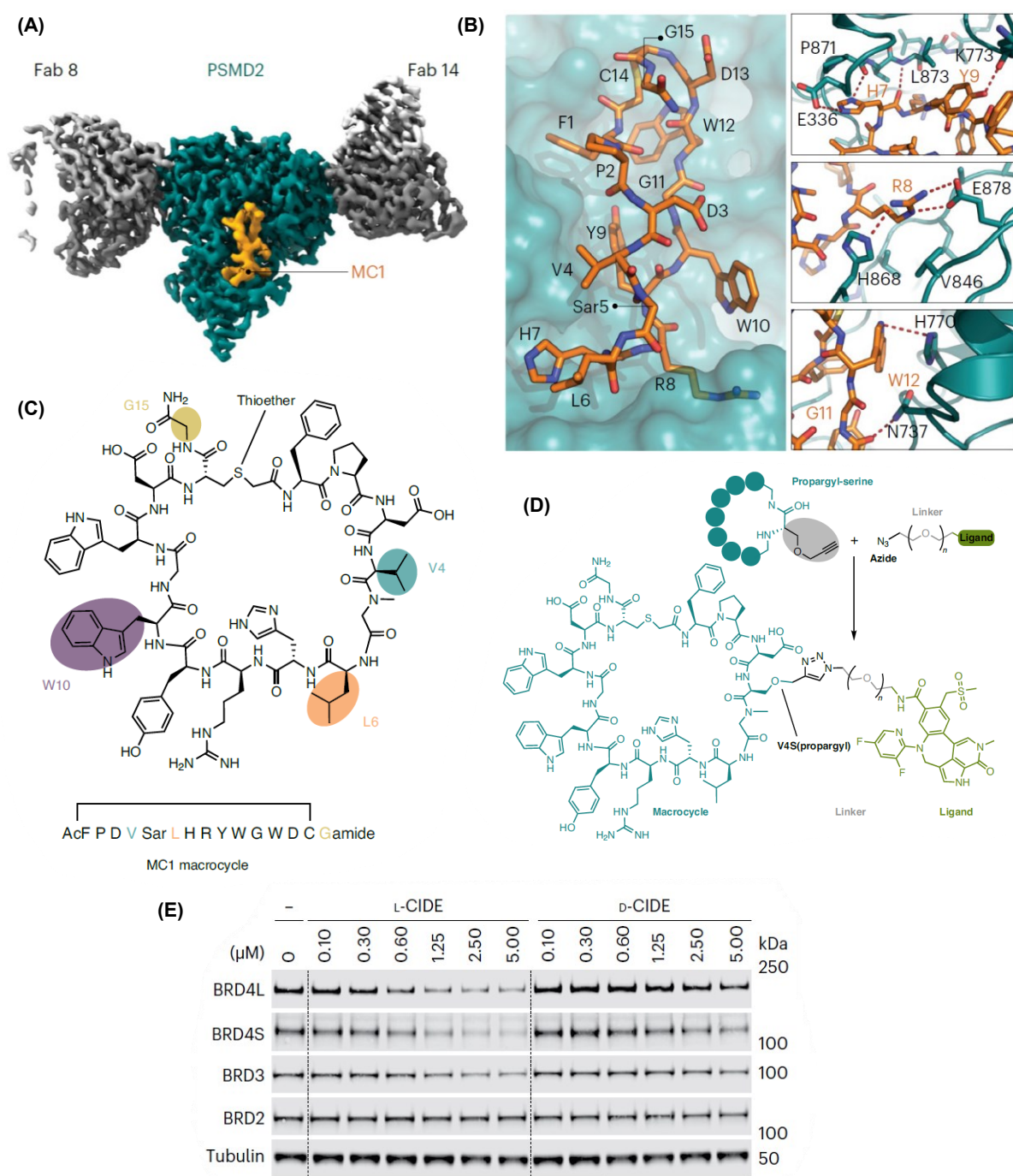


**Figure 3-20. Targeted degradation via direct 26S proteasome recruitment**

(A) The structure of PSMD2 (teal) in complex with two Fabs (grey) and macrocycle MC1 (orange). (B) Interactions between MC1 and PSMD2 with a close-up look at the key interacting residues HRYxGW. (C) Schematic of MC1 and four amino acids chosen as conjugation points. AcF, acetyl l-phenylalanine. (D) The Click-based strategy used to conjugate a BRD4 ligand (BETi) with various linkers to each macrocycle via a propargyl-serine introduced at each of the positions highlighted in (C). The structure of L-CIDE is as shown when  $n = 6$ . (E) Degradation of BRD4 observed by western blotting in HEK293 cells treated with L-CIDE for 20 h, but not with D-CIDE, where D-amino acids were employed. Images adapted with permission from Bashore *et al.*<sup>47</sup>

L-CIDE (V4-P6), achieved a  $DC_{50}$  of 0.73  $\mu$ M in HEK293 cells following 20 h of compound treatment (Figure 3-20E).

These findings underscore the potential of CIDEs as a promising technique for targeted protein degradation through direct recruitment of the proteasome. This method has several advantages over the PROTAC approach, as the CIDE mechanism does not necessitate the formation of a ternary complex or the multiple ubiquitin transfer processes required by PROTACs. This innovative strategy provides an alternative approach to validate our hypothesis and design Ab-peptide constructs. The improved  $DC_{50}$  of L-CIDE also reinforced our confidence in the feasibility of employing antibody-mediated delivery for such constructs. Conjugating antibodies to L-CIDE may lead to more robust cellular protein degradation outcomes compared to the peptide-PROTACs that were previously investigated.

### 3.6.2 Synthesis of QZ-027, an analogue of the reported peptide degrader

In the study of Bashore *et al.*, the recruitment of BRD4 was achieved using a BET bromodomain inhibitor referred to as 'BETi', which has exhibited greater potency in engaging BRD4 compared to the more commonly utilised BET inhibitor JQ1.<sup>254–256</sup> However, due to time constraints and the synthetic challenges posed by the 14-step synthetic route to BETi, I chose to use the commercially available JQ1 for BRD4 recruitment, rather than synthesising BETi. To prepare an azide-functionalised BRD4 ligand from the commercially available (+)-JQ1 ligand, the Boc protecting group on the JQ1 ligand was removed, resulting in a carboxylic acid form (**JQ1-COOH**). This ligand was then coupled to a PEG6 azide linker to generate **JQ1-azide** (Figure 3-21).

For the substitution of the V4 valine on the MC1 peptide, O-propargyl serine was used and manually coupled during the linear peptide synthesis process. After chloro-acetylation at the N-terminus, the peptides were cleaved from the resin exposing the deprotected cysteine residue. Subsequently, the peptide was dissolved in an aqueous solution under appropriate pH conditions to enable in-solution cyclisation between the deprotected cysteine and the chloro-acetylated N-terminus. The resulting cyclised alkyne-bearing MC1 macrocycle, **QZ-026**, was confirmed through LC-MS analysis and used directly without further purification. By employing the copper-catalysed azide-alkyne cycloadditions (CuAAC) method, **QZ-026** was subjected to click chemistry with **JQ1-azide** to produce the CIDE analogue 'CIDE-JQ1', referred to as **QZ-027**.

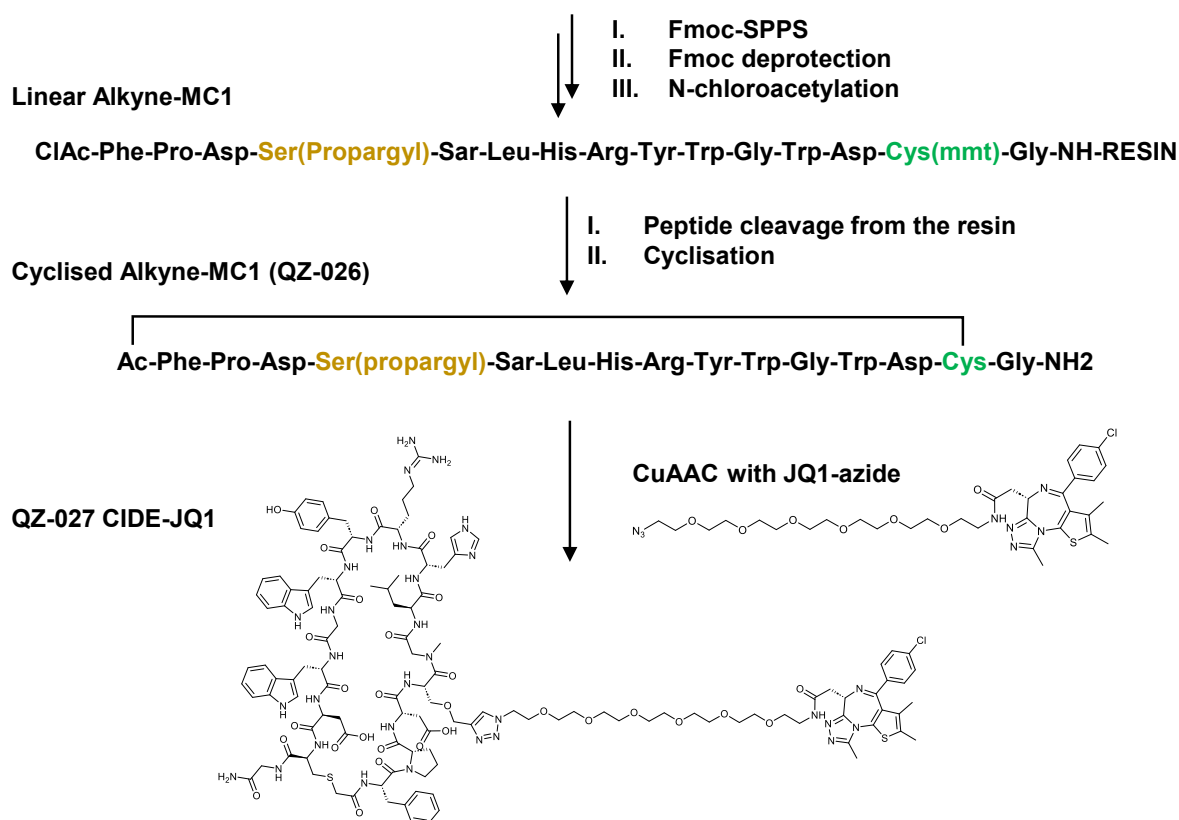


**Figure 3-21. Schematic representation of synthetic routes of CIDE analogue CIDE-JQ1 (QZ-027)**

Reagents and conditions. N-chloroacetylation: chloroacetic anhydride (10 eq.)/DIPEA (10 eq.) in DMF, 1 h. Cyclisation: peptide was dissolved in 50% MeCN in water, pH 8-9, RT, overnight. CuAAC: **QZ-026** (1 eq.), **JQ1-azide** (1 eq.), copper (II) sulphate pentahydrate (0.2 eq.), (+)-sodium L-ascorbate (1 eq.), 10% DMF, 20% MeCN in water, RT, 24 h. Protected amino acids were used during Fmoc-SPPS (not shown on the sequences), including Fmoc-Arg(Pbf)-OH, Fmoc-Asp(O<sup>t</sup>Bu)-OH, Fmoc-His(Trt)-OH, Fmoc-Tyr(<sup>t</sup>Bu)-OH, Fmoc-Sar-OH (Fmoc-N-methylglycine), Fmoc-Ser(Propargyl)-OH.

### 3.6.3 Immunoblot profiling of QZ-027 *in vitro*

Following the successful synthesis and purification of **QZ-027**, cellular immunoblot degradation assays in HEK293 cells were conducted. The cells were treated with increasing concentrations of **QZ-027**, ranging from 0.5  $\mu$ M to 5  $\mu$ M for a duration of 24 h. After the treatment, the cell lysates underwent immunoblot analysis to quantify the protein levels of the BRD4 long isoform (BRD4L, Figure 3-22). Surprisingly, **QZ-027** failed to induce BRD4L degradation even at the highest concentration of 5  $\mu$ M.

These results are in contrast with those reported by Bashore *et al.*, where 600 nM L-CIDE treatment reduced BRD4L levels to around 60%. Moreover, higher concentrations of L-CIDE led to dose-dependent degradation, resulting in a  $D_{\max}$  of 34% with 5  $\mu$ M treatment. The

difference in efficacy between L-CIDE and our analogue, **QZ-027**, might be attributed to the substitution of the BRD4 ligand from BETi to JQ1.

My results suggest that the choice of the target protein ligand within CIDEs significantly impacts their degradation efficacy. While small molecule PROTACs targeting BRD4 through the JQ1 ligand have demonstrated success in many instances in the literature, it is important to acknowledge that the mechanisms of CIDEs fundamentally differ from those of PROTACs.<sup>257</sup> The CIDE mechanism might require a more stringent formation of the POI/CIDE/proteasome complex or a more potent POI ligand than JQ1. The results also suggest a potential limitation in the scope for ligand modification within CIDE design, which could potentially restrict the applicability of this protein degradation approach. However, a more comprehensive investigation is needed to confirm these observations.

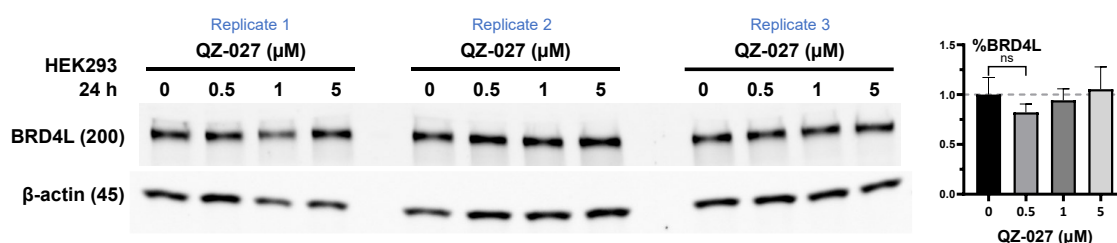


**Figure 3-22. *In vitro* testing of CIDE-JQ1 QZ-027 in HEK293 cell line**

Immunoblots and quantification of the BRD4 long isoform (BRD4L) levels after 24 h treatment with either DMSO control or increasing dose of **QZ-027**. Condition ‘0’ represents the cells were treated with 0.1% DMSO in the medium. Bars represent the mean signal normalised to  $\beta$ -actin, reported as mean  $\pm$  standard deviation (SD,  $n = 3$ ). Unpaired t-test was performed, and all treated groups were not significantly different (ns) from the control group.

### 3.6.4 Design and synthesis of linker-peptide constructs for QZ-027

In the pursuit of developing linker-peptide constructs, the C-terminus of the peptide was determined as the optimal attachment point for ADC linkers. Since the peptides were screened with mRNA attached to the C-terminus during the mRNA display selection, the modifications to the C-terminus of MC1 would not significantly impact its binding to the PSMD2 subunit. The C-terminal glycine residue was substituted with lysine, where the lysine side chain could serve as a coupling site for the ADC linker. The lysine side chain was protected by the ivDde protecting groups (PGs), which could be later removed using hydrazine. For the ADC linker, Linker 3 in combination with the VA dipeptide was selected, based on the previous successful conjugation experiences. This linker enables the thioester bond-based conjugation of the



antibody to the linker-peptide and permits protease cleavage adjacent to the dipeptide. As a result, protease cleavage of the ADC would reveal the free lysine side chain.

The existing synthetic route was modified to synthesise the linker-peptide construct. Orthogonal side chain-protected amino acids, Lys-(ivDde) and Cys-(Mmt), were used for the linear peptide synthesis (Figure 3-23). The cyclisation of MC1 peptide was performed on resin first, which involved the deprotection of Cys-(Mmt) and on-resin cyclisation of cysteine to the N-terminus. This on-resin cyclisation strategy avoided the interaction between nucleophilic cysteine and the maleimide moiety on the ADC linker. Subsequently, ivDde deprotection was

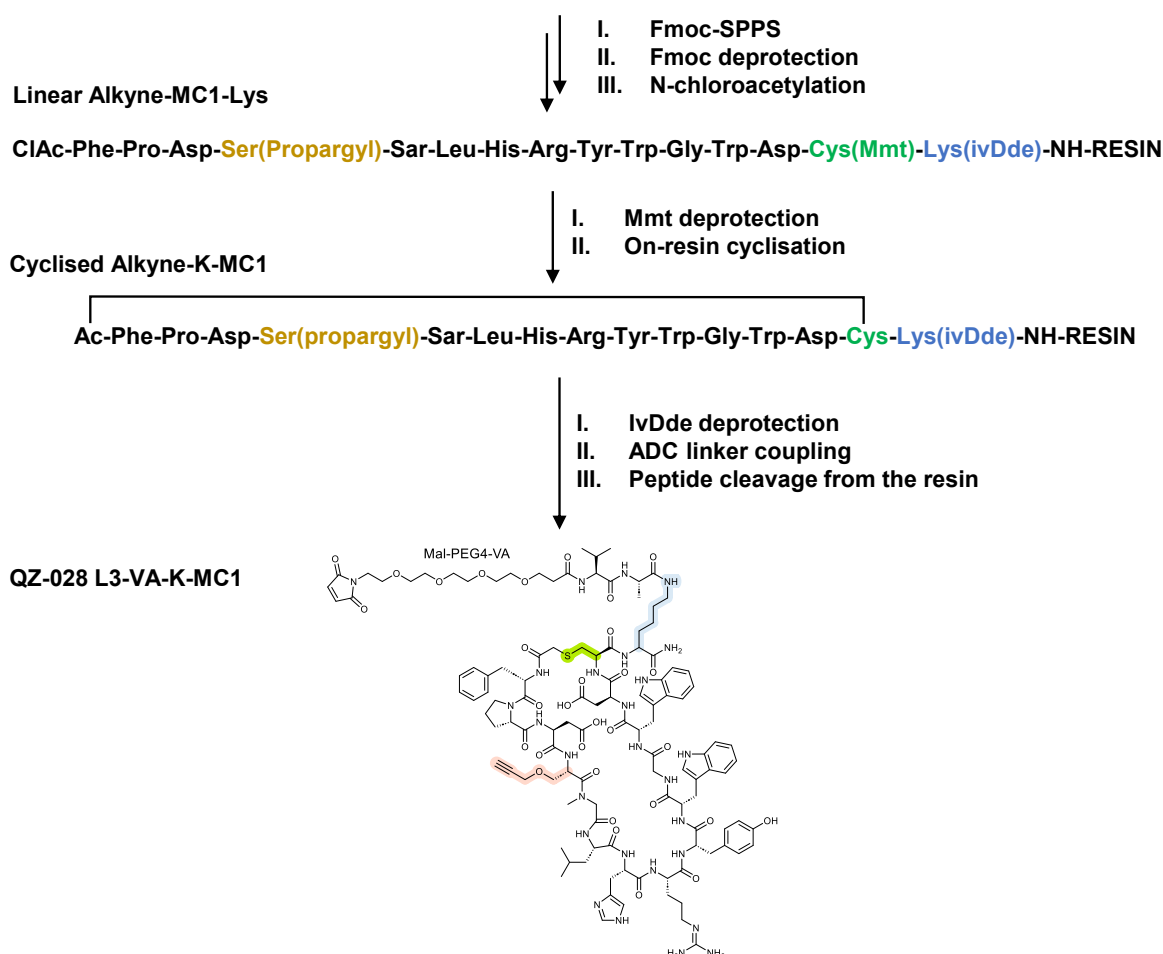


**Figure 3-23. Schematic representation of synthetic routes of MC1 analogue with ADC linker, QZ-028**

Reagents and conditions. Mmt deprotection: cleavage solution (TFA:TIPS:DCM, 5:5:90 v/v/v) 2 mL, 2 min, 25 times, vigorous shaking, RT. On-resin cyclisation: 1% DIPEA in DMF, 10 min, then 1% DBU in DCM, RT, 30 min. IvDde deprotection: 5% v/v hydrazine in DMF, 2 mL, 20 min, 5 times, shaking, RT. ADC linker coupling: the peptide was coupled to alanine and valine first, and then coupled with **L3** (1.5 eq.), HATU (1.5 eq.), DIPEA (5 eq.), dry DMF, N<sub>2</sub>, RT, 30 h. Protected amino acids were used during Fmoc-SPPS (not shown on the sequences), including Fmoc-Asp(O<sup>t</sup>Bu)-OH, Fmoc-Trp(Boc)-OH, Fmoc-Tyr(<sup>t</sup>Bu)-OH, Fmoc-Arg(Pbf)-OH, Fmoc-His(Boc)-OH.

carried out, and the ADC linker was coupled to the exposed lysine side chain of the resin-bound cyclic peptide. After linker coupling, the peptide was cleaved from the resin to give **QZ-028**, an MC1 analogue featuring ADC Linker 3 and an alkyne handle. The successful synthesis of **QZ-028** was confirmed by LC-MS analysis, and it was used without further purification.

Small-scale click reactions between **QZ-028** and **JQ1-azide** were conducted with varying conditions, including different copper reagents, ligands, and solvents (Table 8). Unfortunately, the expected product mass adduct was not detected in the LC-MS analysis of the resulting reaction mixtures, indicating that the attempted click reaction was unsuccessful. Given these results and the failure of **QZ-027** in replicating the degradation activity of the reported degrader L-CIDE, along with time constraints, I decided to temporarily suspend further exploration of this approach.

**Table 8. Attempted CuAAC conditions to conjugate QZ-028 (1 eq.) and JQ1-azide (1 eq.).**

	Copper reagent	Ligands/reduction agent	Solvent	Condition	Results
1	Copper(I) iodide (2 eq.)	(+)-sodium ascorbate (4 eq.)	1 mL of 10% DMF, 20% MeCN in water	RT, 24 h	No desired product mass in LC-MS
2	Copper (II) sulphate pentahydrate (1 eq.)	(+)-sodium ascorbate (4 eq.)	1 mL of 10% DMF, 20% MeCN in water	RT, 3 h, then 60 °C, 3 h	No desired product mass in LC-MS
3	Copper (II) sulphate pentahydrate (2 eq.)	(+)-sodium ascorbate (6 eq.)	0.5 mL of 10% DMF, 20% MeCN in water	RT, 24 h	No desired product mass in LC-MS
4	Tetrakis(acetonitrile)copper(I) hexafluorophosphate (3 eq.)	Tris(hydroxypropyl-triazolylmethyl)amine (THPTA) ligand (10 eq.)	0.5 mL DMF, pH 8	RT, 24 h	No desired product mass in LC-MS

### 3.6.5 Summary

The use of bifunctional peptide-small molecule chimeras, known as CIDEs, for the direct recruitment of the 26S proteasome offers exciting opportunities for targeted protein degradation. I explored the potential of L-CIDE, a peptide degrader with a superior DC<sub>50</sub> compared to previous peptide-based PROTACs, as a payload for antibody-peptide degrader conjugates (Ab-peptides). An analogue of the reported BRD4 degrader L-CIDE, **QZ-027**, was synthesised, substituting the BETi ligand in CIDE with the commercially available BRD4 ligand JQ1. Unfortunately, **QZ-027** did not exhibit a degradation efficacy comparable to L-CIDE. Furthermore, difficulties were encountered in synthesising linker-peptide constructs with click reaction. These challenges prompted the suspension of this study due to time constraints.

In summary, my attempts to replicate the reported degradation efficacy of L-CIDE with the designed analogue **QZ-027** and to generate linker-peptide constructs for ADC-peptide conjugates were unsuccessful. These outcomes raise questions regarding the applicability and generalisability of the CIDE method for the degradation of other protein targets. The limited scope of targeted protein degradation demonstrated in the paper, which focused exclusively on a single protein target within a single cell line, underscores the need for further investigations to understand CIDEs' viability across diverse targets and cellular environments.

### 3.7 Conclusion

In this chapter, I focused on the conversion of three peptide-based protein degraders into linker-peptide constructs, followed by their integration into novel antibody-peptide degrader conjugates (Ab-peptides). Our intent was to investigate whether Ab-peptide could overcome the permeability challenges faced by peptides through antibody-mediated internalisation and achieve enhanced protein degradation. After navigating peptide synthesis challenges, I synthesised three analogues of the reported peptide degrader and conducted *in vitro* evaluations. However, none of the analogues exhibited significant efficacy in degrading the target protein. This raised our questions on the *in vitro* efficacy of these reported peptide-based degraders and, more broadly, the reliability and reproducibility of results reported in the literature.

Attempts were made to conjugate these five linker-peptide constructs to antibodies and produce Ab-peptides. Despite the efforts, successful conjugation was only achieved with two linker-peptides. Further analysis and comparison of the linker structures revealed the vital role played by hydrophilic ADC linkers. Notably, the *in vitro* examinations of the successfully conjugated ADCs unveiled a moderate degradation efficacy against the PROTAC targets ER $\alpha$  and CREPT. Additionally, the EGFR ADCs demonstrated proteasome-independent degradation of the ADC antigen EGFR. These compelling findings offer valuable insights into ADC-mediated surface antigen internalisation and present opportunities for the development of antigen degradation tools harnessing ADC internalisation.

In conclusion, these findings highlight the potential of peptide-based degraders as ADC payloads. However, further investigations into the mechanisms of action of these degrader conjugates are necessary. Advancing the development of peptide degraders with enhanced degradation efficacy will substantially benefit the future development of antibody-peptide conjugates leading to more potent and efficient antibody-facilitated protein degradation.

## Chapter 4 Conclusion, Limitations and Future Directions

### 4.1 Conclusion

Targeted protein degradation using PROTACs represents an innovative therapeutic strategy with the potential to revolutionise the treatment of various diseases. Significant achievements have already been made in this field, particularly in effectively targeting a broad range of proteins. To enable conditional activation of PROTAC-mediated degradation, I developed two novel bifunctional degrader approaches: photoswitchable multi-kinase PROTACs (**AP-PROTAC-2**) and antibody-peptide degrader conjugates (Ab-peptides).

**AP-PROTAC-2** is the first example of a multi-target PROTAC with photoswitchable degradation activity, exhibiting superior photochemical properties compared to previous examples of photoswitchable PROTACs. It also exemplifies the successful application of the arylazopyrazole photoswitch **4** for targeted protein degradation. The multi-kinase inhibitor warhead of **AP-PROTAC-2** enables binding and simultaneous degradation of multiple protein kinases, while exhibiting minimal cell toxicity. Light-mediated switchable degradation of FAK, AURORA-A, and TBK1 was validated using multiplexed whole-cell proteomics and immunoblot experiments. These encouraging results of **AP-PROTAC-2** provided fresh insights into the development of novel light-responsive degraders with spatiotemporal control over multiple kinases.

To enhance the tissue and cell selectivity of PROTACs and overcome limitations encountered with small molecule PROTACs in ligand development for new E3 ligases and undruggable protein targets, the peptide-based degrader designs were integrated with ADC technology to design Ab-peptide degrader conjugates (Ab-peptides). Attempts were made to reproduce peptide-mediated degradation with synthesised degrader analogues; however, these peptide analogues were found inactive under the experimental conditions. Subsequently, three types of novel Ab-peptides targeting different proteins incorporating various ADC linker strategies were developed. Two Ab-peptides were produced and exhibited moderate degradation of target proteins in *in vitro* degradation assays. Overall, these results demonstrated the significant potential of Ab-peptides for targeted protein degradation.

This thesis offers valuable insights into designing conditional targeted protein degradation using PROTACs with enhanced activation precision and selectivity. Photoswitchable

PROTACs combined with promiscuous inhibitors could induce spatiotemporal controlled selective degradation, and they have the potential to serve as light-responsive chemical biology tools to investigate the functions of specific protein kinases within the kinome. The Ab-peptide degrader conjugates could drive innovation in ADC research, and if successful, these approaches might not only enable targeted protein degradation but also advance other cellular manipulations with antibody-delivered bifunctional peptides.

## 4.2 Limitations and future perspectives

### Multi-kinase degradation with Photoswitchable PROTAC (AP-PROTACs)

While **AP-PROTAC-2** has shown significant promise, our study has several limitations with numerous opportunities for improvement. This thesis presents only one instance of AP-PROTAC, employing only one multi-target inhibitor, recruiting one E3 ligase, and offering no further variations in linker length and design. Further optimisation through medicinal chemistry is essential and could be pivotal in enhancing the efficacy of the design. Potential explorations might encompass the introduction of alternative multi-target inhibitors or targeting diverse protein families, thereby broadening the PROTAC target scope and potentially uncovering synergistic effects. The incorporation of alternative E3 ligases could foster ternary complex formation and enhance protein degradation. Refinements in linker design might include adjustments in lengths, structures, and functionalities. Utilising optimal photoswitch designs could enhance the photochemical attributes of the PROTACs. Moreover, further medicinal chemistry efforts could potentially enable the photoswitching between the protein targets. For example, with the *E/Z* isomerisation, the two PROTAC isomers could degrade distinct sets of protein kinases.

In the cellular treatment, the manual intermittent irradiation of compounds was time-consuming and could introduce variability in the results. For treatments with light-responsive compounds, I recommend implementing an automated LED device for compound irradiation. This would improve consistency and precision when modulating the light-responsive characteristics of AP-PROTACs. Additionally, conducting *in vitro* reversible photoswitching experiments would provide more insights into the mechanism of the switchable degradation.

In the multiplexed proteomics experiments, degradation levels of the four identified kinase targets varied between approximately 30% to 50% degradation compared to the control after

treatment with 100 nM of (*E*-enriched)-**AP-PROTAC-2**. A more extensive set of cellular treatment conditions should be explored to identify optimal degradation conditions. Refinements that might improve the kinase coverage and profiling involve using additional cell lines or optimising protein preparation protocols after treatment. It is also advised to adopt proteomics workflows with increased multiplexing capabilities. This would enable a thorough analysis of AP-PROTACs' degradation profiles. Implementing techniques such as ELISA for preliminary screening before western blotting would increase the throughput and guide subsequent medicinal chemistry refinements. Employing methods like KINOMEscan to assess PROTAC target engagement would shed light on the selectivity profiles upon photoisomerisation.

In conclusion, **AP-PROTAC-2** marks a considerable leap in the field of photoswitchable PROTACs. By addressing the current limitations and exploring the suggested future directions, there is significant potential to not only develop more potent and selectively light-responsive PROTACs but also to unveil their clinical potential.

### **Antibody-peptide degrader conjugates (Ab-peptides)**

The exploration of Ab-peptides underscores the potential of peptide-based PROTACs as ADC payloads. However, several challenges were encountered and require exploration across various aspects. To begin with, it is crucial to understand why the synthesised analogue did not replicate the efficacy achieved by the reported peptide-based PROTACs, **TD-PROTAC**, and **PRTC**. One potential approach could involve reaching out to the authors of the publications and requesting access to the compounds or cell stocks necessary for reproducing their results.

For the Ab-peptides generated, both **HER2-15** and **EGFR-21** have demonstrated moderate *in vitro* target protein degradation. However, it was noted that the targeted proteins, ER $\alpha$  and CREPT, are primarily located in the nucleoplasm.<sup>232,258</sup> Investigating the precise degradation pathways responsible for such proteasome-independent degradation of nuclear proteins is necessary. Moreover, these results contradict our initial design hypothesis, which proposed that following the ADC internalisation, the peptide payloads would be released into the cytosol and initiate UPS-mediated target degradation.

To fully comprehend the observed antigen and targeted protein degradation, a thorough investigation is required to probe the target engagement of Ab-peptides and unveil the

degradation mechanism. Evaluations should encompass degradation assays under various conditions and in multiple cell lines, including antigen-negative cell lines. Detailed mechanistic studies are necessary to ascertain the potential involvement of lysosomes, autophagosomes, or other degradation pathways. Fluorescence microscopy could offer invaluable insights into the internalisation of ADCs, potential lysosomal trafficking, and the localisation and engagement of ADCs with their respective proteins or antigen targets. This might require the development of fluorescent antibodies specific to the antigen or the targeted protein, or the development of fluorescent-conjugated ADCs. It is also essential to evaluate the physicochemical properties of ADCs such as employing *in vitro* stability assessments.

Linker optimisation for Ab-peptides is another key aspect. Employing a range of linker strategies and designing bespoke ADC linkers for peptide payloads may enhance the stability, specific payload release, and degradation efficacy of the ADCs. Moreover, this could increase the success rate of antibody conjugation with linker-peptide payloads. An *in vitro* protease cleavage test on the ADCs would be insightful to assess the cleavage efficiency of the peptide payloads.

To unlock the potential of Ab-peptides, the development of more potent peptide-based degraders is important. This involves the optimisation of peptide degraders with an emphasis on improving their target engagement and permeability. Evaluating ADC efficacy in permeabilised cells or adopting peptide delivery methods such as electroporation or polymer carrier systems, could enhance the intracellular delivery efficiency and ensure robust target engagement.

Moving beyond the initial aim of developing Ab-peptides, there are opportunities to extend this antibody-based approach to develop tools for cell-surface protein degradation, complementing proteasome-independent protein degradation strategies like LYTAC technology. To achieve this, it is important to elucidate effective EGFR degradation and study the degradation pathway involved with additional designs of antibody-peptide conjugates. This may necessitate experimenting with a diverse range of peptide payloads and alternative antibodies, allowing for the development and analysis of ADCs with a structure-activity relationship (SAR) approach, much like methods used in medicinal chemistry. Alternatively, employing antibody fragments such as nanobodies or single-chain variable fragments (scFvs), would be helpful to deconvolute the antigen-mediated internalisation process of the antigen.

Such pursuits could deepen our understanding of the observed EGFR degradation and provide proof-of-concept for this proposed novel degradation strategy.

In conclusion, these preliminary studies of the novel Ab-peptide degrader conjugates have yielded promising results. The primary emphasis moving forward will be to delve deeper into the degradation mechanisms involved. Subsequently, the upcoming phase will centre on the employment or screening of novel peptide binders, aiming to develop Ab-peptides to effectively degrade neosubstrates.



## Chapter 5 Materials and methods

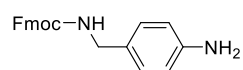
### 5.1 Chemistry

#### 5.1.1 Materials and instrumentations

All reagents were purchased from commercial sources (Sigma-Aldrich, Merck, Fluorochem UK) unless otherwise stated and were used as supplied without further purification. The multi-kinase inhibitor CTx-0294885 was provided by GlaxoSmithKline Medicines Research Centre, Stevenage, or synthesised by Jennifer R. Baker and Adam McCluskey with flow chemistry approaches as previously described.<sup>259</sup> Analytical thin-layer chromatography (TLC) silica gel 60 F254 (Merck) was used and visualized with UV light (254 nm) or appropriate TLC stain to monitor the reactions. Flash column chromatography with silica gel Geduran® Si 60 (0.040-0.063 mm, Merck) was performed for general compound purification. Nuclear Magnetic Resonance (NMR) spectra were recorded on a BRUKER AV-400 spectrometer at 400 MHz (<sup>1</sup>H-NMR) and 101 MHz (<sup>13</sup>C-NMR) in deuterated solvents at 298 K. Chemical shifts are given in parts per million (ppm), coupling constants *J* are given in Hertz (Hz), and spin multiplicities are given as follows: s (singlet), d (doublet), dd (doublet of a doublet), t (triplet), q (quartet), m (multiplet) or br (broad). Spectra were analysed with MestReNova 12. High-resolution mass spectrometry (HRMS) data were acquired by the Imperial Mass Spectrometry service.

#### 5.1.2 Synthesis

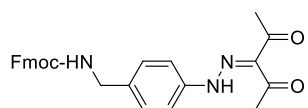
##### *(9H-fluoren-9-yl)methyl (4-aminobenzyl)carbamate (1)*



A solution of 4-(aminomethyl)aniline (1.39 mL, 12.3 mmol) in DCM (80 mL) was combined with DIPEA (2.14 mL, 12.3 mmol) and the mixture was cooled to 0 °C. A solution of 9-fluorenylmethyl *N*-succinimidyl carbonate (Fmoc-OSu, 4.14 g, 12.3 mmol) in DCM (30 mL) was slowly added. The reaction mixture was stirred for 16 h at room temperature. The resulting milky solution was washed with water (80 mL) and the organic layer was concentrated under vacuum. The crude product was purified through flash column chromatography (30% to 80% ethyl acetate in n-hexane) to yield the desired product **1** as a beige solid (3.50 g, 83%). <sup>1</sup>H NMR (400 MHz, DMSO-*d*<sub>6</sub>) δ 7.92 – 7.85 (m, 2H), 7.73 – 7.63 (m, 3H), 7.45 – 7.37 (m, 2H), 7.36 – 7.26 (m, 2H), 6.92 – 6.87 (m, 2H), 6.52

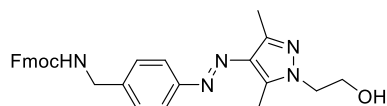
– 6.47 (m, 2H), 4.96 (s, 2H), 4.31 (d,  $J = 7.0$  Hz, 2H), 4.21 (t,  $J = 6.9$  Hz, 1H), 4.00 (d,  $J = 6.1$  Hz, 2H).  $^{13}\text{C}$  NMR (101 MHz, DMSO- $d_6$ )  $\delta$  156.2, 147.5, 143.9, 140.8, 128.1, 127.6, 127.0, 126.7, 125.2, 120.1, 113.7, 65.2, 46.8, 43.6. HRMS (ESI)  $m/z$ : calculated for  $\text{C}_{22}\text{H}_{21}\text{N}_2\text{O}_2^+$ , 345.1603; found 345.1590.

**(9H-fluoren-9-yl)methyl(4-(2-(2,4-dioxopentan-3-ylidene)hydrazineyl)benzyl)carbamate (2)**



A solution of aniline **1** (500 mg, 1.45 mmol) in acetic acid (5.0 mL) was combined with HCl (1.40 mL, 37%) and the solution was then cooled to 0 °C. A solution of sodium nitrite (200 mg, 2.90 mmol) in water (2.0 mL) was added. The resulting reaction mixture was stirred at 0 °C for 1 h, then a solution of acetylacetone (193  $\mu\text{L}$ , 1.88 mmol) and sodium acetate (476 mg, 5.81 mmol) in ethanol (5.0 mL) was added. The bright yellow solution obtained was allowed to warm up to room temperature. After 3 h, the mixture was combined with ethyl acetate (20 mL) and then washed with 0.5 M sodium bicarbonate ( $3 \times 10$  mL) and brine ( $3 \times 10$  mL). The organic layer was dried over  $\text{Na}_2\text{SO}_4$ , filtered, and concentrated. The resulting crude product was further purified by flash column chromatography (40 % ethyl acetate in hexane) to afford diketone **2** as an orange solid (442 mg, 67%).  $^1\text{H}$  NMR (400 MHz,  $\text{CDCl}_3$ )  $\delta$  14.75 (s, 1H), 7.83 – 7.76 (m, 2H), 7.65 – 7.59 (m, 2H), 7.47 – 7.26 (m, 8H), 5.23 (s, 1H), 4.51 (d,  $J = 6.8$  Hz, 2H), 4.39 (d,  $J = 6.1$  Hz, 2H), 4.24 (t,  $J = 6.7$  Hz, 1H), 2.63 (s, 3H), 2.51 (s, 3H).  $^{13}\text{C}$  NMR (101 MHz,  $\text{CDCl}_3$ )  $\delta$  198.1, 197.2, 156.6, 143.9, 141.4, 141.0, 136.4, 133.3, 128.9, 127.8, 127.1, 125.1, 120.1, 116.6, 66.8, 47.4, 44.6, 31.8, 26.8. HRMS (ESI)  $m/z$ : calculated for  $\text{C}_{27}\text{H}_{26}\text{N}_3\text{O}_4^+$ , 456.1923; found 456.1919.

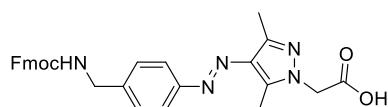
**(9H-fluoren-9-yl)methyl(E)-(4-((1-(2-hydroxyethyl)-3,5-dimethyl-1H-pyrazol-4-yl)diazenyl)benzyl)carbamate (3)**



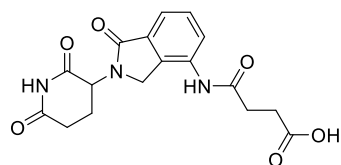
Diketone **2** (150 mg, 0.329 mmol) was dissolved in a mixture of DCM (5.0 mL) and methanol (5.0 mL). 2-Hydrazinoethanol (34  $\mu\text{L}$ , 0.493 mmol) was added, and the mixture was stirred at 50 °C for 2 h. DCM (5.0 mL) and 1 M aqueous hydrochloric acid (5.0 mL) were added to the crude mixture. The extracted organic layer was washed with aq. HCl (1 M,  $3 \times 5.0$  mL), dried over  $\text{Na}_2\text{SO}_4$  and concentrated to yield alcohol **3** as a yellow solid (151 mg, 93%).  $^1\text{H}$

**NMR** (400 MHz, CDCl<sub>3</sub>)  $\delta$  7.80 – 7.72 (m, 5H), 7.64 – 7.57 (m, 2H), 7.45 – 7.29 (m, 5H), 5.13 (s, 1H), 4.49 (d,  $J$  = 6.8 Hz, 2H), 4.44 (d,  $J$  = 6.1 Hz, 2H), 4.28 – 4.23 (m, 3H), 4.09 – 4.04 (m, 2H), 2.63 (s, 3H), 2.55 (s, 3H). **<sup>13</sup>C NMR** (101 MHz, CDCl<sub>3</sub>)  $\delta$  152.9, 144.0, 141.5, 141.3, 128.2, 127.9, 127.2, 125.1, 122.4, 120.2, 106.4, 61.4, 50.3, 47.5, 44.9, 19.2, 13.9, 10.0. **HRMS** (ESI)  $m/z$ : calculated for C<sub>29</sub>H<sub>30</sub>N<sub>5</sub>O<sub>3</sub><sup>+</sup>, 496.2349; found 496.2341.

**(*E*)-2-(4-(((4-((((9*H*-fluoren-9-yl)methoxy)carbonyl)amino) methyl)phenyl)diazenyl)-3,5-dimethyl-1*H*-pyrazol-1-yl) acetic acid (linker 4)**



A solution of alcohol **3** (150 mg, 0.303 mmol) in DMSO (4.0 mL) was added Dess–Martin periodinane (DMP, 381 mg, 0.898 mmol). The solution was stirred for 16 h at room temperature. A solution of sodium chlorite (50 mg, 0.559 mmol) and NaH<sub>2</sub>PO<sub>4</sub> (55 mg, 0.93 mmol) in water (0.50 mL) was added to the mixture, followed by the addition of 2-methylbut-2-ene (100  $\mu$ L, 0.93 mmol). The solution was stirred for 16 h at room temperature. Water (20 mL) was added, and the mixture was filtered to remove the DMP by-product. The filtrate was extracted with ethyl acetate (5  $\times$  10 mL), and the combined organic layer was dried over Na<sub>2</sub>SO<sub>4</sub>, filtered, and concentrated under vacuum. The product was purified by flash column chromatography (3% – 7% methanol in DCM) and freeze-dried to yield linker **4** as a yellow solid (82 mg, 54%). **<sup>1</sup>H NMR** (400 MHz, DMSO-*d*<sub>6</sub>)  $\delta$  7.96 – 7.87 (m, 3H), 7.75 – 7.66 (m, 4H), 7.46 – 7.39 (m, 2H), 7.37 – 7.31 (m, 4H), 4.74 (s, 2H), 4.41 – 4.35 (m, 2H), 4.30 – 4.21 (m, 3H), 2.51 (s, 3H), 2.38 (s, 3H). *Only E isomer was observed.* **<sup>13</sup>C NMR** (101 MHz, DMSO-*d*<sub>6</sub>)  $\delta$  169.6, 156.9, 152.6, 144.4, 141.6, 141.2, 140.7, 135.0, 128.2, 128.1, 127.5, 127.5, 125.6, 121.8, 120.6, 65.8, 52.4, 47.3, 44.0, 14.3, 10.0. **HRMS** (ESI)  $m/z$ : calculated for C<sub>29</sub>H<sub>28</sub>N<sub>5</sub>O<sub>4</sub><sup>+</sup>, 510.2141; found 510.2128.



**4-((2-(2,6-dioxopiperidin-3-yl)-1-oxoisindolin-4-yl)amino)-4-oxobutanoic acid (5)**

To a solution of lenalidomide (100 mg, 0.386 mmol) in DMF (4.0 mL), succinic anhydride (57.9 mg, 0.579 mmol) was added. The solution was stirred at 60 °C for 24 h, then Et<sub>2</sub>O (30 mL) was added, and the mixture was stored at 0 °C overnight for 18 h. A white precipitate was observed and collected by gravity filtration to yield carboxylic acid **5** as a white solid (138 mg, 99%). **<sup>1</sup>H NMR** (400 MHz,

DMSO- $d_6$ )  $\delta$  12.18 (s, 1H), 11.04 (s, 1H), 9.88 (s, 1H), 7.87 – 7.77 (m, 1H), 7.55 – 7.45 (m, 2H), 5.16 (dd,  $J$  = 13.3, 5.1 Hz, 1H), 4.43 – 4.27 (m, 2H), 3.00 – 2.90 (m, 1H), 2.66 – 2.58 (m, 3H), 2.58 – 2.52 (m, 2H), 2.43 – 2.26 (m, 1H), 2.09 – 1.98 (m, 1H).  $^{13}\text{C}$  NMR (101 MHz, DMSO- $d_6$ )  $\delta$  174.3, 173.4, 171.6, 170.8, 168.3, 134.2, 134.1, 133.1, 129.1, 125.5, 119.4, 52.0, 46.9, 31.7, 31.1, 29.4, 23.1. HRMS (ESI)  $m/z$ : calculated for  $\text{C}_{17}\text{H}_{18}\text{N}_3\text{O}_6^+$ , 360.1195; found 360.1194.

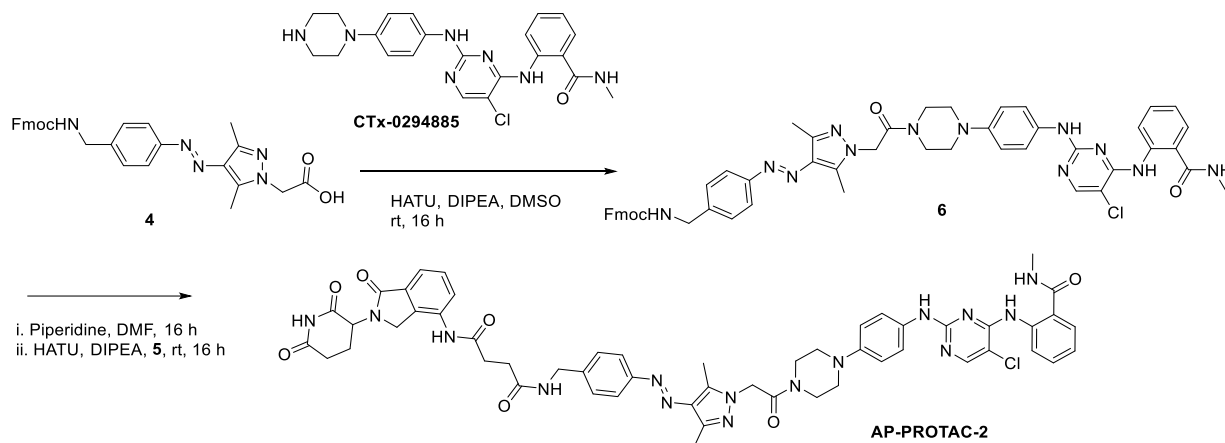


**Figure 5-1. Synthesis of AP-PROTAC-2**

*(E)-N1-(4-((1-(2-(4-(4-((5-chloro-4-((2-(methylcarbamoyl)phenyl)amino)pyrimidin-2-yl)amino)phenyl)piperazin-1-yl)-2-oxoethyl)-3,5-dimethyl-1H-pyrazol-4-yl)diazenyl)benzyl)-N4-(2-(2,6-dioxopiperidin-3-yl)-1-oxoisindolin-4-yl)succinimide (AP-PROTAC-2)*

Carboxylic acid **4** (90 mg, 0.176 mmol) was dissolved in a mixture of DMSO (2.0 mL) and DMF (2.0 mL). Amine CTx0294885 (77 mg, 0.176 mmol), HATU (100 mg, 0.264 mmol) and DIPEA (122  $\mu\text{L}$ , 0.704 mmol) were added to the mixture. The mixture was stirred at room temperature for 16 h. Water (20 mL) was added to the resulting mixture and the solution was extracted with ethyl acetate ( $5 \times 20$  mL). The combined organic layer was washed with brine, dried over  $\text{Na}_2\text{SO}_4$  and concentrated under vacuum. The crude material was purified by flash column chromatography (2%–8% methanol in DCM) to afford intermediate **6** as an orange solid (100 mg) which was used in the subsequent step without further characterisation.

To a solution of intermediate **6** (100 mg, 0.108 mmol) in DMF (2.0 mL), piperidine (0.011 mL, 0.108 mmol) was added. The reaction mixture was stirred at room temperature for 16 h. HATU (62 mg, 0.162 mmol), DIPEA (0.075 mL, 0.149 mmol) and lenalidomide derivative **5** (39 mg, 0.108 mmol) were added to the reaction mixture. The mixture was stirred at room temperature for 16 h. The crude mixture was added water (20 mL) and extracted with ethyl acetate (5 × 20 mL). The combined organic layer was washed with brine, dried over Na<sub>2</sub>SO<sub>4</sub>, filtered, concentrated under vacuum, and freeze-dried. The crude was purified by flash column chromatography (3%–7% methanol in DCM) to give the desired product **AP-PROTAC-2** as a yellow solid (12.5 mg, 6.8% yield over two steps). <sup>1</sup>H NMR (400 MHz, DMSO-*d*<sub>6</sub>) δ 11.61 (s, 1H), 11.03 (s, 1H), 9.27 (s, 1H), 8.80 – 8.75 (m, 2H), 8.55 – 8.49 (m, 1H), 8.17 (s, 1H), 7.90 – 7.81 (m, 1H), 7.79 – 7.72 (m, 1H), 7.70 – 7.62 (m, 2H), 7.56 – 7.42 (m, 5H), 7.42 – 7.35 (m, 2H), 7.27 – 7.23 (m, 1H), 7.18 – 7.08 (m, 1H), 7.00 – 6.89 (m, 2H), 5.22 (s, 2H), 5.18 – 5.03 (m, 1H), 4.43 – 4.24 (m, 4H), 3.73 – 3.60 (m, 4H), 3.21 – 3.16 (m, 2H), 3.13 – 3.06 (m, 2H), 2.98 – 2.84 (m, 1H), 2.81 (d, *J* = 4.5 Hz, 3H), 2.71 – 2.52 (m, 5H), 2.48 (s, 3H), 2.37 (s, 3H), 2.34 – 2.23 (m, 1H), 2.05 – 1.96 (m, 1H). *The Z isomer was detected in the sample, and its presence was determined to be 12% based on the integration of representative pyrazole methyl proton peaks: 2.02 (s, 3H), 1.38 (s, 3H).* <sup>13</sup>C NMR (101 MHz, DMSO-*d*<sub>6</sub>) δ 172.9, 171.3, 171.1, 170.7, 168.9, 167.8, 164.7, 158.0, 154.9, 154.7, 152.0, 146.2, 141.2, 141.1, 140.5, 139.4, 134.5, 133.9, 133.5, 132.9, 132.7, 131.5, 128.6, 128.0, 127.9, 125.0, 121.8, 121.3, 121.2, 120.5, 118.9, 116.5, 104.4, 70.5, 51.5, 50.5, 49.5, 49.1, 46.4, 44.2, 41.8, 41.6, 31.3, 31.2, 30.5, 26.3, 22.7, 13.9, 9.6. MS (MALDI-TOF) *m/z*: calculated for C<sub>53</sub>H<sub>55</sub>ClN<sub>15</sub>O<sub>7</sub><sup>+</sup>, 1048.4; found 1049.0.

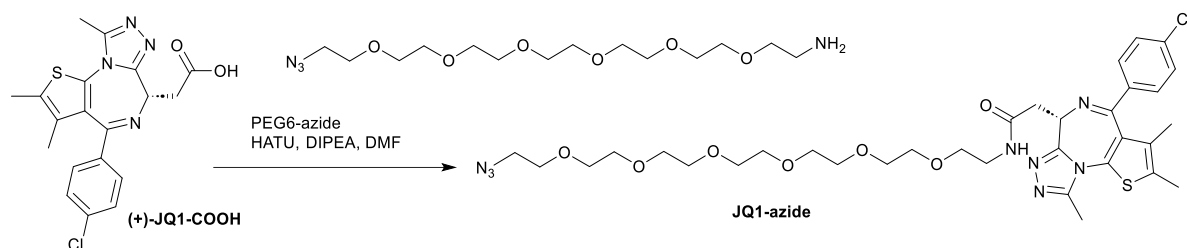
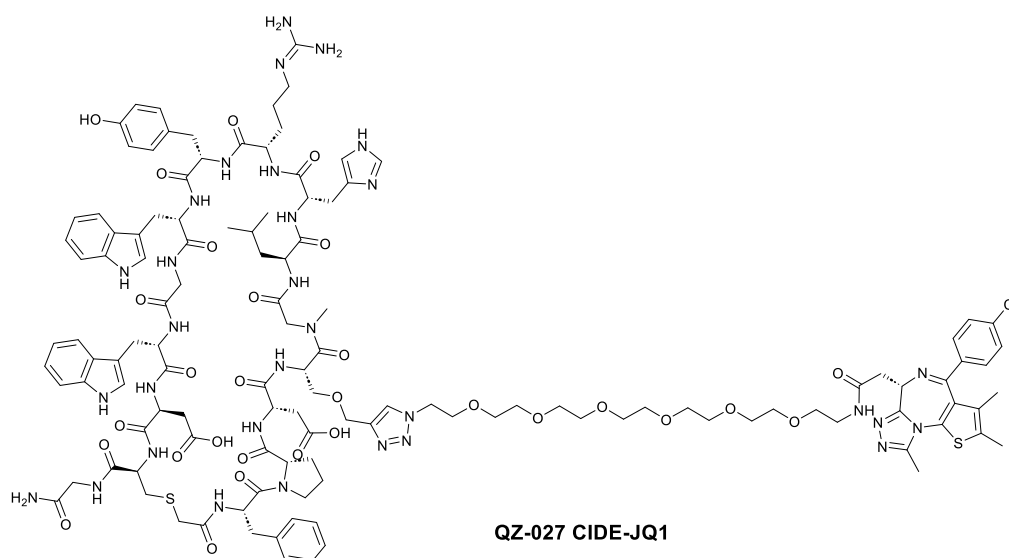


**Figure 5-2. Synthesis of JQ1-azide**

*(S)-N-(20-azido-3,6,9,12,15,18-hexaoxaicosyl)-2-(4-(4-chlorophenyl)-2,3,9-trimethyl-6H-thieno[3,2-*ff*][1,2,4]triazolo[4,3-*a*][1,4]diazepin-6-yl)acetamide (JQ1-azide)*

A solution of Boc deprotected JQ1 ligand, JQ1-COOH (13.6 mg, 0.034 mmol), HATU (19.4 mg, 0.051 mmol) and DIPEA (23.7  $\mu$ L) was stirred in dry DMF (2.0 mL) under nitrogen for 10 min. A solution of 20-azido-3,6,9,12,15,18-hexaoxaicosan-1-amine (PEG6-azide, 13.1 mg, 0.0374 mmol) in 1.0 mL DMF was added to the mixture, and the resulting solution was stirred at room temperature for 4 h. The reaction mixture was added water (20 mL) and extracted with ethyl acetate (50 mL), washed with water, brine and then water ( $5 \times 20$  mL each). The organic layer was dried over Na<sub>2</sub>SO<sub>4</sub>, filtered, and concentrated under vacuum. The crude product **JQ1-azide** was used in the subsequent step without further characterisation or purification.

***CuAAC reaction to synthesise CIDE analogue, CIDE-JQ1 (QZ-027)***



Copper (II) sulphate pentahydrate (0.5 mg, 0.0017 mmol, 0.2 eq.) and (+)-sodium L-ascorbate (1.7 mg, 0.0085 mmol, 1 eq.) were dissolved in 1 mL of water containing 10% DMF and 20% MeCN. Then alkyne-MC1 **QZ-026** (16 mg, 0.0085 mmol, 1 eq.) was added to the solution with stirring, followed by the addition of **JQ1-azide** (approximately 0.0085 mmol). The resulting mixture was stirred at room temperature for 24 h. The progress of the reaction was monitored using analytical LC-MS, and once completed, the reaction mixture was freeze-dried. The desired product **QZ-027** was purified using preparative LC-MS (5.5 mg, 24.7%, Figure 7-22).

### 5.1.3 Peptide synthesis

#### 5.1.3.1 Materials and instrumentation

For peptide synthesis, Fmoc-Dap(Alloc)-OH was purchased from Iris Biotech. Boc-Lys(Fmoc)-OH was purchased from BACHEM. Fmoc-Cys(Mmt)-OH was purchased from Sigma-Aldrich. Fmoc-Asp-OAll, Fmoc-Sar-OH, Fmoc-Lys(ivDde), Fmoc-L-Ser(Propargyl)-OH, Chloroacetic anhydride, Trifluoroacetic acid (TFA) of peptide grade, Triisopropyl silane (TIPS), 2-(7-Aza-1H-benzotriazole-1-yl)-1,1,3,3-tetramethyluronium hexafluorophosphate (HATU), and N,N-Diisopropylethylamine (DIPEA) were from Fluorochem. Tris(3-hydroxypropyltriazolylmethyl)amine (THPTA) was from TCI chemicals. All other Fmoc-protected amino acids and Oxyma pure were from CEM (Buckingham, UK). TentaGel S RAM resin was obtained from Rapp Polymere (Tübingen, Germany). For ADC linkers, (6-(2,5-dioxo-2,5-dihydro-1H-pyrrol-1-yl) hexanoyl)-L-valyl-L-alanine (MC-Val-Ala-OH, Linker 1) was purchased from MedChemExpress, 2-methyl-2-((5-nitropyridin-2-yl)disulfaneyl)propyl (4-nitrophenyl) carbonate (Linker 2) was purchased from Pharmaron, and 1-(2,5-dioxo-2,5-dihydro-1H-pyrrol-1-yl)-3,6,9,12-tetraoxapentadecan-15-oic acid (Mal-PEG4-acid, Linker 3) was purchased from BROADPHARM.

Linear peptides were synthesised using the Liberty Blue<sup>TM</sup> Automated Microwave Peptide Synthesizer connected to HT12 resin loader from CEM. Peptides were analysed or purified with (1) LC-MS that is composed of a Waters high-performance liquid chromatography (HPLC) system, a 2767 autosampler, 515 pump, 2998 photodiode array (PDA) detector (200-600 nm) and a 3100-electrospray ionisation (ESI) mass spectrometer with MassLynx 4.1 software. Peptide separations were performed on Waters XBridge C18 columns (130 Å, 5 µm, 4.6 mm × 100 mm for analytical runs and 130 Å, 5 µm, 19 mm × 100 mm for preparative runs), using an injection volume of 20 µL and a flow rate of 1.2 mL/min. The gradient used was: 5% or 20% to 98% MeCN in water with 0.1% formic acid over 12 min, 98% MeCN for 3 min, and re-equilibration to the starting eluent for 3 min (eq5 or eq20 gradient); (2) Shimadzu LC-20AR preparative HPLC system that with a Shimadzu SIL-10AP autosampler, Shimadzu FRC-10A fraction collector, two Shimadzu LC-20 AR pumps and Phenomenex Aeris Peptide XB-C18 column (150 mm × 21 mm, 5 µm, 100 Å) column coupled to a Shimadzu SPD-20A UV/Vis detector (90-900 nm). The injection volumes were 1 to 5 mL, and the flow rate was 20 mL/min. Detection at 220 nm and 280 nm was used for isolating the

desired products. The gradient used was: 10% to 40% eluent B (MeCN with 0.08% TFA) in eluent A (water with 0.1% TFA) over 23 min, 40% to 95% eluent B in eluent A for 1 min, 95% eluent B in eluent A for 3 min and re-equilibration to the starting eluent for 3 min (10-40-95, 30 min gradient). Ultra-pure water was used for HPLC solutions preparation, obtained from a Millipore Elix Q-Gard purification system. After HPLC purification of cleaved peptides, the pure peptides were lyophilised using an Alpha 2-4 LD Plus freeze-dryer (Christ).

#### **5.1.3.2 General protocols for solid phase peptide synthesis**

The linear peptides were synthesised using Fmoc solid phase peptide synthesis (SPPS) methods on a 50  $\mu\text{m}$  scale, employing TentaGel S RAM resin (207 mg, 0.24 mmol/g) as the solid support.<sup>260</sup> Dry resins were allowed to swell in DMF (20 mL) for 10 min before the synthesis. The amino acid sequence was input into the embedded software of Liberty Blue, which calculated the required quantities of reagents for the synthesis. After preparing and loading the designated concentrations and quantities of reagents onto the Liberty Blue instrument, automated peptide synthesis was initiated. The synthesis was carried out under standard microwave settings as directed by the Liberty Blue instrument's instructions (Table 9).<sup>261</sup>

The procedure involved swelling resins in DMF (10 mL) for 10 min prior to synthesis. The synthesis began with Fmoc deprotection of the resin using 10% piperidine in DMF supplemented with Oxyma pure (0.1 M). This was followed by a resin washing step, and a coupling step using a 5-fold molar excess of the desired Fmoc-protected amino acid (1.25 mL, 250  $\mu\text{mol}$ , 0.2 M solution in DMF) which was preactivated with 5 eq. Oxyma Pure (0.5 mL, 250  $\mu\text{mol}$ , 0.5 M solution in DMF) and 10 eq. DIC (1 mL, 500  $\mu\text{mol}$ , 0.5 M solution in DMF). For amino acids such as Fmoc-Arginine or unnatural amino acids, the coupling step was repeated. The cycle of Fmoc deprotection and amino acid coupling was repeated until the desired peptide sequence was completed. A final Fmoc deprotection step was performed to afford peptides with free N-terminal amines, and the N-terminus was modified if required.

Upon completion of Liberty Blue peptide synthesis, the linear peptides were transferred to a fritted syringe and washed with DMF ( $3 \times 5$  mL) then DCM ( $3 \times 5$  mL) and stored at  $-20^\circ\text{C}$  or used in the subsequent synthesis steps. Prior to the next reaction, peptide-bound resins were removed from  $-20^\circ\text{C}$  freezer storage and gently agitated in 5 mL DMF for 10 min to ensure appropriate swelling.



**Table 9. Microwave methods used**

Standard deprotection				
Stage	Temp (°C)	Power (W)	Time (s)	Delta T
1	75	155	15	2
2	90	30	50	1
Standard Coupling				
Stage	Temp (°C)	Power (W)	Time (s)	Delta T
1	75	170	15	2
2	90	30	110	1
Histidine Coupling				
Stage	Temp (°C)	Power (W)	Time (s)	Delta T
1	25	0	120	2
2	50	35	240	1

### 5.1.3.3 Test mini cleavage

To monitor peptide reactions on the solid phase, a test mini-cleavage of peptides on the resin was performed. A small quantity of peptide-loaded resins (approximately 50 beads) was transferred into an Eppendorf tube. A freshly prepared cleavage cocktail (TFA:TIPS:H<sub>2</sub>O, 95:2.5:2.5 v/v/v, 100 µL) was added to the tube, and the mixture was shaken at 50 °C for 30 min. The liquid in the Eppendorf tube was evaporated under nitrogen, and the residue was dissolved in LC-MS grade solution (water with 5% or 20% MeCN and 0.1% formic acid, 100 µL). The Eppendorf tube was subjected to centrifugation in a bench-top centrifuge (8000 rpm, 1 min) and the resulting supernatant was analysed by LC-MS.

### 5.1.3.4 N-chloro-acetylation

The resin (0.05 mmol) was agitated with a solution of chloroacetic anhydride (85.5 mg, 0.5 mmol, 10.0 eq.) and DIPEA (87.0 µL, 0.5 mmol, 10.0 eq.) in 5 mL DMF at room temperature for 1 h. Reaction completion was monitored with a Ninhydrin test or a test mini cleavage and LC-MS analysis. The resins were subsequently washed with DMF (3 × 5 mL) and DCM (3 × 5 mL).

### 5.1.3.5 Peptide cleavage from resins

The peptide-loaded resins (0.05 mmol) were subjected to thorough washing with DMF (3 × 5 mL), DCM (3 × 5 mL), followed by the addition of methanol (3 × 5 mL) to shrink the

resin (as residual DMF might interfere with the acidolysis of TFA). The washed resins were then transferred into a 24 mL fritted syringe, to which 10 mL of freshly prepared cleavage cocktail (TFA: TIPS: H<sub>2</sub>O: thioanisole, 91:3:3:3 v/v/v/v) was added. The mixture was agitated at room temperature for 2 to 3 hours. The supernatant was collected by filtration into a 50 mL centrifuge tube, and the resins were rinsed with cleavage cocktail (2 × 2 mL). The filtrate was evaporated under nitrogen for an hour to remove excess TFA. The cleaved content was precipitated with the addition of 20 mL cold diethyl ether. The crude peptide precipitate was vigorously agitated and centrifuged at 4000 rpm for 5 min. The ether supernatant was discarded, and the peptide precipitate was further washed twice with cold ether. The precipitate was dissolved in a suitable aqueous buffer and then lyophilised.

#### **5.1.3.6 Cyclisation in solution**

The cleaved peptide (approximately 0.05 mmol) was dissolved in 10 mL of 50% MeCN in water, and the pH was adjusted to 8 - 9 by dropwise addition of NaOH (0.1 M) and HCl (0.1 M). The mixture was stirred overnight, and the completion of the reaction was monitored with LC-MS. Subsequently, the peptide solution was lyophilised and purified by HPLC if needed.

#### **5.1.3.7 Cyclisation on resin**

The *N*-terminal chloro-acetylated resins were first washed with a DIPEA solution (10 mL, 1% (v/v) in DMF), followed by the addition of a 1,8-Diazabicyclo [5.4.0] undec-7-ene (DBU) solution (10 mL, 1% (v/v) in DCM). The reaction was agitated at room temperature for 30 min. Completion of the reaction was monitored through mini-cleavage and LC-MS analysis. Upon completion, the resins were washed with DMF (3 × 5 mL) and then DCM (3 × 5 mL) and were either directly used in the cleavage step or stored at -20 °C.

#### **5.1.3.8 Deprotection of iVDde protecting group**

Peptide-bound resins were treated with a freshly prepared solution of hydrazine monohydrate (5% v/v DMF, 2 mL) for 5 × 20 min at room temperature with shaking. Deprotection efficiency was monitored by performing a mini-cleavage followed by LC-MS analysis and the reaction was repeated if necessary. Upon completion, the resins were washed with DMF (3 × 5 mL) and then DCM (3 × 5 mL).

#### 5.1.3.9 Deprotection of Cysteine Mmt protecting group

The peptide-loaded resins were treated with a freshly prepared Mmt cleavage solution (TFA: TIPS: DCM, 5:5:90 v/v/v, 2 mL) for 25 times at room temperature with vigorous agitation for 2 min each. Successful removal of the Mmt group was indicated by the complete loss of the intense yellow colour (originating from the cleaved methoxytrityl group) in the used cleavage solution. After completion, the resins were washed with DMF ( $3 \times 5$  mL) and DCM ( $3 \times 5$  mL).

#### 5.1.3.10 Deprotection of Alloc and Allyl protecting groups and cyclisation

The allyl ester and allyl carbamate on the resin-bound peptide were removed with the addition of a solution of  $\text{Pd(PPh}_3)_4$  (0.1 eq.) and N,N-dimethylbarbituric acid (4 eq.) in DCM followed by gentle shaking at room temperature for 2 h. The deprotection was repeated overnight to ensure complete removal. Cyclization *via* the amide bond was carried out on the resin with the addition of a solution of PyBOP (2 eq.), HOBt (2 eq.) and N-Methylmorpholine (2.4 eq.) in DMF for 5 h twice. Upon completion, the resins were washed with DMF ( $3 \times 5$  mL) and DCM ( $3 \times 5$  mL).

#### 5.1.3.11 Manual peptide synthesis

For amino acids Fmoc-Ser(propargyl)-OH and Boc-Lys(Fmoc)-OH, manual coupling was performed in a fritted syringe. The Fmoc group was deprotected using 20% piperidine in DMF and agitated for 10 min. The resin was then washed with DMF ( $3 \times 5$  mL) and DCM ( $3 \times 5$  mL). The deprotection step was repeated to ensure complete deprotection. For the resulting resins with free N-terminus, a solution of Fmoc-protected amino acid (3 eq.), HATU (3 eq.) and DIPEA (6 eq.) in DMF were added to the tube and the tube was agitated for 30 min. The coupling efficiency was checked with the Ninhydrin test, and repeated if incomplete coupling was indicated. Excess reagents were drained, and the resin was washed with DMF ( $3 \times 5$  mL) and DCM ( $3 \times 5$  mL).

#### 5.1.3.12 Ninhydrin test

The Ninhydrin test was employed to qualitatively determine the presence of primary amines on resin-bound peptides. Three reagents were prepared as follows: Reagent A: 6.6 mg of KCN was dissolved in 10 mL of distilled water, and 1 mL of the prepared KCN solution was

dissolved in 49 mL of pyridine. Reagent B: 1.0 g of ninhydrin was dissolved in 20 mL of n-butanol. Reagent C: 40 g of phenol was dissolved in 20 mL of n-butanol.

To perform the test, 10-15 resin beads were transferred to a test tube. Three drops of each reagent (A, B, and C) were added to the tube with the resin, as well as to an empty reference tube. The tubes were heated to 95 °C for 5 min. If the beads remained colourless, no primary amine was detected. If the beads were colourless but the solution turned dark blue, a small amount of primary amine was present. If the beads turned blue and the solution became light to intense blue, almost all primary amine was present on the resin, indicating a failed coupling.

## **5.2 Photoswitching properties characterisation**

### **5.2.1 Instrumentation**

UV-Vis spectra were acquired using an Agilent Cary 60 UV-Vis spectrometer (wavelength range: 190 – 1100 nm, resolution: 1.5 nm, Light source: Xenon Flash Lamp 80 Hz) equipped with a temperature controller. Polystyrene semi-micro cuvettes (1.5 mL, 1 cm) sealed with parafilm were used in the measurement. Data analysis was conducted using WinUV software. LC-MS spectra were obtained on a Waters HPLC system with ESI mass spectrometer as previously described. Compounds were separated employing the eq20 gradient. For compound irradiation, custom-made boxes (by Dr. Charlie Saunders, WaveyTech Ltd) installed with 25 mW LED light bulbs with wavelengths of 365 nm, 405 nm, and 457 nm were used.

### **5.2.2 LC-MS method for PSS determination**

A solution of the compound in the LC-MS solvent was prepared. The sample was irradiated at the specified wavelength for a designated period. LC-MS chromatograms of the sample following irradiation were recorded with minimised exposure to ambient light. Compound isomer peaks were identified based on mass spectra and integrated to determine the PSS ratio at that specific wavelength.

### **5.2.3 UV-Vis spectroscopy determination of the PSS of linker 4**

The photostationary state ratios at 365 nm and 457 nm were calculated using Fischer's method.<sup>165</sup> This calculation was based on the assumption that the ratio of quantum yields of the two isomers ( $\Phi_E/\Phi_Z$ ) does not differ at the two selected wavelengths.

$$a_2 = \left( \frac{\Delta_1}{D_{E1}} - \frac{\Delta_2}{D_{E2}} \right) / \left[ 1 + \frac{\Delta_1}{D_{E1}} - n \left( 1 + \frac{\Delta_2}{D_{E2}} \right) \right]$$

$$a_1 = n a_2, n = \frac{D_{obsd\ 1\lambda_{max}} - D_{E\lambda_{max}}}{D_{obsd\ 2\lambda_{max}} - D_{E\lambda_{max}}}$$

$$\Delta = D_{obsd} - D_E$$

Where  $a_1$  and  $a_2$  are the PSS ratios of the less stable *Z* isomer at wavelength 1 and 2.  $D_{obsd}$  is the observed absorbance,  $D_E$  is the absorbance of a solution containing only the more stable *trans* (*E*) isomer. Here, the ‘non-irradiated’ spectrum of linker **4** solution prepared freshly from a DMSO stock stored protected from light was assumed to contain only *trans* (*E*) isomer and used in the calculation.  $\lambda_{max}$  is the wavelength where the maximal absorption difference is found for the *trans* (*E*) isomer and *cis* (*Z*) isomer, which is at 341 nm.

For linker **4**,  $\lambda_{max}$  was 341 nm.

To calculate PSS of linker **4** at 365 nm irradiation, for wavelength 1 (340 nm) and wavelength 2 (365 nm),

$$n = \frac{D_{obsd\ 1\lambda_{max}} - D_{E\lambda_{max}}}{D_{obsd\ 2\lambda_{max}} - D_{E\lambda_{max}}} = \frac{0.00994 - 0.10608}{0.00983 - 0.10608} = 0.9989$$

$$\frac{\Delta_1}{D_{E1}} = \frac{D_{obsd\ 1} - D_{E1}}{D_{E1}} = \frac{0.01083 - 0.10685}{0.10685} = -0.8986$$

$$\frac{\Delta_2}{D_{E2}} = \frac{D_{obsd\ 2} - D_{E2}}{D_{E2}} = \frac{0.00323 - 0.06033}{0.06033} = -0.9465$$

$$a_2 = 0.999 \quad a_1 = n a_2 = 0.998$$

Therefore, at 365 nm PSS there is 99% *Z*-**4** in the solution.

To calculate PSS of linker **4** at 457 nm irradiation, for wavelength 1 (450 nm) and wavelength 2 (457 nm),

$$n = \frac{D_{obsd\ 1\lambda_{max}} - D_{E\lambda_{max}}}{D_{obsd\ 2\lambda_{max}} - D_{E\lambda_{max}}} = \frac{0.10683 - 0.11293}{0.10061 - 0.11293} = 0.495$$

$$\frac{\Delta_1}{D_{E1}} = \frac{D_{obsd\ 1} - D_{E1}}{D_{E1}} = \frac{0.01087 - 0.01053}{0.01053} = 0.0323$$

$$\frac{\Delta_2}{D_{E2}} = \frac{D_{obsd\ 2} - D_{E2}}{D_{E2}} = \frac{0.00788 - 0.00893}{0.00893} = -0.1177$$

$$a_2 = 0.251 \quad a_1 = na_2 = 0.124$$

Therefore, at 457 nm PSS there are 25% *Z*-4 and 75% *E*-4 in the solution.

#### 5.2.4 NMR spectroscopy determination of PSS of linker 4

<sup>1</sup>H NMR spectra (400 MHz, DMSO-*d*<sub>6</sub>) were recorded for compound 4, following irradiation with 457 nm or 365 nm LED light for the indicated time. The irradiation protocol involved 457 nm for 5 minutes, followed by another 5 minutes of 457 nm, then 365 nm irradiation for 3 minutes, succeeded by 5 minutes of 365 nm, followed by two further cycles of 10 minutes each. To minimise light exposure, the samples were handled under foil protection. Peaks corresponding to the methyl groups on *E/Z* isomers were integrated.

#### 5.2.5 UV-Visible spectroscopy determination of thermal half-life

A solution containing 12 μM **AP-PROTAC-2** in 0.1% DMSO in water was irradiated with 365 nm LED light for 3 min. Following irradiation, the solution was incubated at 37 °C in a UV-Vis spectrophotometer temperature control chamber for 24 h. UV-Vis spectra were recorded every 30 min during the incubation. It was assumed that the compound achieved the same conversion ratio with irradiation as observed in the LC-MS experiment (80% *E* with 457 nm and 90% *Z* with 365 nm irradiation).

The percentage of *Z* isomer was plotted against time (Figure 2-7E), and an exponential trendline was fitted to the data:

$$[Z] = [Z]_0 e^{-kt}, \quad y = 0.847e^{-6.08 \times 10^{-6}x} \quad (R^2 = 0.9707)$$

From the rate constant *k*, the thermal half-life of the *Z* isomer was calculated as follows:

$$t_{1/2} = \frac{\ln 2}{k} = 31.7 \text{ h}$$

## 5.3 Bioconjugation<sup>f</sup>

### 5.3.1 Conjugation methods for peptide-based PROTACs

#### HER2-15 (DAR 4)

Trastuzumab (12 mg, 7.5 mg/mL) in PBS was reduced with TCEP (50 mM in water, 4.3 eq.). The mixture was incubated at 22 °C for 1.5 h. Following that, **QZ-015** (10 mM in DMA, 20 eq.) was added and incubated at 22 °C for 1.0 h. The crude conjugate was subjected to analysis with HIC-HPLC for DAR determination and SEC-HPLC for monomeric content. The final conjugate underwent buffer exchange (30 kDa MWCO, Sartorius vivaspin) into Formulation Buffer (30 mM Histidine, 175 mM Sucrose, 0.02% PS20, pH 6.0), and filtered (Millex-GV 0.22 µm).

#### EGFR-21 (DAR 4 and DAR 8)

Cetuximab (10 mg, 2.0 mg/mL) in PBS was reduced with TCEP (10 mM in diH<sub>2</sub>O, 3.5 eq. for DAR 4 and 8 eq. for DAR 8). The mixture was incubated at 22 °C for 1.5 h. Following that, **QZ-021** (10 mM in DMA, 8 eq. for DAR 4 and 12 eq. for DAR 8) was added and incubated at 22 °C for 1.0 h. The crude conjugate was analysed with HIC-HPLC for DAR determination and SEC-HPLC for monomeric content. The final conjugate underwent buffer exchange (30 kDa MWCO, Sartorius vivaspin) into Formulation Buffer (30 mM Histidine, 175 mM Sucrose, 0.02% PS20, pH 6.0), and filtered (Millex-GV 0.22 µm).

#### B12-21 (DAR 4 and DAR 8)

B12 (10 mg, 2.2 mg/mL) in PBS was reduced with TCEP (10 mM in diH<sub>2</sub>O, 3 eq. for DAR 4 and 5 eq. for DAR 8). The mixture was incubated at 22 °C for 1.5 h. Following that, **QZ-021** (10 mM in DMA, 8 eq. for DAR 4 and 12 eq. for DAR 8) was added and incubated at 22 °C for 1.0 h. The crude conjugate was analysed with HIC-HPLC for DAR determination and SEC-HPLC for monomeric content. The final conjugate underwent buffer exchange (30 kDa

---

<sup>f</sup> Bioconjugation was conducted by Dr Alina Chrzastek *et al.*, ADC Therapeutics, Translation & Innovation Hub Building Imperial College White City Campus, 84 Wood Lane, London, W12 0BZ.

MWCO, Sartorius vivaspin) into Formulation Buffer (30 mM Histidine, 175 mM Sucrose, 0.02% PS20, pH 6.0), and filtered (Millex-GV 0.22 µm).

### 5.3.2 Determination of new molecular weight (MW) of the ADC:

MW of ADC = MW of mAb + (DAR x MW of payload)

EC280 of ADC = EC280 of mAb + (DAR x EC280 of payload)

	MW (Da)	EC280 (M <sup>-1</sup> cm <sup>-1</sup> )
Cetuximab	145423.2	217440
B12	148052.3	220420
Trastuzumab	145531.5	215380
QZ-015	2079.52	1210
QZ021	4611.52	2669

### 5.3.3 HIC and SEC analysis

#### Hydrophobic Interaction Chromatography (HIC)

Column	TSKgel Butyl-NPR (2.5 µm, 4.6 mm x 3.5 mm)
Mobile Phase	A: 50 mM NaPi, pH 7, 1.5 M AS B: 50 mM NaPi, pH 7, 20% IPA
Gradient	0%-100% B over 15 min
Flow rate	1.2 mL/min
Detection	UC (DAD): 214 nm, 230 nm, 254 nm, 330 nm
Column Oven	30 °C
Autosampler	10 °C
Injection volume	20 µL/ 4 µg

HIC Methods:

Time (min)	0.0	2.0	12.0	12.0	14.0	14.0
%A	100	100	0	0	0	100
%B	0	0	100	100	100	0

#### Size-exclusion chromatography (SEC)

Method name	SEC Method (10 min isocratic)
Column	Acquity BEH SEC 200A (1.7 µm 4.6x150 mm)
Mobile Phase	A: 0.2 M Potassium Phosphate, pH 6.8, (15% IPA, 0.2 M KCl)
Gradient	100% A over 10 min
Flow rate	0.35 mL/min
Detection	UC (DAD): 214 nm, 230 nm, 254 nm, 330 nm
Column Oven	30 °C
Autosampler	10 °C
Injection volume	1 µL/ 1 µg



SEC methods:

Time (min)	0.0	10.0
%A	100	0
%B	0	100

## 5.4 Biology

### 5.4.1 Cell culture and treatment

Cells were obtained from the Francis Crick Institute cell bank. MDA-MB-231 and MCF-7 cells were cultured in low glucose Dulbecco's Modified Eagle's Medium (DMEM, Sigma, D6046) supplemented with 10% (v/v) fetal bovine serum (FBS, Gibco). T47D cells were cultured in RPMI 1640 Medium (Gibco, 11875-093) supplemented with 10% FBS. HEK293, BT-474 and Panc-1 cells were cultured in high glucose DMEM (Gibco, 61965-026) supplemented with 10% FBS. All cells were grown in a humidified incubator at 37 °C, with 5% CO<sub>2</sub>. The cells were seeded at a density of  $3 \times 10^5$  cells per well in a 6-well plate and allowed to adhere for 24 h. Subsequently, the cells were treated with the specified compounds and duration. Stocks were prepared in DMSO with dry compound and peptide, based on their dry weight, and then diluted to the desired concentration using the cell growth medium. For light-responsive compounds, the cell plates were irradiated for 1 minute using either 365 nm or 457 nm LED light.

### 5.4.2 Cell lysis

Following cell treatment, cells were washed twice with PBS, and then the respective cold lysis buffer was added. The cell suspensions were collected into eppendorf tubes and lysed on ice for 30 min. The collected suspensions were then centrifuged for 10 min at 17,000 g, 4 °C, after which the supernatant was collected. Protein concentration was determined using the DC<sup>TM</sup> Protein assay kit (BIO-RAD) with a bovine serum albumin standard curve in lysis buffer and the sample concentration was normalised. The lysates were used in the subsequent steps, such as immunoblotting, proteomics sample preparation, or stored at −80 °C.

MDA-MB-231 cells were lysed with PBS lysis buffer (1% Triton-X, 0.1% SDS, 1xPBS in Milli-Q purified water, pH 7.4) with freshly added protease inhibitor (cOmplete, EDTA-

free). HEK293, BT-474, MCF-7, T47D and Panc-1 cells were lysed using RIPA buffer (Sigma, R0278) supplemented with protease inhibitor.

### **5.4.3 Immunoblotting**

Lysates containing an equal amount of proteins (10 µg- 20 µg) were mixed at a ratio of 3:1 with 4x Laemmli protein sample buffer (supplemented with 10% 2-mercaptoethanol, BIO-RAD) and denatured at 95 °C for 10 min. Samples were resolved using Mini-PROTEAN® TGX™ Precast 7.5% gels (50 min, 160 V) and then wet transferred onto a nitrocellulose membrane. The membrane was blocked for 1 h at room temperature with 5% skimmed milk in Tris-buffered saline with 0.1 % Tween-20 (TBS-T). Primary antibodies were diluted in 5% milk in TBS-T and incubated with the membrane at 4 °C overnight. The membrane was washed with TBS-T (3 × 10 min), cut and incubated with appropriate IgG H&L HRP-conjugated secondary antibodies for 1 h at RT. The membrane was washed with TBST (3 × 10 min), and the bands were detected by chemiluminescence using the western HRP substrate (Merck Immobilon Crescendo). The images were captured using ImageQuant Las 4000 and processed with ImageJ software. Primary antibodies used (1:1000 dilution): BRD4 (Cell Signalling Technology #13440), FAK (Cell Signalling Technology #3285), TBK1 (Cell Signalling Technology #3504), AURORA-A (Cell Signalling Technology #4718), GAK (Invitrogen #PA5-99201), ERα (Cell Signalling Technology #8644), CREPT/RPRD1B (Cell Signalling Technology #74693), EGFR (Cell Signalling Technology #4267), HER2 (Cell Signalling Technology #4290), β-actin (SIGMA-ALDRICH, A1978, 1:2500), GAPDH (Abcam, ab9485, 1:2500). Secondary antibodies used (1:10,000 dilution): Goat-α-mouse IgG (H+L) HRP conjugate (R-05071-500), Goat-α-rabbit IgG (H+L) HRP conjugate (R-05072-500). Blots were quantified with ImageJ and plotted with GraphPad Prism 9.

### **5.4.4 In-cell western**

The in-cell western assay was conducted using the CellTag 520 Stain ICW Kits following the manufacturer's instructions. Cells were cultured in a 96-well plate (96-well ICW, 926-19156, LI-COR) and treated with media-containing compounds. After cell treatment, cells were fixed directly without washing using a 3.7% formaldehyde solution for 20 min at room temperature without agitation, followed by permeabilization with 0.1% Triton X-100 solution for 20 min with gentle agitation. Subsequently, cells were blocked using the Intercept (TBS) Blocking

Buffer provided in the kit for 1.5 h with gentle agitation. Cells were incubated with antibody dilutions in the blocking buffer at 4 °C overnight (AURORA-A, Cell Signalling Technology #4718, rabbit, 1:100;  $\beta$ -actin, SIGMA-ALDRICH, A1978, mouse, 1:200). The following day, the cells were washed with 0.1% Tween 20 in TBS for 5 min, repeated for four times. Fluorescent labelled secondary antibodies and cell stain were diluted in Intercept T20 Antibody Diluent and incubated with the cells for 1 h at room temperature with gentle agitation (IRDye 800CW Goat anti-Rabbit Secondary Antibody, IRDye 680RD Goat anti-Mouse Secondary Antibody, 1:800; CellTag 520, 1:500). After careful removal of liquid from the wells, cells were washed four times. The plate was imaged using 520 nm, 700 nm and 800 nm channels on the Odyssey M Imaging System.

#### **5.4.5 Cell toxicity assay**

MDA-MB-231 cells were seeded in a 96-well plate (7000 cells/well) and grown in low glucose DMEM with 10% FBS overnight. The following day, the media was replaced with media containing the compound and SYTOX™ Green Nucleic Acid Stain (dye, 250 nM final concentration). For control, cells were treated with media containing 0.1% DMSO without dye, 0.1% DMSO with dye, 2  $\mu$ g/mL puromycin and dye, and 2  $\mu$ g/mL puromycin in 0.1% DMSO with dye. The cell plate was incubated at 37 °C with 5% CO<sub>2</sub> in the incubator. Phase and green fluorescence were imaged every 2 h over 3 days using the Incucyte Live-Cell Analysis Systems.

### **5.5 Proteomics**

#### **5.5.1 Sample preparation**

Lysates of treated cells (100  $\mu$ g, 100  $\mu$ L) were reduced and alkylated by the addition of TCEP (to a final concentration of 5 mM) and chloroacetamide (CAA, to a final concentration of 15 mM) for 45 min at room temperature under vigorous shaking. Proteins were precipitated by adding 2 sample volumes of methanol, 0.5 volume of chloroform and 1 volume of purified water. The mixture was vortexed and centrifuged at 6,000 rpm for 2 min resulting in pellets of precipitated proteins. Pellets were washed with 3 sample volumes of methanol by vortexing and sonicating, then centrifuged at 8,000 rpm for 4 min. The supernatant was discarded, and the washing procedure was repeated an additional four times. The protein precipitate was air-dried for 5 min and redissolved in 100  $\mu$ L of 50 mM HEPES pH 8.0 using sonication and vortexing. The protein solution was digested with

trypsin protease (0.4 µg, 1:250 to protein, Pierce™ 90057) and incubated overnight in a thermoshaker with 800 rpm shaking at 37 °C. Trypsin digestion was quenched with the addition of 0.5% TFA. A peptide quantification assay (Pierce Fluorometric Peptide Assay) was performed. The same volume of peptide digest from each condition was aliquoted and dried with a SpeedVac Vacuum concentrator. The dried peptide samples were labelled with tandem mass tags (TMT10plex ref 90110, Thermo Scientific) for 2 h at room temperature. The TMT labelling reaction was quenched with the addition of 5% hydroxylamine and the samples were vortexed for 5 min and centrifuged at 8,000 rpm for 4 min at room temperature. An equal volume of supernatant from each condition was combined into a single Eppendorf. The combined peptides were fractionated (Pierce high pH Reversed-Phase Peptide Fractionation kit) into 8 fractions and dried with a SpeedVac Vacuum concentrator. The dried fractions were resuspended in 2% MeCN and 0.5% trifluoroacetic acid in water to achieve a concentration of approximately 1 µg/µL.

### **5.5.2 LC-MS/MS and data analysis**

Prepared peptide sample fractions were run using a Thermo Fisher Q-Exactive LC-MS/MS equipped with a Thermo EASY-SPRAY column (500 mm x 75 µm inner diameter, 2 µm particle size) as previously described.<sup>190,262</sup> The data obtained were processed using MaxQuant version 1.6.17.0, where peptides from the MS/MS spectra were searched in the human proteome database (UniProt accessed January 2021) for identification. Further analysis of the data was performed using Perseus 1.6.15.0, Microsoft Office Excel 365, and GraphPad Prism 9. A minimum of 2 unique peptides were selected for protein identification. The mass spectrometry proteomics data has been deposited in the ProteomeXchange Consortium via the PRIDE<sup>263</sup> partner repository with the dataset identifier PXD036224.

## 5.6 Computational modelling of PROTAC ternary complex<sup>g</sup>

The computational modelling of the PROTAC ternary complex was described in detail by Ignatov *et al.*<sup>191</sup> In brief, the structural modelling approach partitions the PROTAC-complex sampling problem into several steps. The process begins with a template-based protein-small-molecule docking protocol ClusPro LigTBM, which orients the half-PROTAC ligands with the corresponding proteins.<sup>264,265</sup> The PROTAC molecule is bisected in the middle atom of the linker, and conformers of the PROTAC halves were generated by the ETKDG method and relaxed with MMFF.<sup>266,267</sup> The resulting half-PROTACs are aligned to the respective protein-ligand complex models and filtered for clashes. The middle atom positions of the remaining conformations were then projected to grids. Next, to find energetically favourable protein-protein complex poses, the FFT-based docking program PIPER was used with an additional ‘silent’ term.<sup>192,193,268</sup> This term convolves the grids and ensures that the middle atoms on both sides overlap during the docking. Consequently, this term partially accounts for PROTAC accessible conformations and helps efficiently filter out unfeasible protein-protein complex poses. Structures in which the half-PROTACs can be successfully joined to form a complete PROTAC are relaxed by Amber energy minimisation and clustered to generate complete ternary PROTAC complex models.<sup>194</sup>

---

<sup>g</sup> Computational modelling was conducted in collaboration with Sergei Kotelnikov, Mikhail Ignatov, and Dima Kozakov from the Department of Applied Mathematics and Statistics and Laufer Center for Physical and Quantitative Biology, Stony Brook University, Stony Brook, NY, USA.

## Chapter 6 Bibliography

1. M. Maneiro, E. De Vita, D. Conole, et al. PROTACs, molecular glues and bifunctionals from bench to bedside: Unlocking the clinical potential of catalytic drugs. *Prog Med Chem* **2021**, 60, 67–190.
2. F.M. Ferguson, N.S. Gray. Kinase inhibitors: The road ahead. *Nat Rev Drug Discov* **2018**, 17 (5), 353–376.
3. A.L. Nelson, E. Dhimolea, J.M. Reichert. Development trends for human monoclonal antibody therapeutics. *Nat Rev Drug Discov* **2010**, 9 (10), 767–774.
4. I. Churcher. Protac-Induced Protein Degradation in Drug Discovery: Breaking the Rules or Just Making New Ones? *J Med Chem* **2018**, 61 (2), 444–452.
5. C. V. Dang, E.P. Reddy, K.M. Shokat, L. Soucek. Drugging the “undruggable” cancer targets. *Nat Rev Cancer* **2017**, 17 (8), 502–508.
6. R.M. Lu, Y.C. Hwang, I.J. Liu, et al. Development of therapeutic antibodies for the treatment of diseases. *J Biomed Sci* **2020**, 27 (1), 1–30.
7. P.P. Chamberlain, L.G. Hamann. Development of targeted protein degradation therapeutics. *Nat Chem Biol* **2019**, 15 (10), 937–944.
8. Cecile M. Pickart. Back to the Future with Ubiquitin. *Cell* **2004**, 116, 181–190.
9. I. Dikic. Proteasomal and Autophagic Degradation Systems. *Annu Rev Biochem* **2017**, 86, 193–224.
10. A.L. Schwartz, A. Ciechanover. Targeting Proteins for Destruction by the Ubiquitin System: Implications for Human Pathobiology. *Annu Rev Pharmacol Toxicol* **2008**, 49, 73–96.
11. M.J. Clague, S. Urbé, D. Komander. Breaking the chains: deubiquitylating enzyme specificity begets function. *Nat Rev Mol Cell Biol* **2019**, 20 (6), 338–352.

12. G. Nalepa, M. Rolfe, J.W. Harper. Drug discovery in the ubiquitin - Proteasome system. *Nat Rev Drug Discov* **2006**, 5 (7), 596–613.
13. O. Kerscher, R. Felberbaum, M. Hochstrasser. Modification of Proteins by Ubiquitin and Ubiquitin-Like Proteins. *Annu Rev Cell Dev Biol* **2006**, 22 (1), 159–180.
14. X. Huang, V.M. Dixit. Drugging the undruggables: Exploring the ubiquitin system for drug development. *Cell Res* **2016**, 26 (4), 484–498.
15. J.H. Kenten, S.F. Roberts. CONTROLLING PROTEIN LEVELS IN EUCARYOTIC ORGANISMS. *U.S. Patent 6,306,663*. 1999.
16. K.M. Sakamoto, K.B. Kim, A. Kumagai, et al. Protacs: Chimeric molecules that target proteins to the Skp1-Cullin-F box complex for ubiquitination and degradation. *Proc Natl Acad Sci U S A* **2001**, 98 (15), 8554–8559.
17. K.M. Sakamoto, K.B. Kim, R. Verma, et al. Development of Protacs to target cancer-promoting proteins for ubiquitination and degradation. *Mol Cell Proteomics* **2003**, 2 (12), 1350–1358.
18. J.S. Schneekloth, F.N. Fonseca, M. Koldobskiy, et al. Chemical Genetic Control of Protein Levels: Selective in Vivo Targeted Degradation. *J Am Chem Soc* **2004**, 126 (12), 3748–3754.
19. E. Metzen, P.J. Ratcliffe. HIF hydroxylation and cellular oxygen sensing. *Biol Chem* **2004**, 385, 223–230.
20. A.R. Schneekloth, M. Pucheault, H.S. Tae, C.M. Crews. Targeted intracellular protein degradation induced by a small molecule: En route to chemical proteomics. *Bioorg Med Chem Lett* **2008**, 18 (22), 5904–5908.
21. L.T. Vassilev, B.T. Vu, B. Graves, et al. In Vivo Activation of the p53 Pathway by Small-Molecule Antagonists of MDM2. *Science (1979)* **2004**, 303 (5659), 844–848.
22. Y. Itoh, M. Ishikawa, M. Naito, Y. Hashimoto. Protein knockdown using methyl bestatin-ligand hybrid molecules: Design and synthesis of inducers of ubiquitination-mediated degradation of cellular retinoic acid-binding proteins. *J Am Chem Soc* **2010**, 132 (16), 5820–5826.

23. K. Okuhira, N. Ohoka, K. Sai, et al. Specific degradation of CRABP-II via cIAP1-mediated ubiquitylation induced by hybrid molecules that crosslink cIAP1 and the target protein. *FEBS Lett* **2011**, 585 (8), 1147–1152.
24. K. Sekine, K. Takubo, R. Kikuchi, et al. Small molecules destabilize cIAP1 by activating auto-ubiquitylation. *Journal of Biological Chemistry* **2008**, 283 (14), 8961–8968.
25. Y. Itoh, M. Ishikawa, R. Kitaguchi, et al. Double protein knockdown of cIAP1 and CRABP-II using a hybrid molecule consisting of ATRA and IAPs antagonist. *Bioorg Med Chem Lett* **2012**, 22 (13), 4453–4457.
26. K. Okuhira, Y. Demizu, T. Hattori, et al. Development of hybrid small molecules that induce degradation of estrogen receptor-alpha and necrotic cell death in breast cancer cells. *Cancer Sci* **2013**, 104 (11), 1492–1498.
27. N. Shibata, K. Nagai, Y. Morita, et al. Development of Protein Degradation Inducers of Androgen Receptor by Conjugation of Androgen Receptor Ligands and Inhibitor of Apoptosis Protein Ligands. *J Med Chem* **2018**, 61 (2), 543–575.
28. N. Ohoka, K. Okuhira, M. Ito, et al. In Vivo Knockdown of Pathogenic Proteins via Specific and Nongenetic Inhibitor of Apoptosis Protein (IAP)-dependent Protein Erasers (SNIPERs). *Journal of Biological Chemistry* **2017**, 292 (11), 4556–4570.
29. T. Ito, H. Ando, T. Suzuki, et al. Identification of a primary target of thalidomide teratogenicity. *Science (1979)* **2010**, 327 (5971), 1345–1350.
30. A. Lopez-Girona, D. Mendy, T. Ito, et al. Cereblon is a direct protein target for immunomodulatory and antiproliferative activities of lenalidomide and pomalidomide. *Leukemia* **2012**, 26 (11), 2326–2335.
31. J. Lu, Y. Qian, M. Altieri, et al. Hijacking the E3 Ubiquitin Ligase Cereblon to Efficiently Target BRD4. *Chem Biol* **2015**, 22 (6), 755–763.
32. G.E. Winter, D.L. Buckley, J. Paulk, et al. Phthalimide conjugation as a strategy for in vivo target protein degradation. *Science (1979)* **2015**, 348 (6241), 1376–1381.
33. S. Gao, S. Wang, Y. Song. Novel immunomodulatory drugs and neo-substrates. *Biomark Res* **2020**, 8 (2), 1–8.



34. M. Zengerle, K.H. Chan, A. Ciulli. Selective Small Molecule Induced Degradation of the BET Bromodomain Protein BRD4. *ACS Chem Biol* **2015**, 10 (8), 1770–1777.
35. D.P. Bondeson, A. Mares, I.E. D Smith, et al. Catalytic in vivo protein knockdown by small-molecule PROTACs. *Nat Chem Biol* **2015**, 11 (8), 611–617.
36. C.S. Kounde, E.W. Tate. Photoactive Bifunctional Degraders: Precision Tools to Regulate Protein Stability. *J Med Chem* **2020**, 63 (24), 15483–15493.
37. T.H. Pillow, P. Adhikari, R.A. Blake, et al. Antibody Conjugation of a Chimeric BET Degradator Enables in vivo Activity. *ChemMedChem* **2020**, 15 (1), 17–25.
38. M. Maneiro, N. Forte, M.M. Shchepinova, et al. Antibody-PROTAC conjugates enable HER2–dependent targeted protein degradation of BRD4. *ACS Chem Biol* **2020**, 15 (6), 1306–1312.
39. L. Zhao, J. Zhao, K. Zhong, A. Tong, D. Jia. Targeted protein degradation: mechanisms, strategies and application. *Signal Transduct Target Ther* **2022**, 7 (113), 1–13.
40. S.M. Banik, K. Pedram, S. Wisnovsky, et al. Lysosome-targeting chimaeras for degradation of extracellular proteins. *Nature* **2020**, 584 (7820), 291–297.
41. Y. Miao, Q. Gao, M. Mao, et al. Bispecific Aptamer Chimeras Enable Targeted Protein Degradation on Cell Membranes. *Angewandte Chemie - International Edition* **2021**, 60 (20), 11267–11271.
42. A.D. Cotton, D.P. Nguyen, J.A. Gramespacher, I.B. Seiple, J.A. Wells. Development of Antibody-Based PROTACs for the Degradation of the Cell-Surface Immune Checkpoint Protein PD-L1. *J Am Chem Soc* **2021**, 143 (2), 593–598.
43. H. Zhang, Y. Han, Y. Yang, et al. Covalently Engineered Nanobody Chimeras for Targeted Membrane Protein Degradation. *J. Am. Chem. Soc* **2021**, 143, 16377–16382.
44. D. Takahashi, J. Moriyama, T. Nakamura, et al. AUTACs: Cargo-Specific Degradators Using Selective Autophagy. *Mol Cell* **2019**, 76 (5), 797-810.e10.
45. Y. Fu, N. Chen, Z. Wang, et al. Degradation of lipid droplets by chimeric autophagy-tethering compounds. *Cell Res* **2021**, 31 (9), 965–979.

46. C. Hoon Ji, H. Yeon Kim, M. Ju Lee, et al. The AUTOTAC chemical biology platform for targeted protein degradation via the autophagy-lysosome system. *Nat Commun* **2022**, 13 (904), 1–14.
47. C. Bashore, S. Prakash, M.C. Johnson, et al. Targeted degradation via direct 26S proteasome recruitment. *Nat Chem Biol* **2023**, 19 (1), 55–63.
48. M. Pettersson, C.M. Crews. PROteolysis TArgeting Chimeras (PROTACs) — Past, present and future. *Drug Discov Today Technol* **2019**, 31, 15–27.
49. S. An, L. Fu. Small-molecule PROTACs: An emerging and promising approach for the development of targeted therapy drugs. *EBioMedicine* **2018**, 36, 553–562.
50. M. He, C. Cao, Z. Ni, et al. PROTACs: great opportunities for academia and industry (an update from 2020 to 2021). *Signal Transduct Target Ther* **2022**, 7 (181), 1–64.
51. J. Salami, C.M. Crews. Waste disposal - An attractive strategy for cancer therapy. *Science (1979)* **2017**, 355 (6330), 1163–1167.
52. K. Moreau, M. Coen, A.X. Zhang, et al. Proteolysis-targeting chimeras in drug development: A safety perspective. *Br J Pharmacol* **2020**, 177 (8), 1709–1718.
53. B. Sun, W. Fiskus, Y. Qian, et al. BET protein proteolysis targeting chimera (PROTAC) exerts potent lethal activity against mantle cell lymphoma cells. *Leukemia* **2018**, 32, 343–352.
54. C.M. Olson, B. Jiang, M.A. Erb, et al. Pharmacological perturbation of CDK9 using selective CDK9 inhibition or degradation. *Nat Chem Biol* **2018**, 14 (2), 163–170.
55. G.M. Burslem, B.E. Smith, A.C. Lai, et al. The Advantages of Targeted Protein Degradation Over Inhibition: An RTK Case Study. *Cell Chem Biol* **2018**, 25, 67–77.
56. K. Raina, J. Lu, Y. Qian, et al. PROTAC-induced BET protein degradation as a therapy for castration-resistant prostate cancer. *Proc Natl Acad Sci U S A* **2016**, 113 (26), 7124–7129.

57. B. Zhou, J. Hu, F. Xu, et al. Discovery of a Small-Molecule Degradator of Bromodomain and Extra-Terminal (BET) Proteins with Picomolar Cellular Potencies and Capable of Achieving Tumor Regression. *J Med Chem* **2018**, 61 (2), 462–481.
58. L. Bai, H. Zhou, R. Xu, et al. A Potent and Selective Small-Molecule Degradator of STAT3 Achieves Complete Tumor Regression In Vivo. *Cancer Cell* **2019**, 36, 498–511.
59. A. Mares, A.H. Miah, I.E.D. Smith, et al. Extended pharmacodynamic responses observed upon PROTAC-mediated degradation of RIPK2. *Commun Biol* **2020**, 3 (140), 1–13.
60. X. Sun, J. Wang, X. Yao, et al. A chemical approach for global protein knockdown from mice to non-human primates. *Cell Discov* **2019**, 5 (10), 1–13.
61. K.-H. Chan, M. Zengerle, A. Testa, A. Ciulli. Impact of Target Warhead and Linkage Vector on Inducing Protein Degradation: Comparison of Bromodomain and Extra-Terminal (BET) Degradators Derived from Triazolodiazepine (JQ1) and Tetrahydroquinoline (I-BET726) BET Inhibitor Scaffolds. *J. Med. Chem.* **2018**, 61, 504–513.
62. D.P. Bondeson, B.E. Smith, G.M. Burslem, et al. Lessons in PROTAC Design from Selective Degradation with a Promiscuous Warhead. *Cell Chem Biol* **2018**, 25, 78–87.
63. S.L. Fisher, A.J. Phillips. Targeted protein degradation and the enzymology of degraders. *Curr Opin Chem Biol* **2018**, 44, 47–55.
64. J. Kim, H. Kim, S.B. Park. Privileged structures: Efficient chemical “navigators” toward unexplored biologically relevant chemical spaces. *J Am Chem Soc* **2014**, 136 (42), 14629–14638.
65. M. Toure, C.M. Crews. Small-molecule PROTACS: New approaches to protein degradation. *Angewandte Chemie - International Edition* **2016**, 55 (6), 1966–1973.
66. C.M. Crews. Targeting the Undruggable Proteome: The Small Molecules of My Dreams. *Chem Biol* **2010**, 17 (6), 551–555.
67. J. Rauch, N. Volinsky, D. Romano, W. Kolch. The secret life of kinases: Functions beyond catalysis. *Cell Communication and Signaling* **2011**, 9 (23), 1–28.

68. P.M. Cromm, K.T.G. Samarasinghe, J. Hines, C.M. Crews. Addressing Kinase-Independent Functions of Fak via PROTAC-Mediated Degradation. *J Am Chem Soc* **2018**, 140 (49), 17019–17026.
69. M.S. Gadd, A. Testa, X. Lucas, et al. Structural basis of PROTAC cooperative recognition for selective protein degradation. *Nat Chem Biol* **2017**, 13 (5), 514–521.
70. D. Remillard, D.L. Buckley, J. Paulk, et al. Degradation of the BAF Complex Factor BRD9 by Heterobifunctional Ligands. *Angewandte Chemie International Edition* **2017**, 56, 5738–5743.
71. B.P. Rubin, A. Duensing. Mechanisms of resistance to small molecule kinase inhibition in the treatment of solid tumors. *Laboratory Investigation* **2006**, 86 (10), 981–986.
72. R. Pisa, T.M. Kapoor. Chemical strategies to overcome resistance against targeted anticancer therapeutics. *Nat Chem Biol* **2020**, 16, 817–825.
73. A.D. Buhimschi, H.A. Armstrong, M. Toure, et al. Targeting the C481S Ibrutinib-Resistance Mutation in Bruton's Tyrosine Kinase Using PROTAC-Mediated Degradation. *Biochemistry* **2018**, 57 (26), 3564–3575.
74. Y. Sun, X. Zhao, N. Ding, et al. PROTAC-induced BTK degradation as a novel therapy for mutated BTK C481S induced ibrutinib-resistant B-cell malignancies. *Cell Res* **2018**, 28, 779–781.
75. Y. Sun, N. Ding, Y. Song, et al. Degradation of Bruton's tyrosine kinase mutants by PROTACs for potential treatment of ibrutinib-resistant non-Hodgkin lymphomas. *Leukemia* **2019**, 33, 2105–2110.
76. J. Salami, S. Alabi, R.R. Willard, et al. Androgen receptor degradation by the proteolysis-targeting chimera ARCC-4 outperforms enzalutamide in cellular models of prostate cancer drug resistance. *Commun Biol* **2018**, 1 (100), 1–9.
77. P. Ottis, C. Palladino, P. Thienger, et al. Cellular Resistance Mechanisms to Targeted Protein Degradation Converge Toward Impairment of the Engaged Ubiquitin Transfer Pathway. *ACS Chem Biol* **2019**, 14 (10), 1–18.

78. L. Zhang, B. Riley-Gillis, P. Vijay, Y. Shen. Acquired resistance to BET-ProTACS (proteolysis-targeting chimeras) caused by genomic alterations in core components of E3 ligase complexes. *Mol Cancer Ther* **2019**, 18 (7), 1302–1311.
79. D. Conole, M. Mondal, J.D. Majmudar, E.W. Tate. Recent Developments in Cell Permeable Deubiquitinating Enzyme Activity-Based Probes. *Front Chem* **2019**, 7 (876), 1–7.
80. F. Cong, A.K. Cheung, S.M.A. Huang. Chemical genetics-based target identification in drug discovery. *Annu Rev Pharmacol Toxicol* **2012**, 52, 57–78.
81. A.C. Lai, C.M. Crews. Induced protein degradation: an emerging drug discovery paradigm. *Nat Rev Drug Discov* **2017**, 16, 101–114.
82. M. Pettersson, C.M. Crews. PROteolysis TArgeting Chimeras (PROTACs) — Past, present and future. *Drug Discov Today Technol* **2019**, 31, 15–27.
83. W. Farnaby, M. Koegl. BAF complex vulnerabilities in cancer demonstrated via structure-based PROTAC design. *Nat Chem Biol* **2019**, 15, 672–680.
84. R.P. Nowak, S.L. DeAngelo, D. Buckley, et al. Plasticity in binding confers selectivity in ligand-induced protein degradation. *Nat Chem Biol* **2018**, 14 (7), 706–714.
85. K. Cyrus, M. Wehenkel, E.Y. Choi, et al. Impact of linker length on the activity of PROTACs. *Mol Biosyst* **2011**, 7 (2), 359–364.
86. B.E. Smith, S.L. Wang, S. Jaime-Figueroa, et al. Differential PROTAC substrate specificity dictated by orientation of recruited E3 ligase. *Nat Commun* **2019**, 10 (131), 1–13.
87. M. Schapira, M.F. Calabrese, A.N. Bullock, C.M. Crews. Targeted protein degradation: expanding the toolbox. *Nat Rev Drug Discov* **2019**, 18 (12), 949–963.
88. Y. Chen, J. Jin. The application of ubiquitin ligases in the PROTAC drug design. *Acta Biochim Biophys Sin (Shanghai)* **2020**, 52 (7), 776–790.

89. Y. Itoh, R. Kitaguchi, M. Ishikawa, M. Naito, Y. Hashimoto. Design, synthesis and biological evaluation of nuclear receptor-degradation inducers. *Bioorg Med Chem* **2011**, 19 (22), 6768–6778.
90. H.J. Maple, N. Clayden, A. Baron, C. Stacey, R. Felix. Developing degraders: Principles and perspectives on design and chemical space. *Medchemcomm* **2019**, 10, 1755–1764.
91. M. Lu, T. Liu, Q. Jiao, et al. Discovery of a Keap1-dependent peptide PROTAC to knockdown Tau by ubiquitination-proteasome degradation pathway. *Eur J Med Chem* **2018**, 146, 251–259.
92. C.C. Ward, J.I. Kleinman, S.M. Brittain, et al. Covalent Ligand Screening Uncovers a RNF4 E3 Ligase Recruiter for Targeted Protein Degradation Applications. *ACS Chem Biol* **2019**, 14 (11), 2430–2440.
93. J.N. Spradlin, X. Hu, C.C. Ward, et al. Harnessing the anti-cancer natural product nimbolide for targeted protein degradation. *Nat Chem Biol* **2019**, 15, 747–755.
94. L. Li, D. Mi, H. Pei, et al. In vivo target protein degradation induced by PROTACs based on E3 ligase DCAF15. *Signal Transduct Target Ther* **2020**, 5 (129), 1–3.
95. X. Zhang, V.M. Crowley, T.G. Wucherpennig, M.M. Dix, B.F. Cravatt. Electrophilic PROTACs that degrade nuclear proteins by engaging DCAF16. *Nat Chem Biol* **2019**, 15, 737–746.
96. N. Ohoka, G. Tsuji, T. Shoda, et al. Development of Small Molecule Chimeras That Recruit AhR E3 Ligase to Target Proteins. *ACS Chem Biol* **2019**, 14 (12), 2822–2832.
97. T. Ishida, A. Ciulli. E3 Ligase Ligands for PROTACs: How They Were Found and How to Discover New Ones. *SLAS Discovery* **2021**, 26 (4), 484–502.
98. Ashton Lai, T. Momar, D. Hellerschmieda, et al. Modular PROTAC Design for the Degradation of Oncogenic BCR-ABL. *Angewandte Chemie International Edition* **2016**, 55 (2), 807–810.
99. R.G. Guenette, S.W. Yang, J. Min, B. Pei, P.R. Potts. Target and tissue selectivity of PROTAC degraders. *Chem Soc Rev* **2022**, 51 (14), 5740–5756.

100. W.A. Velema, W. Szymanski, B.L. Feringa. Photopharmacology: Beyond proof of principle. *J Am Chem Soc* **2014**, 136 (6), 2178–2191.
101. S. Zeng, H. Zhang, Z. Shen, W. Huang. Photopharmacology of Proteolysis-Targeting Chimeras: A New Frontier for Drug Discovery. *Front Chem* **2021**, 9 (639176), 1–11.
102. A. Negi, K.K. Kesari, A.S. Voisin-Chiret. Light-Activating PROTACs in Cancer: Chemical Design, Challenges, and Applications. *Applied Sciences* **2022**, 12 (9674), 1–26.
103. J. Liu, H. Chen, L. Ma, et al. Light-induced control of protein destruction by opto-PROTAC. *Sci Adv* **2020**, 6 (8), 1–12.
104. Y. Naro, K. Darrah, A. Deiters. Optical Control of Small Molecule-Induced Protein Degradation. *J Am Chem Soc* **2020**, 142 (5), 2193–2197.
105. C.S. Kounde, M.M. Shchepinova, C.N. Saunders, et al. A caged E3 ligase ligand for PROTAC-mediated protein degradation with light. *Chemical Communications* **2020**, 56, 5532–5535.
106. G. Xue, K. Wang, D. Zhou, H. Zhong, Z. Pan. Light-Induced Protein Degradation with Photocaged PROTACs. *J Am Chem Soc* **2019**, 141, 18370–18374.
107. P. Pfaff, K.T.G.G. Samarasinghe, C.M. Crews, E.M. Carreira. Reversible Spatiotemporal Control of Induced Protein Degradation by Bistable PhotoPROTACs. *ACS Cent Sci* **2019**, 5 (10), 1682–1690.
108. M. Reynders, B.S. Matsuura, M. Bérouti, et al. PHOTACs enable optical control of protein degradation. *Sci Adv* **2020**, 6 (5064), 1–12.
109. Y.-H.Y. Jin, M.-C.M.M.-C. Lu, Y. Wang, et al. Azo-PROTAC: Novel Light-Controlled Small-Molecule Tool for Protein Knockdown. *J Med Chem* **2020**, 63 (9), 4644–4654.
110. Q. Zhang, C.S. Kounde, M. Mondal, et al. Light-mediated multi-target protein degradation using arylazopyrazole photoswitchable PROTACs (AP-PROTACs). *Chemical Communications* **2022**, 58, 10933–10936.

111. C.M. Olson, B. Jiang, M.A. Erb, et al. Pharmacological perturbation of CDK9 using selective CDK9 inhibition or degradation. *Nat Chem Biol* **2018**, 14 (2), 163–170.
112. H.T. Huang, D. Dobrovolsky, J. Paulk, et al. A Chemoproteomic Approach to Query the Degradable Kinome Using a Multi-kinase Degradator. *Cell Chem Biol* **2018**, 25, 88–99.
113. K.A. Donovan, F.M. Ferguson, J.W. Bushman, et al. Mapping the Degradable Kinome Provides a Resource for Expedited Degradator Development. *Cell* **2020**, 183, 1714–1731.
114. L. Wang, N. Wang, W. Zhang, et al. Therapeutic peptides: current applications and future directions. *Signal Transduct Target Ther* **2022**, 7 (48), 1–27.
115. C. Lamers. Overcoming the shortcomings of peptide-based therapeutics. *Future Drug Discov* **2022**, 4 (2).
116. M. Muttenthaler, G.F. King, D.J. Adams, P.F. Alewood. Trends in peptide drug discovery. *Nat Rev Drug Discov* **2021**, 20 (4), 309–325.
117. N. Tsomaia. Peptide therapeutics: Targeting the undruggable space. *Eur J Med Chem* **2015**, 94, 459–470.
118. L. Diao, B. Meibohm. Pharmacokinetics and pharmacokinetic-pharmacodynamic correlations of therapeutic peptides. *Clin Pharmacokinet* **2013**, 52 (10), 855–868.
119. K. Fosgerau, T. Hoffmann. Peptide therapeutics: current status and future directions. *Drug Discov Today* **2015**, 20 (1), 122–128.
120. George P. Smith. Filamentous Fusion Phage: Novel Expression Vectors That Display Cloned Antigens on the Virion Surface. *Science (1979)* **1985**, 228 (4705), 1315–1317.
121. J. Pande, M.M. Szewczyk, A.K. Grover. Phage display: Concept, innovations, applications and future. *Biotechnol Adv* **2010**, 28 (6), 849–858.
122. M. Hamzeh-Mivehroud, A.A. Alizadeh, M.B. Morris, W. Bret Church, S. Dastmalchi. Phage display as a technology delivering on the promise of peptide drug discovery. *Drug Discov Today* **2013**, 18 (23–24), 1144–1157.



123. Y. Yamagishi, I. Shoji, S. Miyagawa, et al. Natural product-like macrocyclic N-methyl-peptide inhibitors against a ubiquitin ligase uncovered from a ribosome-expressed de novo library. *Chem Biol* **2011**, 18 (12), 1562–1570.
124. Y. Goto, H. Suga. The RaPID Platform for the Discovery of Pseudo-Natural Macrocyclic Peptides. *Acc Chem Res* **2021**, 54 (18), 3604–3617.
125. C. Sohrabi, A. Foster, A. Tavassoli. Methods for generating and screening libraries of genetically encoded cyclic peptides in drug discovery. *Nat Rev Chem* **2020**, 4, 90–101.
126. W. Jaroszewicz, J. Morcinek-Orłowska, K. Pierzynowska, L. Gaffke, G. Węgrzyn. Phage display and other peptide display technologies. *FEMS Microbiol Rev* **2022**, 46 (2), 1–25.
127. J. Jin, Y. Wu, J. Chen, et al. The peptide PROTAC modality: A novel strategy for targeted protein ubiquitination. *Theranostics* **2020**, 10 (22), 10141–10153.
128. M. Pelay-Gimeno, A. Glas, O. Koch, T.N. Grossmann. Structure-Based Design of Inhibitors of Protein-Protein Interactions: Mimicking Peptide Binding Epitopes. *Angewandte Chemie International Edition* **2015**, 54, 8896–8927.
129. K. Bozovičar, T. Bratkovič. Evolving a peptide: Library platforms and diversification strategies. *Int J Mol Sci* **2020**, 21 (215), 1–31.
130. R.K. Henning, J.O. Varghese, S. Das, et al. Degradation of Akt using protein-catalyzed capture agents. *Journal of Peptide Science* **2016**, 22 (4), 196–200.
131. Y. Jiang, Q. Deng, H. Zhao, et al. Development of Stabilized Peptide-Based PROTACs against Estrogen Receptor  $\alpha$ . *ACS Chem Biol* **2018**, 13 (3), 628–635.
132. D. Ma, Y. Zou, Y. Chu, et al. A cell-permeable peptide-based PROTAC against the oncoprotein CREPT proficiently inhibits pancreatic cancer. *Theranostics* **2020**, 10 (8), 3708–3721.
133. H. Liao, X. Li, L. Zhao, et al. A PROTAC peptide induces durable  $\beta$ -catenin degradation and suppresses Wnt-dependent intestinal cancer. *Cell Discov* **2020**, 6 (35), 1–12.

134. H.E. Marei, C. Cenciarelli, A. Hasan. Potential of antibody–drug conjugates (ADCs) for cancer therapy. *Cancer Cell Int* **2022**, 22 (255), 1–12.
135. E. Ferraro, J.Z. Drago, S. Modi. Implementing antibody-drug conjugates (ADCs) in HER2-positive breast cancer: state of the art and future directions. *Breast Cancer Research* **2021**, 23 (84), 1–11.
136. Z. Fu, S. Li, S. Han, C. Shi, Y. Zhang. Antibody drug conjugate: the “biological missile” for targeted cancer therapy. *Signal Transduct Target Ther* **2022**, 7 (93), 1–25.
137. A.H. Staudacher, M.P. Brown. Antibody drug conjugates and bystander killing: is antigen-dependent internalisation required. *Br J Cancer* **2017**, 117, 1736–1742.
138. S. Xu. Internalization, Trafficking, Intracellular Processing and Actions of Antibody-Drug Conjugates. *Pharm Res* **2015**, 32 (11), 3577–3583.
139. Q. Zhou. Site-specific antibody conjugation for ADC and beyond. *Biomedicines* **2017**, 5 (64), 1–15.
140. William R. F. Goundry, Jeremy S. Parker. Payloads for Antibody–Drug Conjugates. *Organic Process Research & Development* **2022**, 26 (8), 2121–2123.
141. J.D. Bargh, A. Isidro-Llobet, J.S. Parker, D.R. Spring. Cleavable linkers in antibody-drug conjugates. *Chem Soc Rev* **2019**, 48 (16), 4361–4374.
142. J.D. Bargh, S.J. Walsh, N. Ashman, et al. A dual-enzyme cleavable linker for antibody-drug conjugates. *Chemical Communications* **2021**, 57 (28), 3457–3460.
143. S. Chuprakov, A.O. Ogunkoya, R.M. Barfield, et al. Tandem-Cleavage Linkers Improve the in Vivo Stability and Tolerability of Antibody-Drug Conjugates. *Bioconjug Chem* **2021**, 32 (4), 746–754.
144. B.A. Teicher, R.V.J. Chari. Antibody Conjugate Therapeutics: Challenges and Potential. *Clinical Cancer Research* **2011**, 17 (20), 6389–6397.
145. P.S. Dragovich. Degradable-antibody conjugates. *Chem Soc Rev* **2022**, 51, 3886–3897.

146. M. Maneiro, N. Forte, M.M. Shchepinova, et al. Antibody-PROTAC Conjugates Enable HER2-Dependent Targeted Protein Degradation of BRD4. *ACS Chem Biol* **2020**, 15 (6), 1306–1312.
147. N. Forte, V. Chudasama, J.R. Baker. Homogeneous antibody-drug conjugates via site-selective disulfide bridging. *Drug Discov Today Technol* **2018**, 30, 11–20.
148. T.H. Pillow, P. Adhikari, R.A. Blake, et al. Antibody Conjugation of a Chimeric BET Degradator Enables in vivo Activity. *ChemMedChem* **2020**, 15, 17–25.
149. P.S. Dragovich, T.H. Pillow, R.A. Blake, et al. Antibody-Mediated Delivery of Chimeric BRD4 Degradators. Part 1: Exploration of Antibody Linker, Payload Loading, and Payload Molecular Properties. *J Med Chem* **2021**, 64 (5), 2534–2575.
150. P.S. Dragovich, T.H. Pillow, R.A. Blake, et al. Antibody-Mediated Delivery of Chimeric BRD4 Degradators. Part 2: Improvement of In Vitro Antiproliferation Activity and In Vivo Antitumor Efficacy. *J. Med. Chem* **2021**, 64 (5), 26.
151. V.G. Klein, C.E. Townsend, A. Testa, et al. Understanding and Improving the Membrane Permeability of VH032-Based PROTACs. *ACS Med Chem Lett* **2020**, 11 (9), 1732–1738.
152. S.D. Edmondson, B. Yang, C. Fallan. Proteolysis targeting chimeras (PROTACs) in ‘beyond rule-of-five’ chemical space: Recent progress and future challenges. *Bioorg Med Chem Lett* **2019**, 29 (13), 1555–1564.
153. A. Negi, C. Kieffer, A.S. Voisin-Chiret. Azobenzene Photoswitches in Proteolysis Targeting Chimeras: Photochemical Control Strategies and Therapeutic Benefits. *ChemistrySelect* **2022**, 7 (23), 1–12.
154. G. Mayer, A. Hechel. Biologically active molecules with a “light switch.” *Angewandte Chemie International Edition* **2006**, 45 (30), 4900–4921.
155. W. Szymański, J.M. Beierle, H.A.V. Kistemaker, W.A. Velema, B.L. Feringa. Reversible photocontrol of biological systems by the incorporation of molecular photoswitches. *Chem Rev* **2013**, 113, 6114–6178.

156. K. Hüll, J. Morstein, D. Trauner. In Vivo Photopharmacology. *Chem Rev* **2018**, 118 (21), 10710–10747.
157. K.L. Montgomery, A.J. Yeh, J.S. Ho, et al. Wirelessly powered, fully internal optogenetics for brain, spinal and peripheral circuits in mice. *Nat Methods* **2015**, 12 (10), 969–974.
158. J. Broichhagen, J.A. Frank, D. Trauner. A Roadmap to Success in Photopharmacology. *Acc Chem Res* **2015**, 48 (7), 1947–1960.
159. H.M.D. Bandara, S.C. Burdette. Photoisomerization in different classes of azobenzene. *Chem Soc Rev* **2012**, 41 (5), 1809–1825.
160. A.A. Beharry, G.A. Woolley. Azobenzene photoswitches for biomolecules. *Chem Soc Rev* **2011**, 40 (8), 4422–4437.
161. C.E. Weston, R.D. Richardson, P.R. Haycock, A.J.P.P. White, M.J. Fuchter. Arylazopyrazoles: Azoheteroarene photoswitches offering quantitative isomerization and long thermal half-lives. *J Am Chem Soc* **2014**, 136 (34), 11878–11881.
162. J. Calbo, C.E. Weston, A.J.P. White, et al. Tuning Azoheteroarene Photoswitch Performance through Heteroaryl Design. *J Am Chem Soc* **2016**, 139, 1261–1274.
163. S. Crespi, N.A. Simeth, B. König. Heteroaryl azo dyes as molecular photoswitches. *Nat Rev Chem* **2019**, 3 (3), 133–146.
164. Cyrille Stephane Kounde. Doctoral thesis: Bifunctional chemical tools for the conditional control of targeted protein degradation, Imperial College London, **2023**.
165. Ernst Fischer. Calculation of photostationary states in systems A/B when only A is known. *J. Phys. Chem.* **1967**, 71 (11), 3704–3706.
166. E. Stadler, S. Tassoti, P. Lentes, et al. In Situ Observation of Photoswitching by NMR Spectroscopy: A Photochemical Analogue to the Exchange Spectroscopy Experiment. *Anal Chem* **2019**, 91 (17), 11367–11373.

167. K. Stranius, K. Börjesson. Determining the photoisomerization quantum yield of photoswitchable molecules in solution and in the solid state. *Sci Rep* **2017**, 7 (41145), 1–9.
168. P. Blume-Jensen, T. Hunter. Oncogenic kinase signalling. *Nature* **2001**, 411, 355–365.
169. P.A. Futreal, L. Coin, M. Marshall, et al. A census of human cancer genes. *Nat Rev Cancer* **2004**, 4 (3), 177–183.
170. C. Greenman, P. Stephens, R. Smith, et al. Patterns of somatic mutation in human cancer genomes. *Nature* **2007**, 446 (7132), 153–158.
171. L.J. Wilson, A. Linley, D.E. Hammond, et al. New Perspectives, opportunities, and challenges in exploring the human protein kinome. *Cancer Res* **2018**, 78 (1), 15–29.
172. L. Zhong, Y. Li, L. Xiong, et al. Small molecules in targeted cancer therapy: advances, challenges, and future perspectives. *Signal Transduct Target Ther* **2021**, 6 (201), 1–48.
173. O. Fedorov, S. Müller, S. Knapp. The (un)targeted cancer kinome. *Nat Chem Biol* **2010**, 6, 166–169.
174. R. Roskoski. Properties of FDA-approved small molecule protein kinase inhibitors: A 2023 update. *Pharmacol Res* **2023**, 187 (106552), 1–21.
175. J. Zhang, P.L. Yang, N.S. Gray. Targeting cancer with small molecule kinase inhibitors. *Nat Rev Cancer* **2009**, 9, 28–39.
176. F. Yu, M. Cai, L. Shao, J. Zhang. Targeting Protein Kinases Degradation by PROTACs. *Front Chem* **2021**, 9 (679120), 1–12.
177. L.N. Johnson. Protein kinase inhibitors: Contributions from structure to clinical compounds. *Q Rev Biophys* **2009**, 42, 1–40.
178. K. Ghoreschi, A. Laurence, J.J. O'shea. Selectivity and therapeutic inhibition of kinases: to be or not to be? NIH Public Access. *Nat Immunol* **2009**, 10 (4), 356–360.
179. K.S. Bhullar, N.O. Lagarón, E.M. McGowan, et al. Kinase-targeted cancer therapies: progress, challenges and future directions. *Mol Cancer* **2018**, 17 (48), 1–20.

180. O. Fedorov, B. Marsden, V. Pogacic, et al. A systematic interaction map of validated kinase inhibitors with Ser/Thr kinases. *Proceedings of the National Academy of Sciences* **2007**, 104 (51), 20523–20528.
181. M.A. Fabian, W.H. Biggs, D.K. Treiber, et al. A small molecule-kinase interaction map for clinical kinase inhibitors. *Nat Biotechnol* **2005**, 23 (3), 329–336.
182. M. Bantscheff, D. Eberhard, Y. Abraham, et al. Quantitative chemical proteomics reveals mechanisms of action of clinical ABL kinase inhibitors. *Nat Biotechnol* **2007**, 25 (9), 1035–1044.
183. S. Müller, A. Chaikuad, N.S. Gray, S. Knapp. The ins and outs of selective kinase inhibitor development. *Nat Chem Biol* **2015**, 11 (11), 818–821.
184. L. Zhang, I.P. Holmes, F. Hochgräfe, et al. Characterization of the novel broad-spectrum kinase inhibitor CTx-0294885 as an affinity reagent for mass spectrometry-based kinome profiling. *J Proteome Res* **2013**, 12 (7), 3104–3116.
185. T. Asatsuma-Okumura, T. Ito, H. Handa. Molecular mechanisms of cereblon-based drugs. *Pharmacol Ther* **2019**, 202, 132–139.
186. J. Krönke, E.C. Fink, P.W. Hollenbach, et al. Lenalidomide induces ubiquitination and degradation of CK1 $\alpha$  in del(5q) MDS. *Nature* **2015**, 523 (7559), 183–188.
187. E.S. Fischer, K. Böhm, J.R. Lydeard, et al. Structure of the DDB1-CRBN E3 ubiquitin ligase in complex with thalidomide. *Nature* **2014**, 512 (1), 49–53.
188. C. Russell, A.J.S. Lin, P. Hains, et al. An integrated flow and microwave approach to a broad spectrum protein kinase inhibitor. *RSC Adv* **2015**, 5 (113), 93433–93437.
189. J.S. Duncan, M.C. Whittle, K. Nakamura, et al. Dynamic reprogramming of the kinome in response to targeted MEK inhibition in triple-negative breast cancer. *Cell* **2012**, 149 (2), 307–321.
190. W.W. Kallemeijn, T. Lanyon-Hogg, N. Panyain, et al. Proteome-wide analysis of protein lipidation using chemical probes: in-gel fluorescence visualization, identification and quantification of N-myristoylation, N- and S-acylation, O-

- cholesterylation, S-farnesylation and S-geranylgeranylation. *Nat Protoc* **2021**, 16, 5083–5122.
191. M. Ignatov, A. Jindal, S. Kotelnikov, et al. High Accuracy Prediction of PROTAC Complex Structures. *J Am Chem Soc* **2023**, 145 (13), 7123–7135.
  192. D. Kozakov, D.R. Hall, B. Xia, et al. The ClusPro web server for protein-protein docking. *Nat Protoc* **2017**, 12 (2), 255–278.
  193. D. Kozakov, R. Brenke, S.R. Comeau, S. Vajda. PIPER: An FFT-based protein docking program with pairwise potentials. *Proteins: Structure, Function and Genetics* **2006**, 65 (2), 392–406.
  194. D.A. Case, T.E. Cheatham, T. Darden, et al. The Amber biomolecular simulation programs. *J Comput Chem* **2005**, 26 (16), 1668–1688.
  195. N. Bai, S.A. Miller, G. V Andrianov, et al. Rationalizing PROTAC-Mediated Ternary Complex Formation Using Rosetta. *J. Chem. Inf. Model* **2021**, 61, 1368–1382.
  196. D.L. Daniels, K.M. Riching, M. Urh. Monitoring and deciphering protein degradation pathways inside cells. *Drug Discov Today Technol* **2019**, 31, 61–68.
  197. L. Pillai-Kastoori, A.R. Schutz-Geschwender, J.A. Harford. A systematic approach to quantitative Western blot analysis. *Anal Biochem* **2020**, 593 (113508), 1–16.
  198. M. Yan, C. Wang, B. He, et al. Aurora-A Kinase: A Potent Oncogene and Target for Cancer Therapy. *Med Res Rev* **2016**, 36 (6), 1036–1079.
  199. F.J. Sulzmaier, C. Jean, D.D. Schlaepfer. FAK in cancer: Mechanistic findings and clinical applications. *Nat Rev Cancer* **2014**, 14 (9), 598–610.
  200. R.P. Law, J. Nunes, C. wa Chung, et al. Discovery and Characterisation of Highly Cooperative FAK-Degrading PROTACs. *Angewandte Chemie - International Edition* **2021**, 60 (43), 23327–23334.
  201. A. Pike, B. Williamson, S. Harlfinger, S. Martin, D.F. McGinnity. Optimising proteolysis-targeting chimeras (PROTACs) for oral drug delivery: a drug metabolism and pharmacokinetics perspective. *Drug Discov Today* **2020**, 25 (10), 1793–1800.

202. M.D. Michael Shultz. Two Decades under the Influence of the Rule of Five and the Changing Properties of Approved Oral Drugs. *J Med Chem* **2019**, 62, 1701–1714.
203. V. Erckes, C. Steuer. A story of peptides, lipophilicity and chromatography - back and forth in time. *RSC Med Chem* **2022**, 13 (6), 676–687.
204. D. Su, D. Zhang. Linker Design Impacts Antibody-Drug Conjugate Pharmacokinetics and Efficacy via Modulating the Stability and Payload Release Efficiency. *Front Pharmacol* **2021**, 12 (687926), 1–8.
205. P. Agarwal, C.R. Bertozzi. Site-specific antibody-drug conjugates: The nexus of bioorthogonal chemistry, protein engineering, and drug development. *Bioconjug Chem* **2015**, 26 (2), 176–192.
206. N. Jain, S.W. Smith, S. Ghone, B. Tomczuk. Current ADC Linker Chemistry. *Pharm Res* **2015**, 32, 3526–3540.
207. P.D. Senter, E.L. Sievers. The discovery and development of brentuximab vedotin for use in relapsed Hodgkin lymphoma and systemic anaplastic large cell lymphoma. *Nat Biotechnol* **2012**, 30 (7), 631–637.
208. Z. Su, D. Xiao, F. Xie, et al. Antibody–drug conjugates: Recent advances in linker chemistry. *Acta Pharm Sin B* **2021**, 11 (12), 3889–3907.
209. Y. Wang, S. Fan, W. Zhong, X. Zhou, S. Li. Development and properties of valine-alanine based antibody-drug conjugates with monomethyl auristatin E as the potent payload. *Int J Mol Sci* **2017**, 18 (1860), 1–19.
210. W. Huang, X. Wu, X. Gao, et al. Maleimide–thiol adducts stabilized through stretching. *Nat Chem* **2019**, 11 (4), 310–319.
211. J.D. Sadowsky, T.H. Pillow, J. Chen, et al. Development of Efficient Chemistry to Generate Site-Specific Disulfide-Linked Protein- and Peptide-Payload Conjugates: Application to THIOMAB Antibody-Drug Conjugates. *Bioconjug Chem* **2017**, 28 (8), 2086–2098.
212. R. Sheyi, B.G. De La Torre, F. Albericio. Linkers: An Assurance for Controlled Delivery of Antibody-Drug Conjugate. *Pharmaceutics* **2022**, 14 (396), 1–27.



213. F. Holst, P.R. Stahl, C. Ruiz, et al. Estrogen receptor alpha (ESR1) gene amplification is frequent in breast cancer. *Nat Genet* **2007**, 39 (5), 655–660.
214. F. Rastinejad, P. Huang, V. Chandra, S. Khorasanizadeh. Understanding nuclear receptor form and function using structural biology. *J Mol Endocrinol* **2013**, 51 (3), 1–21.
215. E.A. Musgrove, R.L. Sutherland. Biological determinants of endocrine resistance in breast cancer. *Nat Rev Cancer* **2009**, 9, 631–643.
216. L. Wang, A. Sharma. SERDs: a case study in targeted protein degradation. *Chem. Soc. Rev* **2022**, 51, 8149.
217. X. Lin, H. Xiang, G. Luo. Targeting estrogen receptor  $\alpha$  for degradation with PROTACs: A promising approach to overcome endocrine resistance. *Eur J Med Chem* **2020**, 206 (112689), 1–19.
218. Y. Jiang, Q. Deng, H. Zhao, et al. Development of Stabilized Peptide-Based PROTACs against Estrogen Receptor  $\alpha$ . *ACS Chem Biol* **2018**, 13 (3), 628–635.
219. A. Rodriguez-Gonzalez, K. Cyrus, M. Salcius, et al. Targeting steroid hormone receptors for ubiquitination and degradation in breast and prostate cancer. *Oncogene* **2008**, 27, 7201–7211.
220. H. Zhao, Q.-S.S. Liu, H. Geng, et al. Crosslinked Aspartic Acids as Helix-Nucleating Templates. *Angewandte Chemie - International Edition* **2016**, 55 (39), 12088–12093.
221. A.M. Leduc, J.O. Trent, J.L. Wittliff, et al. Helix-stabilized cyclic peptides as selective inhibitors of steroid receptor - Coactivator interactions. *Proc Natl Acad Sci U S A* **2003**, 100 (20), 11273–11278.
222. J.M. Lambert, R.V.J. Chari. Ado-trastuzumab Emtansine (T-DM1): An Antibody–Drug Conjugate (ADC) for HER2-Positive Breast Cancer. *J Med Chem* **2014**, 57, 6949–6964.
223. E. Rassy, L. Rached, B. Pistilli. Antibody drug conjugates targeting HER2: Clinical development in metastatic breast cancer. *The Breast* **2022**, 66, 960–9776.

224. R. Subir Os-Funosas, A. El-Faham, F. Albericio. Aspartimide formation in peptide chemistry: occurrence, prevention strategies and the role of N-hydroxylamines. *Tetrahedron* **2011**, 67, 8595–8606.
225. M. Mergler, F. Dick. The aspartimide problem in Fmoc-based SPPS. Part III. *Journal of Peptide Science* **2005**, 11 (10), 650–657.
226. D. Samson, D. Rentsch, | Marco Minuth, T. Meier, G. Loidl. The aspartimide problem persists: Fluorenylmethyloxycarbonyl-solid-phase peptide synthesis (Fmoc-SPPS) chain termination due to formation of N-terminal piperazine-2,5-diones. *Journal of Peptide Science* **2019**, 25 (e3193), 1–11.
227. P. Stathopoulos, S. Papas, S. Kostidis, V. Tsikaris.  $\alpha$ - and  $\beta$ - Aspartyl peptide ester formation via aspartimide ring opening. *Journal of Peptide Science* **2005**, 11 (10), 658–664.
228. Y. Dai, N. Yue, J. Gong, et al. Development of cell-permeable peptide-based PROTACs targeting estrogen receptor  $\alpha$ . *Eur J Med Chem* **2020**, 187 (111967), 1–11.
229. L.M. Simpson, L. Glennie, A. Brewer, et al. Target protein localization and its impact on PROTAC-mediated degradation. *Cell Chem Biol* **2022**, 29, 1482–1504.
230. J. Shi, Y. Ma, J. Zhu, et al. A review on electroporation-based intracellular delivery. *Molecules* **2018**, 23 (3044), 1–19.
231. S.S. Banerjee, N. Aher, R. Patil, J. Khandare. Poly(ethylene glycol)-Prodrug Conjugates: Concept, Design, and Applications. *J Drug Deliv* **2012**, 2012 (103973), 1–17.
232. D. Lu, Y. Wu, Y. Wang, et al. Crept accelerates tumorigenesis by regulating the transcription of cell-cycle-related genes. *Cancer Cell* **2012**, 21, 92–104.
233. Y. Zhang, C. Liu, X. Duan, et al. CREPT/RPRD1B, a recently identified novel protein highly expressed in tumors, enhances the  $\beta$ -catenin-TCF4 transcriptional activity in response to Wnt signaling. *Journal of Biological Chemistry* **2014**, 289 (33), 22589–22599.

234. D. Ma, Y. Zou, Y. Chu, et al. A cell-permeable peptide-based PROTAC against the oncoprotein CREPT proficiently inhibits pancreatic cancer. *Theranostics* **2020**, 10 (8), 3708–3721.
235. J.-H. Min, H. Yang, M. Ivan, et al. Structure of an HIF-1 $\alpha$ -pVHL complex: Hydroxyproline recognition in signaling. *Science (1979)* **2002**, 296 (5574), 1886–1889.
236. J. Yu, T. Fang, C. Yun, X. Liu, X. Cai. Antibody-Drug Conjugates Targeting the Human Epidermal Growth Factor Receptor Family in Cancers. *Front Mol Biosci* **2022**, 9 (847835), 1–11.
237. M.J. Wieduwilt, M.M. Moasser. The epidermal growth factor receptor family: Biology driving targeted therapeutics. *Cellular and Molecular Life Sciences* **2008**, 65 (10), 1566–1584.
238. P. Seshacharyulu, M.P. Ponnusamy, D. Haridas, et al. Targeting the EGFR signaling pathway in cancer therapy. *Expert Opin Ther Targets* **2012**, 16 (1), 15–31.
239. T. Troiani, E. Martinelli, A. Capasso, et al. Targeting EGFR in Pancreatic Cancer Treatment. *Curr Drug Targets* **2012**, 13, 802–810.
240. C.M. Mckertish, V. Kayser. Advances and limitations of antibody drug conjugates for cancer. *Biomedicines* **2021**, 9 (872), 1–25.
241. I. Hollander, A. Kunz, P.R. Hamann. Selection of reaction additives used in the preparation of monomeric antibody-calicheamicin conjugates. *Bioconjug Chem* **2008**, 19 (1), 358–361.
242. R.Y. Zhao, S.D. Wilhelm, C. Audette, et al. Synthesis and evaluation of hydrophilic linkers for antibody-maytansinoid conjugates. *J Med Chem* **2011**, 54 (10), 3606–3623.
243. C.-L. Law, C.G. Cervený, K.A. Gordon, et al. Efficient Elimination of B-Lineage Lymphomas by Anti-CD20-Auristatin Conjugates. *Clinical Cancer Research* **2004**, 10, 7842–7851.
244. L.M. Smith, A. Nesterova, S.C. Alley, M.Y. Torgov, P.J. Carter. Potent cytotoxicity of an auristatin-containing antibody-drug conjugate targeting melanoma cells expressing melanotransferrin/p97. *Mol Cancer Ther* **2006**, 5 (6), 1474–1482.

245. S. Xu, B.Z. Olenyuk, C.T. Okamoto, S.F. Hamm-Alvarez. Targeting receptor-mediated endocytotic pathways with nanoparticles: Rationale and advances. *Adv Drug Deliv Rev* **2013**, 65, 121–138.
246. H.T. McMahon, E. Boucrot. Molecular mechanism and physiological functions of clathrin-mediated endocytosis. *Nat Rev Mol Cell Biol* **2011**, 12 (8), 517–533.
247. C. Berger, I.H. Madhus, E. Stang. Cetuximab in combination with anti-human IgG antibodies efficiently down-regulates the EGF receptor by macropinocytosis. *Exp Cell Res* **2012**, 318 (20), 2578–2591.
248. T. Hu, C. Li. Convergence between Wnt- $\beta$ -catenin and EGFR signaling in cancer. *Mol Cancer* **2010**, 9 (236), 1–7.
249. G. Singh, M. Hossain, A. Qadir Bhat, et al. Identification of a cross-talk between EGFR and Wnt/beta-catenin signaling pathways in HepG2 liver cancer cells. *Cell Signal* **2021**, 79 (109885), 1–7.
250. F. Huang, D. Kirkpatrick, X. Jiang, S. Gygi, A. Sorkin. Differential regulation of EGF receptor internalization and degradation by multiubiquitination within the kinase domain. *Mol Cell* **2006**, 21 (6), 737–748.
251. H. Ye, M. Chen, F. Cao, et al. Chloroquine, an autophagy inhibitor, potentiates the radiosensitivity of glioma initiating cells by inhibiting autophagy and activating apoptosis. *BMC Neurol* **2016**, 16 (178), 1–8.
252. M. Mauthe, I. Orhon, C. Rocchi, et al. Chloroquine inhibits autophagic flux by decreasing autophagosome-lysosome fusion. *Autophagy* **2018**, 14 (8), 1435–1455.
253. R. Vartak, B. Deore, C.A. Sanhueza, K. Patel. Cetuximab-based PROteolysis targeting chimera for effectual downregulation of NSCLC with varied EGFR mutations. *Int J Biol Macromol* **2023**, 252 (126413), 1–15.
254. S.D. FIDANZE, D. LIU, R.A. MANTEI, et al. Tetracyclic bromodomain inhibitors. WO 2014/139324, September 18, 2014.
255. P. Filippakopoulos, J. Qi, S. Picaud, et al. Selective inhibition of BET bromodomains. *Nature* **2010**, 468 (7327), 1067–1073.

256. S.D. Fidanze, D. Liu, R.A. Mantei, et al. Discovery and optimization of novel constrained pyrrolopyridone BET family inhibitors. *Bioorg Med Chem Lett* **2018**, 28 (10), 1804–1810.
257. C. Wang, Y. Zhang, S. Yang, W. Chen, D. Xing. PROTACs for BRDs proteins in cancer therapy: a review. *J Enzyme Inhib Med Chem* **2022**, 37 (1), 1694–1703.
258. S. Kocanova, M. Mazaheri, S. Caze-Subra, K. Bystricky. Ligands specify estrogen receptor alpha nuclear localization and degradation. *BMC Cell Biol* **2010**, 11 (98), 1–13.
259. C. Russell, A.J.S. Lin, P. Hains, et al. An integrated flow and microwave approach to a broad spectrum protein kinase inhibitor. *RSC Adv* **2015**, 5 (113), 93433–93437.
260. I. Coin, M. Beyermann, M. Bienert. Solid-phase peptide synthesis: from standard procedures to the synthesis of difficult sequences. *Nat Protoc* **2007**, 2 (12), 3247–3256.
261. J.M. Collins, K.A. Porter, S.K. Singh, G.S. Vanier. High-Efficiency Solid Phase Peptide Synthesis (HE-SPPS). *Org. Lett.* **2014**, 16 (3), 940–943.
262. L. Zhang, S. Lovell, E. De Vita, et al. A KLK6 Activity-Based Probe Reveals a Role for KLK6 Activity in Pancreatic Cancer Cell Invasion. *J Am Chem Soc* **2022**, 144 (49), 22493–22504.
263. Y. Perez-Riverol, J. Bai, C. Bandla, et al. The PRIDE database resources in 2022: a hub for mass spectrometry-based proteomics evidences. *Nucleic Acids Res* **2022**, 50, D543–D552.
264. S. Kotelnikov, A. Alekseenko, · Cong Liu, et al. Sampling and refinement protocols for template-based macrocycle docking: 2018 D3R Grand Challenge 4. *J Comput Aided Mol Des* **2020**, 34, 179–189.
265. A. Alekseenko, S. Kotelnikov, M. Ignatov, et al. ClusPro LigTBM: Automated Template-based Small Molecule Docking. *J Mol Biol* **2020**, 432 (11), 3404–3410.
266. S. Riniker, G.A. Landrum. Better Informed Distance Geometry: Using What We Know to Improve Conformation Generation. *J Chem Inf Model* **2015**, 55 (12), 2562–2574.

267. P. Tosco, N. Stiefl, G. Landrum. Bringing the MMFF force field to the RDKit: implementation and validation. *J Cheminform* **2014**, 6 (37), 1–4.
268. D. Padhorny, A. Kazennov, B.S. Zerbe, et al. Protein-protein docking by fast generalized Fourier transforms on 5D rotational manifolds. *Proc Natl Acad Sci U S A* **2016**, 113 (30), E4286–E4293.
269. F. Hamon, F. Djedaini-Pilard, F. Barbot, C. Len. Azobenzenes-synthesis and carbohydrate applications. *Tetrahedron* **2009**, 65 (49), 10105–10123.
270. A.M. Leduc, J.O. Trent, J.L. Wittliff, et al. Helix-stabilized cyclic peptides as selective inhibitors of steroid receptor - Coactivator interactions. *Proc Natl Acad Sci U S A* **2003**, 100 (20), 11273–11278.

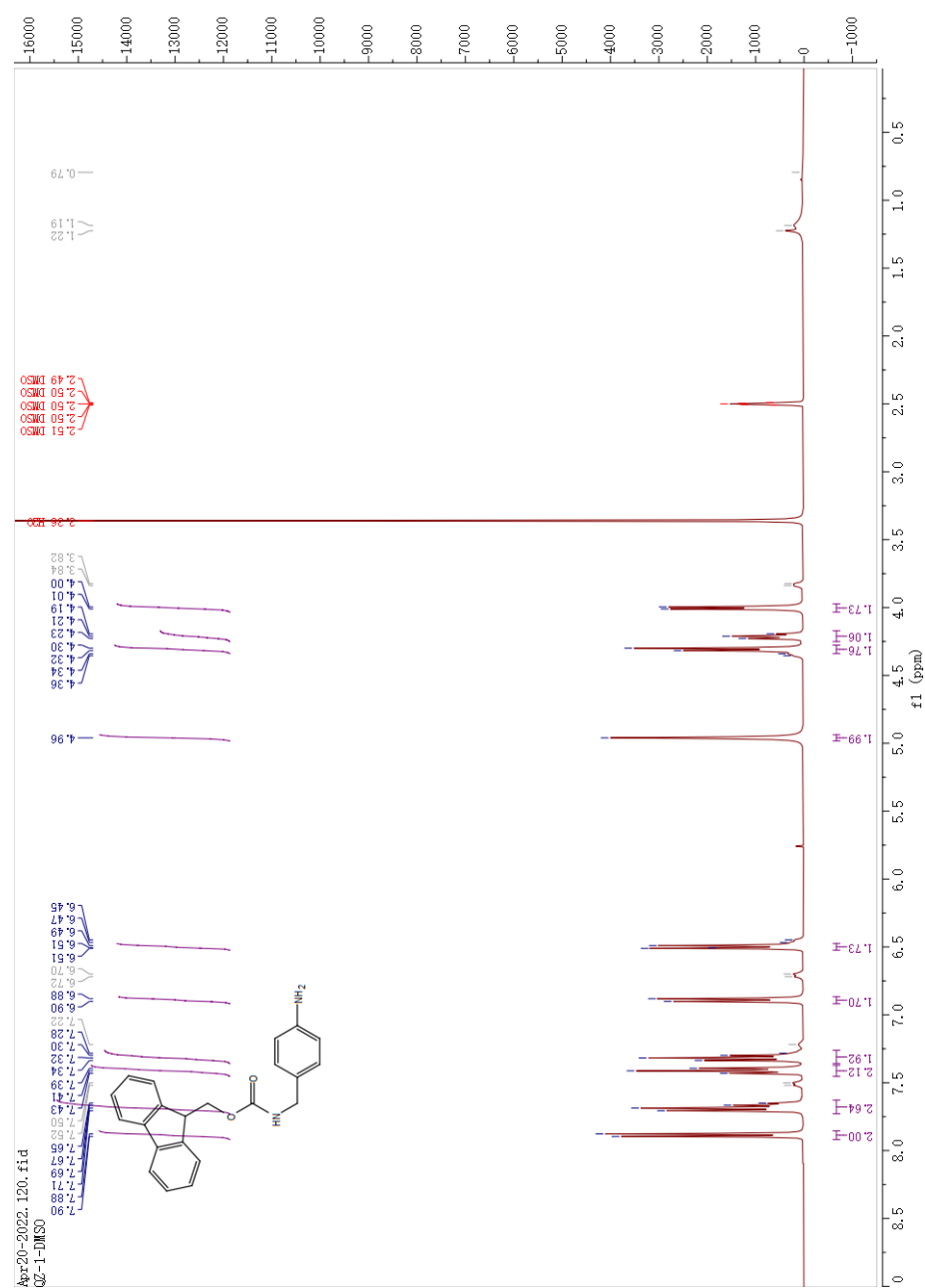
# Chapter 7 Appendix

## 7.1 Chapter 2 Additional data

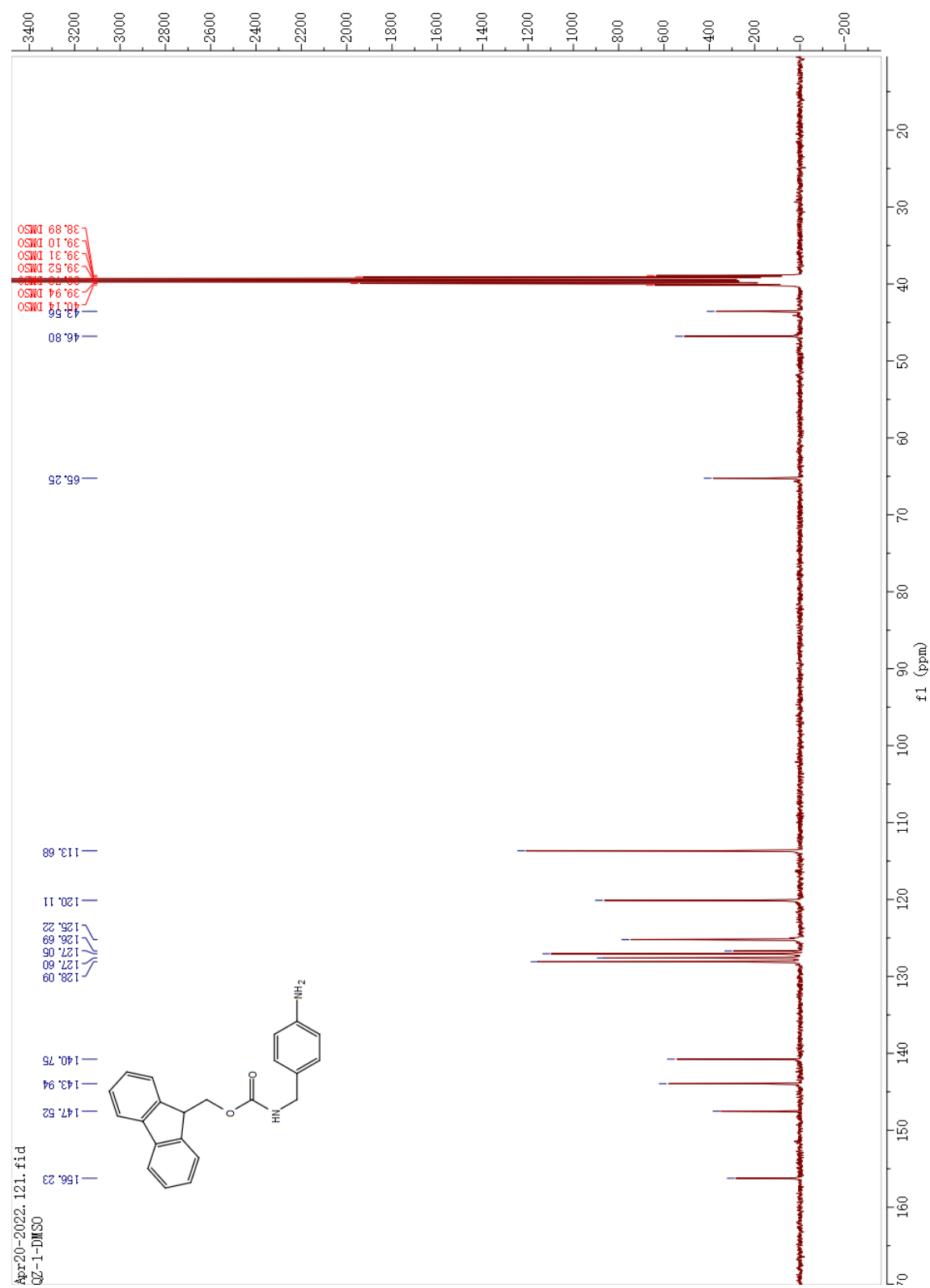
### 7.1.1 NMR spectra of Chapter 2 compounds

#### *(9H-fluoren-9-yl)methyl (4-aminobenzyl)carbamate (1)*

$^1\text{H}$  NMR (400 MHz, DMSO- $d_6$ )



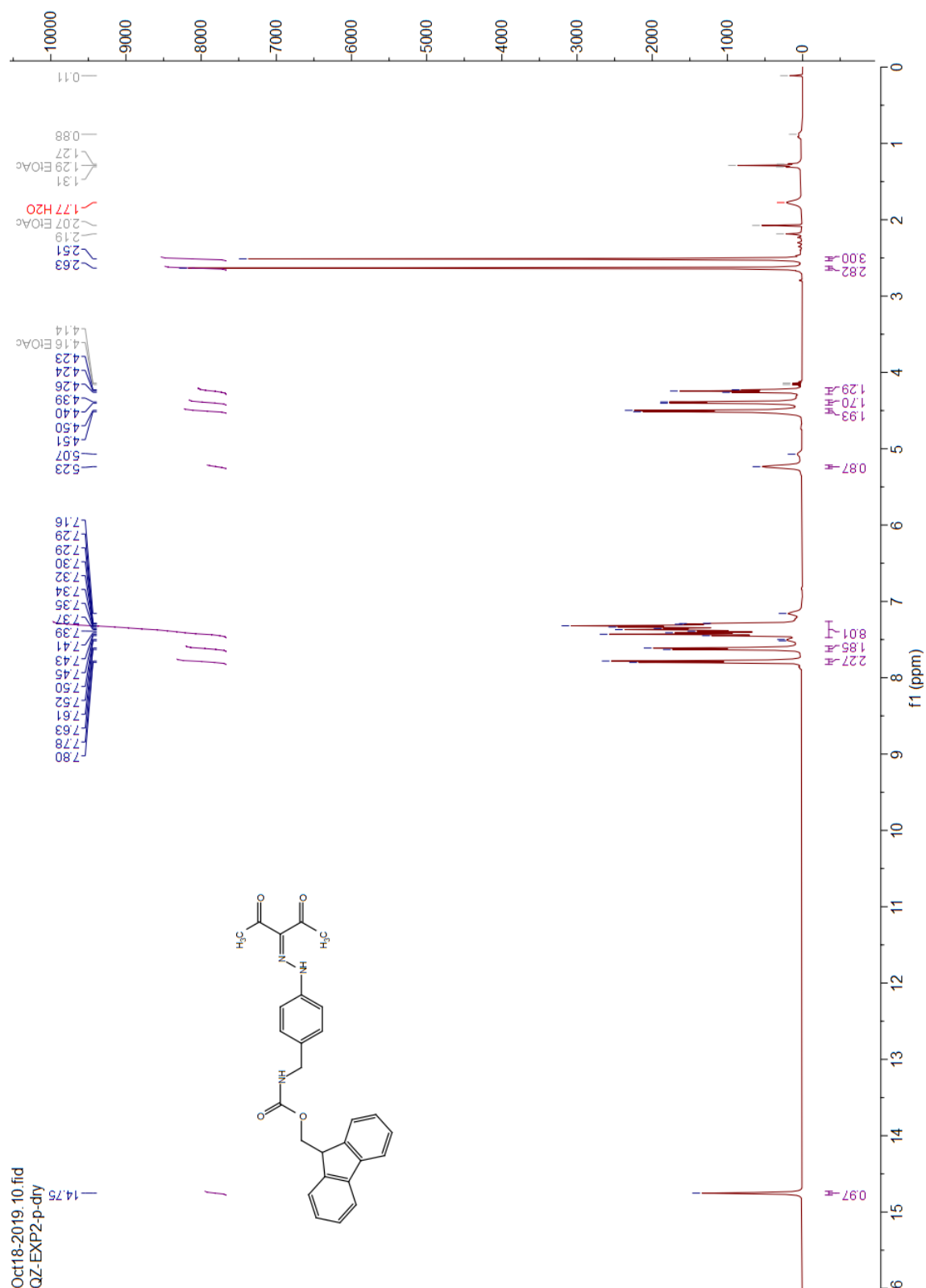
$^{13}\text{C}$  NMR (101 MHz,  $\text{DMSO}-d_6$ )



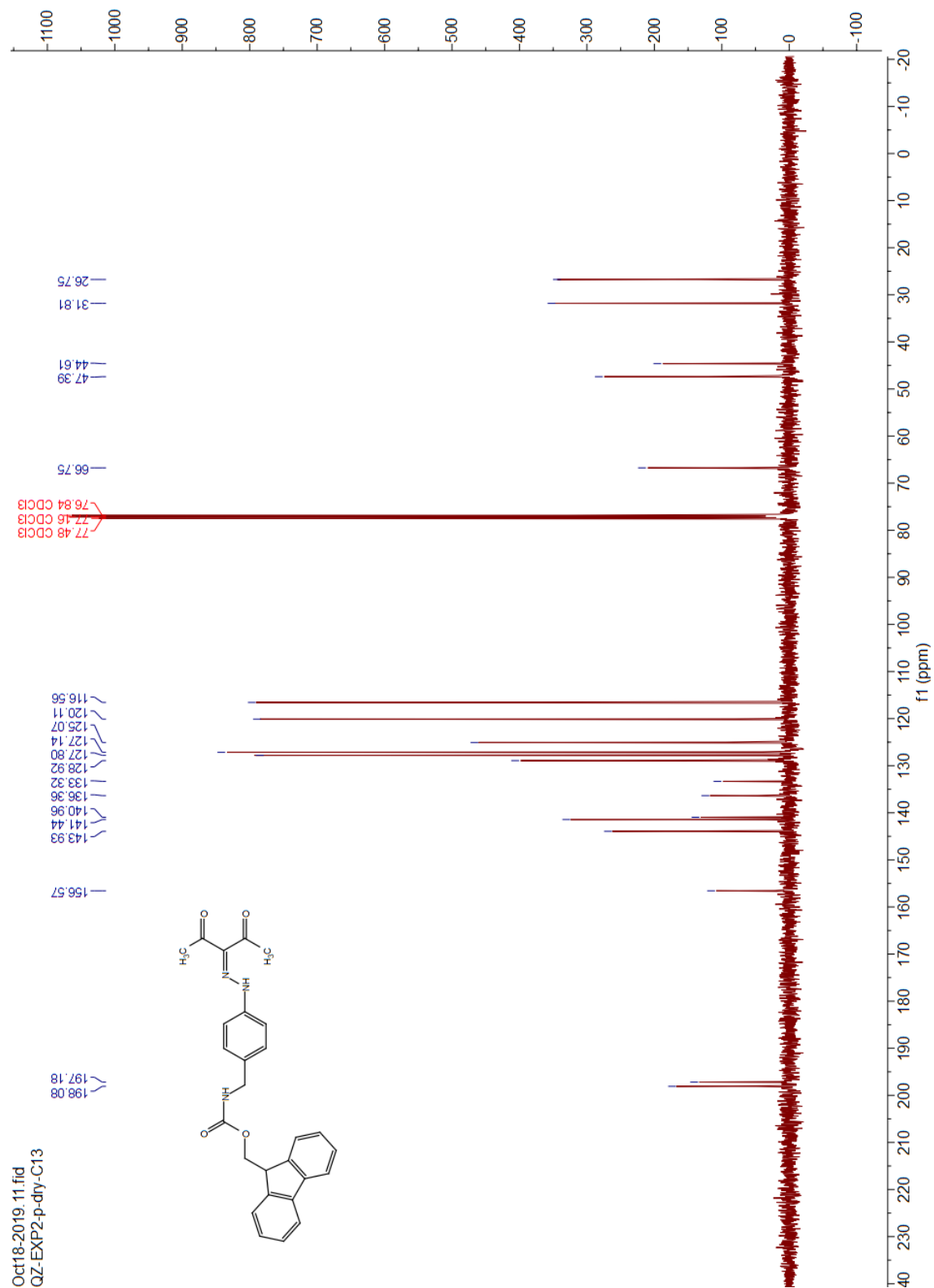


**(9H-fluoren-9-yl)methyl(4-(2-(2,4-dioxopentan-3-ylidene)hydrazineyl)benzyl)carbamate (2)**

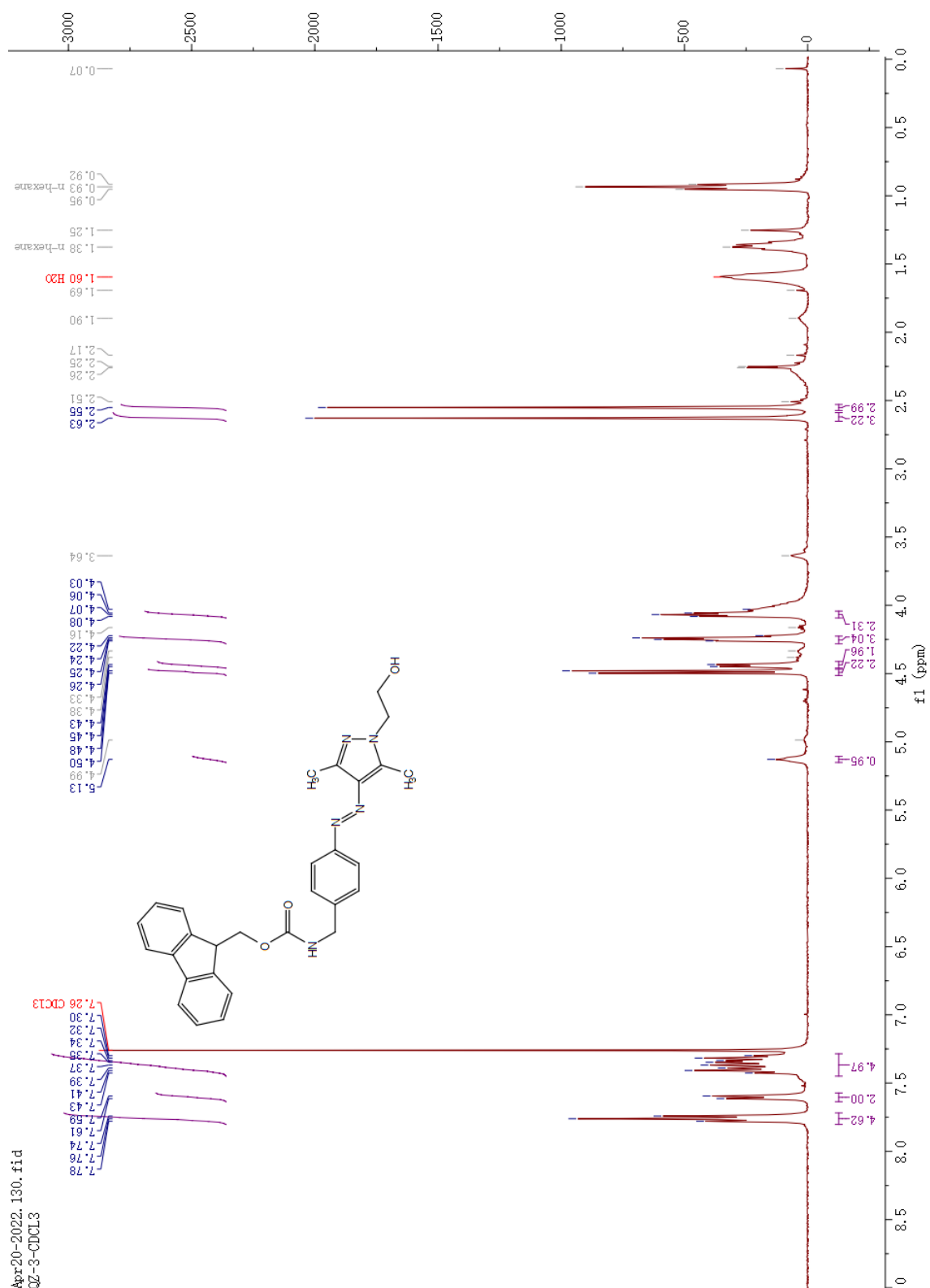
<sup>1</sup>H NMR (400 MHz, CDCl<sub>3</sub>)



**$^{13}\text{C}$  NMR (101 MHz,  $\text{CDCl}_3$ )**



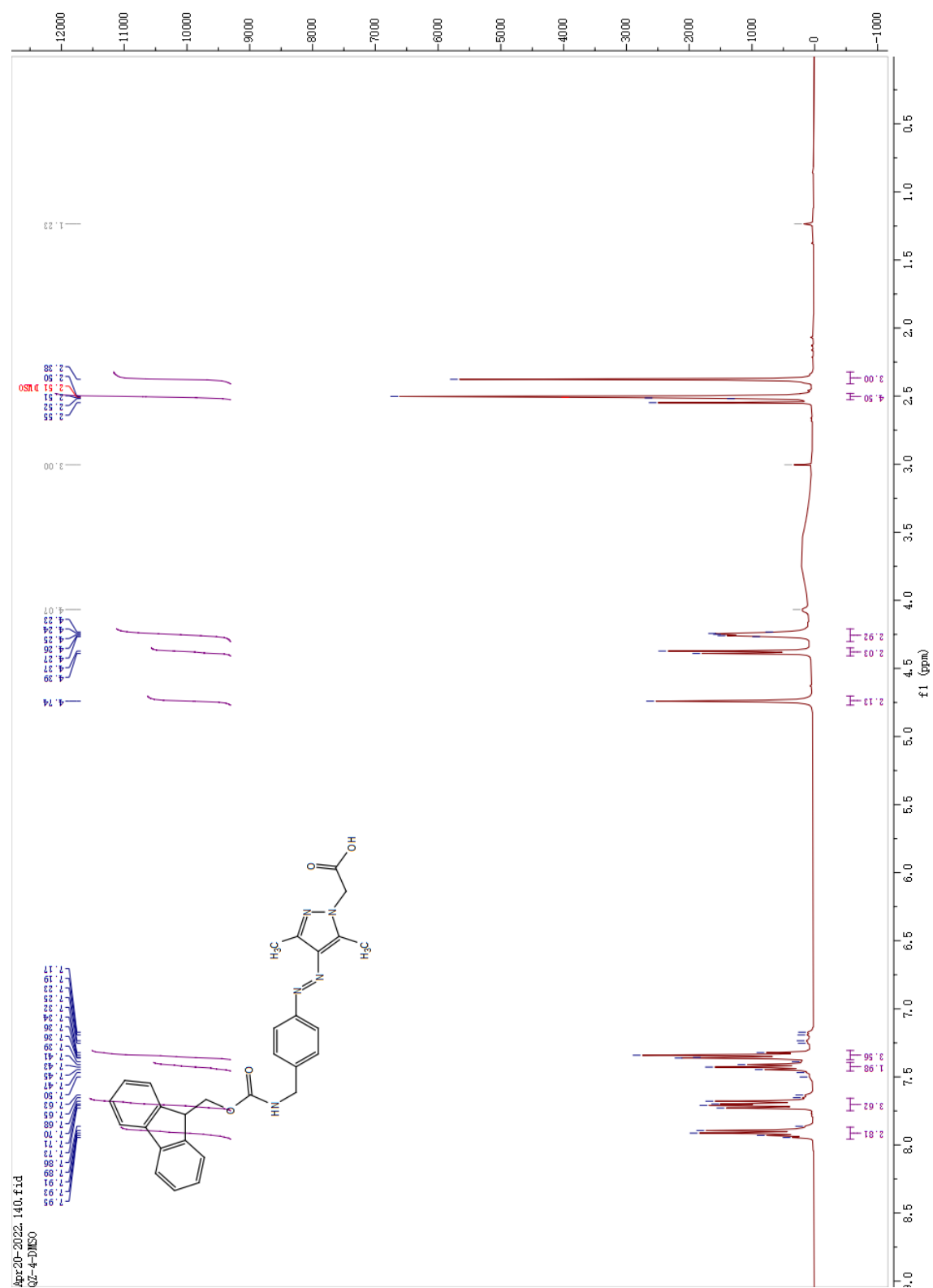
Oct18-2019\_11.fid  
QZ-EXP2-p-dty-C13

<sup>1</sup>H NMR (400 MHz, CDCl<sub>3</sub>)

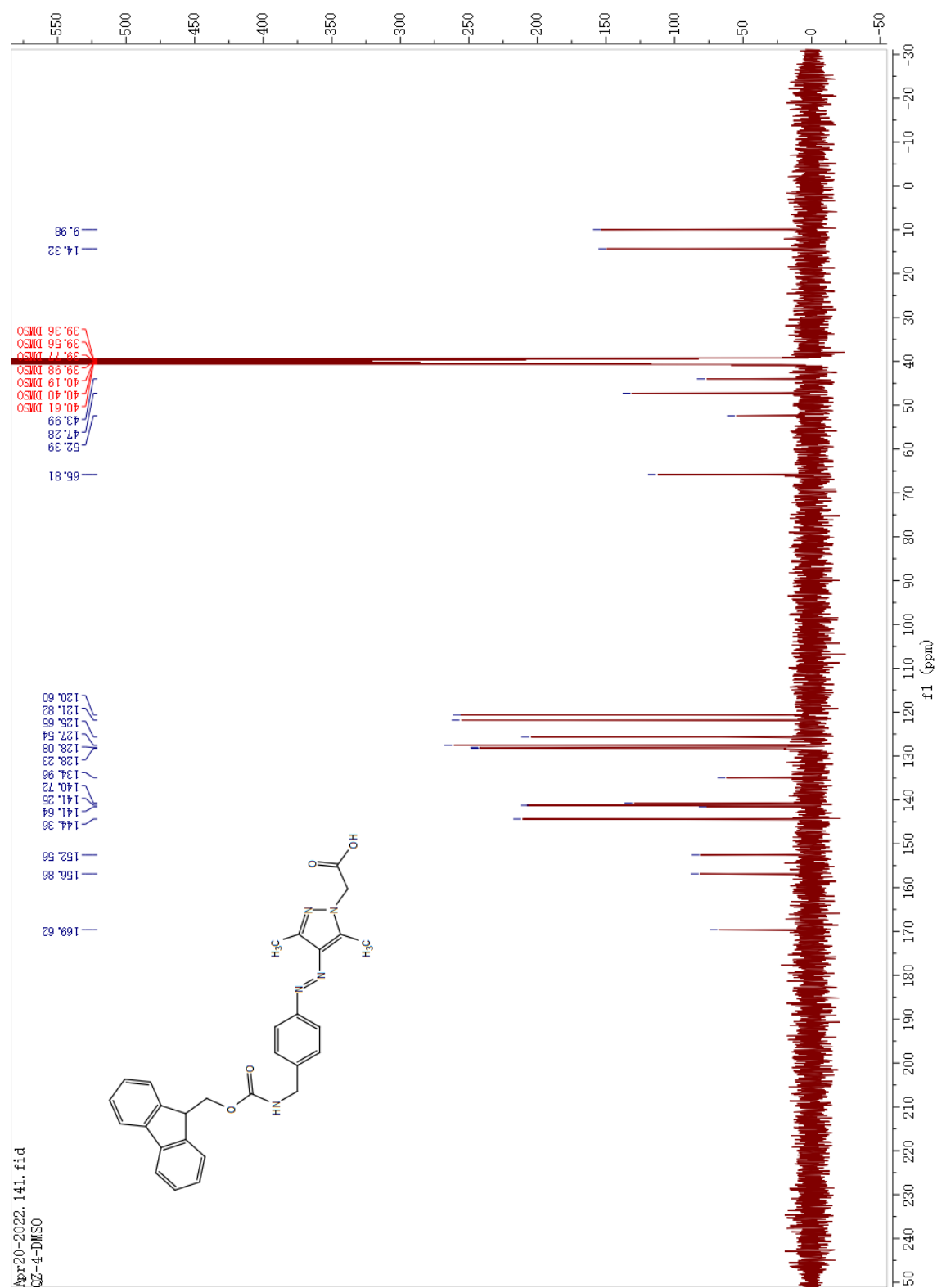
Chemical structure of compound 13l is shown as an inset. The structure is a triazole derivative with a fluorenyl group, a benzamide group, and a hydroxymethyl group. The <sup>13</sup>C NMR spectrum (CDCl<sub>3</sub>) shows the following peaks (ppm): 152.96, 144.02, 141.50, 128.23, 128.86, 127.85, 126.21, 125.14, 122.40, 120.15, 61.44, 50.30, 47.45, 44.94, 77.47 (CDCl<sub>3</sub>), 76.84 (CDCl<sub>3</sub>), 19.24, 13.87, 10.00.

**(E)-2-(4-(((4-((((9H-fluoren-9-yl)methoxy)carbonyl)amino) methyl)phenyl)diazenyl)-3,5-dimethyl-1H-pyrazol-1-yl) acetic acid (linker 4)**

<sup>1</sup>H NMR (400 MHz, DMSO-d<sub>6</sub>), >99.9% *E* isomer

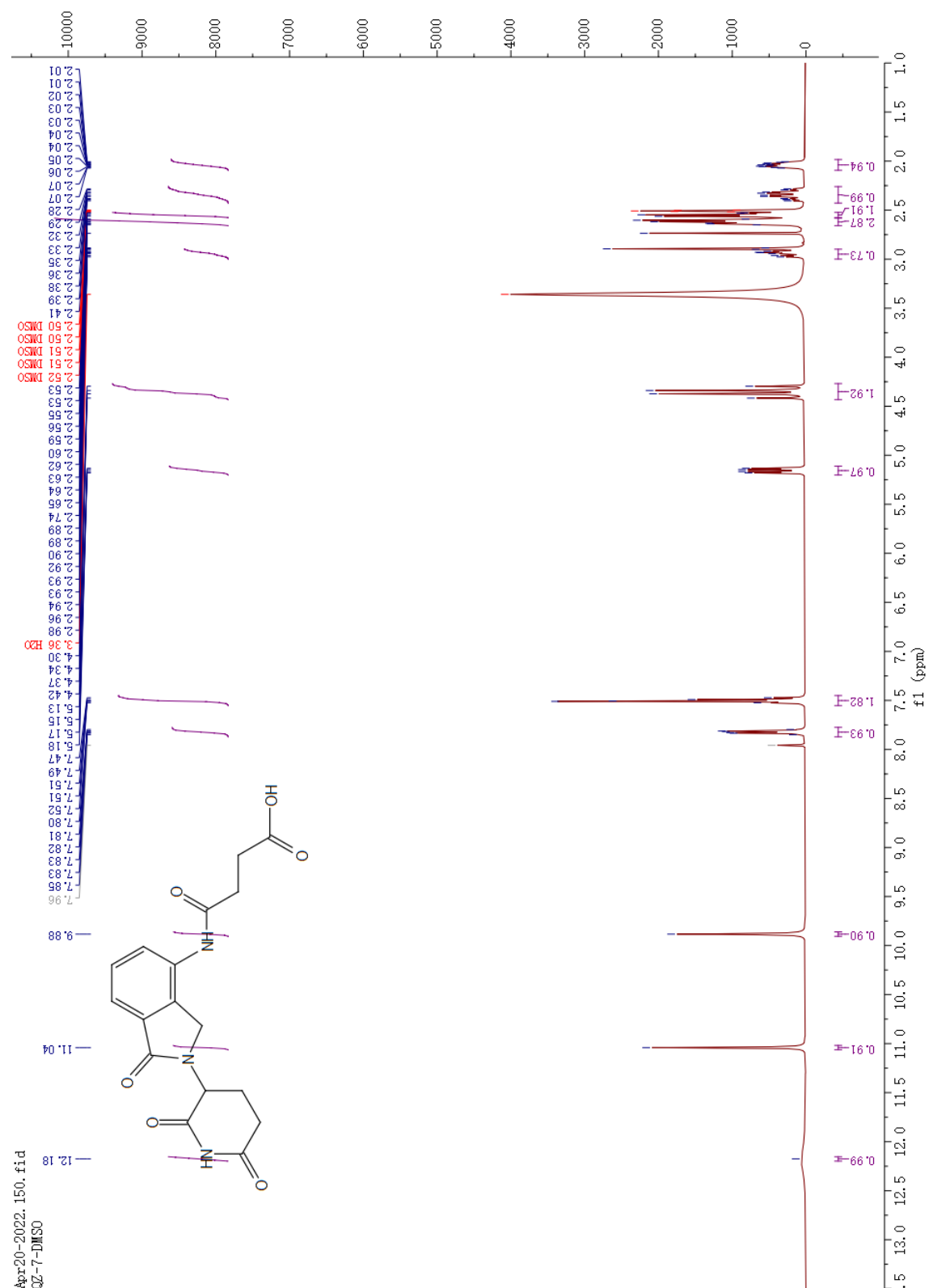


**$^{13}\text{C}$  NMR (101 MHz, DMSO- $d_6$ )**

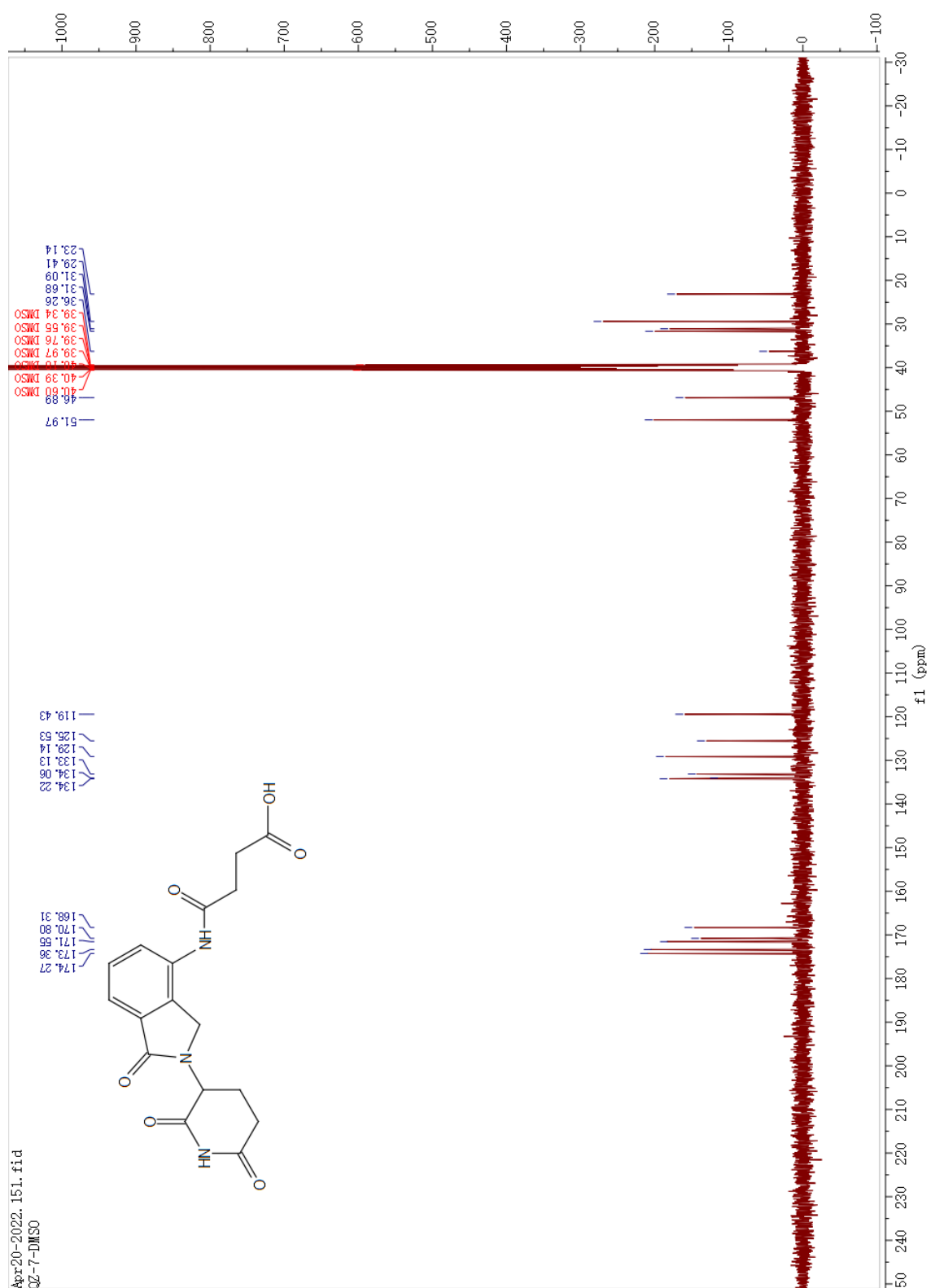


**4-((2-(2,6-dioxopiperidin-3-yl)-1-oxoisindolin-4-yl)amino)-4-oxobutanoic acid (5)**

<sup>1</sup>H NMR (400 MHz, DMSO-d<sub>6</sub>)



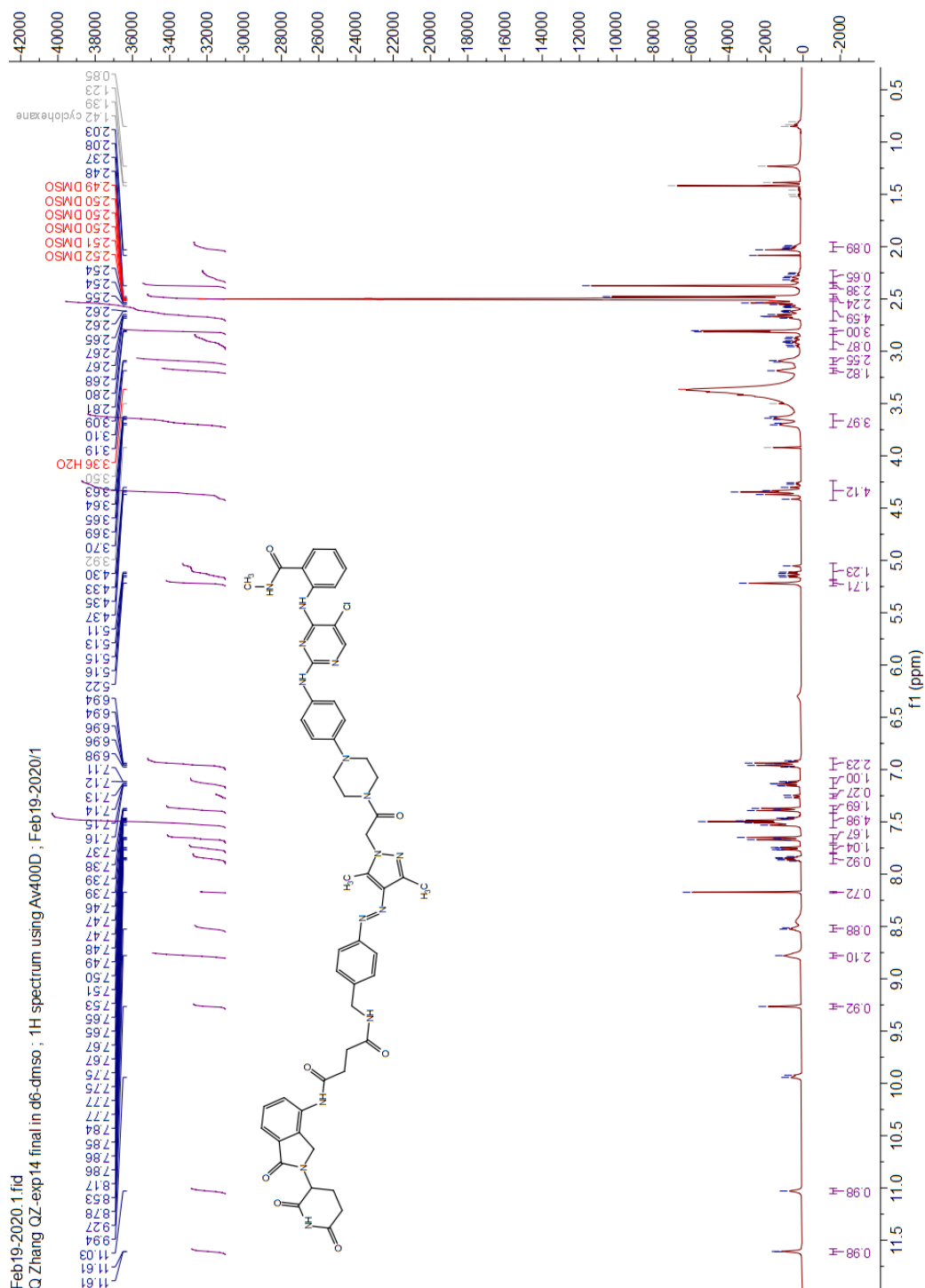
**$^{13}\text{C}$  NMR (101 MHz,  $\text{DMSO}-d_6$ )**



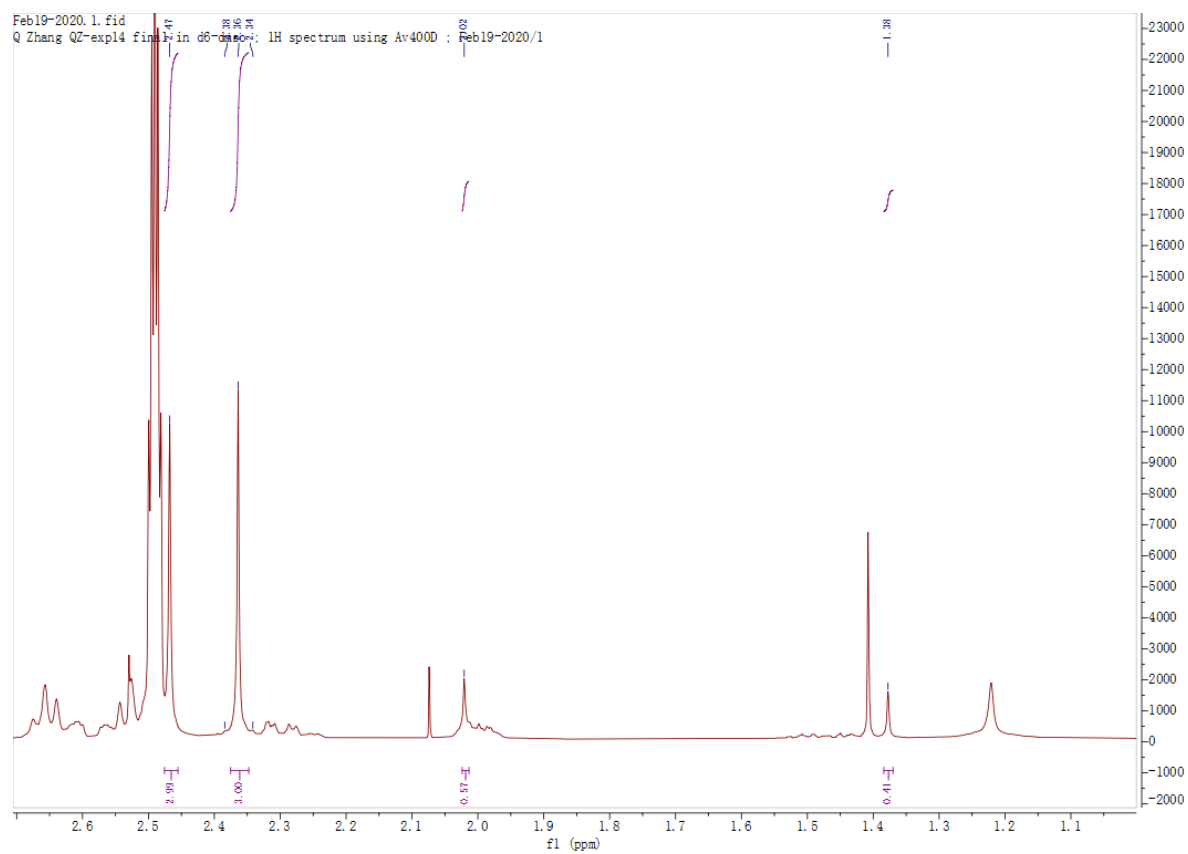


**(E)-N1-(4-((1-(2-(4-(4-((5-chloro-4-((2-(methylcarbamoyl)phenyl)amino)pyrimidin-2-yl)amino)phenyl)piperazin-1-yl)-2-oxoethyl)-3,5-dimethyl-1H-pyrazol-4-yl)diazenyl)benzyl)-N4-(2-(2,6-dioxopiperidin-3-yl)-1-oxoisindolin-4-yl)succinimide (7, AP-PROTAC-2)**

<sup>1</sup>H NMR (400 MHz, DMSO-d<sub>6</sub>)

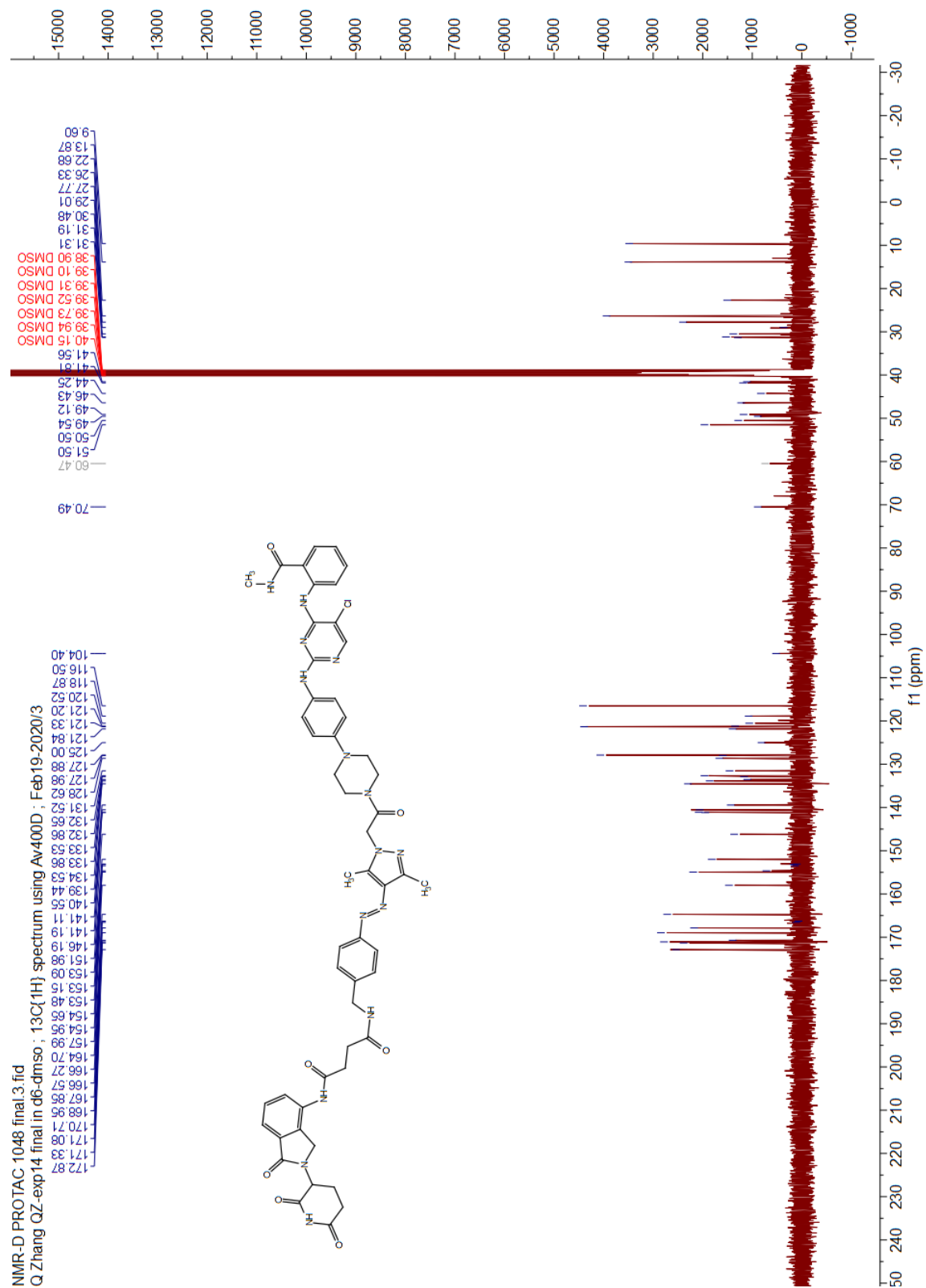


**$^1\text{H}$  NMR (400 MHz, DMSO- $d_6$ ), zoomed in**



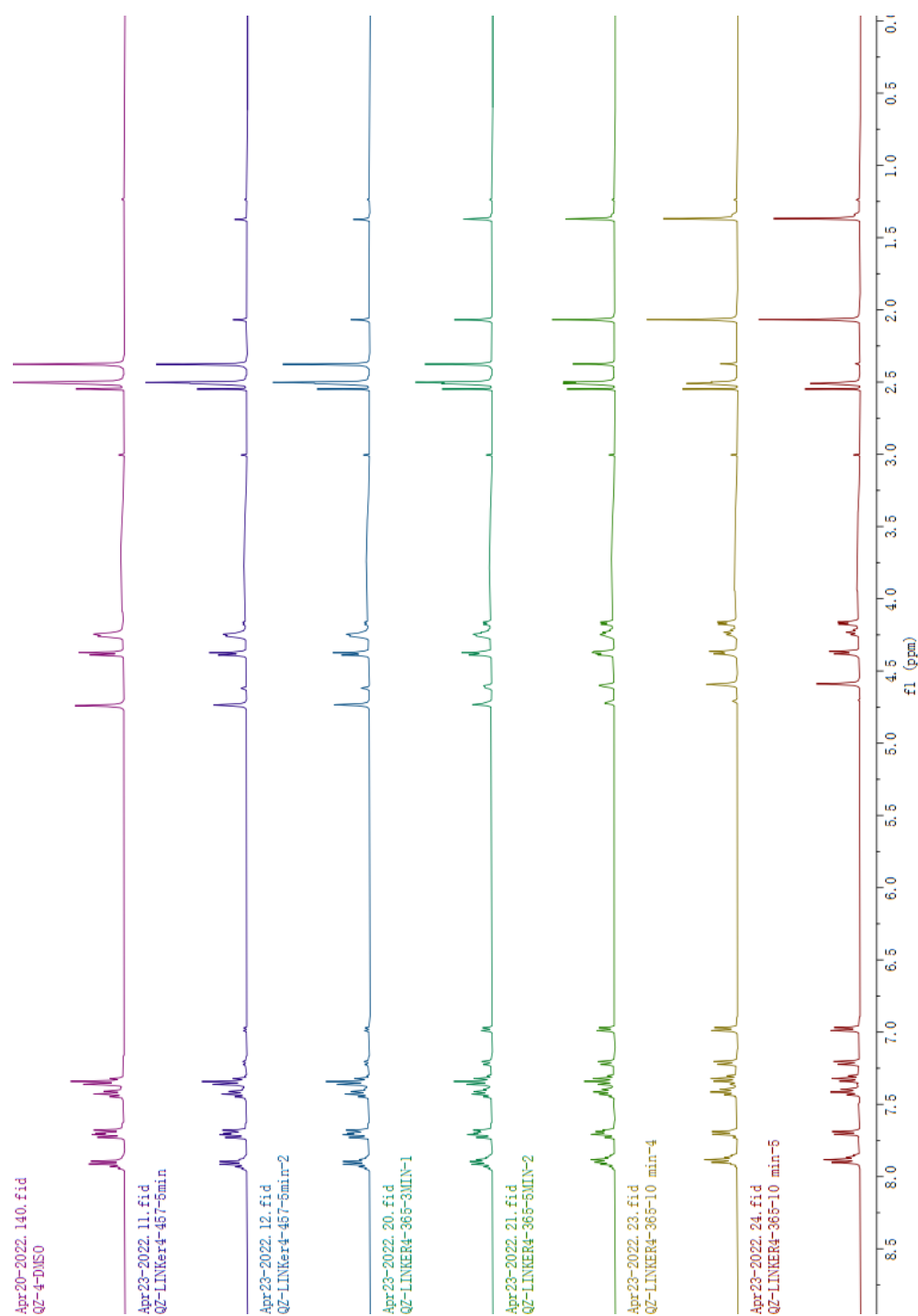
Representative pyrazole methyl proton peaks: *E* isomer: 2.48 (s, 3H), 2.37 (s, 3H). *Z* isomer: 2.02 (s, 3H), 1.38 (s, 3H).

$^{13}\text{C}$  NMR (101 MHz,  $\text{DMSO}-d_6$ )

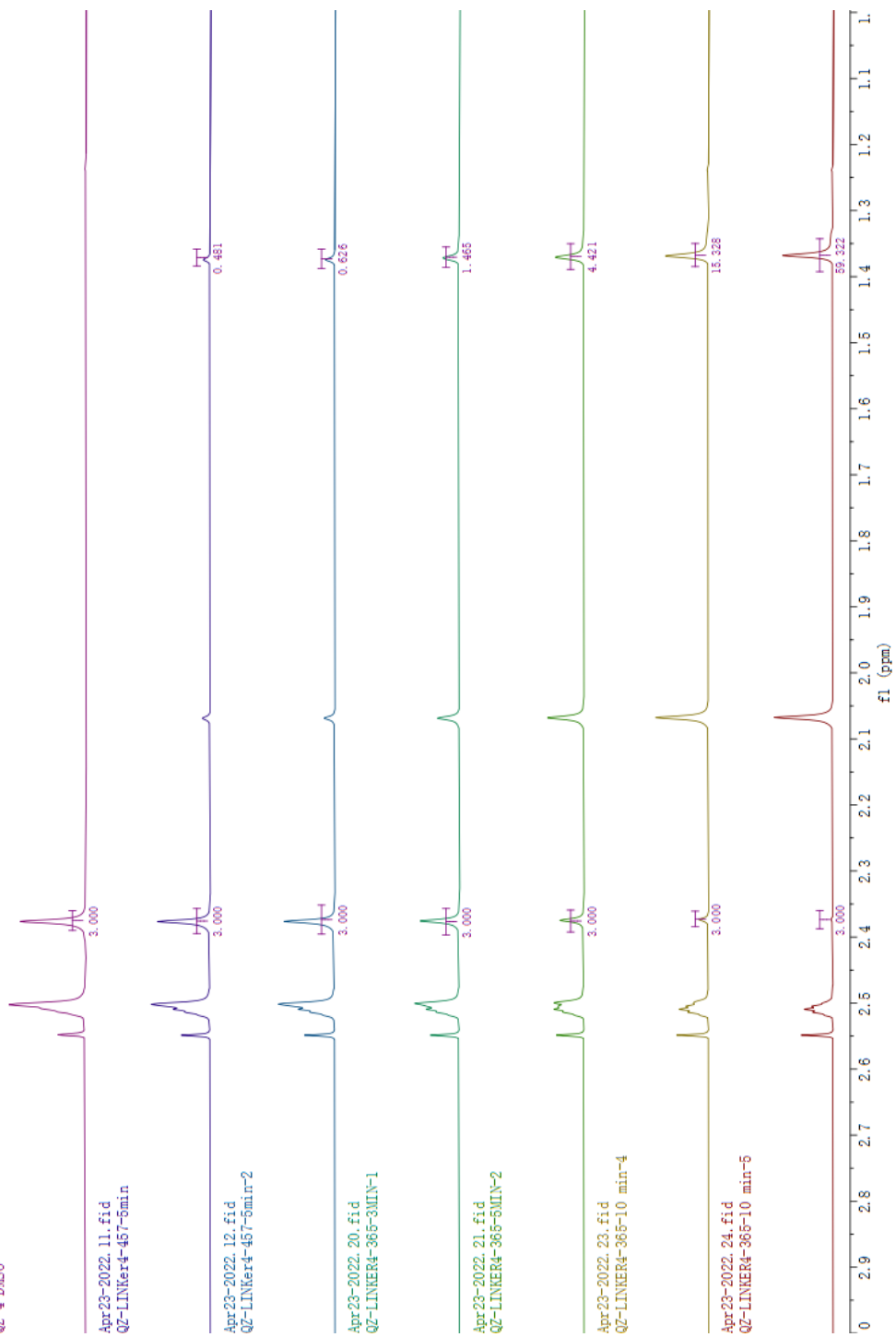


NMR-D PROTAC 1048 final.3.fid  
Q Zhang QZ-exp 14 final in d6-dmso ;  $^{13}\text{C}\{^1\text{H}\}$  spectrum using Av400D ; Feb 19-2020/3

## 7.1.2 NMR spectroscopy determination of PSS of linker 4



Apr20-2022\_140.fid  
QZ-4-DMSO



### 7.1.3 LC-MS chromatograms

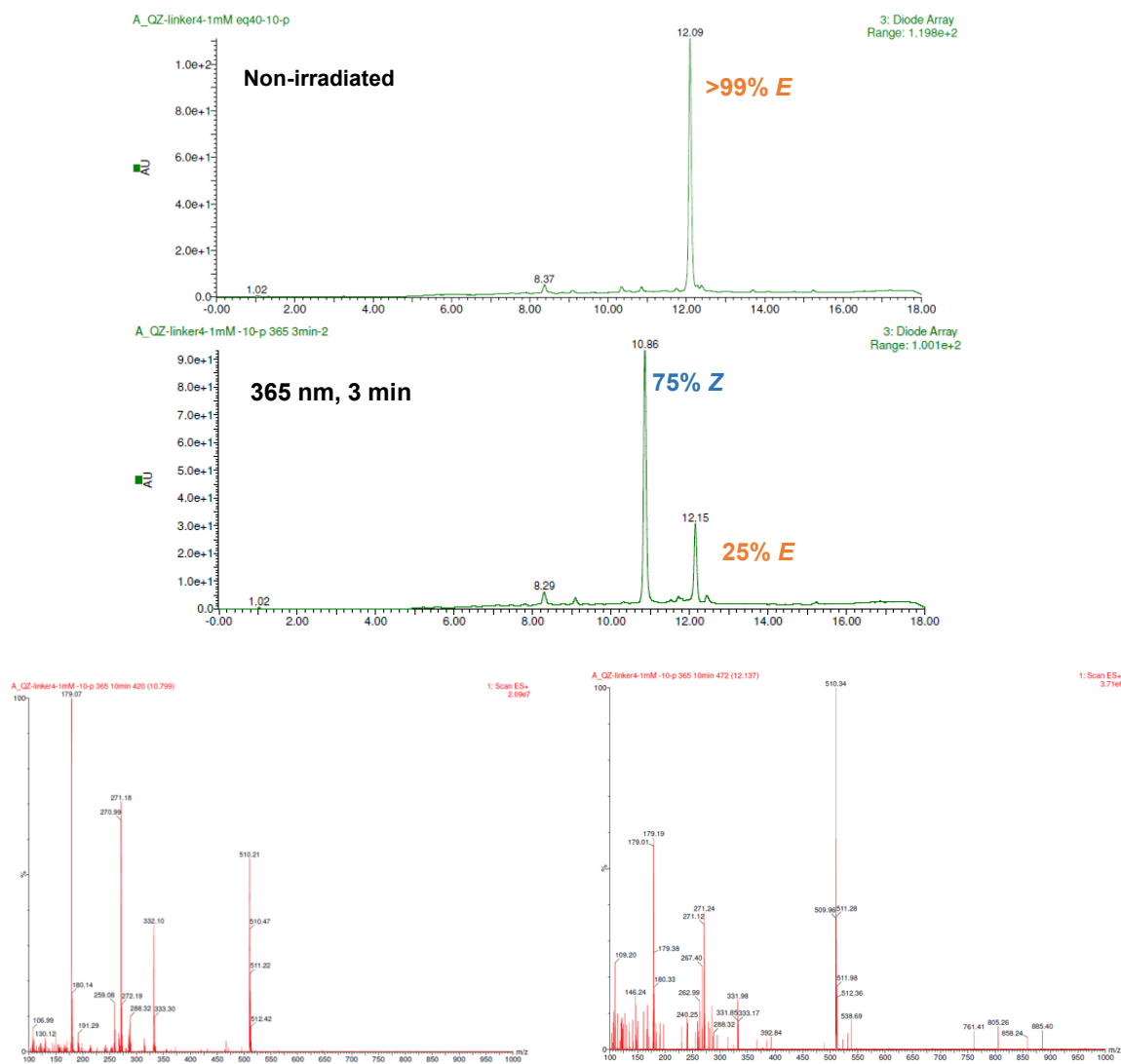


**Figure 7-1 LC-MS chromatograms of AAP linker 4**

Top: LC-MS chromatograms of a solution of 1 mM AAP linker 4 in 40% acetonitrile in water with 0.1% formic acid, recorded without irradiation or after irradiated with 365 nm LED for 3 min. Bottom: Positive mass profile at 10.8 min and 12.1 min after irradiation.

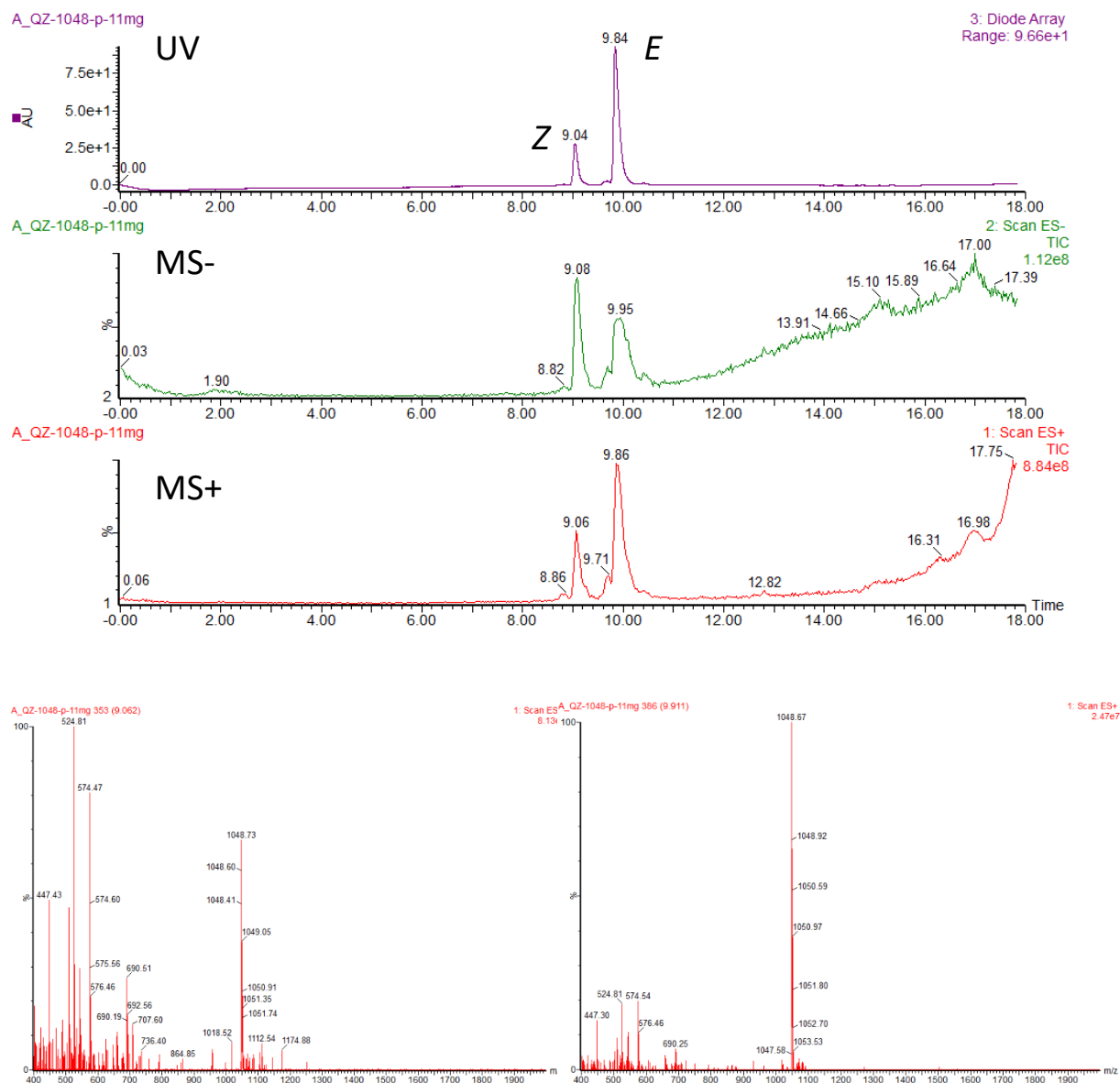


**Figure 7-2. LC-MS chromatograms of AP-PROTAC-2**

LC-MS chromatograms of a 0.1 mM solution of AP-PROTAC-2 in water with 20% acetonitrile, non-irradiated, and exposed to ambient light. Bottom: Positive mass profile at 9.06 min and 9.91 min.

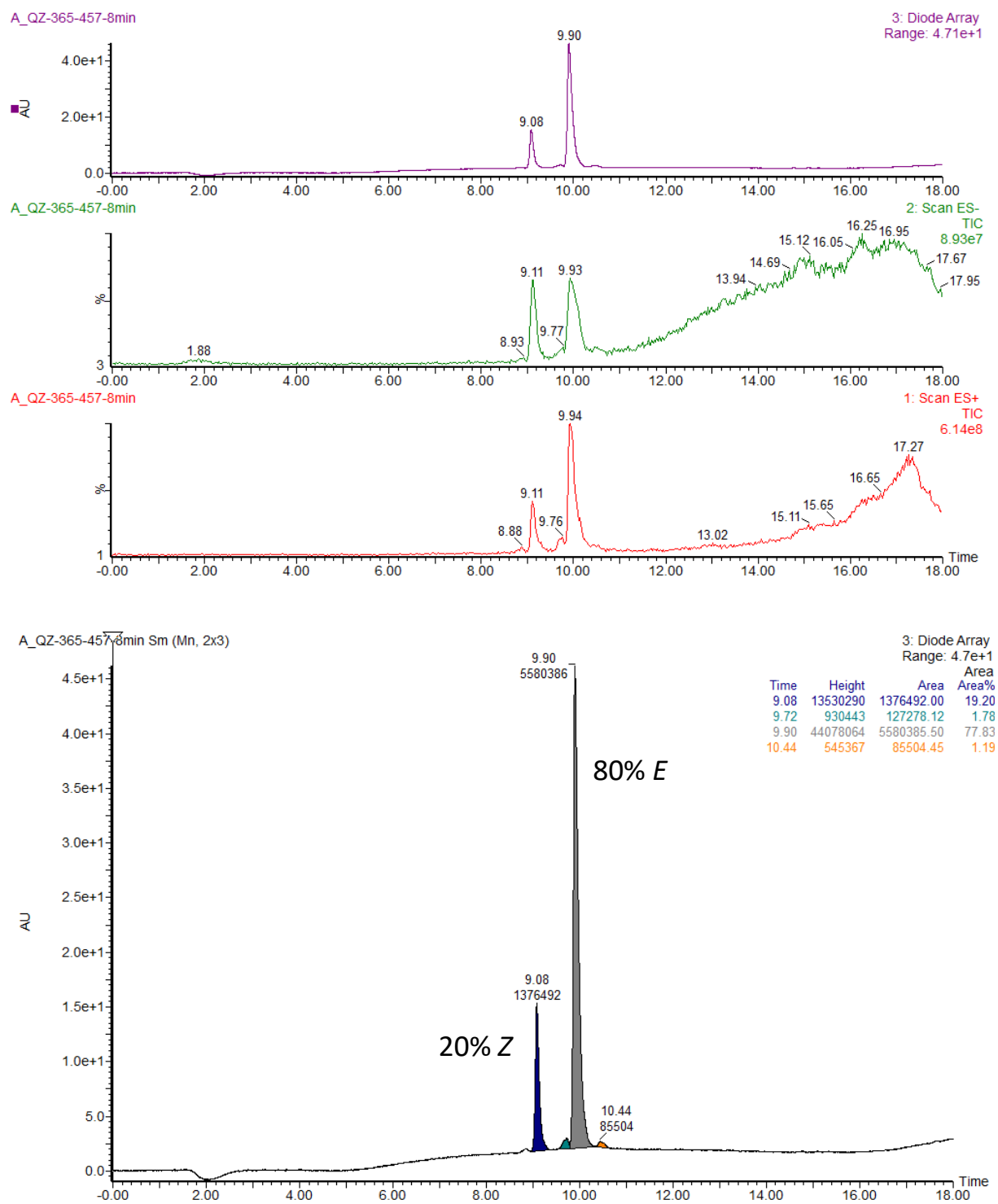


**Figure 7-3. LC-MS chromatograms of AP-PROTAC-2, after 8 min of 457 nm irradiation**

LC-MS chromatograms of a 0.1 mM solution of AP-PROTAC-2 in water with 20% acetonitrile, after 8 min of 457 nm irradiation. The area under the curve of the diode array showed a PSS of 80% E and 20% Z.



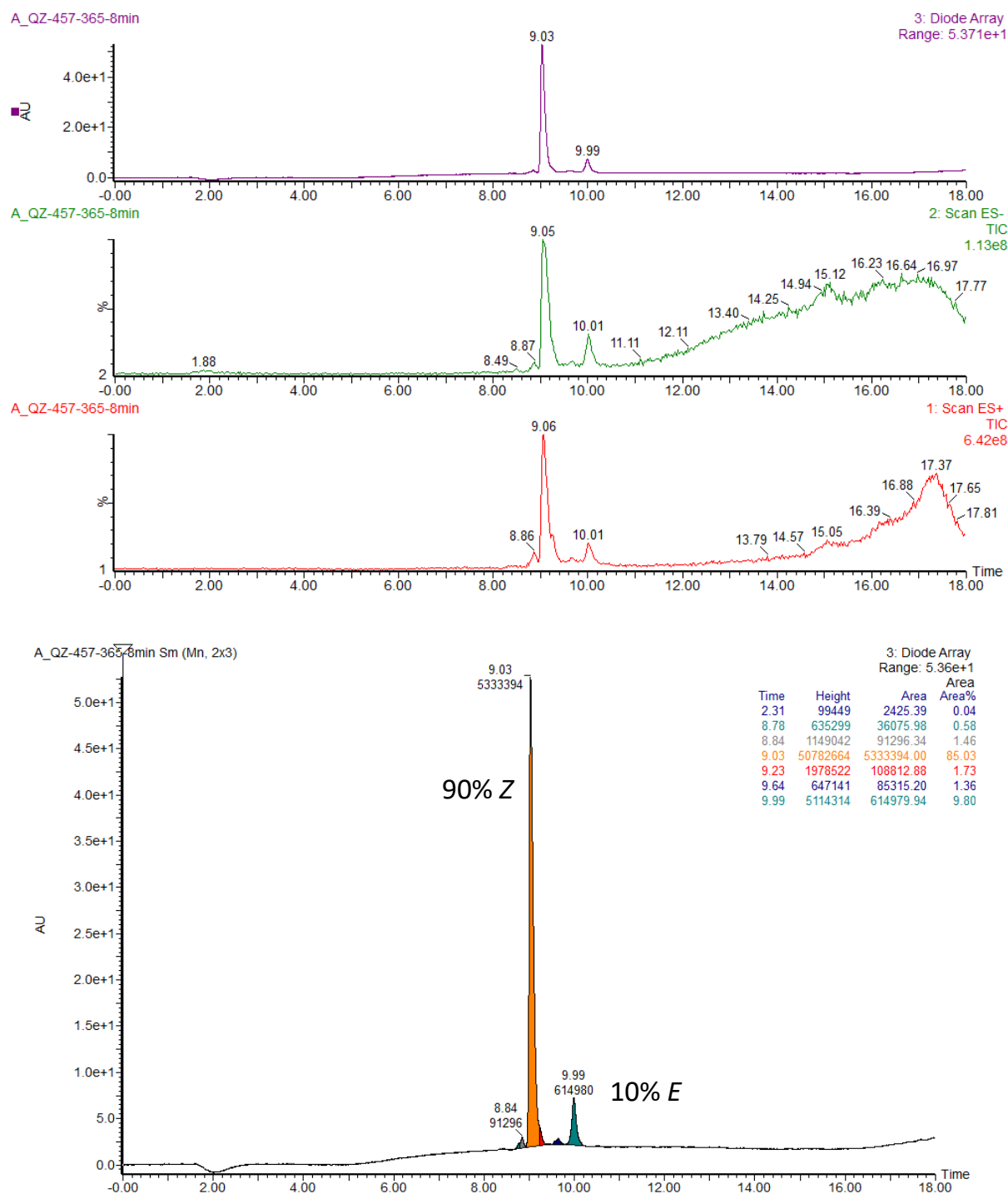


**Figure 7-4. LC-MS chromatograms of AP-PROTAC-2 with irradiation, after 8 min of 457 nm irradiation and followed by 8 min of 365 nm irradiation**

LC-MS chromatograms of a 0.1 mM solution of AP-PROTAC-2 in water with 20% acetonitrile, after 8 min of 457 nm irradiation and followed by 8 min of 365 nm irradiation. The area under the curve of the diode array showed a PSS showed a PSS of 90% Z and 10% E.

### 7.1.4 UV-Vis spectra

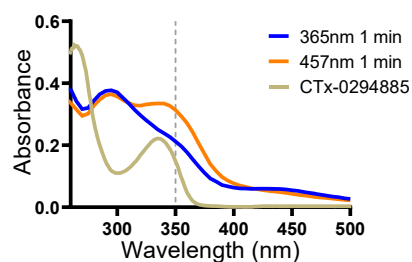


**Figure 7-5 UV-Vis spectra of a solution of CTx-0294885 in DMSO (ca. 10 µM)**

For comparison, the spectra of *E* or *Z*-enriched AP-PROTAC-2 were plotted in the same graph.

### 7.1.5 Cytotoxicity assay of AP-PROTAC-2

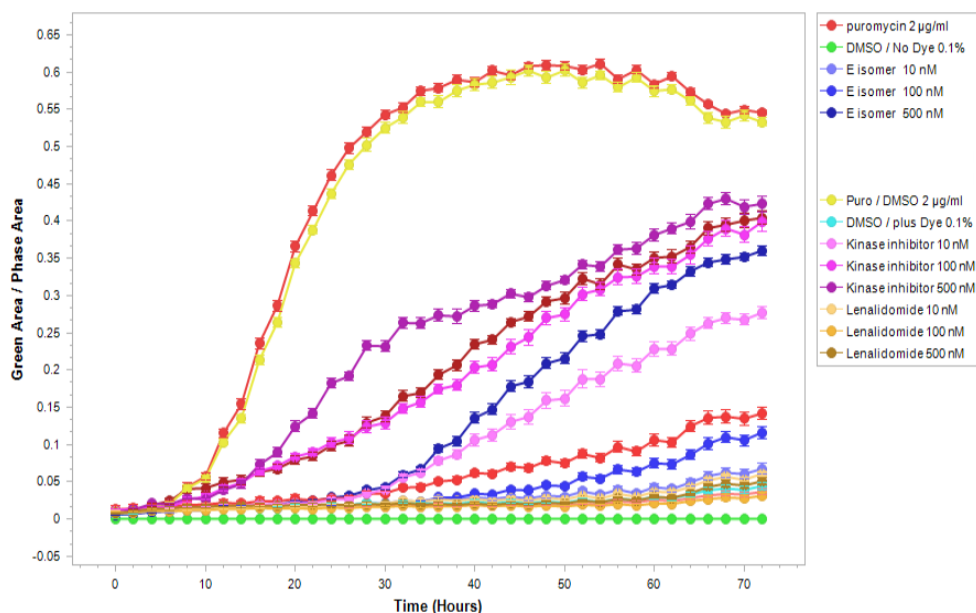


**Figure 7-6 Cytotoxicity assays of AP-PROTAC-2**

MDA-MD-231 cells were treated with 10 nM, 100 nM, 500 nM of (*E*-enriched)-AP-PROTAC-2, kinase inhibitor CTx-0294885, lenalidomide, or 0.1% DMSO and puromycin (2 µg/mL). The signal of SYTOX™ Green Nucleic Acid Stain over cell phase area was plotted against time of treatment.

### 7.1.6 Fold change plot in proteomics analysis of AP-PROTAC-2

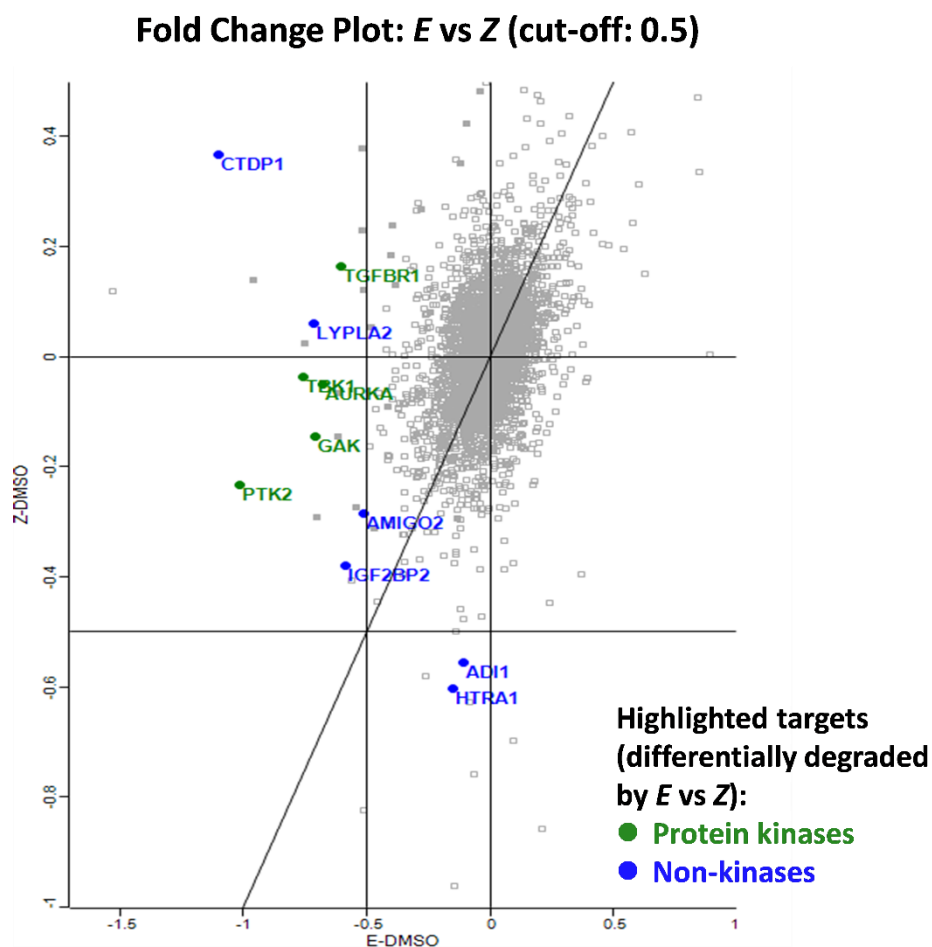


**Figure 7-7 Fold change plot in proteomics analysis of AP-PROTAC-2**

Fold change (FC) of (*E*-enriched)-AP-PROTAC-2 treated sample versus DMSO control group (*E*-enriched–DMSO) plotted against Fold change of (*Z*-enriched)-AP-PROTAC-2 treated sample versus DMSO control (*Z*-enriched–DMSO). Highlighted are possible proteins differentially degraded with (*E*-enriched) or (*Z*-enriched)-AP-PROTAC-2 treatment.

### 7.1.7 Immunoblots

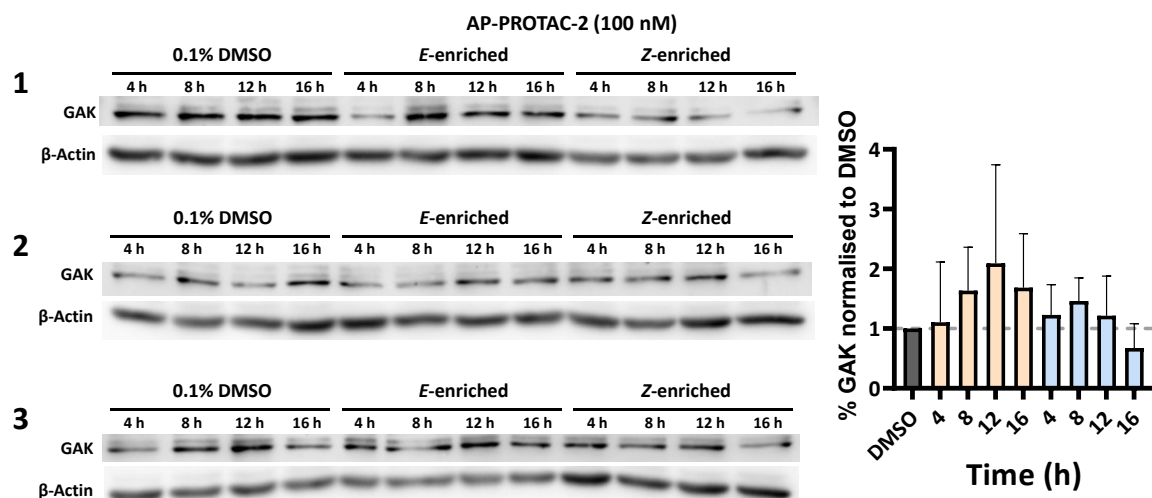


**Figure 7-8. Immunoblots and quantification of GAK and  $\beta$ -actin in MDA-MB-231 cells after treatment**

Immunoblots and quantification of GAK and  $\beta$ -actin in MDA-MB-231 cells after 4 h, 8 h, 12 h, or 16 h treatment of 100 nM (*E*-enriched)-AP-PROTAC-2 or (*Z*-enriched) isomer (with intermittent irradiation every 3 h for *Z* isomer treated cells). Bars represent mean signal normalized to  $\beta$ -actin, reported as the mean and SD of  $n = 3$  biological replicates.

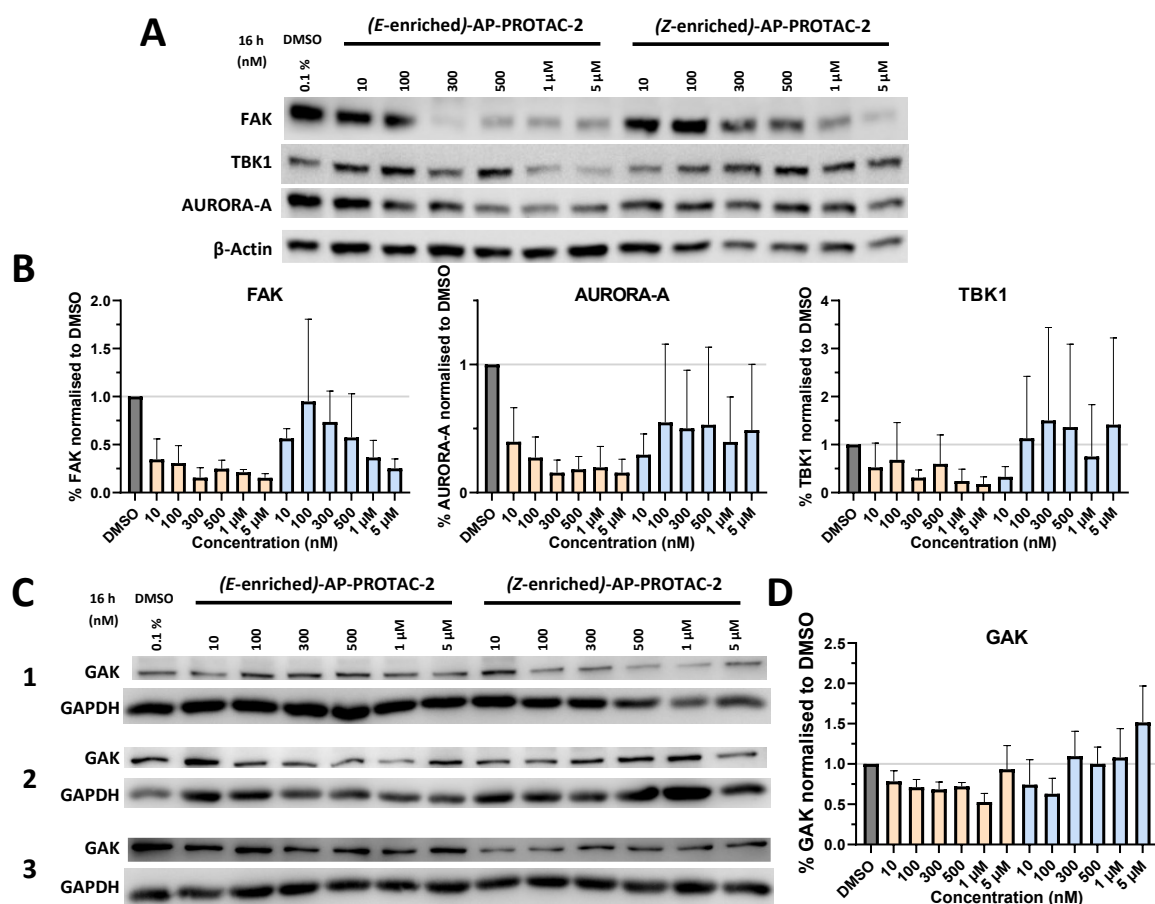


**Figure 7-9. Immunoblots and quantification of FAK, AURORA-A, TBK1, GAK in MDA-MB-231 cells after treatment**

(A) Immunoblots and (B) quantification of FAK, TBK1, AURORA-A, and  $\beta$ -actin in MDA-MB-231 cells after 16 h treatment of indicated concentrations of compounds. (C) Immunoblots and (D) quantification of GAK, and  $\beta$ -actin in the same treatment. Bars represent mean signal normalized to  $\beta$ -actin, reported as the mean and SD of  $n = 3$  biological replicates.

## 7.2 Chapter 3 Additional data

### 7.2.1 LC-MS spectra of ADC linkers in TFA

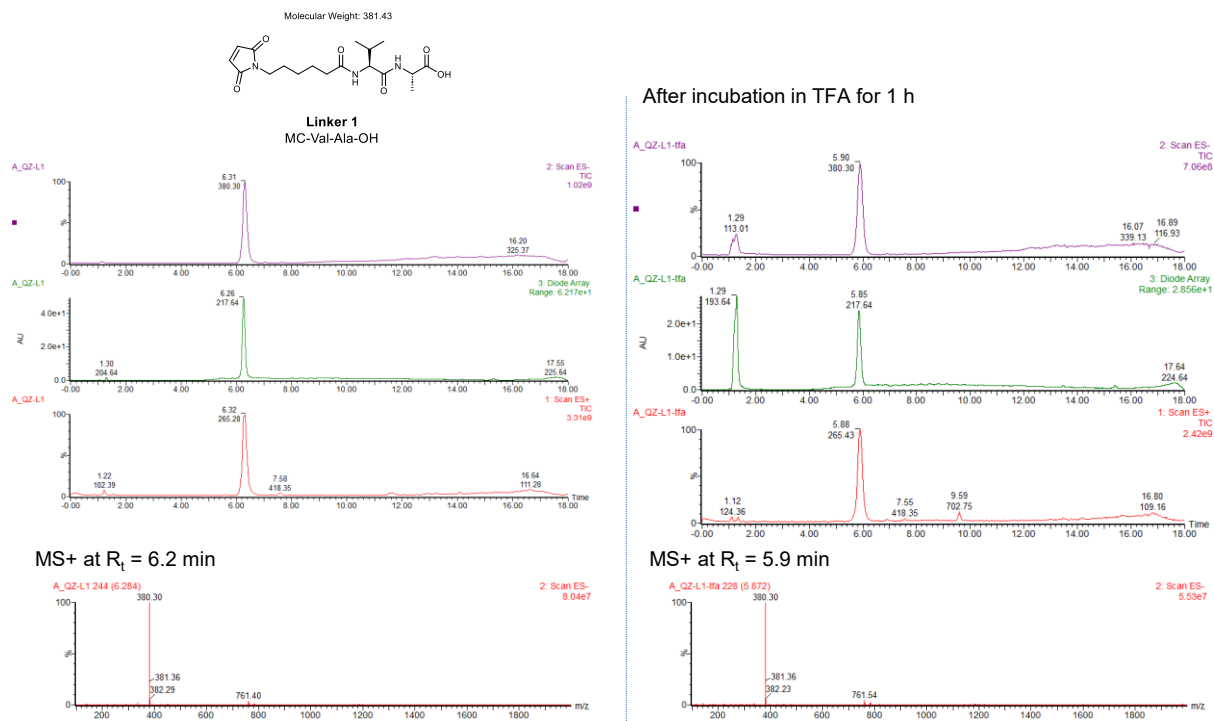


**Figure 7-10** LC-MS spectra of ADC linker 1 in 20% MeCN in water with 0.1% formic acid with eq20 gradient

Left: before incubation with TFA; Right: Compounds were incubated in pure TFA for 1 h with shaking and recorded LC-MS spectra in 20% MeCN in water with 0.1% formic acid with eq20 gradient.



## 7.2.2 Investigation of aspartimide formation during the synthesis of TD-PROTAC

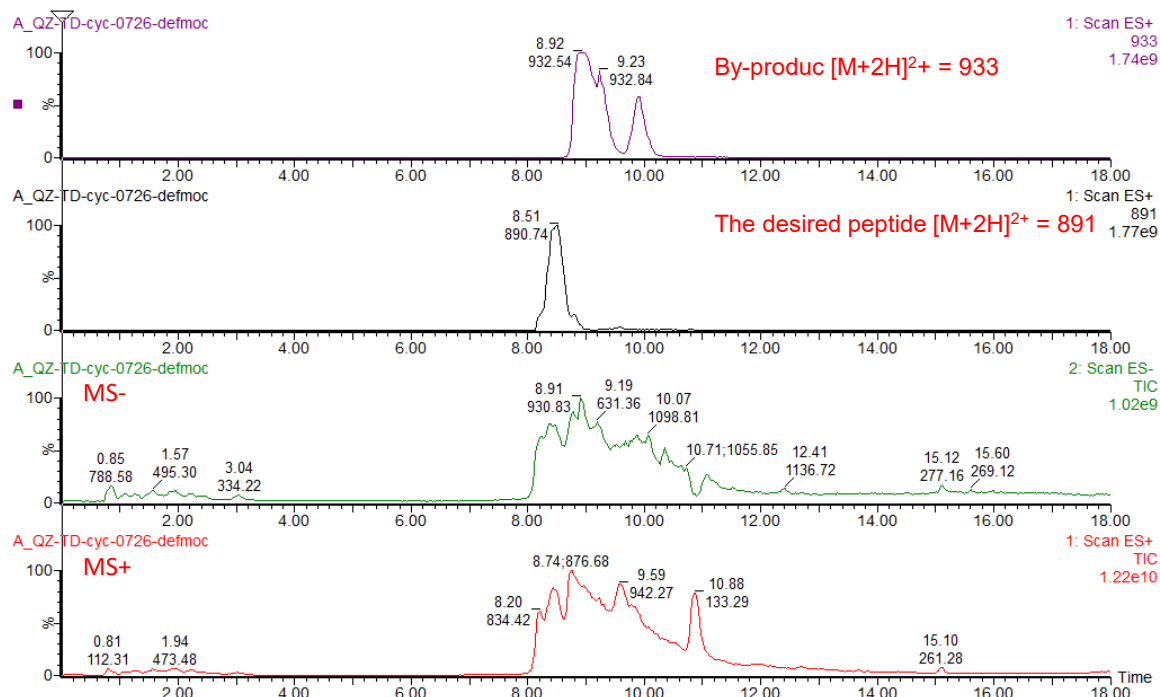


**Figure 7-13. Investigation of aspartimide formation during synthesis of TD-PROTAC**

LC-MS spectra of the cleaved mixture in synthesis of TD-PROTAC and m/z search for the desired product.



## 7.2.3 HPLC traces and LC-MS spectra of peptides in Chapter 3

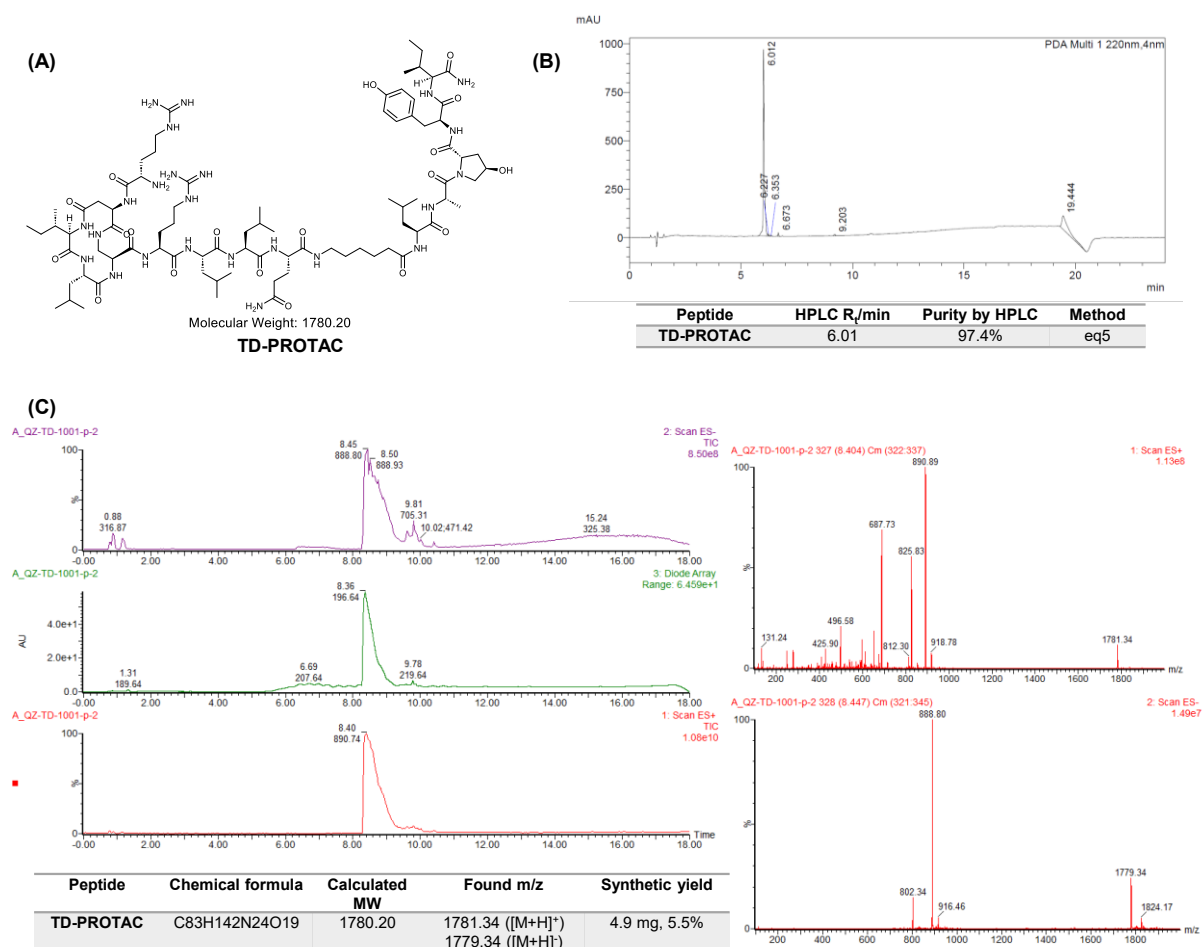


**Figure 7-14. TD-PROTAC peptide characterisation**

(A) Chemical structure of TD-PROTAC. (B) HPLC chromatogram using eq5 gradient. (C) LC-MS chromatograms using eq20 gradient, UV trace, MS positive and negative spectra.

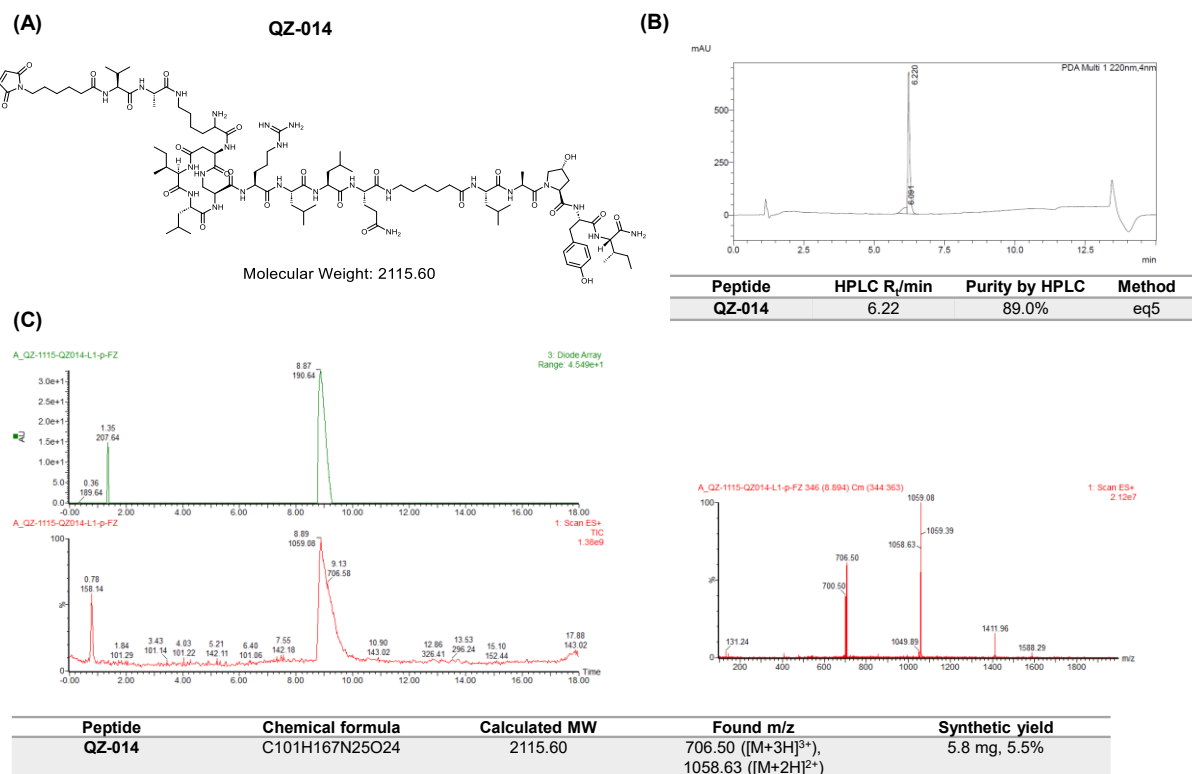


**Figure 7-15. QZ-014 peptide characterisation**

(A) Chemical structure of **QZ-014**. (B) HPLC chromatogram using eq5 gradient. (C) LC-MS chromatograms using eq20 gradient, UV trace, MS positive spectra.

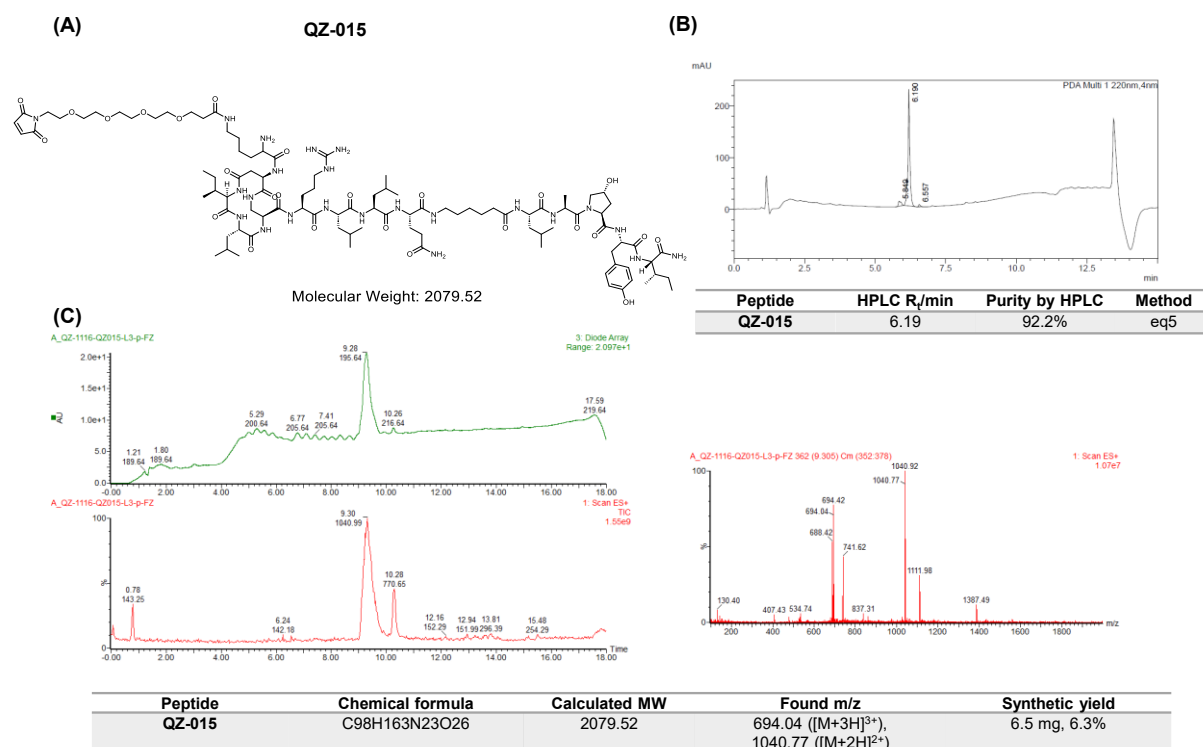


**Figure 7-16. QZ-015 peptide characterisation**

(A) Chemical structure of **QZ-015**. (B) HPLC chromatogram using eq5 gradient. (C) LC-MS chromatograms using eq20 gradient, UV trace, MS positive spectra.

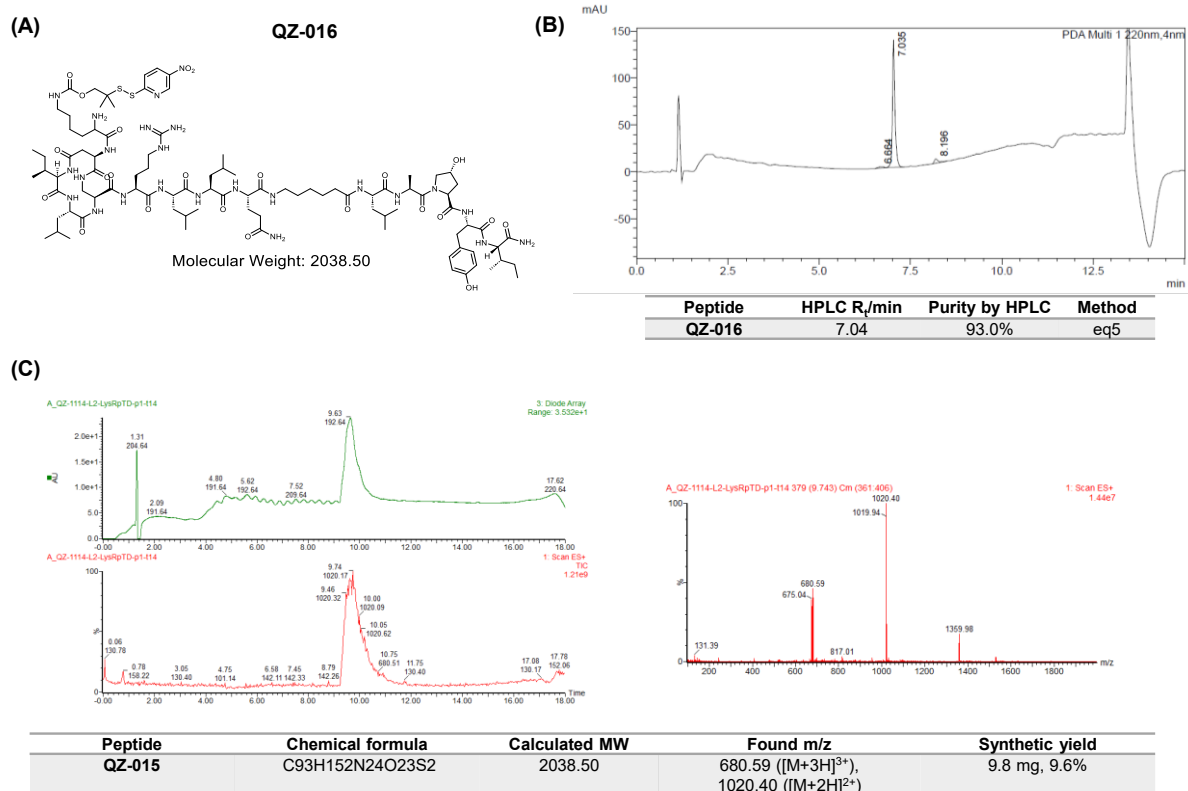


**Figure 7-17. QZ-016 peptide characterisation**

(A) Chemical structure of **QZ-016**. (B) HPLC chromatogram using eq5 gradient. (C) LC-MS chromatograms using eq20 gradient, UV trace, MS positive spectra.

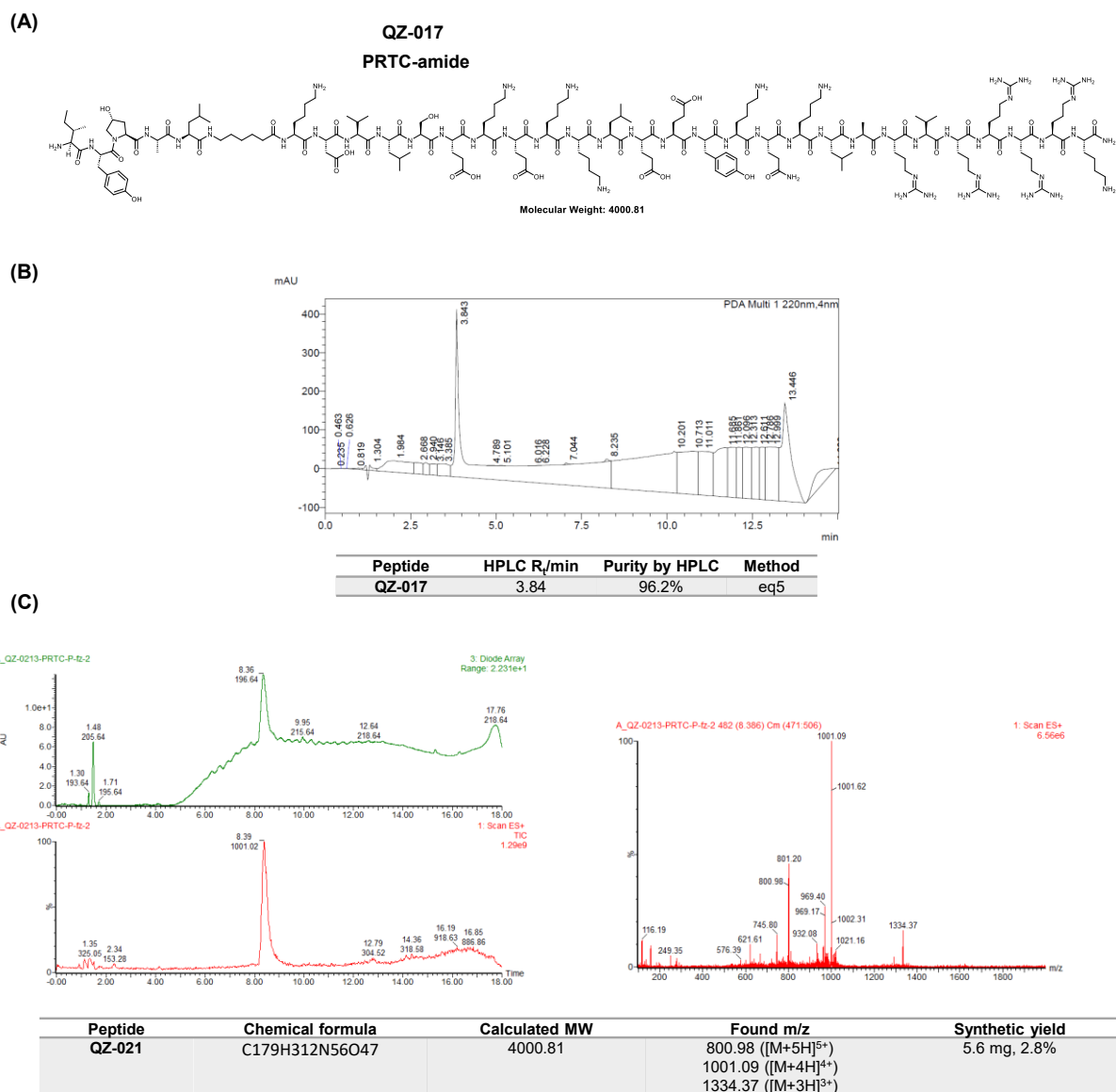


**Figure 7-18 QZ-017 peptide characterisation**

(A) Chemical structure of **QZ-017**. (B) HPLC chromatogram using eq5 gradient. (C) LC-MS chromatograms using eq20 gradient, UV trace, MS positive spectra.

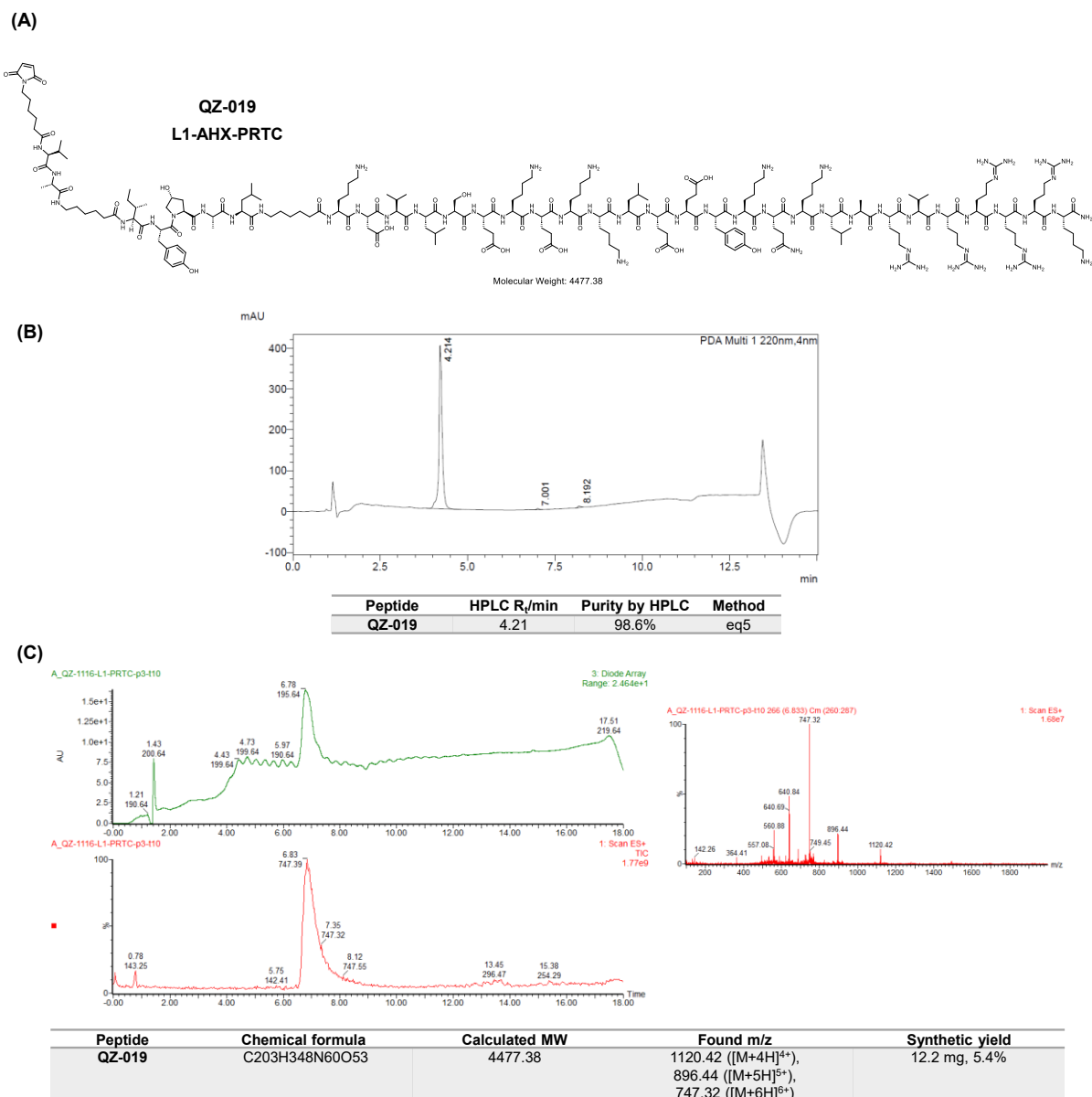


**Figure 7-19. QZ-019 peptide characterisation**

(A) Chemical structure of **QZ-019**. (B) HPLC chromatogram using eq5 gradient. (C) LC-MS chromatograms using eq20 gradient, UV trace, MS positive spectra.

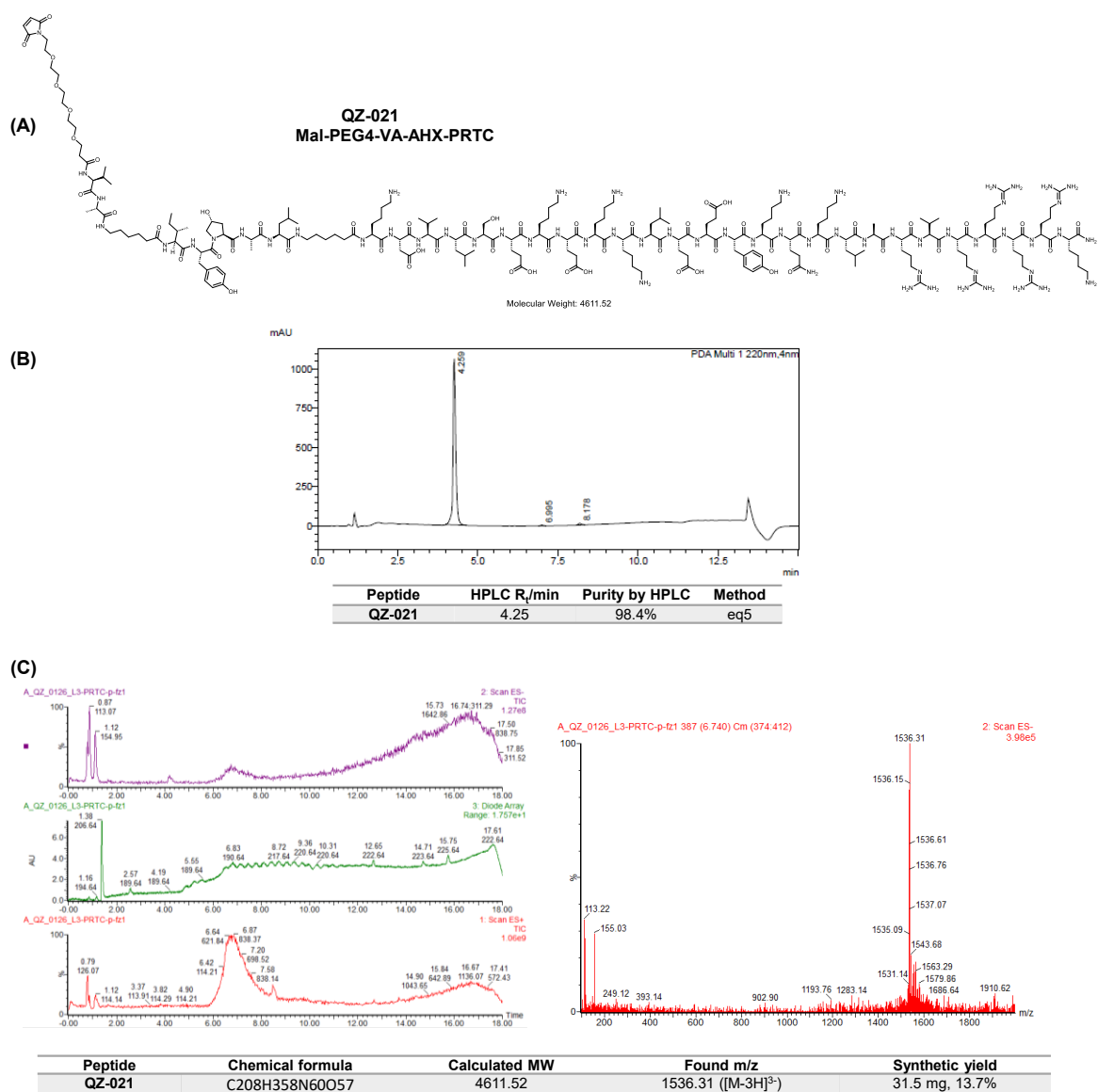


**Figure 7-20. QZ-021 peptide characterisation**

(A) Chemical structure of **QZ-021**. (B) HPLC chromatogram using eq5 gradient. (C) LC-MS chromatograms using eq20 gradient, UV trace, MS negative spectra.

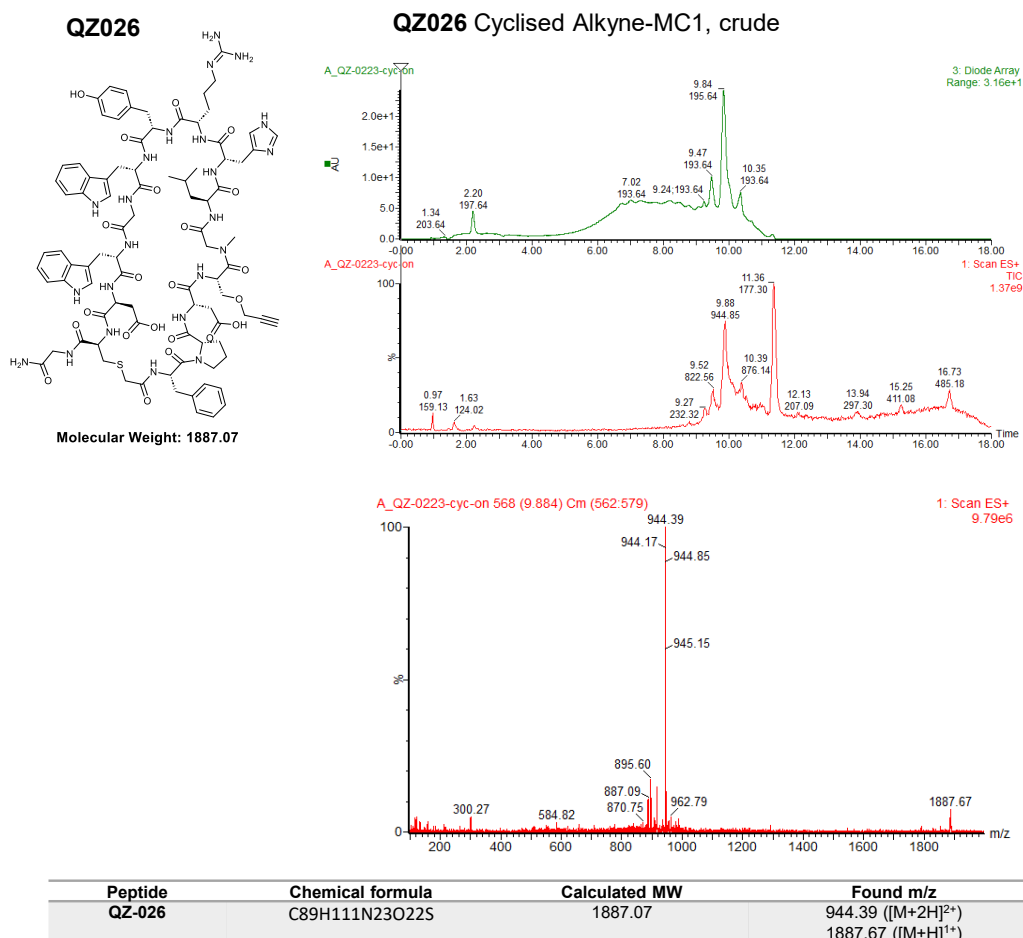


**Figure 7-21. QZ-026 crude peptide characterisation**

Chemical structure of **QZ-026** and the LC-MS chromatograms of the crude peptide using eq20 gradient, UV trace, MS positive spectra.



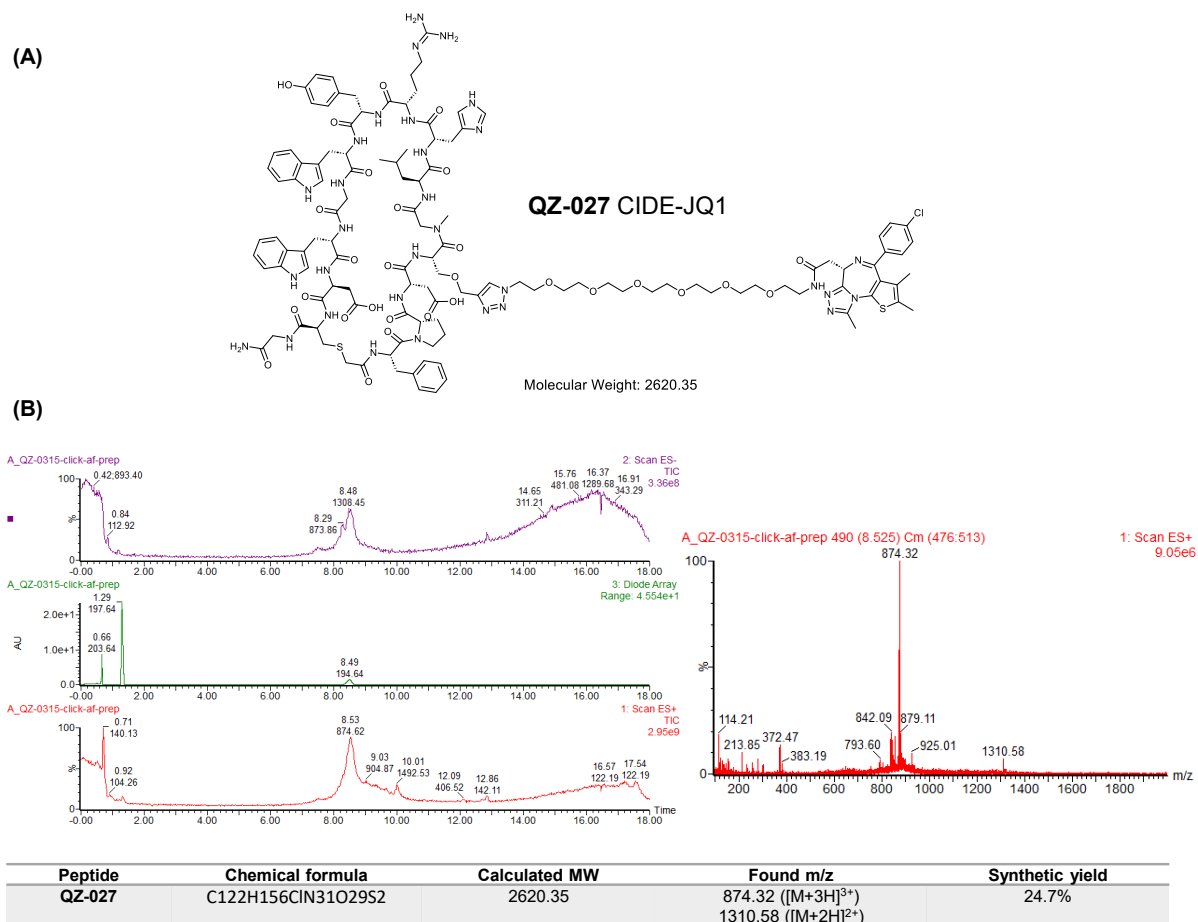


**Figure 7-22. QZ-027 peptide characterisation**

(A) Chemical structure of **QZ-027**. (B) LC-MS chromatograms using eq20 gradient, UV trace, MS positive spectra.

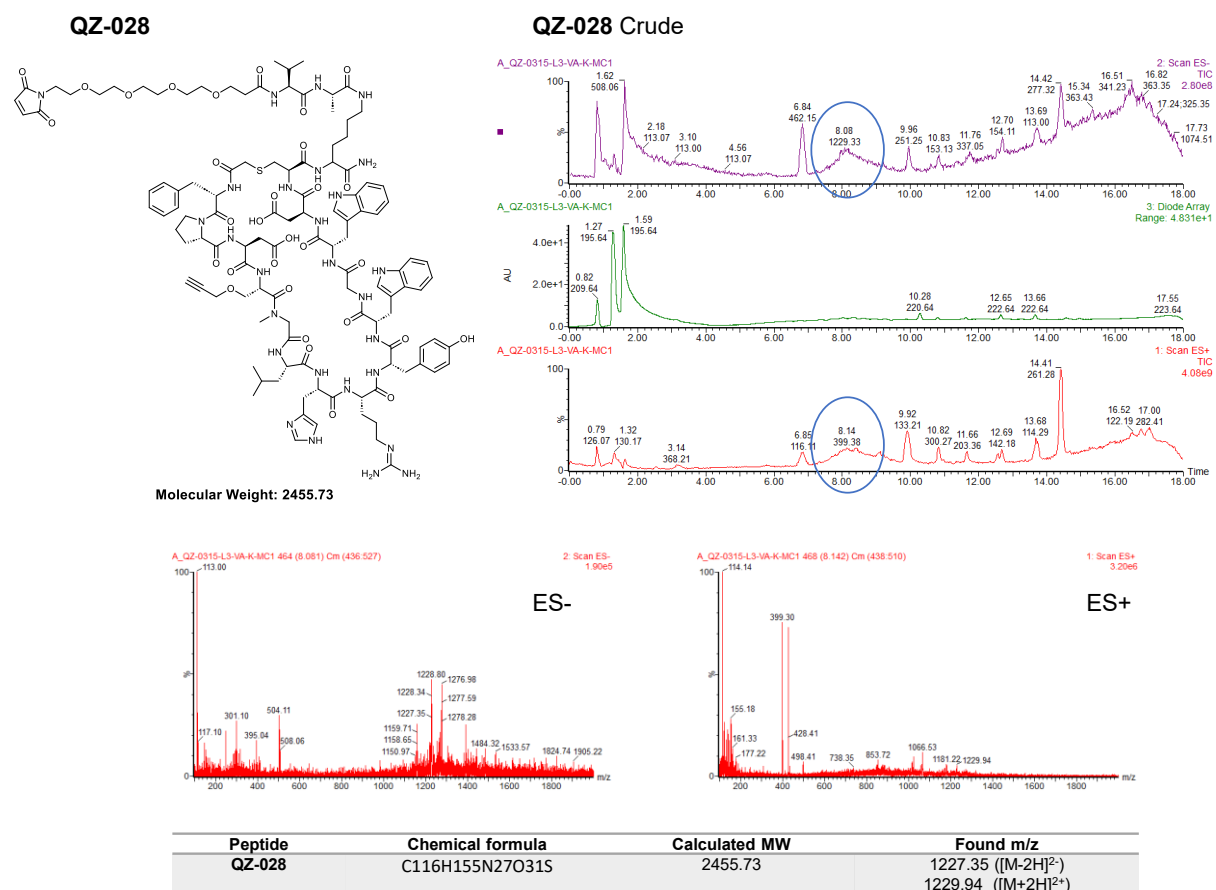


**Figure 7-23. QZ-028 crude peptide characterisation**

Chemical structure of **QZ-028** and LC-MS chromatograms using eq20 gradient, UV trace, MS positive and negative spectra.

## 7.2.4 Characterisation of ADCs in Chapter 3

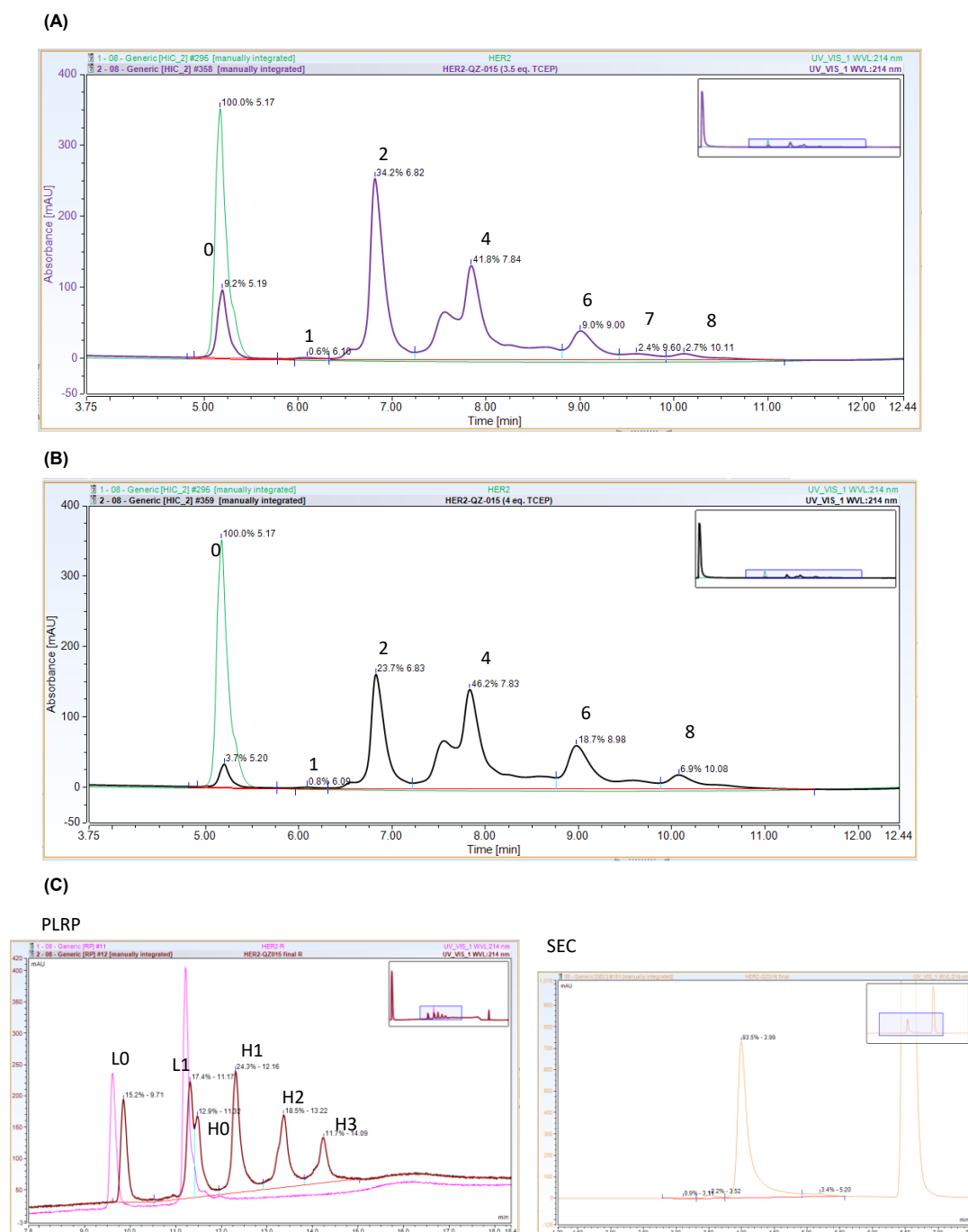


**Figure 7-24. Trastuzumab-QZ015 (HER2-15) ADC characterisation with hydrophobic interaction chromatography (HIC)**

Conditions: (A) TCEP (2.0 eq.), Linker-peptide (12 eq.), giving ADCs with DAR 3.3. (B) TCEP (2.3 eq.), Linker-peptide (12 eq.), giving ADCs with DAR 4. (C) TCEP (2.3 eq.), Linker-peptide (10.8 eq.), giving ADCs with DAR 3.8; MW: 153018 Da; EC280: 219736; Abs 0.1%: 1.436; Concentration: 5.85 mg/ml; DAR (PLRP): 3.6; Monomer (SEC): 93.5%; Endotoxin level: 0.121 EU/mg; Buffer: 30 mM Histidine, 175 mM Sucrose, PS20 0.02%, pH 6.

### B12

Concentration: 2.175 mg/mL in PBS

Volume: 2.12 mL

Amount: 4.61 mg

MW: 148052.26

EC280 = 220420 M<sup>-1</sup> cm<sup>-1</sup>

Abs 0.1% (=1 g/l) = 1.489

Endotoxin level: 0.092 EU/mg

Storage: +4°C

### B12-21 DAR 4

(3 eq., TCEP, 8 eq. payload)

DAR (HIC): 4.9

Monomer (SEC): 99.4%

Concentration: 4.93 mg/mL in FB

Volume: 2.1 mL

Amount: 10.4 mg

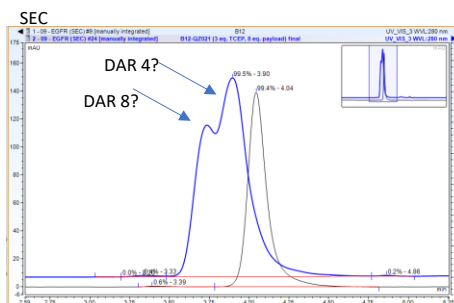
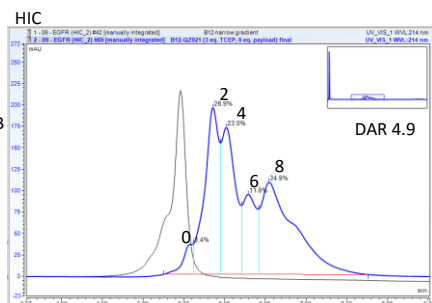
MW: 171110.86

EC280: 233765 M<sup>-1</sup> cm<sup>-1</sup>

Abs 0.1% (=1 g/l) = 1.366

Endotoxin level: 0.203 EU/mg

Storage: -20°C or below



### B12-21 DAR 8

(8 eq., TCEP, 12 eq. payload)

DAR (HIC): 7.1

Monomer (SEC): 99.3%

Concentration: 7.23 mg/mL in FB

Volume: 1.36 mL

Amount: 9.8 mg

MW: 180794.05

EC280: 239370 M<sup>-1</sup> cm<sup>-1</sup>

Abs 0.1% (=1 g/l) = 1.324

Endotoxin level: 0.209 EU/mg

Storage: -20°C or below

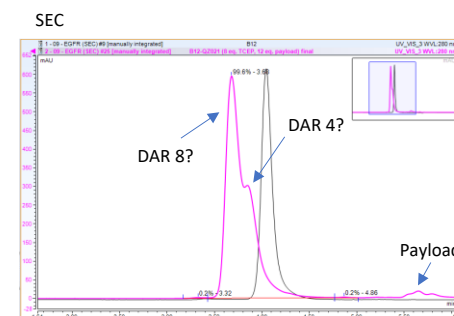
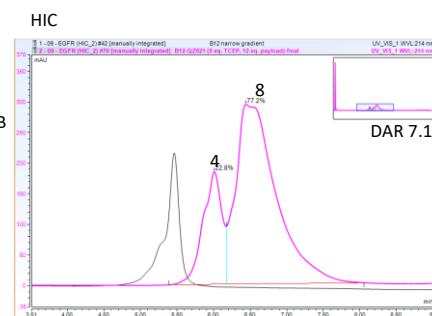


**Figure 7-25. B12-21 ADC characterisation data**

Formulation Buffer: 30 mM Histidine, 175 mM Sucrose, 0.02% PS20, pH 6.

### Cetuximab

Concentration: 1.99 mg/mL in PBS

Volume: 2.07 mL

Amount: 4.12 mg

MW: 145423.20

EC280 = 217440 M<sup>-1</sup> cm<sup>-1</sup>

Abs 0.1% (=1 g/l) = 1.495

Endotoxin level: 0.100 EU/mg

Storage: +4°C

### EGFR-21 DAR 4

(3 eq. TCEP, 8 eq. payload)

DAR (HIC): 4.2

Monomer (SEC): 99.1%

Concentration: 4.94 mg/mL in FB

Volume: 1.44 mL

Amount: 7.12 mg

MW: 160180.0

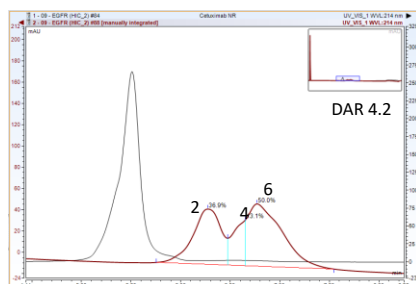
EC280: 225981 M<sup>-1</sup> cm<sup>-1</sup>

Abs 0.1% (=1 g/l) = 1.411

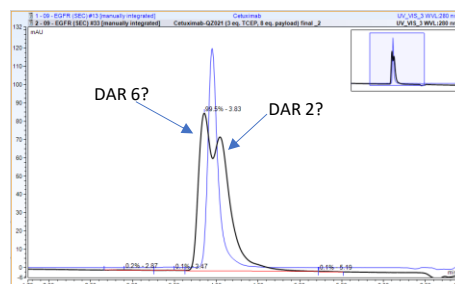
Endotoxin level: 3.724 EU/mg

Storage: -20°C or below

HIC



SEC



### EGFR-21 DAR 8

(8 eq. TCEP, 12 eq. payload)

DAR (HIC): 7.8

Monomer (SEC): 99.5%

Concentration: 3.66 mg/mL in FB

Volume: 1.42 mL

Amount: 5.2 mg

MW: 181393.06

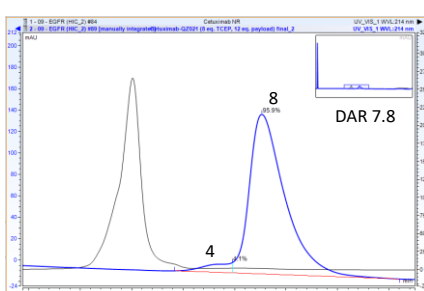
EC280: 238258 M<sup>-1</sup> cm<sup>-1</sup>

Abs 0.1% (=1 g/l) = 1.313

Endotoxin level: 3.912 EU/mg

Storage: -20°C or below

HIC



SEC

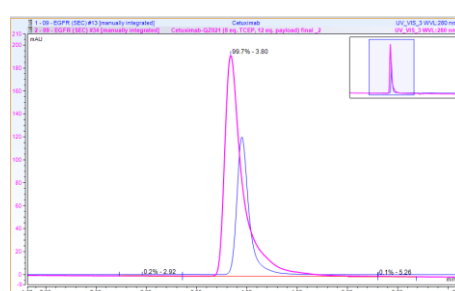


**Figure 7-26. EGFR-21 ADC characterisation data**

Formulation Buffer: 30 mM Histidine, 175 mM Sucrose, 0.02% PS20, pH 6.

## 7.2.5 Investigation of antibody conjugation: NAC assay of QZ-015

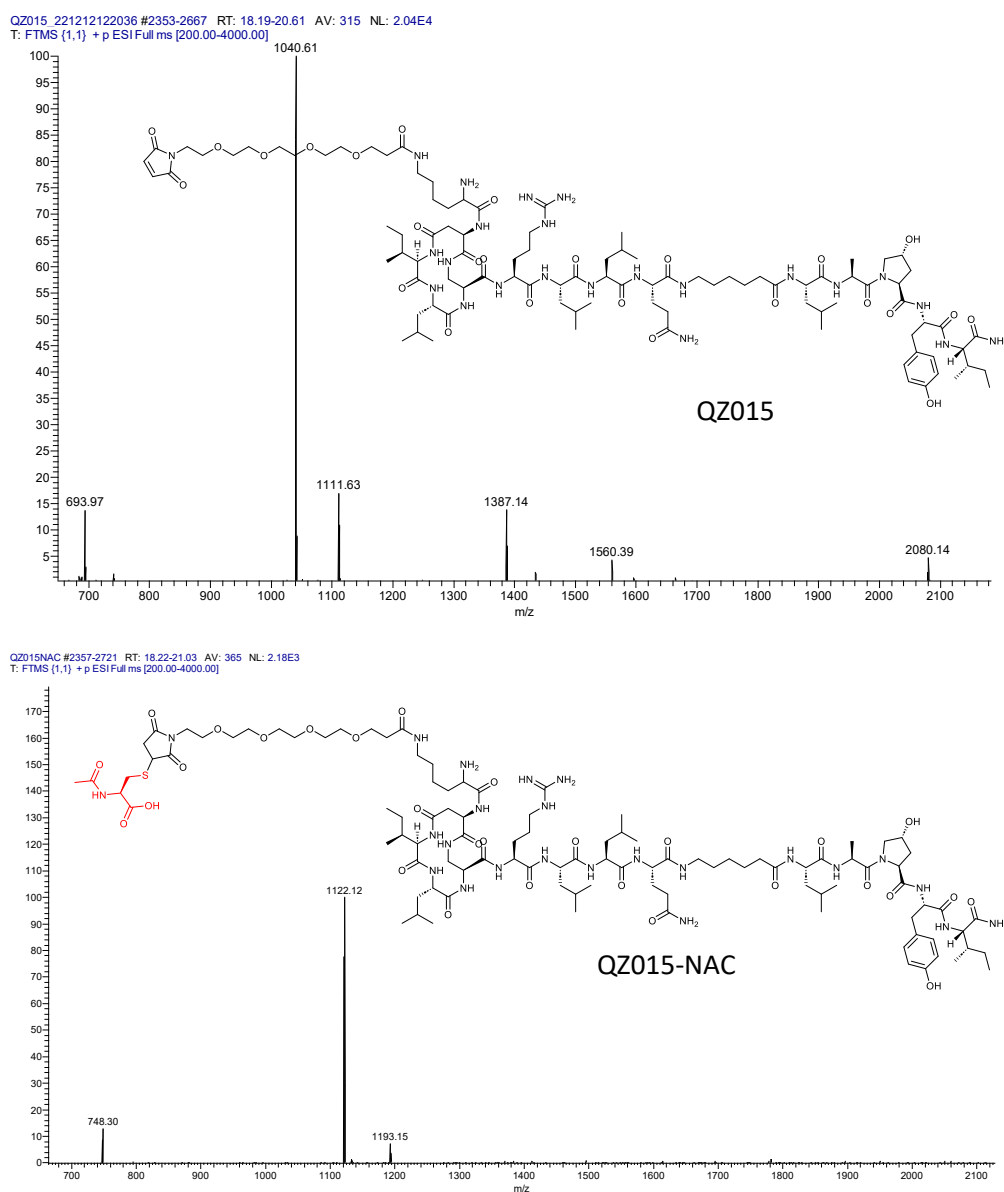


**Figure 7-27. Structure and MS positive spectra of QZ-015 before and after reaction with NAC.**

## 7.3 Reprint Permissions

Permissions to reproduce published figures and data are included in this section.

### Chapter 1

#### Section 1.1 to 1.4

2023/6/2 15:04	RightsLink Printable License	2023/6/2 15:04	RightsLink Printable License
ELSEVIER LICENSE TERMS AND CONDITIONS		I am an academic or government institution with a full-text subscription to this journal and the audience of the material consists of students and/or employees of this institute?	
Jun 02, 2023		No	
<hr/>		Portion	
This Agreement between Imperial College London -- Qisi Zhang ("You") and Elsevier ("Elsevier") consists of your license details and the terms and conditions provided by Elsevier and Copyright Clearance Center.		full chapter	
License Number		5518691360514	
License date		Mar 30, 2023	
Licensed Content Publisher		Elsevier	
Licensed Content Publication		Elsevier Books	
Licensed Content Title		Progress in Medicinal Chemistry	
Licensed Content Author		M. Maneiro,E. De Vita,D. Conole,C.S. Kounde,Q. Zhang,E.W. Tate	
Licensed Content Date		Jan 1, 2021	
Licensed Content Volume		60	
Licensed Content Issue		n/a	
Licensed Content Pages		124	
Start Page		67	
End Page		190	
Type of Use		reuse in a thesis/dissertation	
https://s100.copyright.com/CustomerAdmin/PLF.jsp?ref=1553e449-3df7-4fde-a45c-61dce167b210		1/9	
		https://s100.copyright.com/CustomerAdmin/PLF.jsp?ref=1553e449-3df7-4fde-a45c-61dce167b210	
		I am an academic or government institution with a full-text subscription to this journal and the audience of the material consists of students and/or employees of this institute?	
		No	
		Portion	
		full chapter	
		Circulation	
		100	
		Format	
		both print and electronic	
		Are you the author of this Elsevier chapter?	
		Yes	
		How many pages did you author in this Elsevier book?	
		13	
		Will you be translating?	
		No	
		Title	
		PhD thesis: Conditional Protein Degradation with Novel PROteolysis-Targeting Chimeras (PROTACs) and the Exploration of New Modalities	
		Institution name	
		Imperial College London	
		Expected presentation date	
		Nov 2023	
		Requestor Location	
		Molecular Sciences Research Hub 82 Wood Ln Imperial College London LONDON, W12 0BZ United Kingdom Attn: Imperial College London	
		Publisher Tax ID	
		GB 494 6272 12	

## Figure 1-9D

2023/10/19 17:44	RightsLink Printable License	2023/10/19 17:44	RightsLink Printable License
ELSEVIER LICENSE TERMS AND CONDITIONS		Start Page	1714
Oct 19, 2023		End Page	1731.e10
		Type of Use	reuse in a thesis/dissertation
		Portion	figures/tables/illustrations
		Number of figures/tables/illustrations	1
		Format	both print and electronic
		Are you the author of this Elsevier article?	No
		Will you be translating?	No
		Title of new work	PhD thesis: Conditional Protein Degradation with Novel PROteolysis-Targeting Chimeras (PROTACs) and the Exploration of New Modalities
		Institution name	Imperial College London
		Expected presentation date	Nov 2023
		Portions	Figure 2-B
		Requestor Location	Imperial College London 10 Shinfield Street First floor LONDON, W12 0HN United Kingdom Attn: Imperial College London
		Publisher Tax ID	GB 494 6272 12
<p>This Agreement between Imperial College London -- Qisi Zhang ("You") and Elsevier ("Elsevier") consists of your license details and the terms and conditions provided by Elsevier and Copyright Clearance Center.</p> <p>License Number 5652581291745</p> <p>License date Oct 19, 2023</p> <p>Licensed Content Publisher Elsevier</p> <p>Licensed Content Publication Cell</p> <p>Licensed Content Title Mapping the Degradable Kinome Provides a Resource for Expedited Degradation Development</p> <p>Licensed Content Author Katherine A. Donovan, Fleur M. Ferguson, Jonathan W. Bushman, Nicholas A. Eleuteri, Debabrata Bhunia, SeongShick Ryu, Li Tan, Kun Shi, Hong Yue, Xiaoxi Liu, Dennis Dobrovolsky, Baishan Jiang, Jinhua Wang, Mingfeng Hao, Inchul You, Mingxing Teng, Yanke Liang et al.</p> <p>Licensed Content Date Dec 10, 2020</p> <p>Licensed Content Volume 183</p> <p>Licensed Content Issue 6</p> <p>Licensed Content Pages 28</p>		<p>https://s100.copyright.com/CustomerAdmin/PLF.jpg?ref=04aeaa4f-dab9-4847-82ab-03a758990536</p> <p>1/9</p> <p>https://s100.copyright.com/CustomerAdmin/PLF.jpg?ref=04aeaa4f-dab9-4847-82ab-03a758990536</p>	

## Figure 1-13

ACS Publications  
Most Trusted. Most Cited. Most Read.

My Activity
 Publications

---

[RETURN TO ISSUE](#) | [< PREV](#) **LETTERS** [NEXT >](#)

### Antibody-PROTAC Conjugates Enable HER2-Dependent Targeted Protein Degradation of BRD4

Maria Maneiro, Nafsika Forte, Maria M. Shchepinova, Cyrille S. Kounde, Vijay Chudasama, James Richard Baker, and Edward W. Tate\*

**Cite This:** *ACS Chem. Biol.* 2020, 15, 6, 1306–1312  
 Publication Date: April 27, 2020  
<https://doi.org/10.1021/acscchembio.0c00285>  
 Copyright © 2020 American Chemical Society. This publication is licensed under [CC-BY](#).  
[Open Access](#)

Article Views: **34854**  
 Altmetric: **51**  
 Citations: **129**  
[LEARN ABOUT THESE METRICS](#)

[Share](#) [Add to](#) [Export](#)

ACS Chemical Biology

**PDF (4 MB)**

**Supporting Info (1)**

**SUBJECTS:** Biopolymers, Conjugate acid-base pairs, Degradation, Immunology, Peptides and proteins



## Chapter 2

Chapter 2 was based on the author's previous publication licensed under a Creative Commons Attribution 3.0 Unported Licence.

### Light-mediated multi-target protein degradation using arylazopyrazole photoswitchable PROTACs (AP-PROTACs)

Q. Zhang, C. S. Kounde, M. Mondal, J. L. Greenfield, J. R. Baker, S. Kotelnikov, M. Ignatov, C. P. Tinworth, L. Zhang, D. Conole, E. De Vita, D. Kozakov, A. McCluskey, J. D. Harling, M. J. Fuchter and E. W. Tate, *Chem. Commun.*, 2022, **58**, 10933 DOI: 10.1039/D2CC03092F

This article is licensed under a [Creative Commons Attribution 3.0 Unported Licence](#). You can use material from this article in other publications without requesting further permissions from the RSC, provided that the correct acknowledgement is given.

Read more about [how to correctly acknowledge RSC content](#).

## Figure 2-1B

2023/8/30 21:44

RightsLink Printable License

### ELSEVIER LICENSE TERMS AND CONDITIONS

Aug 30, 2023

This Agreement between Imperial College London -- Qisi Zhang ("You") and Elsevier ("Elsevier") consists of your license details and the terms and conditions provided by Elsevier and Copyright Clearance Center.

License Number	5618961307297
License date	Aug 30, 2023
Licensed Content Publisher	Elsevier
Licensed Content Publication	Tetrahedron
Licensed Content Title	Azobenzenes—synthesis and carbohydrate applications
Licensed Content Author	Florian Hamon,Florence Djedaini-Pilard,Francis Barbot,Christophe Len
Licensed Content Date	Dec 5, 2009
Licensed Content Volume	65
Licensed Content Issue	49
Licensed Content Pages	19
Start Page	10105
End Page	10123

<https://s100.copyright.com/CustomerAdmin/PLF.jsp?ref=07df453-99a0-4ded-95d0-589f9df2337f>


2023/8/30 21:44

RightsLink Printable License


Type of Use	reuse in a thesis/dissertation
Portion	figures/tables/illustrations
Number of figures/tables/illustrations	1
Format	both print and electronic
Are you the author of this Elsevier article?	No
Will you be translating?	No
Title	PhD thesis: Conditional Protein Degradation with Novel PROteolysis-TArgeting Chimeras (PROTACs) and the Exploration of New Modalities
Institution name	Imperial College London
Expected presentation date	Nov 2023
Portions	Figure 4
Requestor Location	Imperial College London 10 Shinfield Street First floor LONDON, W12 0HN United Kingdom Attn: Imperial College London
Publisher Tax ID	GB 494 6272 12
Total	0.00 GBP
Terms and Conditions	

<https://s100.copyright.com/CustomerAdmin/PLF.jsp?ref=07df453-99a0-4ded-95d0-589f9df2337f>

Figure 2-2B



[Home](#)[Help](#)[Live Chat](#)[Qisi Zhang](#)



**Arylazopyrazoles: Azoheteroarene Photoswitches Offering Quantitative Isomerization and Long Thermal Half-Lives**

Author: Claire E. Weston, Robert D. Richardson, Peter R. Haycock, et al  
Publication: Journal of the American Chemical Society  
Publisher: American Chemical Society  
Date: Aug 1, 2014

Copyright © 2014, American Chemical Society

**PERMISSION/LICENSE IS GRANTED FOR YOUR ORDER AT NO CHARGE**

This type of permission/license, instead of the standard Terms and Conditions, is sent to you because no fee is being charged for your order. Please note the following:


- Permission is granted for your request in both print and electronic formats, and translations.
- If figures and/or tables were requested, they may be adapted or used in part.
- Please print this page for your records and send a copy of it to your publisher/graduate school.
- Appropriate credit for the requested material should be given as follows: "Reprinted (adapted) with permission from {COMPLETE REFERENCE CITATION}. Copyright {YEAR} American Chemical Society." Insert appropriate information in place of the capitalized words.
- One-time permission is granted only for the use specified in your RightsLink request. No additional uses are granted (such as derivative works or other editions). For any uses, please submit a new request.

If credit is given to another source for the material you requested from RightsLink, permission must be obtained from that source.


[BACK](#)[CLOSE WINDOW](#)

© 2023 Copyright - All Rights Reserved | Copyright Clearance Center, Inc. | Privacy statement | Data Security and Privacy  
| For California Residents | Terms and ConditionsComments? We would like to hear from you. E-mail us at  
customercare@copyright.com

Figure 3-4



[Home](#)[Help](#)[Live Chat](#)[Qisi Zhang](#)



**Development of Stabilized Peptide-Based PROTACs against Estrogen Receptor  $\alpha$**

Author: Yanhong Jiang, Qiwen Deng, Hui Zhao, et al  
Publication: ACS Chemical Biology  
Publisher: American Chemical Society  
Date: Mar 1, 2018

Copyright © 2018, American Chemical Society

**PERMISSION/LICENSE IS GRANTED FOR YOUR ORDER AT NO CHARGE**

This type of permission/license, instead of the standard Terms and Conditions, is sent to you because no fee is being charged for your order. Please note the following:

- Permission is granted for your request in both print and electronic formats, and translations.
- If figures and/or tables were requested, they may be adapted or used in part.
- Please print this page for your records and send a copy of it to your publisher/graduate school.
- Appropriate credit for the requested material should be given as follows: "Reprinted (adapted) with permission from {COMPLETE REFERENCE CITATION}. Copyright {YEAR} American Chemical Society." Insert appropriate information in place of the capitalized words.
- One-time permission is granted only for the use specified in your RightsLink request. No additional uses are granted (such as derivative works or other editions). For any uses, please submit a new request.

If credit is given to another source for the material you requested from RightsLink, permission must be obtained from that source.

[BACK](#)[CLOSE WINDOW](#)

© 2023 Copyright - All Rights Reserved | Copyright Clearance Center, Inc. | Privacy statement | Data Security and Privacy  
| For California Residents | Terms and ConditionsComments? We would like to hear from you. E-mail us at  
customercare@copyright.com

**Figure 3-11**

2023/8/30 22:01 RightsLink Printable License		2023/8/30 22:01 RightsLink Printable License	
ELSEVIER LICENSE TERMS AND CONDITIONS		Type of Use	reuse in a thesis/dissertation
Aug 30, 2023		Portion	figures/tables/illustrations
This Agreement between Imperial College London -- Qisi Zhang ("You") and Elsevier ("Elsevier") consists of your license details and the terms and conditions provided by Elsevier and Copyright Clearance Center.		Number of figures/tables/illustrations	2
License Number 5560851052732		Format	both print and electronic
License date Jun 02, 2023		Are you the author of this Elsevier article?	No
Licensed Content Publisher Elsevier		Will you be translating?	No
Licensed Content Publication European Journal of Medicinal Chemistry		Title	PhD thesis: Conditional Protein Degradation with Novel PROteolysis-Targeting Chimeras (PROTACs) and the Exploration of New Modalities
Licensed Content Title Development of cell-permeable peptide-based PROTACs targeting estrogen receptor $\alpha$		Institution name	Imperial College London
Licensed Content Author Yuxuan Dai, Na Yue, Junni Gong, Chunxia Liu, Qifei Li, Jiaqi Zhou, Wenlong Huang, Hai Qian		Expected presentation date	Nov 2023
Licensed Content Date Feb 1, 2020		Portions	Table 1 and Figure 4A, 4B
Licensed Content Volume 187		Requestor Location	Imperial College London 10 Shinfield Street First floor LONDON, W12 0HN United Kingdom Attn: Imperial College London
Licensed Content Issue n/a		Publisher Tax ID	GB 494 6272 12
Licensed Content Pages 1		Total	0.00 GBP
Start Page 111967		Terms and Conditions	
End Page 0			
<a href="https://s100.copyright.com/CustomerAdmin/PLF.jsp?ref=f17b8d5f-1b83-4dd6-948a-5ea16640da87">https://s100.copyright.com/CustomerAdmin/PLF.jsp?ref=f17b8d5f-1b83-4dd6-948a-5ea16640da87</a>		<a href="https://s100.copyright.com/CustomerAdmin/PLF.jsp?ref=f17b8d5f-1b83-4dd6-948a-5ea16640da87">https://s100.copyright.com/CustomerAdmin/PLF.jsp?ref=f17b8d5f-1b83-4dd6-948a-5ea16640da87</a>	

**Figure 3-14**

[Theranostics](#), 2020; 10(8): 3708–3721.

Published online 2020 Feb 19. doi: [10.7150/thno.41677](https://doi.org/10.7150/thno.41677)

PMCID: PMC7069095

PMID: [32206117](https://pubmed.ncbi.nlm.nih.gov/32206117/)

## A cell-permeable peptide-based PROTAC against the oncoprotein CREPT proficiently inhibits pancreatic cancer


[Danhui Ma](#),<sup>1</sup> [Yutian Zou](#),<sup>1,2</sup> [Yunxiang Chu](#),<sup>3</sup> [Zhengsheng Liu](#),<sup>4</sup> [Gaochao Liu](#),<sup>5</sup> [Jun Chu](#),<sup>1</sup> [Mengdi Li](#),<sup>1</sup> [Jiayu Wang](#),<sup>1</sup> [Shi-yong Sun](#),<sup>6,✉</sup> and [Zhijie Chang](#)<sup>1,✉</sup>

► [Author information](#) ► [Article notes](#) ► [Copyright and License information](#) ► [PMC Disclaimer](#)

[Copyright](#) © The author(s)

This is an open access article distributed under the terms of the Creative Commons Attribution License (<https://creativecommons.org/licenses/by/4.0/>). See <http://ivyspring.com/terms> for full terms and conditions.


Figure 3-20



?

Help ▾

Live Chat



**Targeted degradation via direct 26S proteasome recruitment**

**Author:** Charlene Bashore et al  
**Publication:** Nature Chemical Biology  
**Publisher:** Springer Nature  
**Date:** Dec 28, 2022

Copyright © 2022, Genentech, Inc. 2022

**Creative Commons**

This is an open access article distributed under the terms of the [Creative Commons CC BY](#) license, which permits unrestricted use, distribution, and reproduction in any medium, provided the original work is properly cited.

You are not required to obtain permission to reuse this article.

To request permission for a type of use not listed, please contact [Springer Nature](#)

© 2023 Copyright - All Rights Reserved | [Copyright Clearance Center, Inc.](#) | [Privacy statement](#) | [Data Security and Privacy](#)  
| [For California Residents](#) | [Terms and Conditions](#)Comments? We would like to hear from you. E-mail us at [customer@copyright.com](mailto:customer@copyright.com)